

Naval Research Laboratory

Washington, DC 20375-5320



NRL/MR/6720--96-7802

Advanced Radiation Theory Support Annual Report 1995, Final Report

*Hydrodynamics Branch
Plasma Physics Division*

March 18, 1996

19960411 103

Approved for public release; distribution unlimited.

DTIC QUALITY INSPECTED 1

REPORT DOCUMENTATION PAGE			Form Approved OMB No. 0704-0188
<p>Public reporting burden for this collection of information is estimated to average 1 hour per response, including the time for reviewing instructions, searching existing data sources, gathering and maintaining the data needed, and completing and reviewing the collection of information. Send comments regarding this burden estimate or any other aspect of this collection of information, including suggestions for reducing this burden, to Washington Headquarters Services, Directorate for Information Operations and Reports, 1215 Jefferson Davis Highway, Suite 1204, Arlington, VA 22202-4302, and to the Office of Management and Budget, Paperwork Reduction Project (0704-0188), Washington, DC 20503.</p>			
1. AGENCY USE ONLY (Leave Blank)	2. REPORT DATE	3. REPORT TYPE AND DATES COVERED	
	March 18, 1996		
4. TITLE AND SUBTITLE Advanced Radiation Theory Support Annual Report 1995, Final Report			5. FUNDING NUMBERS
6. AUTHOR(S) Radiation Hydrodynamics Branch			
7. PERFORMING ORGANIZATION NAME(S) AND ADDRESS(ES) Naval Research Laboratory Washington, DC 20375-5320			8. PERFORMING ORGANIZATION REPORT NUMBER NRL/MR/6720-96-7802
9. SPONSORING/MONITORING AGENCY NAME(S) AND ADDRESS(ES) Defense Nuclear Agency 6801 Telegraph Road Alexandria, VA 22310-3398			10. SPONSORING/MONITORING AGENCY REPORT NUMBER
11. SUPPLEMENTARY NOTES This research was sponsored by the Defense Nuclear Agency under Job order Title, "Advanced Concepts," MIPR No. 95-2062			
12a. DISTRIBUTION/AVAILABILITY STATEMENT Approved for public release; distribution unlimited.		12b. DISTRIBUTION CODE A	
13. ABSTRACT (Maximum 200 words) This report describes the work of the Radiation Hydrodynamics Branch during FY 95 in support of the DNA PRS program. Critical issues covered are: (1) Design and diagnosis of ACE 4 simulator experiments, (2) Investigations of K-shell emission from medium atomic number elements, (3) Non-thermal warm x-rays, (4) Puff-on-wire Z pinch loads, (5) Implosion stability, (6) Stabilization of implosions through rotation, (7) Diagnosing medium atomic number plasmas, (8) Calculating measurable radiation profiles, and (9) Radiation physics issues in yield and fidelity enhancement.			
14. SUBJECT TERMS Z-pinch Plasma radiation sources Radiation MHD			15. NUMBER OF PAGES 152
ACE 4 Medium atomic number elements Implosion stability			16. PRICE CODE
17. SECURITY CLASSIFICATION OF REPORT UNCLASSIFIED	18. SECURITY CLASSIFICATION OF THIS PAGE UNCLASSIFIED	19. SECURITY CLASSIFICATION OF ABSTRACT UNCLASSIFIED	20. LIMITATION OF ABSTRACT UL

CONTENTS

Executive Summary	E-1
I. Designing and diagnosing ACE 4 aluminum array experiments	1
II. Investigation of K shell emission from moderate atomic number implosions	20
III. Nonthermal radiation from imploding Z pinch plasmas	42
IV. Puff-on-wire Z pinch loads	48
V. Implosion stability	55
VI. Implosions, equilibria, and stability of rotating radiating Z-pinch plasmas	81
VII. Diagnosing mid-atomic number Z pinch plasmas	106
VIII. Calculating measurable x-ray quantities from simulated PRS implosions ..	128
IX. Yield and fidelity enhancement by exploiting the radiation physics of optimized mixtures	140

EXECUTIVE SUMMARY

This report presents in detail the theory support of DNA's Plasma Radiation Source (PRS) RAST program carried out by NRL's Radiation Hydrodynamics Branch (Code 6720) in FY 1995. The major and continuing goals of the PRS program are focused in two areas: improved yields and fidelity. Put another way, both *adequate* and *accurate* doses must be available for meaningful effects testing. Of course, unlimited resources are not available to accomplish this mission, and one promising option for cost-effective testing is embodied in ACE 4, the most powerful of the inductive energy store (IES) machines yet built. The work described in this report's nine sections is aimed not only at the general objectives of yield and fidelity, but specifically, how to accomplish them in the environment of the particular challenges posed by ACE 4. The subjects discussed are, section by section:

- (1) A series of initial Al wire array experiments on ACE 4 was carefully designed using all of the knowledge which has been obtained by careful benchmark experiments on other high-current machines. ACE 4 performed poorly compared to these other machines (Double EAGLE, Phoenix, Saturn, and Blackjack 5), with K shell yields about an order of magnitude below that routinely obtained at similar currents. This section discusses what is known about the load dynamics requirements for good yield, as well as the thorough and systematic experiments on several machines which have provided such knowledge. Although load stability is undoubtedly an important issue, the initial poor results on ACE 4 probably resulted from power flow problems. Methods of correcting and/or working around these problems are suggested and will be pursued.
- (2) One of the requirements for greater fidelity is to produce harder x-rays. This means stripping higher atomic number elements of more electrons, which will inevitably strain available machine energies. This section describes an extensive preliminary investigation of this problem carried out with detailed radiation hydrodynamic simulations. Specific results are presented for Al, Ar, Ti, and Kr. Two of the important conclusions are that there was a Z dependent lag in ionization into the K shell that adversely affects the emission, becoming worse with increasing atomic number, and that opacity and inner shell absorption were also important limiters of the K shell power. The plasma loads generally remained in the inefficient regime in these simulations, in which emission scales as

the square of the mass.

(3) One option for obtaining hard photons that initially seems very attractive is to employ nonthermal processes in which hot electrons either produce bremsstrahlung within the load plasma or excite inner shell K alpha radiation. In this section it is shown quantitatively, using optimistic assumptions regarding the internal pinch physics, that these processes are so inefficient that they are not likely to be interesting sources in the 20-100 keV range.

(4) A possible technique to improve both yield and fidelity in the mass squared regime of machine-load coupling is to implode a gas puff onto a wire located on axis. 1-D modeling of the radiative implosion dynamics of such an approach is described in Sec. IV. Theory indicates that at small mass loads the puff-on-wire configuration should outperform the puff-only loads on ACE 4. The presence of the on-axis wire serves to increase the ion density. An initial series of experiments on Double EAGLE in which an Ar puff stagnated onto a central Ti wire showed significant increases in the yield above photon energies of 4 keV. This bodes well for the technique as a fidelity as well as yield enhancer.

(5) The Rayleigh-Taylor (RT) instability is a potential threat to the viability of PRS loads, especially when the initial radius, runin time, and/or current risetimes are large. The RT instability occurs in the Z pinch environment because a magnetic field, with essentially no mass or inertia, accelerates a fluid, namely the pinch plasma, of finite mass. X-ray yields are reduced when this instability grows too rapidly since some fraction of the radial kinetic energy will be transformed to axial kinetic energy, and the compression will be disrupted. Section V presents detailed results for growth rates for loads smoothly varied from a shell to a uniform fill. A tradeoff is noted between the enhanced stability of filled cylinders and the attendant reduction in load kinetic energy. The calculated yields of the stable loads are superior to those of thin shells, indicating in this case that the tradeoff is worthwhile. An investigation of more complex tailored density distributions has been undertaken, and will be continued in the future.

(6) Countering the threat of RT instabilities by deliberately inducing rotation in Z pinches is investigated in this section. It is found that such a technique does help stabilize long-wavelength modes in the run-in phase. However, the short-wavelength modes are not likely to be affected by rotation, and therefore, to improve the yield and/or power in PRS applications, this method should

be employed in combination with other methods of stabilization such as tailored density profiles.

(7) For years, the K shells of several elements, such as neon, aluminum, and argon, have served the dual role of both providing the radiation needed for DNA's simulation capability and diagnosing the pinch. There is of course no fundamental reason why other atomic shells should not be satisfactory for such purposes, especially when enhanced fidelity is desired and the load design is constrained by the chemical or mechanical properties of the materials. The L shell of krypton, for instance, radiates copiously in the 1.6-2.0 keV region of the x-ray spectrum. This section presents the results of an effort to bring the Branch's L shell data base closer to the standard of comprehensiveness set by our extensive K shell capability. Of great importance is the discovery of several new diagnostics of the plasma conditions, including the use of satellite to resonance line ratios to infer the heating rate of the pinch.

(8) The ultimate test of any theory or numerical simulation is: does it agree in large measure with experiment? Can it be used to interpret experimental results and also to study tradeoffs in experimental design? To ascertain the degree to which this is true or false requires that the simulation predict quantities which are measureable, preferably those which are readily and routinely measured. Much of the data from Z pinch experiments consists of filtered spectrally and spatially resolved radiation profiles. This section describes progress and results in developing the capability to predict pinhole images of pinches, resolved and spectrally filtered to whatever degree is required to conform to the capabilities of the instruments deployed on a particular experiment. An example of how this diagnostic comparison will be carried out in practice is given for an aluminum wire array implosion.

(9) Last year's report described how both yield and fidelity were improved by using Mg-coated Al wires on Double EAGLE. Reduction of the average line opacity improved the K shell emissivity, and adding x-rays from a broader range of energies enhanced simulation fidelity. To move toward *optimization* of this highly promising approach, the final section of this report investigates *all four* elements with atomic numbers 11-14. It is concluded that the method is amenable to increased atomic number elements, and that had the Mg coat been a Si coat, the yield would have doubled instead of increasing by 28-50%. This conclusion assumes that the Si cold start would be similar spatially and thermally to that of the Mg in the Double EAGLE experiments.

I. DESIGNING AND DIAGNOSING ACE 4 ALUMINUM ARRAY EXPERIMENTS

A. Background: Double Eagle, Saturn, BJ5, and Phoenix Experiments

ACE 4 is the first inductive-store generator to be considered for use as a plasma radiation source (PRS) for NWET applications. Some PRS work had been done on the FALCON generator at Physics International Co. (PI) to demonstrate the role of a plasma opening switch (POS) on PRS performance. It was used to shorten the current risetime and to increase K-shell yields from given initial diameter, neon gas puff implosions.¹ The shortened risetime allowed more kinetic energy to be generated starting from the given initial diameter. The larger implosion energy allowed neon to enter a region in (gas puff mass) - (implosion velocity) space where the most efficient conversion of kinetic energy into K-shell radiation takes place. Generally, an inductive-store machine is designed to have a long current risetime and a POS that shortens this risetime. ACE 4 was designed as a bremsstrahlung machine with a large inductance and with this long risetime feature built in.

Because ACE 4 has a relatively long current risetime, with or without an opening switch, it is necessary to do large radius PRS experiments in order to ignite the K-shell of either aluminum or argon. In general, as pulse-power machines scale up in energy, it is necessary to initiate PRS implosions from larger radii. For this reason, the viability of large radii implosions needs to be assessed on existing non-inductive-store machines in order to establish benchmarks for similar experiments on ACE 4.

Aluminum Double Eagle experiments were designed late last fiscal year to increase K-shell yields at large array radii (and, therefore, for longer run-in time implosions). These experiments achieved higher K-shell yields from larger array diameters than had ever been achieved before.² The measured yields and the calculated conversion efficiencies (of kinetic energy into kilovolt x rays) are listed in Table I. The newly measured Double Eagle yields differed in another way from the old yields: they had a maximum that was shifted to higher implosion velocities (see Fig. (1)). This put Double Eagle in closer agreement with Saturn and Phoenix results than it had been before.³ These three sets of experiments clearly established that K-shell yields were maximized in a region of (load mass) - (implosion velocity) space, shown in Fig. (1), that is predictable from present theory. This result provides an important benchmark for ACE 4.

The analysis and interpretation of some Saturn Al spectral data was also finished late last year and documented.⁴ The data was several years old and had been obtained through partial DNA support. It consisted of pinhole photographs, which were scanned; PCD traces giving the x-ray pulselwidth of the implosion; digitized spectral data; and electrical and thermal measurements of power and yield. The K-shell yield data, which is shown in Fig. (2) of Ref. (5) on page 42, exhibited a well-defined peak when plotted as a function of the diameter of the wires used in each of the loads. Software was developed to automatically determine a consistent set of pinch parameters from the complete set of spectral data. These parameters included pinch diameter, pulselwidth, average power output, and spectral line ratios. The observed power and the computed line ratios were then compared to theoretical predictions of these quantities, which had been calculated as a function of an average electron temperature and an average ion density of the observed-sized

Table I. New Double Eagle Al Z-pinch Experiments

Wire Diam (mil)	Array Mass ($\mu\text{g}/\text{cm}$)	Array Diam (cm)	η	Number of wires	Kinetic Energy (kJ)	K-shell Yield (kJ)	Conversion Efficiency (%)
0.7	161	3.8	6.2	24	80	31.7	40
0.7	161	3.2	5.1	24	66	34.4	52
0.8	210	4.0	4.8	24	85	31.3	37
0.8	210	2.75	3.5	24	61	40.0	66
1.0	246	2.55	2.85	18	59	55.4	94
1.0	328	2.2	2.0	24	54	42.2	78

emission region. A relative measure of the amounts of mass radiating in the K-shell in this series of experiments could thus be obtained from the inferred ion densities of the known-sized plasmas. The ratios of the masses of the radiating regions to the masses of the original wire arrays were then computed. These mass fractions are plotted in Fig. (3) of Ref. (5) on page 43 as a function of the diameter of the wires used in the arrays. Figs. (2) and (3) of Ref. (5) showed a one-to-one correspondence between the yields that were observed in the Saturn experiments and the fractional amounts of load mass that were able to radiate in the K-shell on-axis. Since ACE 4 is expected to produce currents that are comparable to Saturn's, the same data analysis procedures will be needed in analyzing ACE 4 experiments and in benchmarking them against these Saturn results.

The data analysis that produced Fig. (3) of Ref. (5) provided an essential insight into the dynamics of wire array z-pinches. It suggested that when the wires were too large, they did not explode properly, and, when they were too small, they did not implode properly. The inferred trend in radiating mass proved that wire thickness is an important factor in determining K-shell yield, especially on a short risetime machine like Saturn. A new set of large array diameter Al experiments was then designed to demonstrate that one could work around the negative yield findings that had shown up in the early Saturn experiments. These new experiments were proposed to Sandia during the DNA/French data exchange meeting, which was held at Sandia. They were successfully performed on Saturn shortly thereafter and their yield behavior was discussed at the DNA PRS Workshop by C. Deeney.

The shot matrix for this second set of Saturn experiments is given in Table II. The location of these shots in (load mass) - (implosion velocity) space, i.e., in $(m - v_f)$ space, is shown in Fig. (2). Mainly, the experiments were designed to investigate yield behavior around the upper boundary, $(m_{BP})_{Soft}$, of the efficient emission region. This (mass breakpoint) boundary was calculated using soft implosion, z-pinch calculations.⁶ The location of the boundary, $(m_{BP})_{Hard}$, that is calculated from hard implosion calculations⁷ is also shown in Fig. (2). As the 30 wire datapoint at $263 \mu\text{g}/\text{cm}$ shows, there was little, if any, falloff in yield near the hard implosion boundary in these experiments. This demonstrates that some of the softening of implosions may be caused by shear-driven turbulence when an insufficient number of wires are used in the implosion.

These experiments were designed to increase the mass participation in K-shell emission on-

axis by increasing the number of wires in the arrays, by decreasing their size, and by moving the return current path out to a radius of 2.5 cm in order to reduce implosion asymmetries. The larger wire number and larger return current radius increased the symmetry and, therefore, the 1-D character of the implosions. The smaller wire sizes allowed the wires to explode more completely before implosion began. However, by increasing the wire number, the current flow to each wire was reduced. The low yields of the 1.2 and 1.0 mil 42 wire shots indicate that this reduction may have contributed to an inadequate explosion of these wires. When only 30 wires were used, the 1.0 mil wire shot performance improved markedly. The 30, 1 mil, wire shot also outperformed the best yielding of the shots in Fig. (2) of Ref. (5). This shift up the mass breakpoint curve of the maximum yielding of the aluminum wire shots on Saturn, which was predicted, is displayed in Fig. (1).

These experiments also produced a somewhat unexpected result. While the yields of the 42 wire shots were slightly lower than those of the nearby 30 wire shots, the x-ray pulsewidths of the 42 wire shots were shorter than those of the 30 wire shots, i.e., the x-ray powers had increased. This suggested that both x-ray yield and pulsewidth could be independently controlled by carefully adjusting both the wire number and wire size in PRS loads. To test this idea, a new set of experiments needed to be done in which the array mass was fixed and the number of wires was varied. The design of such experiments is facilitated by plotting mass contours in (wire-size) - (wire-number) space. Two were computed. They are shown in Figs. (3) and (4) for Al and Ti wires respectively. The circles on the Al wire contours show, for example, how one could approximately construct a $200 \mu\text{g}/\text{cm}^2$ load from 0.6, 0.7, 0.8, 0.9, or 1.0 mil wires by using 40, 30, 23, 18, or 14 wires respectively. These contours were presented to Sandia, and they stimulated a new series of experiments on Saturn that did, indeed, produce x-ray pulsewidth variations for approximately a given K-shell yield. However, the total yields did go up as the power increased. As the wire number increased and the gap spacing between wires decreased, the implosions became more symmetric and 1-D-like. These experiments indicate that arrays will implode to the same final pinch radius, independent of the initial array radius, when the gap spacing between wires is initially less than 1 mm. These findings will need to be carried over and tested on ACE 4.

Finally, because Double Eagle, Phoenix, and Blackjack 5 (BJ5) generate comparable currents, it is puzzling that the maximum yields seen on Double Eagle and Phoenix occurred at different locations in the efficient emission region^{2,3} (see Fig. (1)). Moreover, the Double Eagle yields appear to be in agreement with earlier published, BJ5 yields.^{8,9} However, this BJ5 data was incomplete. More data is needed to help resolve the difference between Phoenix and Double Eagle results and between Double Eagle and Saturn results. However, during the year, BJ5 experiments had to be piggybacked onto debris and diagnostic testing at MLI. This testing placed constraints on the kind and number of experiments that could be done, so the results obtained from them were suggestive, but not definitive. Two centimeter length wires could not be used, for example, nor could small diameter arrays or large wire number arrays. Undiagnosed changes in machine power flow had also occurred, so that BJ5 could not reproduce earlier yield benchmarks that had been obtained with a canonical MLI load. The yields were lower as a result of power flow degradation.

The proposed BJ5 experiments and the measured yields are shown in Table III. The experiments were designed to explore regions of $m - v_f$ space where Phoenix and Double Eagle had their best performance (see Fig. (1)), albeit with 2 cm length loads. There was also an attempt to compare

Table II. Saturn Thin-wire Aluminum Experiments

Return current radius = 2.5 cm, array length = 2.0 cm

Wire Diam (mil)	Array Mass ($\mu\text{g}/\text{cm}$)	Array Diam (mm)	# Wires	η	Y_K (kJ)
1.2	827	15.8	42	2.7	13
1.0	575	20.5	42	4.6	22
0.9	465	30.0	42	7.4	72
0.9	465	24.0	42	6.5	65
0.9	465	18.6	42	5.15	64
1.0	410	30.0	30	8.5	87
1.0	410	24.0	30	7.25	93
0.8	368	30.0	42	9.4	70
0.8	368	24.0	42	7.95	75
0.8	368	22.2	42	7.4	66
0.8	263	30.0	30	12.8	77

18 wire with 24 wire performance (as had been done on Double Eagle), and to see if one could get reasonable performance at large array diameters by taking advantage of the large 10 cm return current diameter that was being used in the debris tests. The results from these experiments are shown in Fig. (5). There is a suggestion in these results that BJ5 matches Double Eagle more than Phoenix performance. They also suggest the importance of wire size, wire length, array diameter, and the generator on the PRS performance of large diameter, long run-in time implosions.

Table III. Blackjack 5 Aluminum Experiments

Return current radius = 5.0 cm, array length = 4.0 cm

Wire Diam (mil)	Wire Mass ($\mu\text{g}/\text{cm}$)	Array Diam (mm)	K.E. (kJ)	# Wires	η	Y_K (kJ)
0.8	158	30	115	18	4.3	24
0.9	199	40	152	18	4.5	24
1.0	246	30	128	18	3.1	29
0.9	266	35	145	24	3.2	19

There is one important load parameter whose influence on PRS performance has yet to be systematically investigated. An early set of experiments at Phoenix using both 2 cm and 3 cm

length arrays had produced low yields for the 3 cm shots that could not be explained. Their x-ray conversion efficiencies were less than 30%. Earlier shots on Phoenix with 4 and 5 cm length wires had 30% or more conversion efficiencies. A series of experiments was, therefore, planned on Phoenix to investigate systematically whether or not an array length dependence to PRS performance existed. DNA/RAST had funded these experiments a year ago on Phoenix, but they were not done because of machine problems. The power flow on Phoenix has since been improved, transmission line parameters have been measured, and a more reliable circuit model has been derived than had existed as part of the original machine design. Thus, a new attempt was made to reevaluate the design and to carry out the length variation experiments this year, but it also failed. Thus, no guidance is yet available on how to optimize load performance on ACE 4 as a function of array length.

B. ACE 4 Circuit Models

The biggest risk to scaling PRS loads to high current, inductive-store machines is often assumed to be the requirement for stable, large array diameter implosions. This assumption is misleading. An equal, perhaps greater, risk is that the power flow to the load will not be well understood or controlled. Load performance degradation occurs at any array diameter when power flow symmetry is not maintained since asymmetries drive load instabilities, which lead to bad implosions, and bad implosions do not have large x-ray yields. The Double Eagle and Saturn experiments described above demonstrate that pulse power generators can be built with symmetric and reproducible power flow, which can be described by dependable circuit models. Load designs can then be found that convert 6% and more of the Marx bank energy into kilovolt x rays.

ACE 4 was originally conceived to be a relatively low (26 nH) inductive store coupled by way of a low inductance MITL (10 nH) to PRS loads (see Fig. (6)). The short-circuit load current from this generator is shown in Fig. (7). It rises to 8 MA in roughly 120 ns following the opening of the POS at 1 μ s. This version of ACE 4 is capable of imploding a 4 cm long aluminum load of 328 μ g/cm from a radius of 3 cm to energies in excess of 300 kJ. This implosion is optimal for producing K-shell x rays, and it corresponds to roughly 7% conversion of the stored 4.66 MJ of Marx bank energy into load kinetic energy. One would expect in excess of 150 kJ of kilovolt radiation would be produced if half of this kinetic energy could be radiated in the K-shell.

The Fig. (6) version of ACE 4 has yet to be realized. A later, more inductive version, shown in Fig. (8), began to be tested this year. Only half of the potentially available Marx bank energy was, at present, utilized, i.e., connected to the PRS load; and half of the power flow through the transmission line was inductively grounded (600 nH). The plasma opening switch was changed to a plasma flow switch (depicted as a coaxial section with a variable inductance initially at 27 nH), and the machine was operated in a tandem puff mode. Note that the circuit in Fig. (8) has 150 nH more inductance connecting the Marx bank to the load than the circuit in Fig. (6). Some of this inductance has recently been removed. The 94 nH feed was reduced to 60 nH; also, the inductive ground was removed.

How the plasma flow switch works is uncertain. Two versions of its operation were used to project ACE 4, PRS load performance. In one, the switch is given a low impedance and the current into a short circuit rises slowly in 100 ns. This power flow model is labeled 2a. If the switch is given a much higher impedance, the current into a short circuit load rises much more rapidly (within 20

ns). This power flow model is labeled 2b. A second version of model 2b, labeled 2c, was also investigated. In this case the inductive ground was eliminated and the 94 nH inductance between the Marx bank and the coaxial switch was reduced to 60 nH. This had the effect of increasing the current flow into a short-circuit load by 1 MA. The short-circuit currents for each of these three power flow models are presented in Fig. (9). For each of these cases, the initial Marx bank energy was 2 MJ, corresponding roughly to an erected voltage on the Marx capacitor of 470 kV.

C. Experimental Results and Interpretation

Given the three circuit models for the ACE 4 generator, a set of large radius experiments could be designed to evaluate ACE 4's aluminum wire PRS performance capabilities. These experiments would indirectly test ACE 4's capability to transfer current effectively from the plasma flow switch into the diode region and then to a wire load. A number of questions were to be addressed by these experiments:

- Assuming some current is switched from the flashboard plasma to an aluminum array load, will the array implode?
- Is the tandem puff opening switch operation understood, i.e., are the circuit models correct? Should the switch be removed altogether?
- Will aluminum implode symmetrically and efficiently to produce K-shell x rays from the large array diameters required by ACE 4's present design? If not, how much of a deleterious effect will there be and can we work around it?

The shot matrix for ACE 4, Al wire, PRS experiments that was proposed, which is given in the following Tables IV-VI, was designed to address these questions and to reveal the ability of the present ACE 4 configuration to transfer current to the wires and to implode them semi-uniformly. It was proposed that a set of experiments be run for fixed wire configurations by varying the driving Marx voltage for each configuration between 480 and 640 kV. The circuit modeling of ACE 4 showed that it was far from an ideal generator in its present configuration since, to produce K-shell radiation, the experiments would have to be stretching the envelope of what has been achieved to date at large diameters with wire loads on other pulse-power generators. The problem was that ACE 4's current risetime required large diameter loads to make PRS work, but that it did not have the current to implode enough mass from large radii. For this reason, it was suggested that 4 cm diameter loads comprised of 0.8 and 0.9 mil diameter wires be used initially to do the voltage scan. Then, if these shots proved to be reasonably successful, the larger 6 cm diameter arrays of 0.8 and 0.9 mil wires could be used for a new scan. An array diameter of 7.4 cm was needed to do a useful 1.0 mil wire scan.

Six different experiments in a family of experiments using 0.6, 0.7, 0.8, and 0.9 mil diameter wires were carried out. The arrays were each of length $\ell = 3$ cm long. They were composed of 24 wires with an array diameter of 4 cm. The yield data are best displayed in an $m - v_f$ plot of the experiments, which is presented in Fig. (10). The 2 sets of (circle and triangle) points locates each of these arrays in the figure by their initial mass per length. The triangle points are obtained when the 2a circuit model, described above, is used to inwardly accelerate the loads, while the

Table IV: Proposed ACE 4 Aluminum ExperimentsReturn current radius = 7.0 cm, array length = 3.0 cm

Wire Diam (mil)	Wire Mass ($\mu\text{g}/\text{cm}$)	Array Diam (mm)	# Wires	η	Marx Voltage (kV)
0.6	118	40	24	1.9	585
0.8	210	40	24	0.95	470
0.8	210	40	24	1.35	600
0.9	266	40	24	0.95	525
0.9	266	40	24	1.15	595

Table V: Proposed ACE 4 Aluminum ExperimentsReturn current radius = 7.0 cm, array length = 3.0 cm

Wire Diam (mil)	Wire Mass ($\mu\text{g}/\text{cm}$)	Array Diam (mm)	# Wires	η	Marx Voltage (kV)
0.8	210	60	24	1.15	490
0.8	210	60	24	1.65	635
0.9	266	60	24	1.4	625

Table VI: Proposed ACE 4 Aluminum ExperimentsReturn current radius = 7.0 cm, array length = 3.0 cm

Wire Diam (mil)	Wire Mass ($\mu\text{g}/\text{cm}$)	Array Diam (mm)	# Wires	η	Marx Voltage (kV)
0.9	266	74	24	1.45	595
1.0	328	74	24	1.18	585
1.0	328	74	24	1.45	665

circle points correspond to the 2c circuit. A different final implosion velocity, v_f , is calculated depending on which circuit model is used. The maximum measured K-shell yields, taken from Table VII, are listed above the circle points. The predicted total kinetic energy generated in each (m, v_f) experiment can be computed for each case. It is $1/2mv_f^2\ell$ and is also listed in Table VII.

Thus, Fig. (10) implicitly contains two important pieces of information about ACE 4 conversion efficiencies. They show that ACE 4 performed poorly in these experiments in each of two ways. Less than 4% of ACE 4's Marx bank energy was converted into kinetic energy, and less than 4% of this kinetic energy was converted into kilovolt x-rays.

Table VII: ACE 4 Aluminum Experiments

Return current radius = 7.0 cm, array length = 3.0 cm

Array diameter = 4.0 cm, number of wires = 24

Wire Diam (mil)	Wire Mass ($\mu\text{g}/\text{cm}$)	Marx Voltage (kV)	Y_K (kJ)	K.E. (kJ)	C.E. %
0.6	118	480	5.0	86	5.8
0.6	118	480	3.95	86	4.6
0.7	161	480	0.15	86.7	0.17
0.8	210	480	2.25	87.3	2.6
0.9	266	480	2.4	88	2.7
0.9	266	480	1.2	88	1.4

D. Diagnostic Issues

The ACE 4 aluminum results for 0.8 mil wires were much worse than those obtained in a similar Double Eagle experiment (see Table I, the third entry) and indicate problems with power flow to the load. When dealing with unpredictable PRS/POS behavior, one must rely on experimental and theoretical diagnostics to sort out and quantify the difficulties. Two important suggestions could be drawn from the above circuit model predictions and the x-ray measurements. To determine whether or not the circuit model is correct, accurate measurements of the wire explosion and implosion times must be made. For this task, fiduciated streak camera and x-ray diode measurements must be made. The x-ray yield data suggests that the implosion was poor, but how it compares to the circuit model predictions remains to be determined. The ability of the current to be brought down from 7 cm to 2 cm before it couples to the wires must also be tested. If unmodelable current asymmetries are present in tandem puff operation, they must be measured and then eliminated. There is already experimental evidence for this problem.

A number of different loads designs can be tried in order to work around some of the power flow problems. For example, because of the $(N_i^2 - \text{mass}^2 - I^4)$ scaling of K-shell emission in the inefficient scaling regime, argon load designs that promote higher densities on axis offer the potential of significantly lowering energy requirements for obtaining higher K-shell yields. The puff on wire configuration is a design that has the potential on ACE 4 of increasing K-shell emission from gas-puff plasmas because it promotes higher densities on axis. 1-D calculations performed with an argon gas puff stagnating onto a titanium wire show that in the inefficient K-shell scaling

regime the presence of a relatively low mass wire on axis does produce substantially higher total K-shell yields than just the argon puff gas configuration. Calculations show that a 100 $\mu\text{g}/\text{cm}$ argon gas puff stagnating upon a single 0.8 or 1.0 mil titanium wire should give in excess of 1 kJ/cm of additional K-shell emission. The source of this additional emission is the titanium wire. If, instead of pure Ti, a coating of KCl were put onto a carbon or titanium fiber and then the imploded argon would contact high density potassium chloride on axis, and one could expect both yield and spectrum enhancements in the vicinity of the argon K-series lines.

In addition to increasing kilovolt x-ray yields, the use of multi-material load designs provides opportunities for diagnosing load performance and for identifying and quantifying power flow problems. One way to evaluate the quality of an implosion is to gauge its convergence on axis, which could be measured by its interaction with an on-axis wire. For this purpose, spectral diagnostics are needed that can distinguish core plasma from surface plasma conditions in a pinch. A small coating of selenium to the on-axis wire or a small admixture of krypton to the argon gas could provide such a diagnostic. This L-shell diagnostic development is discussed in another section of this report.

REFERENCES

1. C. Deeney, P. D. LePell, I. Roth, T. Nash, L. Warren, R. R. Prasad, C. McDonald, F. K. Childers, P. Sincery, M. C. Coulter, and K. G. Whitney, *J. Appl. Phys.* **72**, 1297 (1992).
2. K. G. Whitney, J. W. Thornhill, J. P. Apruzese, J. Davis, C. Deeney, R. R. Prasad, and L. Warren, *Phys. Plasmas* **50**, 2166 (1995).
3. K. G. Whitney, J. W. Thornhill, J. L. Giuliani, Jr., J. Davis, L. A. Miles, E. E. Nolting, V. L. Kenyon, W. A. Speicer, J. A. Draper, C. R. Parsons, P. Dang, R. B. Spielman, T. J. Nash, J. S. McGurn, L. E. Ruggles, C. Deeney, R. R. Prasad, and L. Warren, *Phys. Rev. E* **50**, 2166 (1994).
4. "Systematic Analysis of Saturn Wire Array Implosion Observations" Naval Research Laboratory Memorandum Report 6720-95-7659, April 19, 1995.
5. "Advanced Radiation Theory Support Annual Report 1994, Final Report" Naval Research Laboratory Memorandum Report 6722-95-7656, July 28, 1995.
6. J. W. Thornhill, K. G. Whitney, C. Deeney, and P. D. LePell, *Phys. Plasmas* **1**, 321 (1994).
7. K. G. Whitney, J. W. Thornhill, J. P. Apruzese, and J. Davis, *J. Appl. Phys.* **67**, 1725 (1990).
8. C. Deeney, T. Nash, R. R. Prasad, L. Warren, K. G. Whitney, J. W. Thornhill, and M. C. Coulter, *Phys. Rev. A* **44**, 6762 (1991).
9. M. Gersten, W. Clark, J. E. Rauch, G. M. Wilkinson, J. Katzenstein, R. D. Richardson, J. Davis, D. Duston, J. P. Apruzese, and R. Clark, *Phys. Rev. A* **33**, 477 (1986).

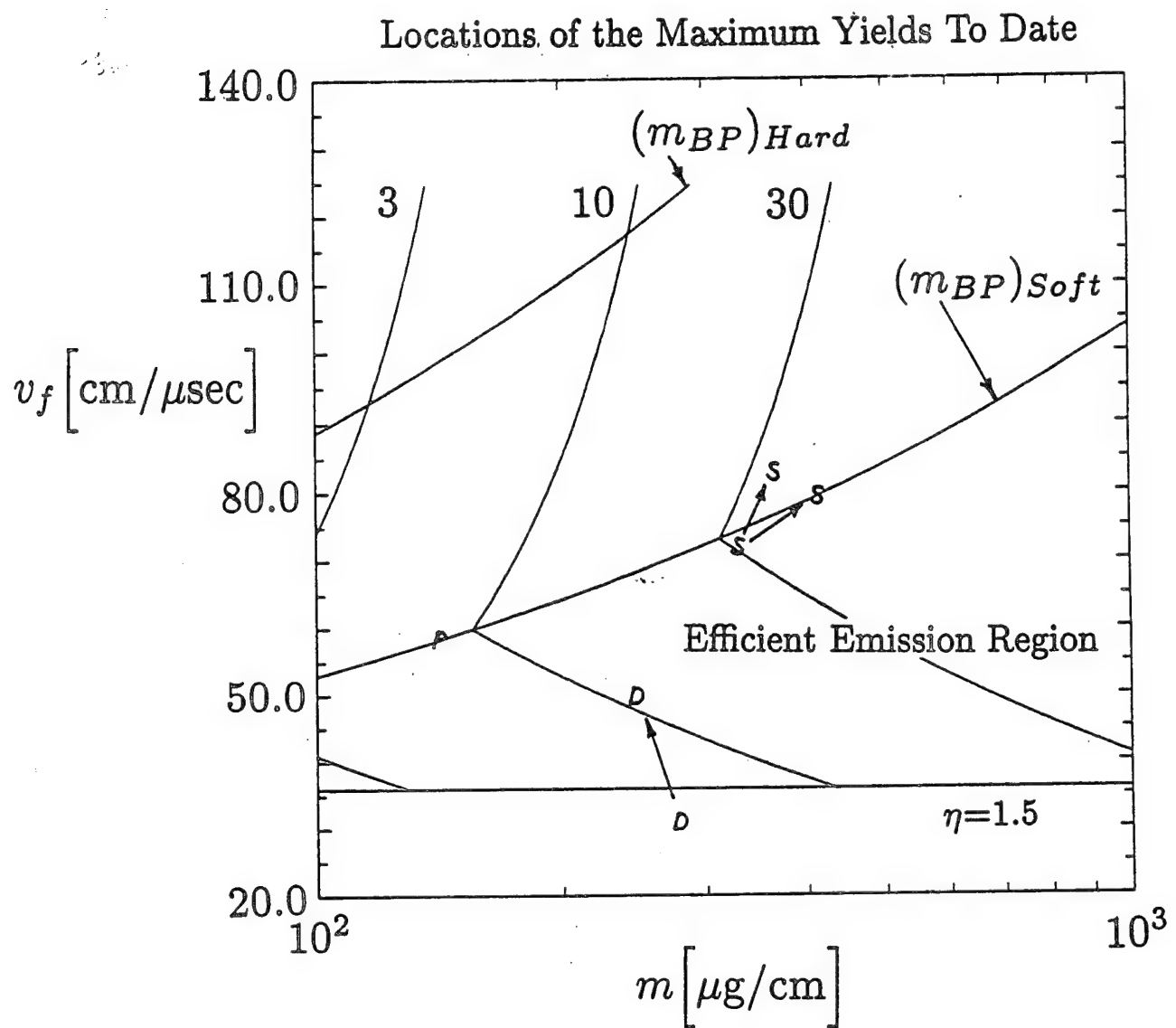


Figure 1. The experiments on Phoenix, Double Eagle, and Saturn generators, labeled P, D, and S respectively, that produced the most K-shell emission from aluminum implosions are shown. They are located by the initial mass and by the calculated final implosion velocity, v_f , of the array in each case. The arrows connect the locations of the previous maximum yield experiments on Double Eagle and Saturn to the current ones. The region predicted to efficiently convert array kinetic energy into K-shell x rays lies between the $\eta=1.5$ and the $(m_{BP})_{Soft}$ boundary curves. Early predicted yield contours for 3, 10, and 30 kJ/cm are also shown.

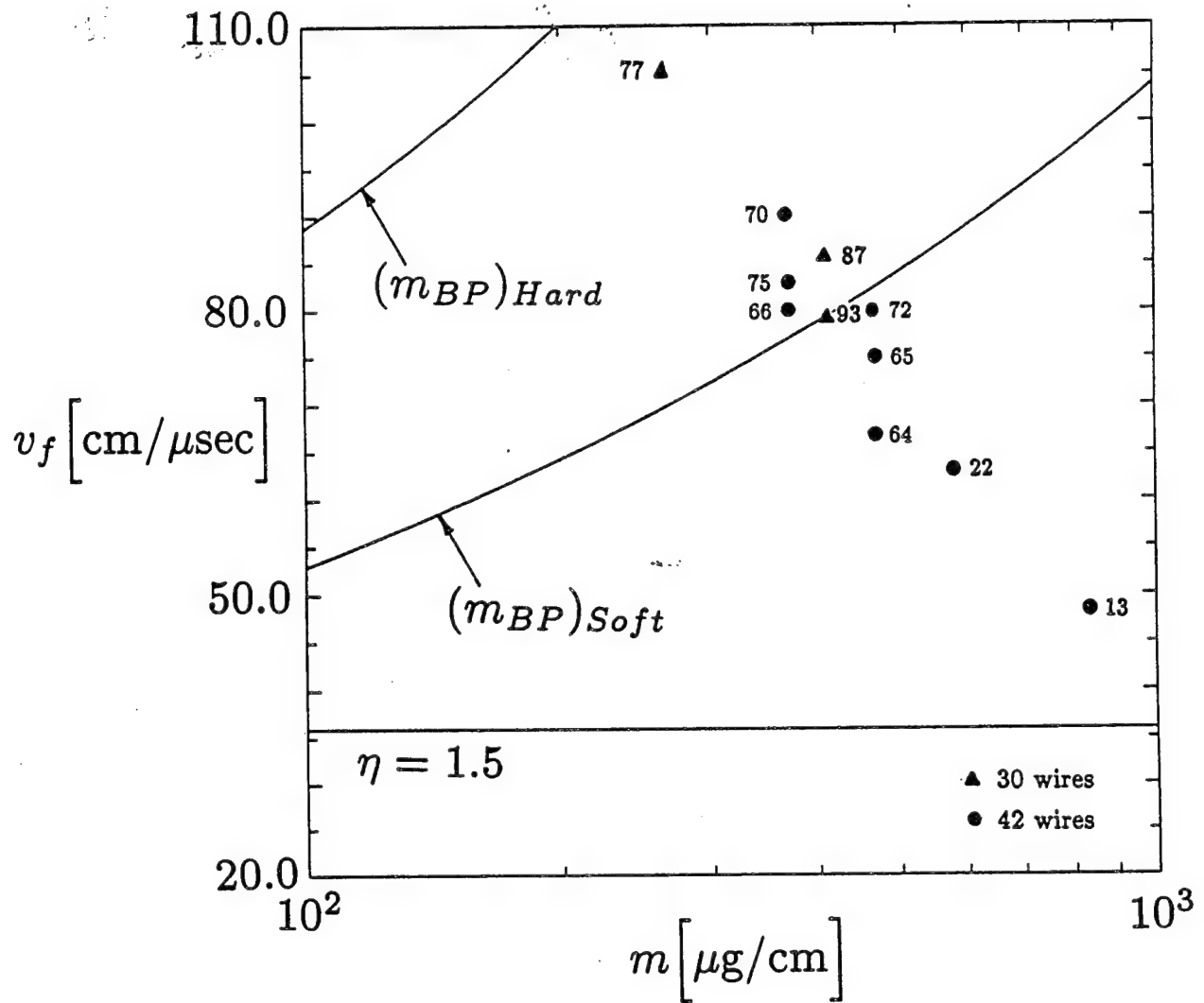


Figure 2. Recent Saturn experiments that probed the yield behavior of 30 and 42 wire aluminum arrays near and away from the soft-implosion mass breakpoint boundary, $(m_{BP})_{Soft}$, are located by their mass and calculated final implosion velocity. The measured K-shell yields are displayed next to the experimental locations. Note, there is a tendency for the yields to decrease away from the $(m_{BP})_{Soft}$ boundary, but the falloff as the $(m_{BP})_{Hard}$ boundary is approached is small for the 30 wire case shown.

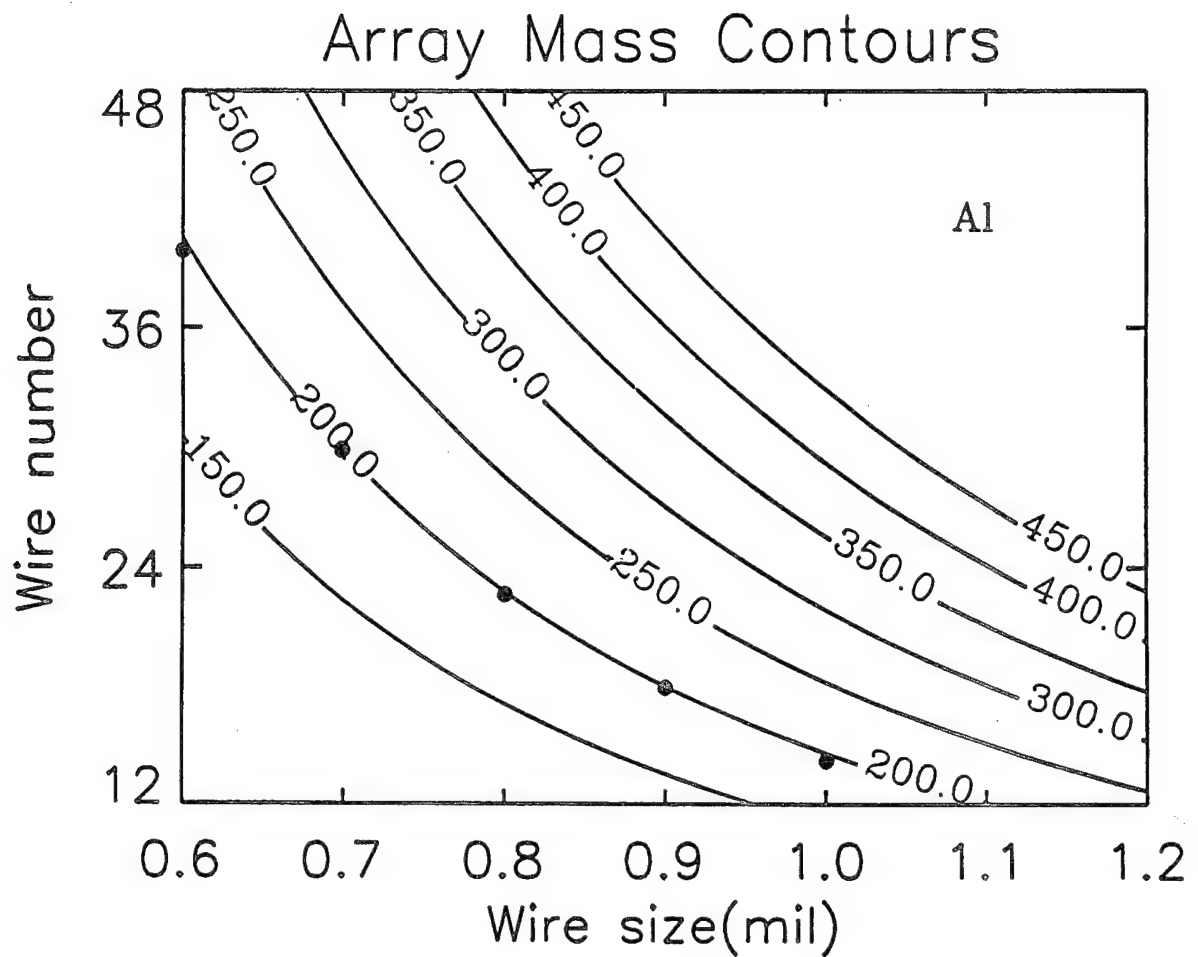


Figure 3. Contours for given mass/centimeter aluminum arrays are shown as a function of the size of the wires in mils and the number of wires used in the arrays. The dots on the $200 \mu\text{g}/\text{cm}^2$ contour correspond to the use of 0.6, 0.7, 0.8, 0.9, and 1.0 mil wires and require roughly 40, 30, 23, 18, and 14 wires respectively.

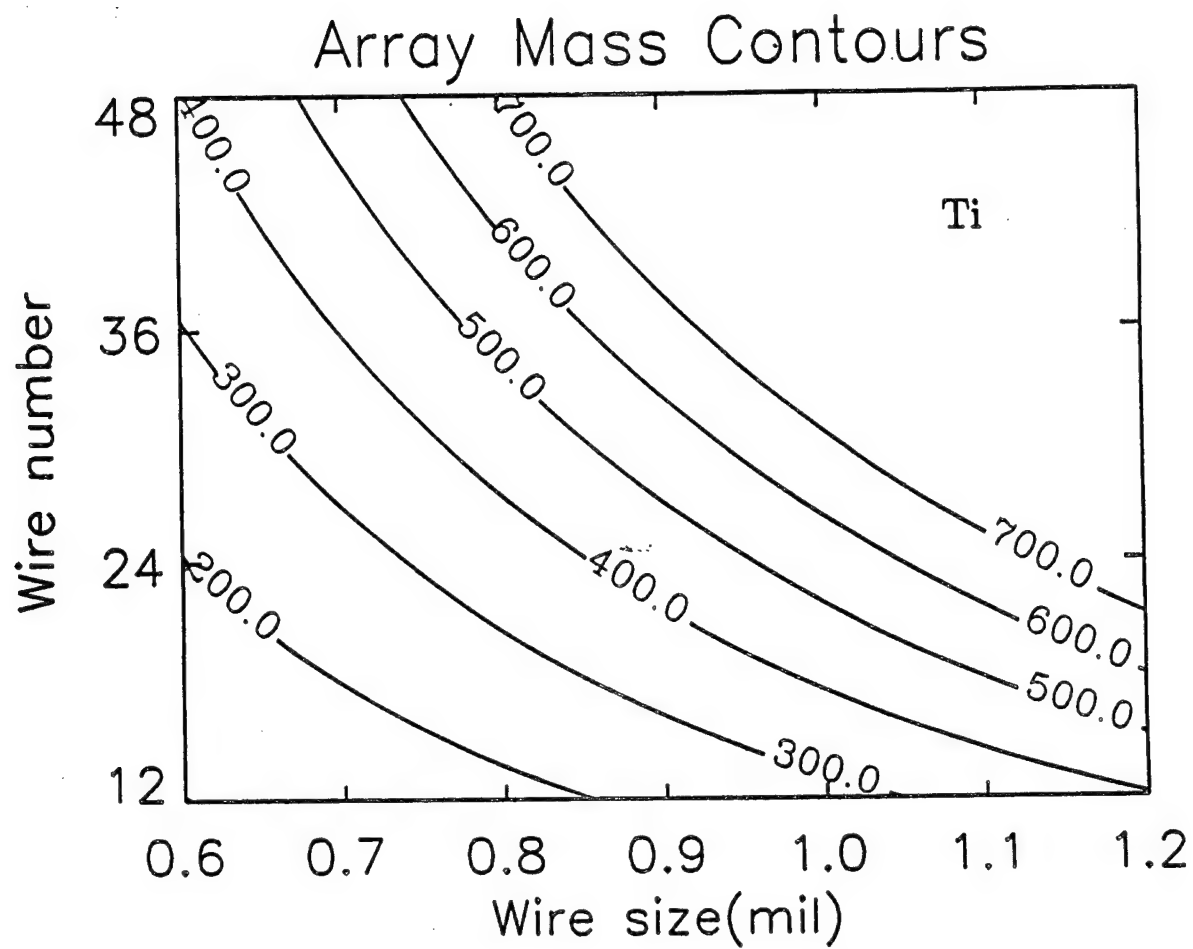


Figure 4. Contours for given mass/centimeter (in units of $\mu\text{g}/\text{cm}$) titanium arrays are shown as a function of the size of the wires in mils and the number of wires used in the arrays.

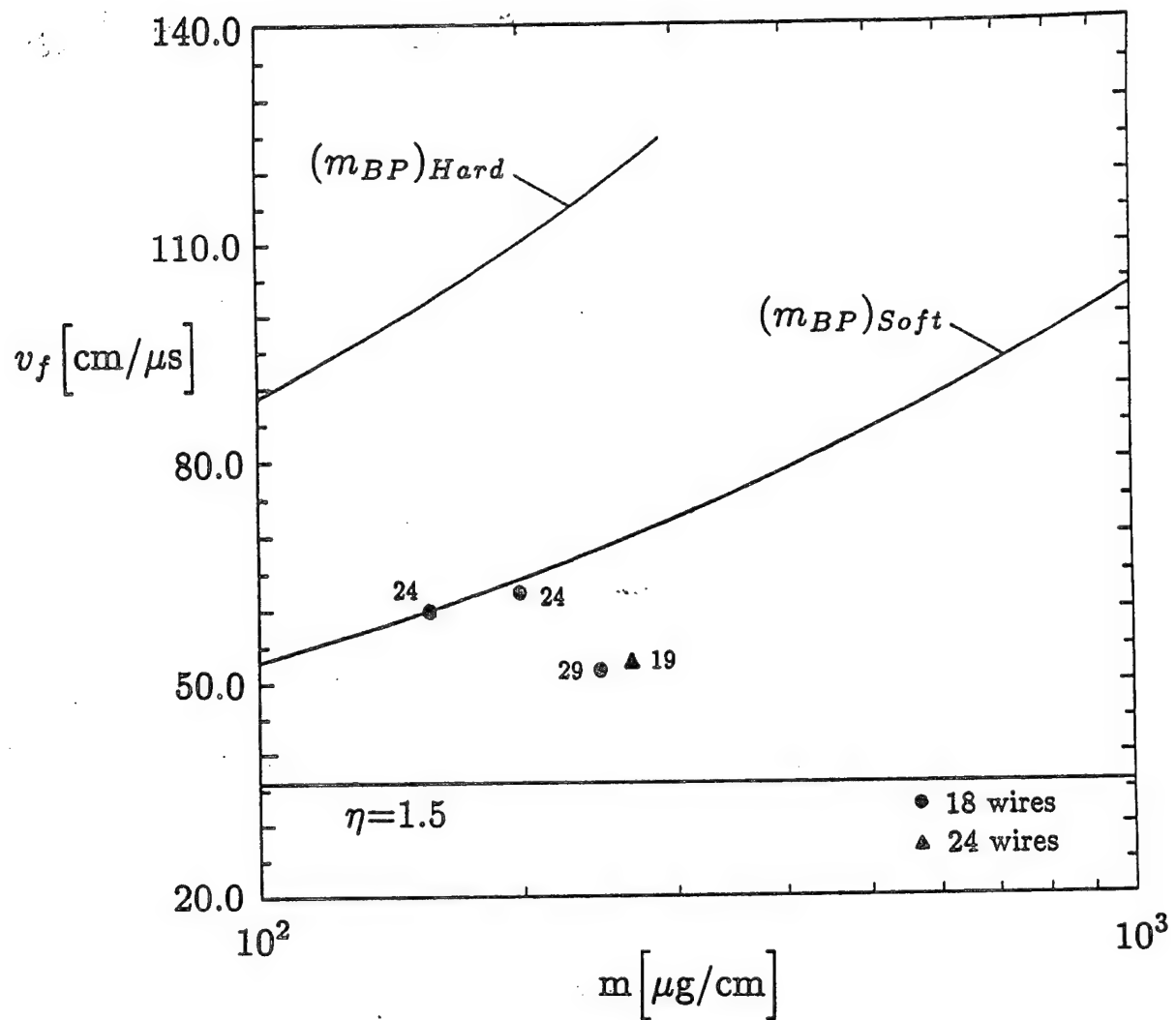


Figure 5. The locations and measured K-shell yields of four Blackjack 5 experiments are shown. They suggest that Blackjack 5 would confirm the Double Eagle more than the Phoenix or Saturn maximum yield behavior.

ACE 4 Circuit Model #1

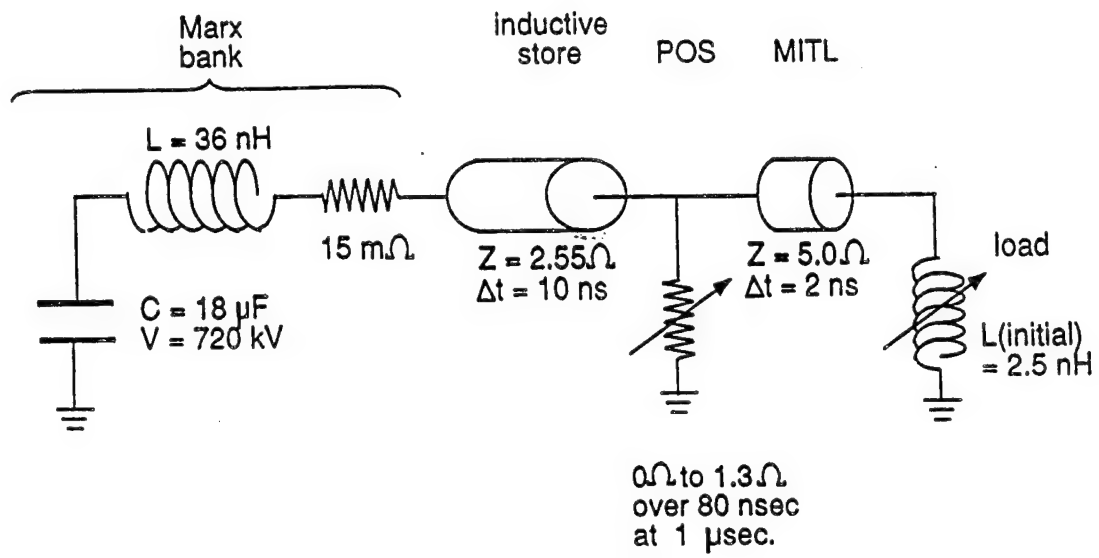


Figure 6. This is the circuit of the ACE 4 generator as it was originally conceived.

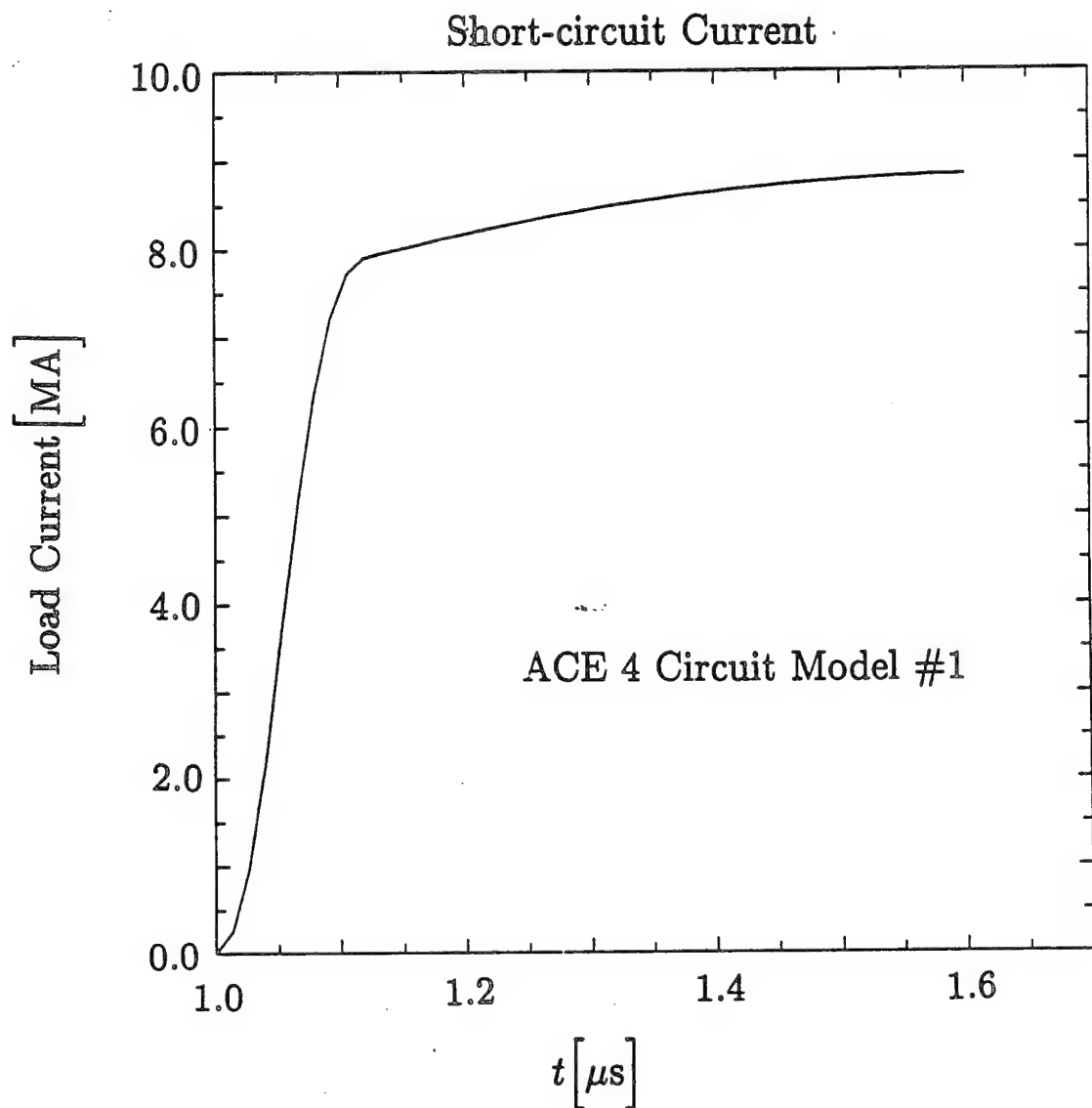
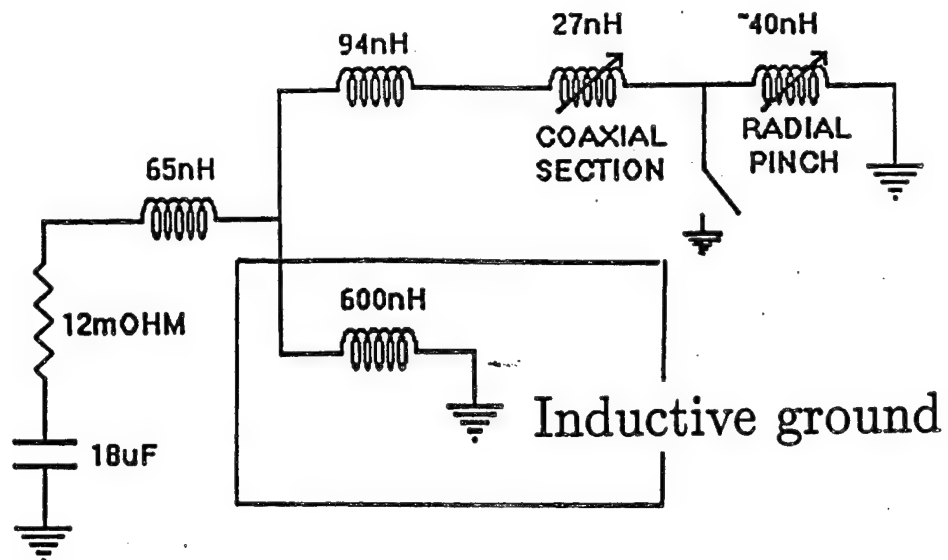


Figure 7. The current into a short-circuit load on ACE 4 was originally predicted to reach 8 MA in roughly 100 ns once the POS opened as shown in this figure. This calculated result assumed a MITL inductance of 15 nH.

ACE 4 Circuit Model #2



POS #2: Tandem Puff

Figure 8. This is the circuit of the ACE 4 generator as it is currently conceived to operate.

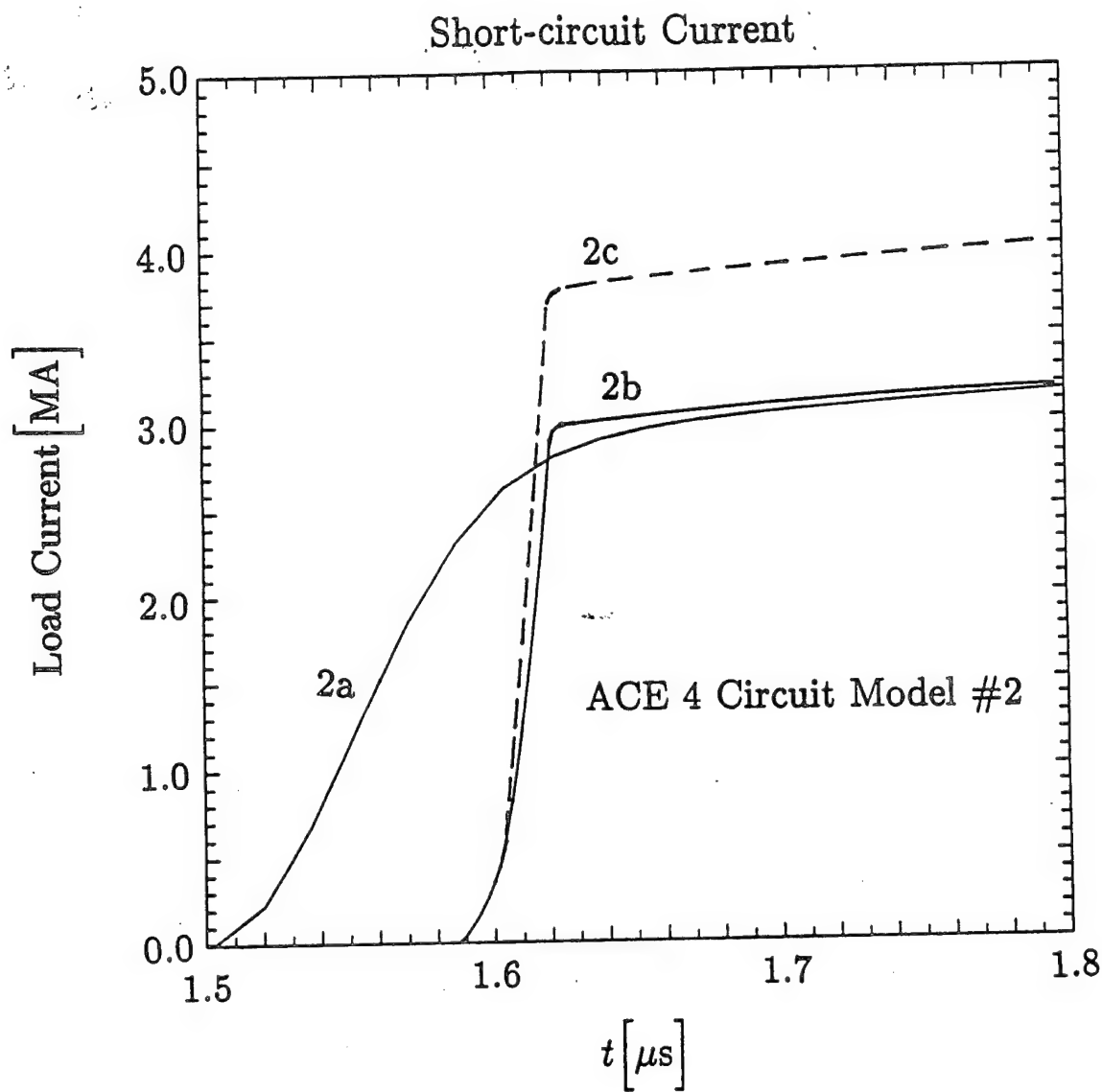


Figure 9. Three calculated currents into a short-circuit load are shown for the tandem puff circuit model. Curves 2a and 2b represent the current under the assumption of a low or high impedance plasma flow switch respectively. Curve 2c shows what happens in the 2b case when the inductive ground is eliminated and the inductance between the Marx bank and the coaxial switch is reduced to 60 nH.

ACE 4 ALUMINUM EXPERIMENTS

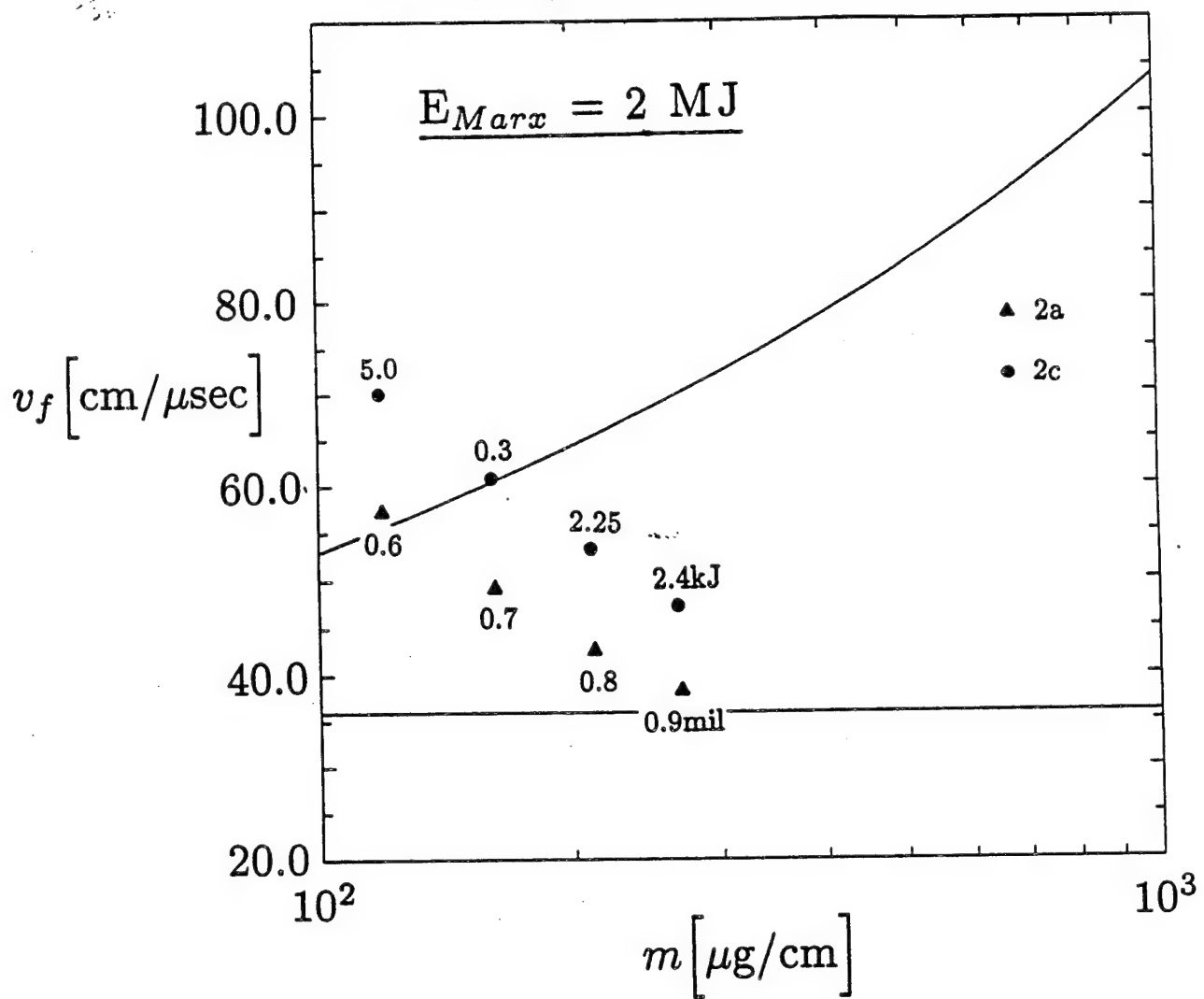


Figure 10. The ACE 4 experiments of Table VII are located in (m, v_f) space differently depending on whether circuit 2a (the triangles) or circuit 2c (the circles) is used. The milages of the wires used in the experiments are listed under the triangle points; the maximum measured K-shell yields are listed above the circle points. Based on the behavior of the other generators (Phoenix, Double Eagle, and Saturn), one might infer that circuit 2a better describes the array implosions than circuit 2c. However, this interpretation is highly uncertain since power flow problems were detected after the experiments were finished. It is also suspected, based on the low yield measured, that the 0.7 mil wires were not aluminum.

II. INVESTIGATION OF K-SHELL EMISSION FROM MODERATE ATOMIC NUMBER IMPLOSIONS

A. Introduction

A previous theoretical phenomenological investigation was carried out into the effects of magnetohydrodynamic (MHD) turbulence on the stagnation dynamics of aluminum wire array and argon gas puff z-pinch implosions.¹⁻³ It showed that ad hoc increases in the plasma viscosity, heat conductivity, and electrical conductivity (as modeled by using a fixed set of multipliers for these quantities in one dimensional (1-D) MHD calculations) reasonably duplicated the average electron temperatures, ion densities, and mass of the K-shell emission region that were measured at stagnation for a variety of Physics International (PI) aluminum wire and argon gas puff experiments. While this phenomenological modeling does not represent a first principles approach to incorporating turbulence effects in 1-D MHD calculations, it does suggest the existence of these strong multidimensional effects, some of which may be produced by the unequal forces acting on small wire number array loads. In particular, the major effect of increasing the transport coefficients was to "soften" the 1-D implosions by decreasing the ion densities that were achieved at stagnation by several orders of magnitude.

This "soft" implosion modeling was used in Ref. 1 to reexamine the scaling of K-shell yield with load mass for a fixed implosion velocity. The results of this study suggested that it would require a factor of 6 more mass and kinetic energy than was calculated originally using "hard" (no enhanced transport) 1-D implosion calculations to attain efficient K-shell X-ray yields (K-shell yield $> 30\%$ of the kinetic energy that is coupled to the load before stagnation) from a moderate-Z plasma. The original K-shell yield scaling predictions were then modified to reflect this shift in mass and they were then compared in Ref. 4 with aluminum results obtained from experiments performed on Saturn, Double EAGLE, and Phoenix pulse power machines. In general K-shell yield comparisons between measured Saturn and Phoenix yields and theoretical predictions were favorable, whereas Double EAGLE produced over twice the predicted K-shell yield. Similarly, Double EAGLE outperformed both Saturn and Phoenix in terms of conversion efficiency, which is the K-shell yield produced per unit of calculated kinetic energy delivered to the load. The fact that Double EAGLE produced approximately twice the predicted yield points out one of the limitations of the scaling calculations to date, which is that the current in the calculations is terminated just before stagnation in order to focus on the K-shell emission that is produced primarily due to thermalization of kinetic energy. Since the load current does not shut off in the experiments, energy continues to flow into the plasma and to confine the pinch. Both of these mechanisms could lead to an increased radiative output that is not reflected in previous K-shell yield scaling studies. Later experiments suggest why aluminum conversion efficiencies have been higher on Double EAGLE than on Phoenix and Saturn.⁵ They provide some evidence that the larger yields may be related to a greater late-time current energy coupling and plasma confinement achieved on Double EAGLE.

Soft implosion calculations show, because of the large kinetic energy needed for efficiently generating K-shell photons, that higher Z ($Z > 22$) experiments performed on existing pulse power machines will optimize K-shell emission at low- η values, where η is defined as the ratio of the maximum kinetic energy per ion achievable prior to stagnation to the minimum energy per ion, E_{min} , needed to instantly heat and to ionize a plasma into the K shell upon stagnation. For elements up to krypton, $E_{min} \cong 1.012Z^{3.662}$ eV/ion.⁶ Note, this formula accounts only for ionization and

thermal energies and not radiation or turbulence losses encountered as the plasma ionizes to the K shell. Since there have been no systematic theoretical or experimental investigations of the Z scaling of K-shell emission generated from low- η implosions, in anticipation of such future experiments we report on the results of our theoretical investigation into this regime. In particular aluminum, argon, titanium, and krypton plasmas are studied using a soft implosion model analysis. The results of this study have identified the following important effects: low- η plasmas apparently remain in an inefficient $mass^2$ (or I^4 , where I is current) scaling regime at much higher masses than predicted by the modified hard implosion model scaling formulas,⁴ innershell absorption of photons emitted from the hot plasma core and absorbed in colder outer regions of the plasma can substantially reduce the K-shell yield for large mass loads, and there is a time dependent lag in ionization into the K-shell that increases with the Z of the plasma. These issues and how they influence the design of future experiments are discussed in the results and conclusion sections of this paper.

B. Model

The 1-D MHD calculations are similar to those described in references 6, 1, and 7. They contain a comprehensive time dependent description of the ionization dynamics of z-pinch plasmas, a description of the transport of line radiation within these optically thick plasmas,⁸⁻¹⁰ and the self-consistent coupling of these dynamics to each other and to the fluid dynamics. The model employs the same enhanced transport coefficients that gave reasonable agreement with the state of the plasma at the time of stagnation of numerous PI experimental argon and aluminum pinches.^{1,2} The multipliers on classical transport coefficients used in the model are 20 for resistivity, 30 for heat conduction, and 40 for viscosity. The calculations are begun with the plasma at an average radius of 1.25 cm. 93 % of its mass is concentrated in a 0.05 cm sized shell; the remaining mass is distributed in 6 inner cells inside the shell with a mass density that decreases exponentially towards the axis. The exterior region will be referred to as the shell and the interior region as the core. This initialization procedure provides the calculations with numerical stability, and it also simulates the back-pressure effects of plasma mass that is blown towards the axis by shocks, $J \times B$ forces, or gas jets. It is important for modeling the core physics that both ion and electron temperatures be included in the MHD equations. If there are no energy sources coupled into a local plasma region, then the ions and electrons would equilibrate their temperatures typically on sub-nanosecond time scales in the plasma core; however, the ions are preferentially heated rapidly by thermalized kinetic energy to hotter temperature than the electrons.^{11,12} This nonequilibrium condition affects the core physics in that internal energy residing in the ions cannot be radiated until it is transferred to the electrons. This effect is pronounced in these studies because of the way viscosity is enhanced to phenomenologically model turbulence.

In these calculations a large parameter range in (η , mass, Z) space was examined. Thus, in order to minimize the zone to zone coupling required to transport the large number of M-shell, L-shell, and K-shell emission lines of the moderate Z elements, it was necessary to limit the number of zones used. On the other hand one cannot do a single zone, single temperature, calculation by averaging over all the gradients in the plasma when in some calculations (and experiments) that emission is produced only in the hot core of the plasma, which may contain less than 5 % of the total mass. A credible calculation requires transporting enough spectral lines to do a reasonable job of modeling the radiative loss rates¹³ and at least enough computational zones to reasonably

resolve the gradients in temperature and density that occur in the plasma core. It is also necessary to resolve the outer boundary of the pinch because that is where the current flows and penetrates into the plasma. Too coarse a zoning in this region averages over too much of the colder interior plasma causing lower electron temperatures to be calculated, which in turn, causes too much field penetration and ohmic heating. Empirically, we found that an adequate description of the effect of plasma gradients on K-shell emission could be obtained using 15 radial zones in the aluminum calculation and 20 zones in the argon, titanium, and krypton calculations. Note, therefore, for the aluminum calculations, the core region contains 11 % of the total plasma mass.

Each calculated implosion is driven by a linearly ramped current profile that is terminated when the energy input to the plasma, which is described by a parameter, η^* , reaches a preset value. η^* , which is more general than η , is defined as the ratio of the total energy coupled to the z-pinch per ion to E_{min} . The total-energy-per-ion consists of the sum of kinetic, internal and prior radiated energies of the plasma at the time that the current is cut-off divided by the number of ions. As in our past work,^{1,4-7,14} these 1-D calculations are used to explore how effectively the thermalization of kinetic energy acts to drive the plasma on axis into the K shell and how effectively the total-energy per-ion is converted into K-shell radiation. With the increased plasma back-pressure that results from enhanced viscosity and resistive heating, a large portion of the energy coupled to the plasma is in the form of compressional work and ohmic heating. In order to minimize the effects of this back-pressure the calculations are designed so that the specific η^* of interest is achieved in a 0-D slug model calculation⁴ when the outer radius of the plasma is a substantial distance, 0.5 cm, from the axis. In the aluminum calculation, this results in ~ 50 % of the plasma energy being kinetic when $\eta^* = 1$ at the time of current termination. For all the other higher Z or higher η^* calculations, the proportion of kinetic energy was higher than 50 %. For the largest velocity case of krypton at $\eta^* = 1$ the proportion was ~ 75 %. Thus, calculations based on $\eta = 4$, in earlier work with aluminum and argon,¹ correspond approximately with calculations having $\eta^* = 6$.

Note, care must be taken when comparing the results of this work with experiments or with other calculations, not only because of the model limitations listed above, but also because it is easy to imagine pinch configurations that would not have as large a proportion of the total input energy being kinetic as is modeled here (such as those having initial outer radii very close to the axis or uniformly distributed gas loads).¹⁵ Alternatively, one can imagine other pinch configurations that achieve higher proportions of kinetic energy. Even though it is determined in this study that the old scaling laws⁶ do not well represent the low- η regime, we made no attempt to reformulate scaling in this regime because such a model would only be quantitatively applicable to a limited range of experiments. This point was also made in Ref. (5), where the K-shell yield scaling of aluminum plasmas was determined for a class of soft implosions ($\eta/\eta^* = 2/3$).

C. Results and Discussion

Some of the important features of K-shell yield scaling as a function of mass loading for $\eta = 4$ ($\eta^* \approx 6$) are illustrated in Fig. 1, which is taken from the argon soft implosion calculations discussed in Ref. 1. The *mass*² scaling regime is characterized by a < 30 % conversion of coupled energy into K-shell emission. This inefficiency occurs when the radiative cooling rates, which scale as the square of the ion density (N_i^2) or as *mass*² for low mass plasmas, are too small to effectively influence the dynamics of the pinch. Under these low mass conditions, the stagnation is characterized by an elastic collision whereby the plasma runs in, converts its kinetic energy into

internal energy, and then expands to essentially the same kinetic energy as it had during the run-in phase. The inability of the plasma to radiate at maximum efficiency in this regime also makes plasma compression more difficult as is characteristic of strong shock behavior with $\gamma > 1$ (γ is the ratio of specific heats at constant pressure to constant volume). As the mass is increased, radiation cooling becomes sufficiently large that a significant fraction of the plasma energy can be radiated away during the stagnation phase and the time the plasma is on axis, thereby markedly reducing the pinch's rebound dynamics. K-shell emission, in this regime, scales linearly with the input energy,¹⁶ which is proportional to the load *mass*. In this case, over 30 % of the kinetic energy coupled to the load before stagnation can be emitted as K-shell radiation. The mass at which the transition between *mass*² and *mass* scaling occurs is denoted the massbreak point M_{bp} . Because this transition point is not as clearly defined for "soft" implosions as it is for "hard",⁵ for the purposes of discussion in this study, the least efficient scaling regime is the *mass*² regime and a more efficient regime begins when it is obvious that the scaling has been reduced below *mass*². Therefore, the criterion of achieving > 30% conversion of kinetic energy into K-shell photons as being a condition of reaching the efficient scaling regime, which was used in earlier work,^{1,4,6} is not strictly adhered to in this study.

It is easier to insure efficient production of K-shell emission by imploding a plasma load in the high-mass high- η scaling regime; however, except for low-Z loads, the coupled load energy required to operate in this regime quickly becomes prohibitive as Z increases. This is illustrated in Fig. 2 where calculated load energies required to obtain 10 % conversion of coupled energy into K-shell X rays are shown as a function of Z. For titanium it is estimated that approximately 100 kJ/cm of energy must be delivered to the load while krypton requires 7 MJ/cm. For elements with higher atomic number than Z = 22 (titanium), more energy is required to obtain 10% efficiency than can be delivered by existing pulse power machines. Because of this energy limitation, moderate-Z experiments performed on existing pulse power generators will take place in low- η scaling regimes.

K-shell aluminum yields as a function of load mass for various η^* are displayed in Fig. 3. Each solid line curve corresponds to a fixed value of η^* attained at the time of current termination. The solid curves in this figure shows that an inefficient scaling regime extends to much larger mass loads than predicted by earlier modeling work. For example, the *mass*² scaling regime extends to between 100 and 200 $\mu\text{g}/\text{cm}$ for all values of η^* between 1 and 6. Earlier predictions for the M_{bp} 's are 10, 35, and 124 $\mu\text{g}/\text{cm}$, for $\eta = 1$ (2), 2 (3), and 4 (6).^{1,4} The numbers in parentheses are roughly the equivalent η^* values. The earlier predictions are based on hard implosion scaling laws that were modified by a factor of six more mass to match soft implosion $\eta = 4$ calculations. Obviously, our present calculations predict that more than this factor of six adjustment to the hard implosion scaling relations is necessary in order to capture the dynamics of K-shell yield scaling in the low- η^* regime.

The dashed curves in Fig. 3 show the K-shell yield as a function of mass, but with energy delivered to the load as a parameter rather than η^* . These curves have a consistent trend. They show that the peak in yield production rises with η^* as the energy delivered to the load increases. Thus, at small energy coupling, the optimal choice is to take advantage of the N_i^2 dependence of K-shell line radiation and to implode as much mass as possible with $\eta^* \approx 1$. However, as the mass increases, two mechanisms begin to limit K-shell emission from $\eta^* = 1$ implosions. First, temperatures fall because the plasma's ability to radiate rises more rapidly than its ability to thermalize kinetic

energy, and second, K-shell line opacity (including that due to innershell absorption) also rises. These mechanisms gradually change the optimal conditions for K-shell yield production at the larger energy couplings to favor lower mass loads and higher implosion velocities (higher values of η^*).

The dynamics of the first mechanism are illustrated in Fig. 4, which compares one power input to two power outputs as a function of load mass for $\eta^* = 1$: the peak rate of kinetic energy thermalization, the peak total radiative power, and the peak K-shell radiative power. In the low mass scaling regime both radiative powers increase with *mass*²; whereas, the rate at which kinetic energy thermalizes rises linearly with *mass*. This more rapid rise in the ability of the plasma to radiate compared with its ability to generate and thermalize input energy produces a fall off of plasma temperature with rising mass as depicted in Fig. 5. In this figure, the mass averaged and time averaged (over the full-width-half-maximum of the K-shell radiative emission pulse) core and shell temperatures are graphed as a function of mass load along with the mass and time averaged ion densities. As the load mass increases and the average peak temperature falls, a large fraction of the plasma becomes incapable of ionizing to the He-like or H-like stages, and less of the shell plasma emits in the K-shell. This effect is quantified in Fig. 6 where the fractional mass emitting K-shell radiation is seen to drop as a function of mass load for three different η^* . This fractional mass represents the source region for 90 % of the K-shell radiation. Only those zones having more time integrated emission than absorption are considered as part of this region. The proportion of the plasma emitting in the K-shell increases with η^* because of the additional energy available to ionize the plasma into the K shell. Fig. 6 also shows that even for relatively large values of η^* the fractional mass emitting in the K-shell decreases with mass. The source of the K-shell emission for the large mass plasmas is the core and nearby regions. The K-shell spectrum transitions from being predominantly lines for the low mass implosions to being mostly recombination radiation for the high mass implosions.

For large mass loads, the amount of K-shell radiation that ultimately escapes the plasma is much less than that escaping the source region. This reduction occurs because the K-shell photons generated in the hot interior source region are absorbed by innershell photoionization in the colder exterior plasma. The strength of this process is shown in Fig. 7, where the K-shell yields of two cases are shown as a function of mass loading for an $\eta^* = 1$ implosion. In one case, the yield is calculated under full opacity conditions, while in the other case no innershell opacity is considered. This figure shows that the amount of calculated K-shell emission escaping from a 2000 $\mu\text{g}/\text{cm}^2$ plasma was diminished by 50 % when innershell photoabsorption was taken into account. For larger values than $\eta^* = 1$, the effect of innershell absorption is not as pronounced for any specific mass load because there is less cold absorbing plasma (Fig. 6). For higher Z elements than aluminum, innershell absorption also reduces K-shell emission but now at mass loads that scale with Z^3 from the aluminum mass where this effect occurs. This finding reflects the Z dependence of the innershell absorption coefficient,¹⁷ σ , i.e.,

$$\sigma = k \lambda^3 Z^3 \quad (\text{g}/\text{cm}^2), \quad (1)$$

where k is a constant, Z is the atomic number of the absorber and λ is the photon wavelength. Since $\lambda \propto Z^{-2}$ for above K-edge threshold photons, the Z dependence of σ is Z^{-3} . These aluminum calculations suggest that the effects of innershell absorption on K-shell radiative yield can be

minimized by using a mixture plasma that consists of a different Z exterior plasma whose K-edge lies far from the K-shell photon energies of the interior plasma. Recently performed experiments,¹¹ which were based on the idea of using plasma mixtures to reduce the overall opacity of the plasma,¹⁸ provide evidence that the effects of reabsorption can be large and can be lessened by this technique. As Fig. 5 shows, radiation generated by the interior plasma becomes trapped by the exterior plasma and causes the shell temperature to rise slowly with mass when the opacity is sufficiently large in large mass load.

The yield predictions of Fig. 3 are normalized to the coupled energy to show the efficiency of converting coupled energy into K-shell emission as a function of mass load in Fig. 8. Since $\eta^* = 1$ implosions barely have enough energy to ionize the entire plasma into the K-shell (and this consideration neglects radiation losses) one might expect a more precipitous drop in the peak efficiency of producing K-shell emission as η^* approaches 1. The reason this drop does not occur is that the geometry and implosion dynamics of the z-pinch focuses the implosion energy towards the axis so that the η^* values in the core of the pinch, which is where the K-shell photons are generated, can be much greater than one.

It was mentioned earlier that the inability of a plasma to radiate fast enough relative to the rate kinetic energy is thermalized leads to an implosion dynamics that is characteristic of strong shock behavior; consequently, it is difficult to compress a low mass plasma. This incompressibility is illustrated by Fig. 9. In this figure, the mass and time averaged shell and core ion densities and electron temperatures are shown as a function of η^* for a 100 $\mu\text{g}/\text{cm}^2$ aluminum load. The time average is carried out over the full width half maximum of the K-shell emission pulse width. Fig. 9 shows that the core ion density is insensitive to the velocity of the implosion, and to a lesser extent the same is true for the shell ion density. If the implosions are modeled using a circuit model appropriate for a real machine, and the current is not terminated prior to stagnation, one finds that the energy that can be coupled into a low mass load is significantly limited by the inability of the current to do compressional work on the plasma.

Figs. 10 and 11 display K-shell yields as a function of mass load and η^* for argon and titanium. In these, as in the aluminum calculations (Fig. 3), 1) there is a characteristic *mass*² scaling regime that transitions to a more efficient scaling regime as the mass is increased and the radiation rates begin to compare with the rate kinetic energy is thermalized, 2) the transition from an inefficient to an efficient scaling regime occurs at much larger mass loads than predicted by earlier scaling laws, 3) yield predictions for a fixed amount of coupled machine energy (dashed curves) show that the optimal load choice for producing K-shell emission favors larger masses and lower implosion velocities (lower η^*) at low machine energy coupling, and 4) the peak efficiency of producing K-shell emission diminishes with η^* (not shown). The peak efficiencies for argon with $\eta^* = 1, 2, 3$, and 4 are respectively, 24, 27, 32, and 33 %. For titanium with $\eta^* = 1, 2$, and 3 the efficiencies are 18, 23, and 27 %.

The cross-hatched regions shown in Fig. 11 represent predicted operating regions for optimizing K-shell X-ray production on Double EAGLE, Blackjack 5, Phoenix, and Saturn class machines. They represent good regions in which the Z-scaling of K-shell emission can be investigated experimentally. Titanium is a good load choice because: 1) its atomic number, Z=22, is significantly above that of argon, which has been extensively explored, 2) a large mass of titanium can be ionized into the K-shell by existing pulse power machines, and 3) titanium can be

fabricated into wires or coated onto other wires such as aluminum. However, the effects described in Figs. 3 - 11 manifest themselves most clearly when the stagnation of the experimental plasma on axis has 1-D symmetry. Recent Al, and Al coated with Mg experiments performed at Physics International and Sandia National Laboratory stressed the importance of improving the symmetry of the implosions by using the correct number of wires in the array and by improving the current return geometry by putting the return current path at a larger radius.¹¹

The aluminum, argon, and titanium K-shell emission results presented in Figs. 3, 10, and 11, respectively, are nearly independent of whether a collisional radiative equilibrium (CRE) or a time dependent CR ionization dynamics model is employed. However, as the Z of the material is increased beyond titanium it becomes increasingly necessary to use time dependent ionization dynamics,^{18,20} as illustrated in Fig. 12. In this figure, krypton K-shell yields as a function of mass load are compared using CRE and time dependent CR models. The comparison is made for $\eta^* = 1$ implosions because the coupled energy requirements for larger η^* values are even more prohibitive than those shown in Fig. 12. Time dependent calculations for the lower mass loads show that they do not effectively ionize into the K-shell, i.e., the effective charge of the core region is less than 34. Consequently, the calculated transient K-shell emission is over an order of magnitude less than that calculated with the CRE model for a 1 mg/cm load. The mass load needs to be on the order of 5 mg/cm before the electron density is large enough at stagnation for krypton to ionize to the He-like and H-like ionization states in a time short enough to come into CRE at the calculated plasma density and temperature. In the $\eta^* = 1$ calculations these conducive conditions exist for a time of order 5 ns for krypton and 20 ns for aluminum. This time period is long enough for the core region of the low mass aluminum loads (Fig. 3) to effectively ionize into the K-shell but it is not long enough for the lower mass krypton loads (Fig. 12). The period for ionizing into the K shell is largely influenced by the total radiation rate and the rate kinetic energy is thermalized..

For a fixed electron density, this time increases with the atomic number of the load material. If electron impact ionization dominates the stripping during the stagnation phase, then the ionization time required to reach the next sequential ionization stage is given by $\tau = (N_e X)^{-1}$, where N_e is the electron density and X is the collisional ionization rate coefficient for ionizing to the next ionization stage. The total time required to ionize into the He-like stage is the sum of all the sequential ionization times beginning with the transition from the neutral atom to the singly ionized stage. A minimum estimate of this time is given by τ_{Li-He} , which is the time required to ionize from the Li-like to the He-like stage. From Lotz's formula for the collisional ionization rate,²¹ τ_{Li-He} is written

$$\tau > \tau_{Li-He} = \left(\frac{3.0 \times 10^{-6}}{\chi_I T_e^{1/2}} E_1 \left(\frac{\chi_I}{T_e} \right) N_e \right)^{-1} \text{ sec,} \quad (2)$$

where E_1 is the first exponential integral, and χ_I is the ionization potential of the Li-like stage. The temperature that gives a minimum value of τ_{Li-He} (which can be achieved for the minimum amount of machine energy coupled to the load) can be estimated by replacing N_e by $N_e \approx P/(kT_e)$, where P is the pressure in the core at stagnation and k is Boltzmann's constant. This minimum value of τ_{Li-He} occurs at a temperature of 5 keV for krypton and at 530 eV for aluminum. The value of τ_{Li-He} for krypton is $3.0 \times 10^{11}/N_e$ and it is $1.2 \times 10^{10}/N_e$ for aluminum. Therefore, to achieve an ionization time of 1 ns for the least pressure requires a minimum electron density of 10^{19} cm^{-3} for aluminum and approximately 25 times this density for krypton.

Besides the necessity of higher electron density, more sequential ionization, and short ionization times, the enhanced viscosity employed in our model makes it more difficult in theory for the higher Z elements to ionize into the K shell. This is because the enhanced viscosity produces core ion temperatures during the stagnation phase of the implosion that are orders of magnitude larger than the electron temperatures. Significant energy residing in the ions makes it more difficult to compress the plasma which behaves like an ideal gas until the energy is transferred to the electrons where it can be radiated out of the plasma. Lower compression implies lower N_e which in turn implies longer ionization times and also longer time for the electrons to equilibrate with the ions since the ion electron heating rate scales as N_e^2 .

D. Summary and Conclusions

Recent investigations into phenomenological turbulence modeling showed that the enhancement of viscosity, heat conduction, and resistivity in 1-D MHD calculations could lead to reasonable agreement with the average stagnation state of the experimental plasmas.^{1,2} In particular stagnation ion densities were reduced by several orders of magnitude over the densities predicted using classical transport coefficients. This same modeling was used in the work presented here to further investigate the Z-scaling of K-shell emission from moderate- Z plasmas at low- η . The low- η regime is investigated because of limits on energy available from current pulse power machines to drive loads with higher atomic number than Z=22 (titanium). The results of our 1-D study have identified several important effects that will influence the scaling of K-shell emission on these machines. First, low- η plasmas remain in an inefficient *mass*² scaling regime at much higher masses than predicted by our earlier work.^{1,6} Secondly, opacity and innershell absorption limit the K-shell radiative capabilities of the higher mass loads. Thirdly, there is a Z dependent lag in ionization into the K-shell that increases with the Z of the plasma and adversely affects the K-shell emission.

It was shown in Ref. 1 that there is a factor of 6 upward shift in the minimum load mass needed for producing efficient K-shell yields in $\eta = 4$ "soft" as opposed to "hard" implosion calculations. However, one would mistakenly predict $M_{bp}(\eta)$ "soft" = $6 \times M_{bp}(\eta)$ "hard" for low- η implosions. This erroneous result would also assume that one can extrapolate the "hard" implosion scaling $M_{bp}(\eta)$ to low η . We found that 1-D soft implosion calculations do not support this assumption. We found that low- η plasmas remain in an inefficient scaling regime at much higher masses than predicted earlier, e.g. $M_{bp}(\eta = 1)$ "soft" $\approx 60 \times M_{bp}(\eta = 1)$ "hard" for aluminum. Because the calculations predict that more mass will be needed to obtain an efficient generation of K-shell emission than earlier predictions they also predict more energy will be required.

Our calculations consistently show that the optimal conditions for generating K-shell photons, for a specific load energy coupling, transition from low- η^* higher mass implosion conditions to higher η^* lower mass conditions as the coupled energy is increased. Two mechanisms that influence this transition are: 1) bulk plasma temperatures falling with increased mass as the radiative cooling rate (scales with *mass*²) begins to compare with the rate kinetic energy is thermalized (scales with *mass*), and 2) K-shell photons initially emitted from the core are increasingly absorbed by innershell processes in colder outer regions of the plasma as the mass is increased.

In both "soft" and "hard" implosion calculations the core region is much hotter than the surrounding shell plasma during the stagnation phase of the implosion. This hot core is more

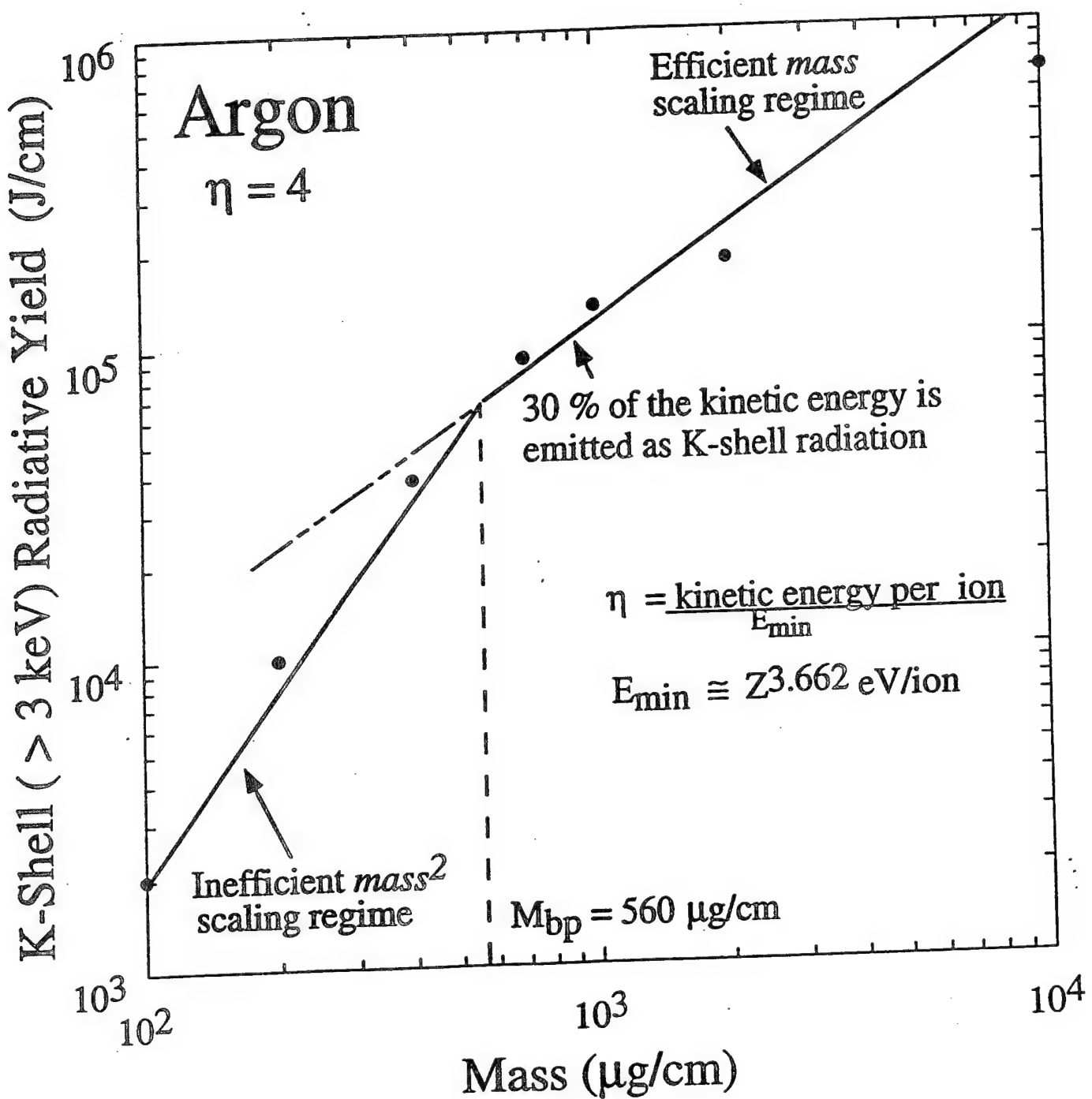
extensive and its ion temperatures are substantially higher than the electron temperatures when "soft" calculations are performed. The Mg coated Al wire experiments performed on Double EAGLE also provide experimental evidence that the state of the core plasma is much different than that of the shell.¹¹ In these experiments it was determined that the core region was approximately twice as hot as the shell. In order to gain better knowledge of how K-shell radiation is generated it is clear that more experiments are needed to observe and to quantify the state of the core and shell regions.

If, for example, on a specific pulse power machine it were possible to couple as much total energy into shorter length more massive loads as into longer length less massive loads, and if the machine were energy limited and forced to operate in an inefficient scaling regime for a given element, then it would be advantageous to implode a more massive shorter length load in order to take advantage of $mass^2$ scaling. For higher Z loads like krypton, there is a double advantage for using the largest mass per unit length. For this element, yield scaling in the inefficient regime is even steeper than $mass^2$ (Fig. 12) because of the of the longer times required for ionization into the K shell. For similar reasons, load designs that promote higher mass and energy density at stagnation, such as convergent geometry loads^{22,23} or loads that implode onto a wire on axis, may also improve the efficiency of generating K-shell emission. In addition, improving the symmetry of the implosion by going to more wires and more symmetric return current geometries^{4,5} may reduce plasma shearing on axis and the need to enhance transport coefficients in order to attain 1-D model agreement with present day experimental stagnation conditions. If this is the case, then the energy requirements predicted here for attaining efficient K-shell emission may be substantially reduced and become more in accord with the original scaling laws.⁶ These matters need to be investigated experimentally.

References

1. J. W. Thornhill, K. G. Whitney, C. Deeney and P. D. LePell, Phys. Plasmas **1**, 321 (1994).
2. C. Deeney, P. D. LePell, B. H. Failor, J. . S. Meachum, S. Wong, J. W. Thornhill, K. G. Whitney, and M. C. Coulter, J. Appl. Phys., **75**, 2781 (1994).
3. C. Deeney, T. Nash, R. R. Prasad, L. Warren, J. W. Thornhill, and M. C. Coulter, Phys. Rev. A, **44**, 6742 (1991).
4. K. G. Whitney, J. W. Thornhill, J. L. Giuliani, Jr., J. Davis, L. A. Miles, E. E. Nolting, V. L. Kenyon, W. A. Speicer, J. A. Draper, C. R. Parsons, P. Dang, R. B. Spielman, T. J. Nash, J. McGurn, L. E. Ruggles, C. Deeney, R. R. Prasad, and L. Warren, Phys. Rev. E, **50**, 2166 (1994).
5. K. G. Whitney, J. W. Thornhill, J. P. Apruzese, J. Davis, C. Deeney, P. D. LePell and B. H. Failor, Phys. Plasmas **2**, 2590 (1995).
6. K. G. Whitney, J. W. Thornhill, J. P. Apruzese and J. Davis, J. Appl. Phys. **67**, 1725 (1990).
7. J. W. Thornhill, K. G. Whitney and J. Davis, J. Quant. Spectrosc. Radiat. Transfer **44**, 251 (1990).
8. D. Duston, R. W. Clark, J. Davis, and J. P. Apruzese, Phys. Rev. A **27**, 1441 (1983).

9. J. P. Apruzese, J. Davis, D. Duston, and R. W. Clark, *Phys. Rev. A* **29**, 246 (1984).
10. J. P. Apruzese, J. Davis, D. Duston, and K. G. Whitney, *J. Quant. Spectrosc. Radiat. Transfer* **23**, 479 (1980).
11. C. Deeney, P. D. LePell, B. H. Failor, S. L. Wong, J. P. Apruzese, K. G. Whitney, J. W. Thornhill, J. Davis, E. Yadlowsky, R. C. Hazelton, J. J. Moschella, T. Nash and N. Loter, *Phys. Rev. E*, **51**, 4823 (1995).
12. J. P. Apruzese, R. W. Clark, and J. W. Thornhill, *J. Comp. Phys.* **119**, 156 (1994).
13. J. Davis, J. L. Giuliani, Jr., and M. Mulbrandon, *Phys. Plasmas* **2**, 1766 (1995).
14. J. P. Apruzese and J. Davis, Naval Research Laboratory Memorandum Report No. 5406 (1984).
15. F. L. Cochran, J. Davis, and A. L. Velikovich, *Phys. Plasmas* **2**, 2765 (1995).
16. This concept was suggested by R. B. Spielman of Sandia National Laboratories in a private communication.
17. B. Cullity, in *Elements of X-Ray Diffraction*, (Addison-Wesley, 1978).
18. J. P. Apruzese and J. Davis, *J. Appl. Physics* **57**, 4349 (1985).
19. The fact that modeling time dependent ionization dynamics is important for krypton z-pinch implosions was suggested by T. Nash of Sandia National Laboratories in a private communication.
20. R. B. Spielman, D. L. Hanson, M. A. Palmer, M. K. Maatzen, T. W. Hussey, and J. M. Peek, *J. Appl. Phys.* **57**, 830 (1985).
21. W. Lotz, *Z. Phys.* **216**, 241 (1968).
22. J. H. Degnan, F. M. Lehr, J. D. Beason, G. P. Baca, D. C. Bell, A. L. Chesley, D. Dietz, D. B. Dunlap, S. E. Englert, T. J. Englert, D. G. Gale, J. D. Graham, C. D. Holmberg, T. W. Hussey, R. A. Lewis, C. A. Outten, R. E. Peterkin, Jr., D. W. Price, N. F. Roderick, E. L. Ruden, U. Shumlak, G. A. Smith, and P. J. Turchi, *Phys. Rev. Lett.* **74**, 98 (1994).
23. I. V. Sokolov, *Sov. Phys. Usp.* **33**, 960 (1990).



Argon K-shell yield scaling with mass for $\eta = 4$ implosions.

Fig. 1

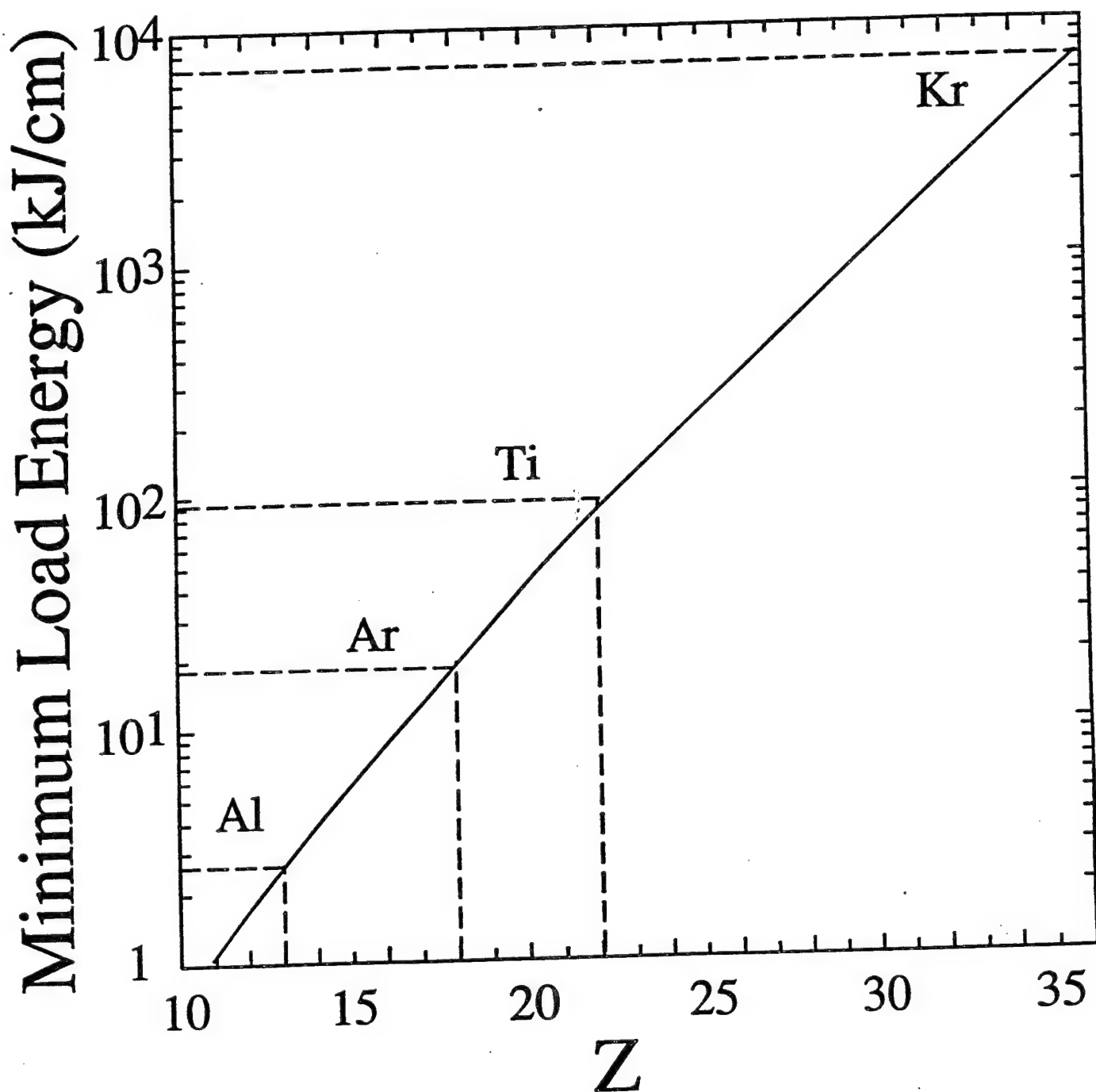


Figure 2. Minimum load energy requirements for obtaining 10 percent conversion of energy coupled to the load into K-shell photons as a function of atomic number.

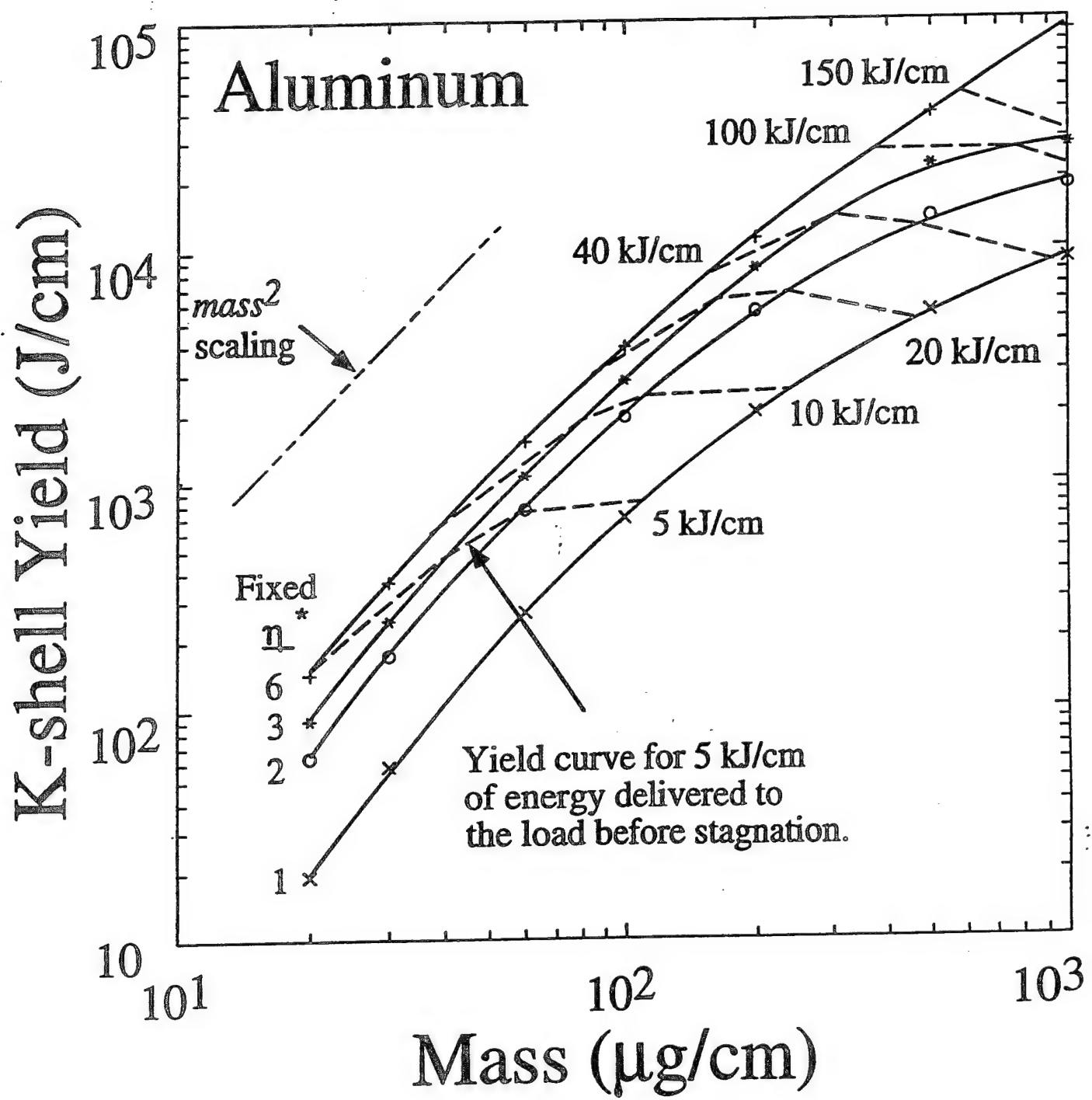


Figure 3. Aluminum K-shell yields as a function of mass load and η^* .

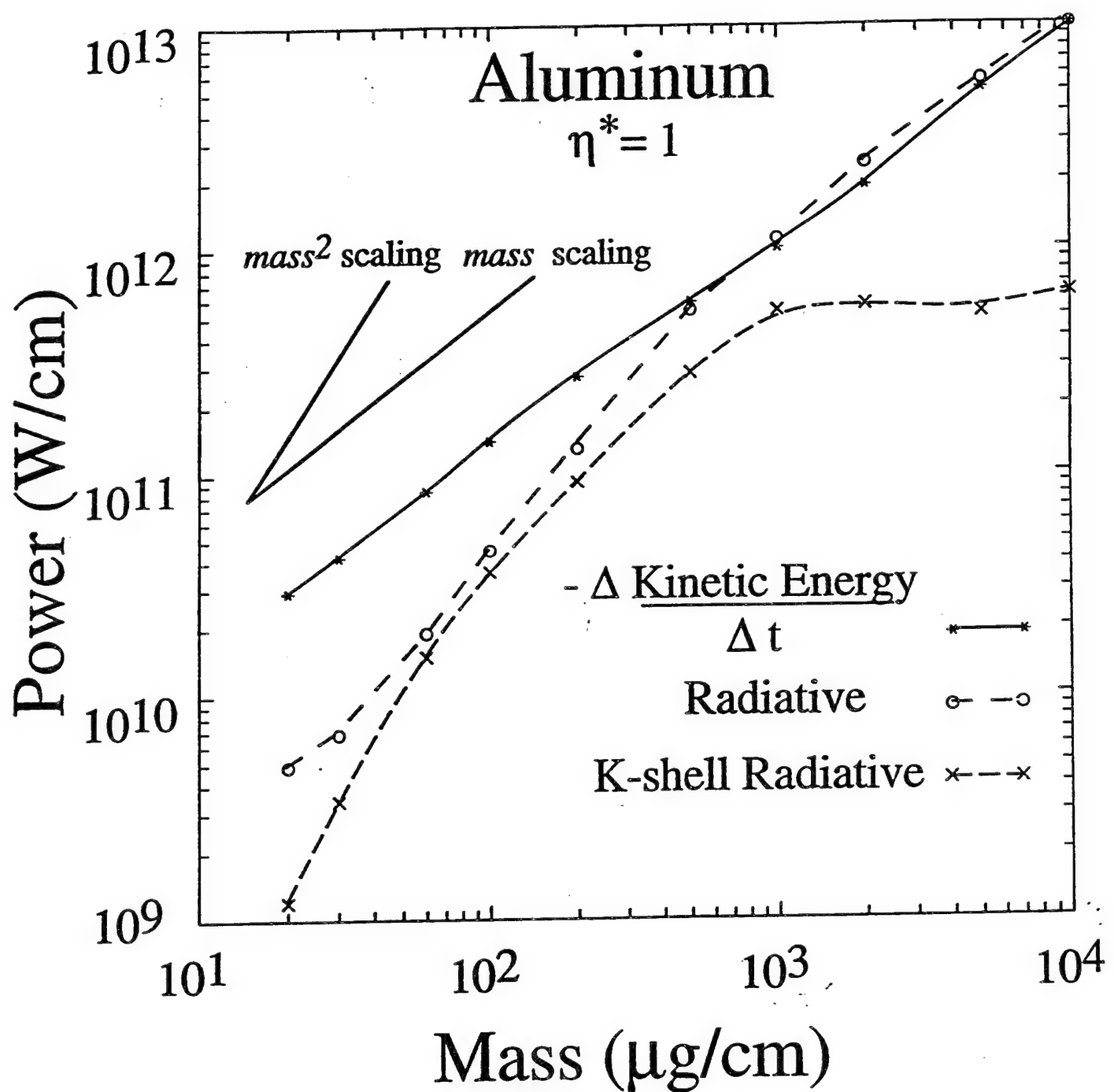


Figure 4. Kinetic energy thermalization rate, total radiative power, and K-shell radiative power as a function of mass load for $\eta^* = 1$ aluminum z-pinch implosions.

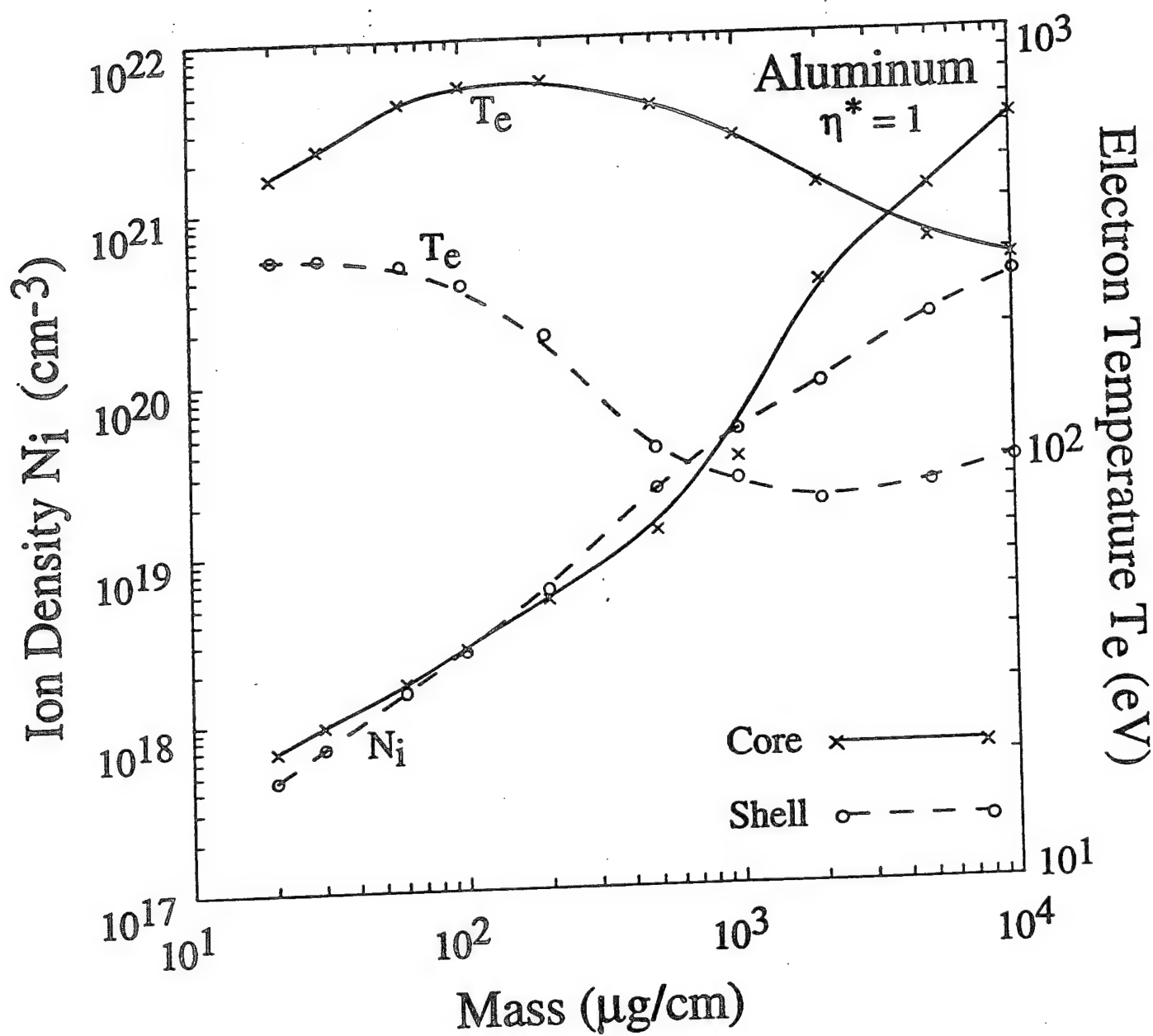


Figure 5. Mass and time averaged electron temperatures and ion densities of the core and shell regions of an aluminum $\eta^* = 1$ plasma as a function of mass load. The averaging is over the full-width-half-maximum of the K-shell emission pulse.

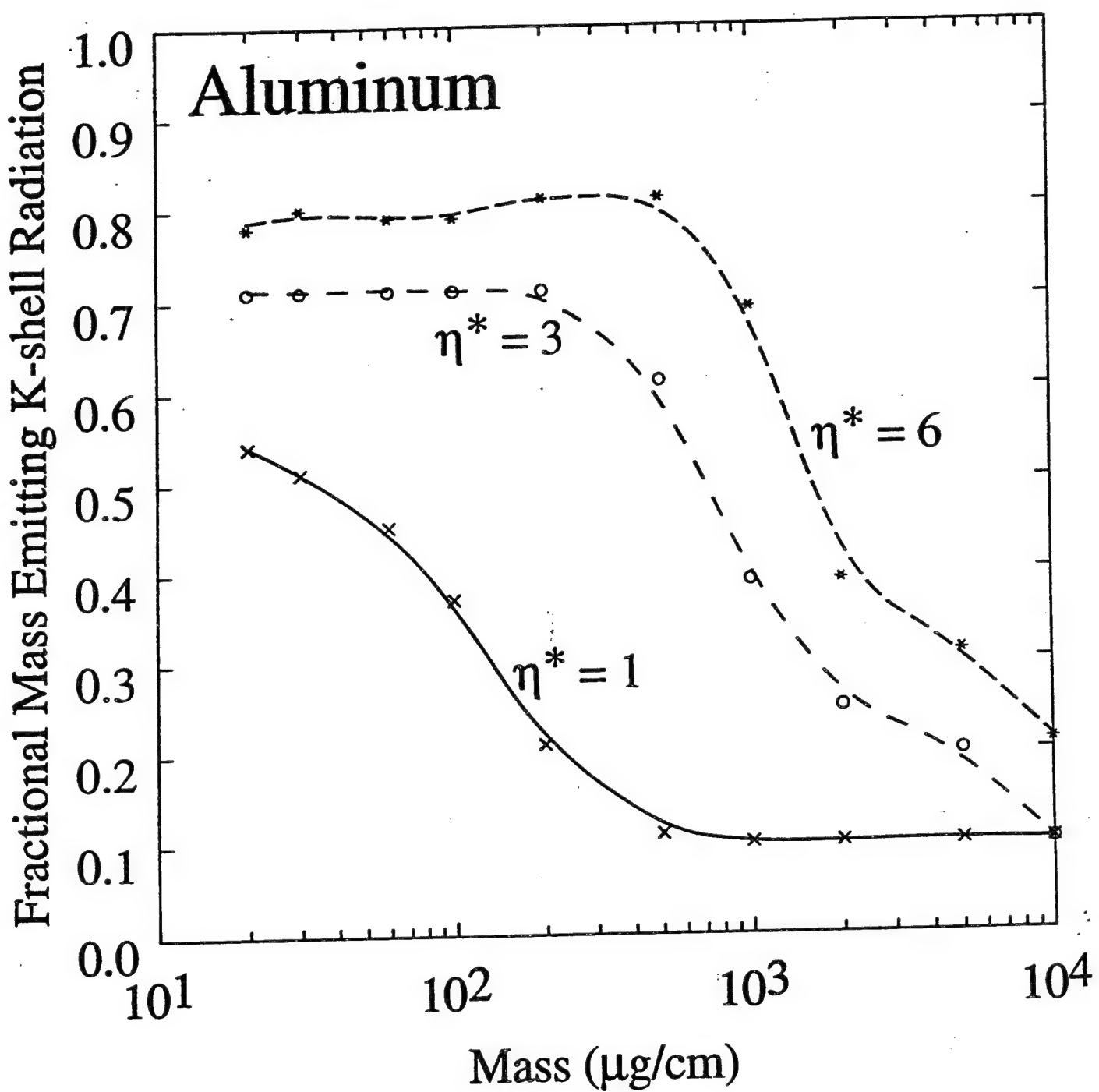


Figure 6. Fractional mass emitting K-shell radiation as a function of mass load and η^* for aluminum z-pinch implosions.

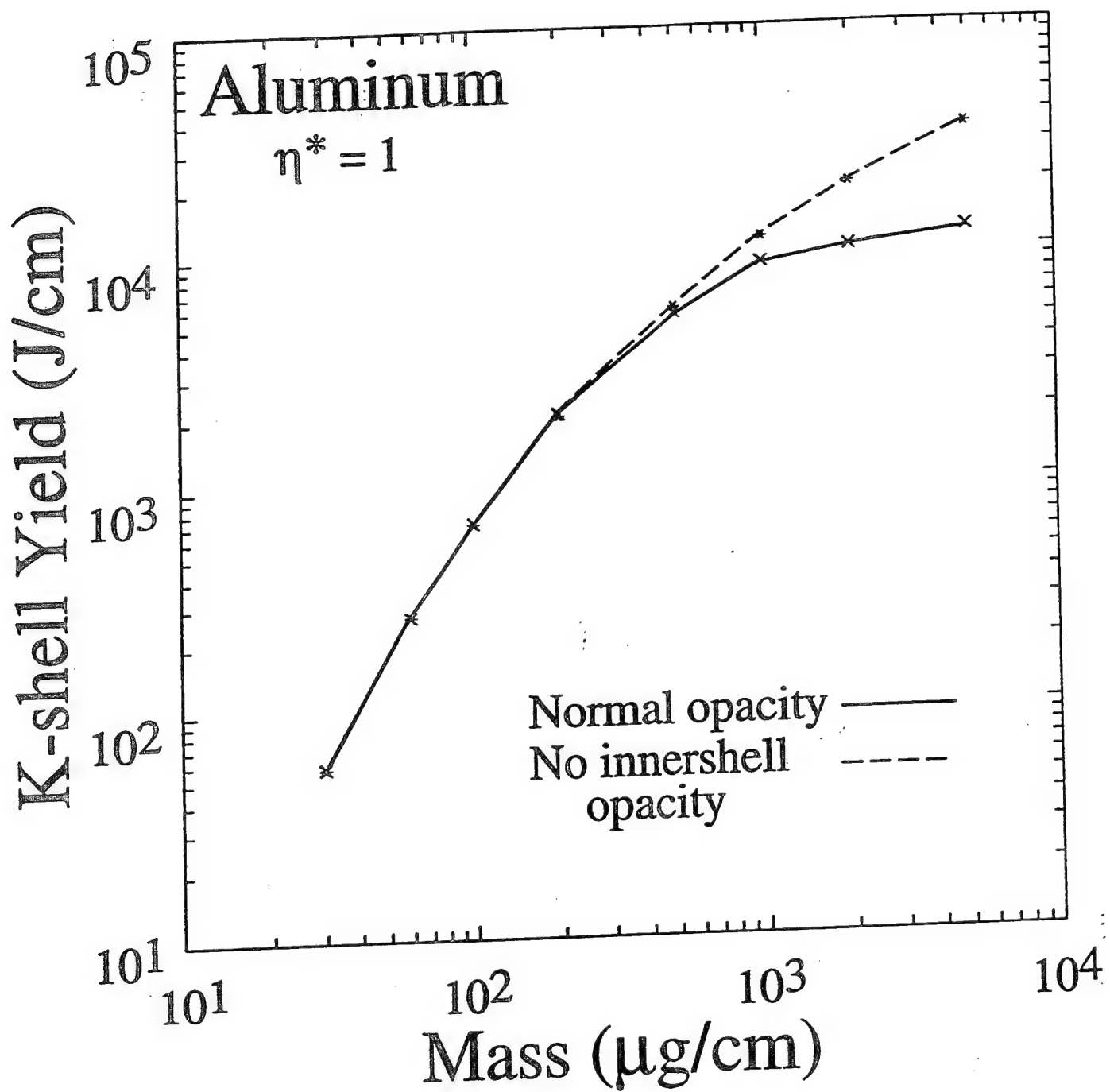


Figure 7. Aluminum K-shell yields as a function of mass load for $\eta^* = 1$ z-pinch implosions with and without innershell photoabsorption.

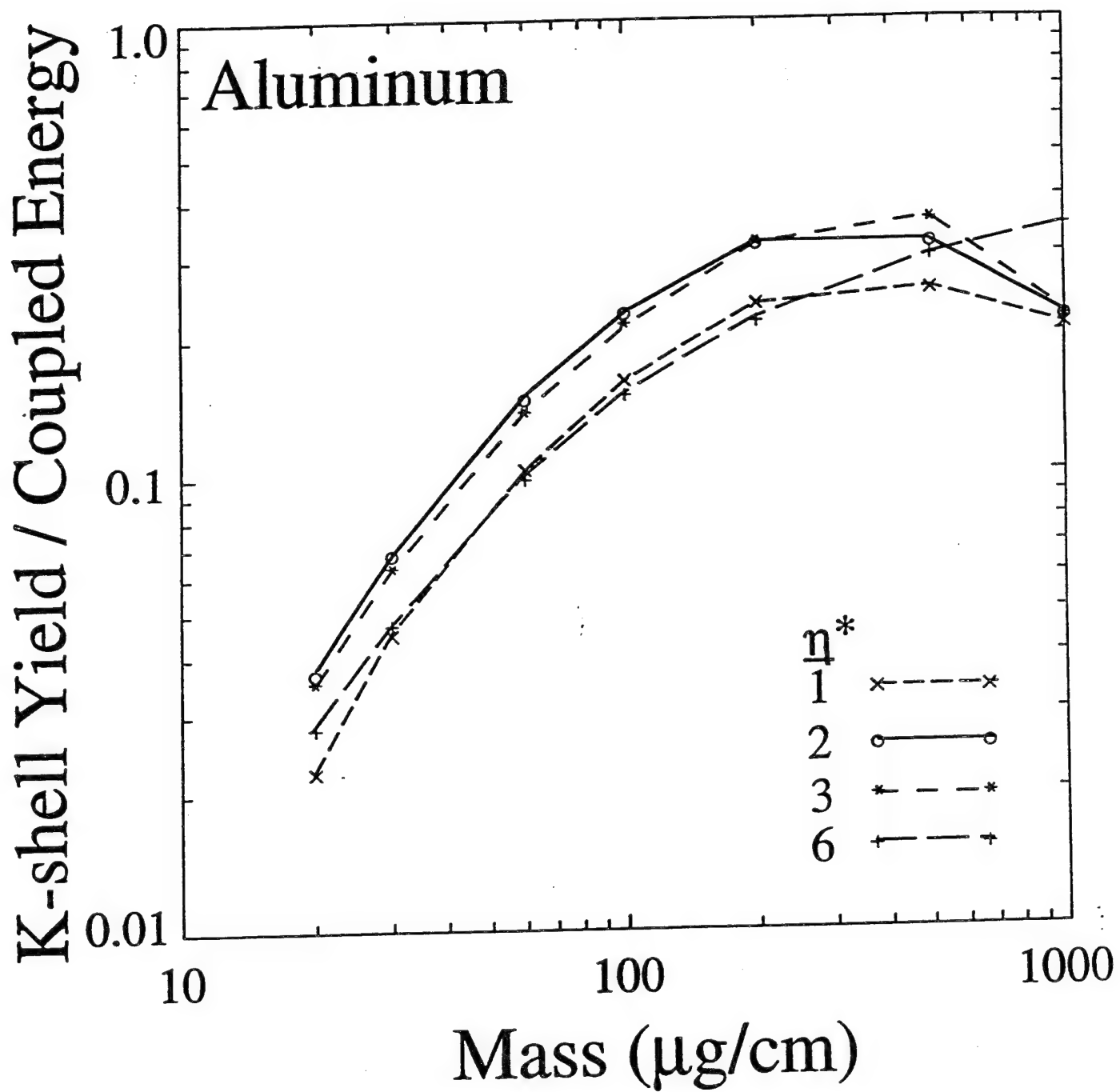


Figure 8. Efficiency of converting energy coupled to the load into aluminum K-shell photons.

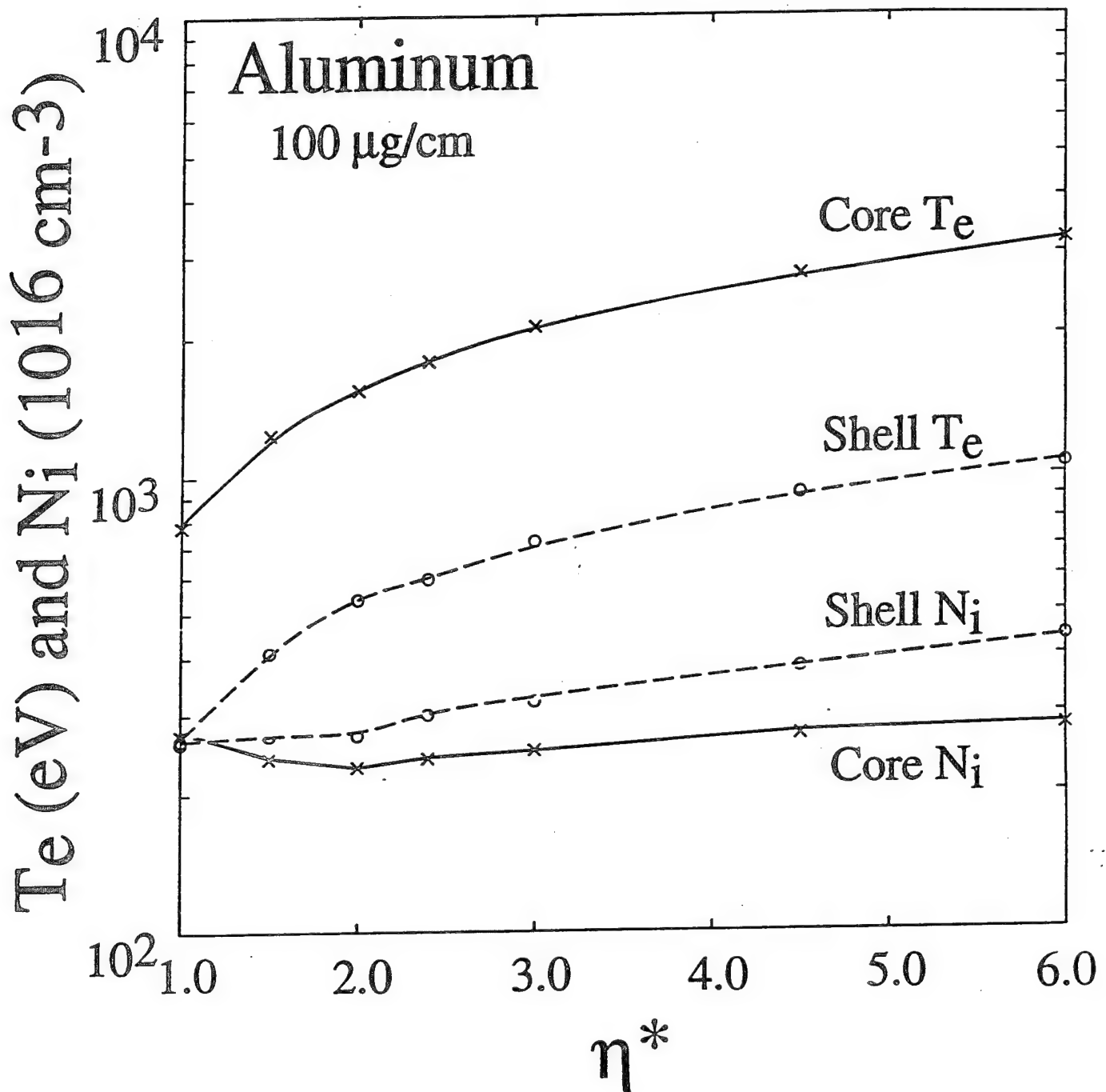


Figure 9. Mass and time averaged electron temperatures and ion densities of the core and shell regions of the plasma as a function of η^* for 100 $\mu\text{g}/\text{cm}$ aluminum z-pinch implosions. The averaging is over the full-width-half-maximum of the K-shell emission pulse.

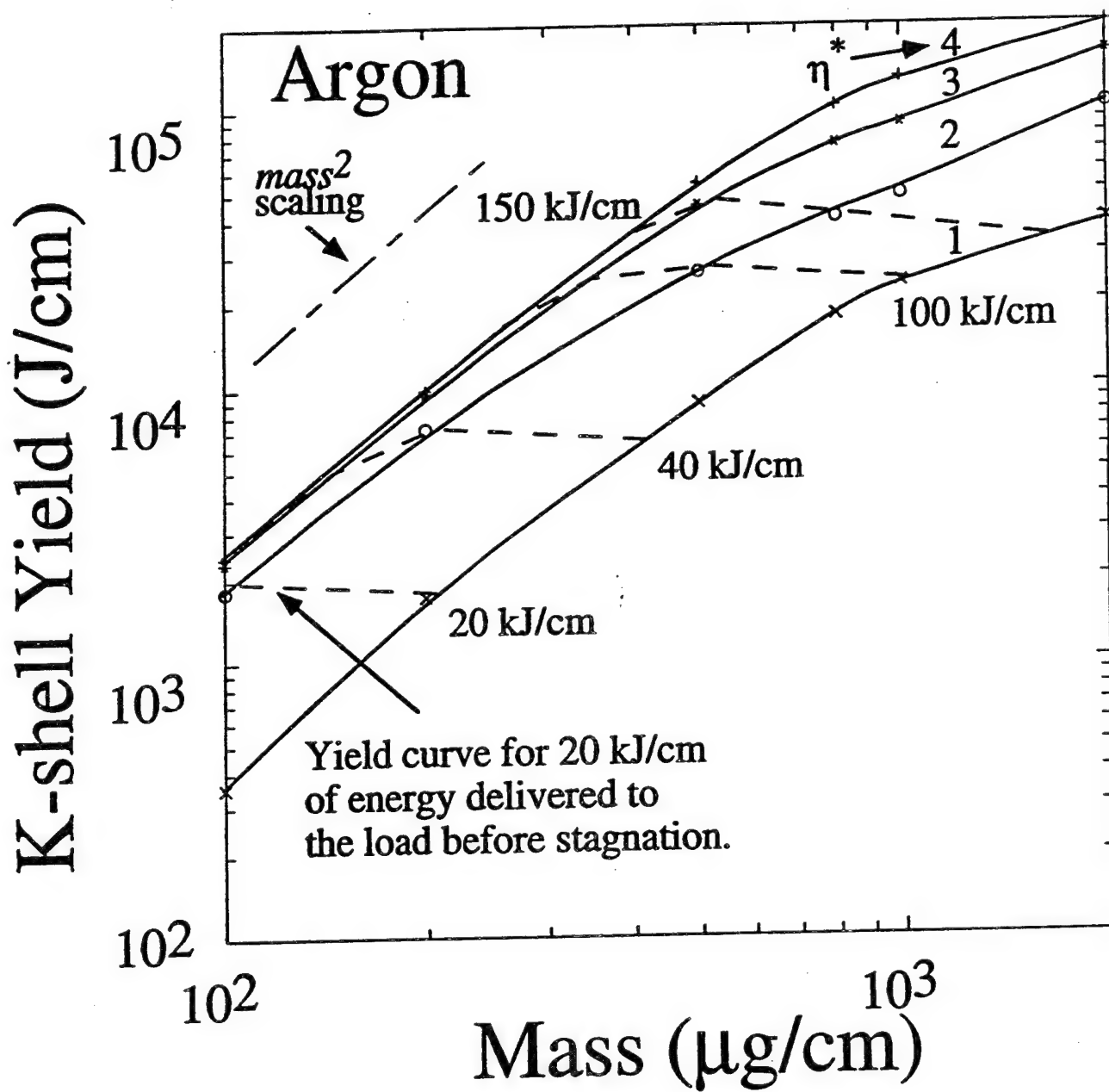


Figure 10. Argon K-shell yields as a function of mass load and η^* .

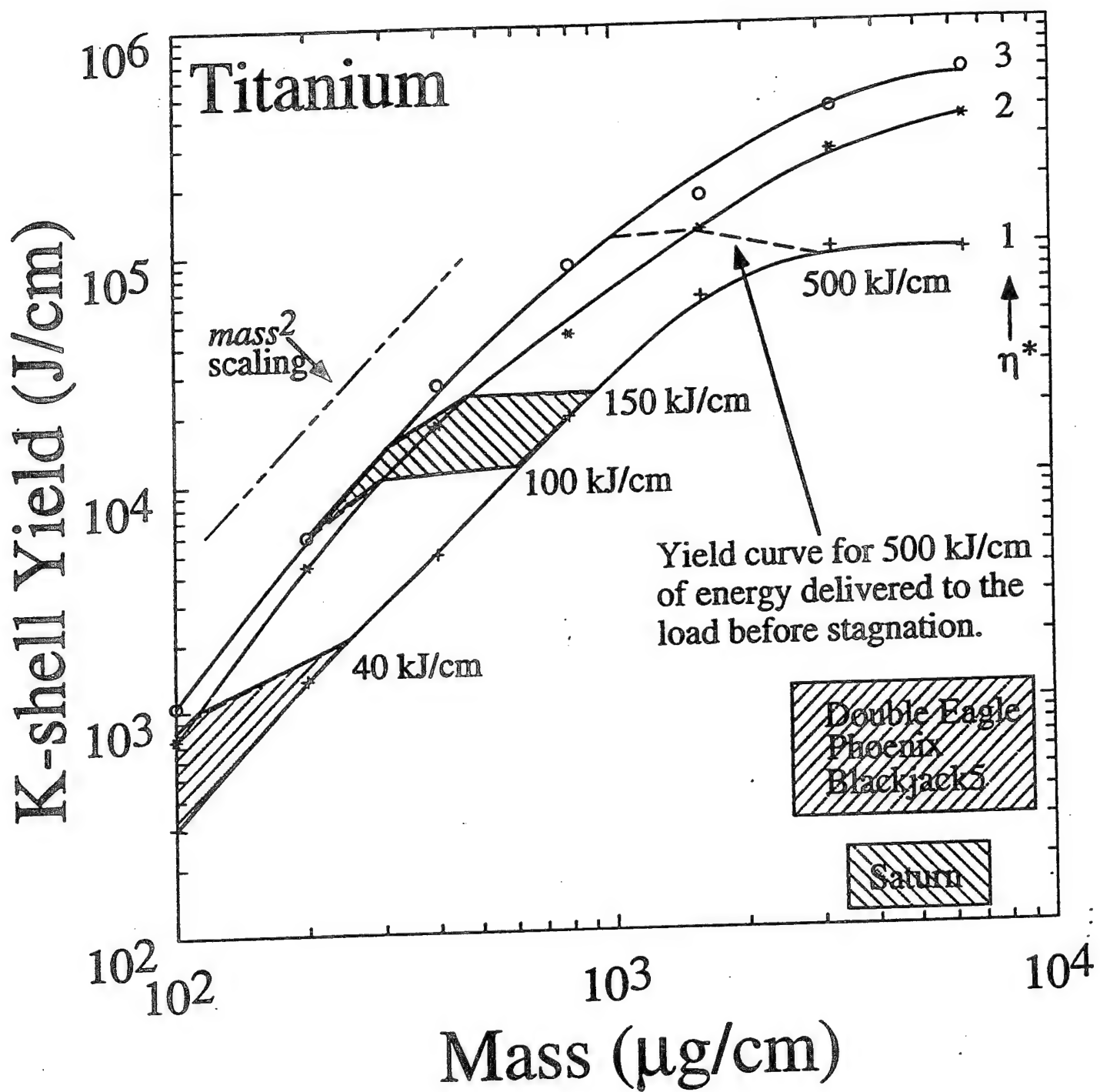


Figure 11. Titanium K-shell yields as a function of mass load and η^* .

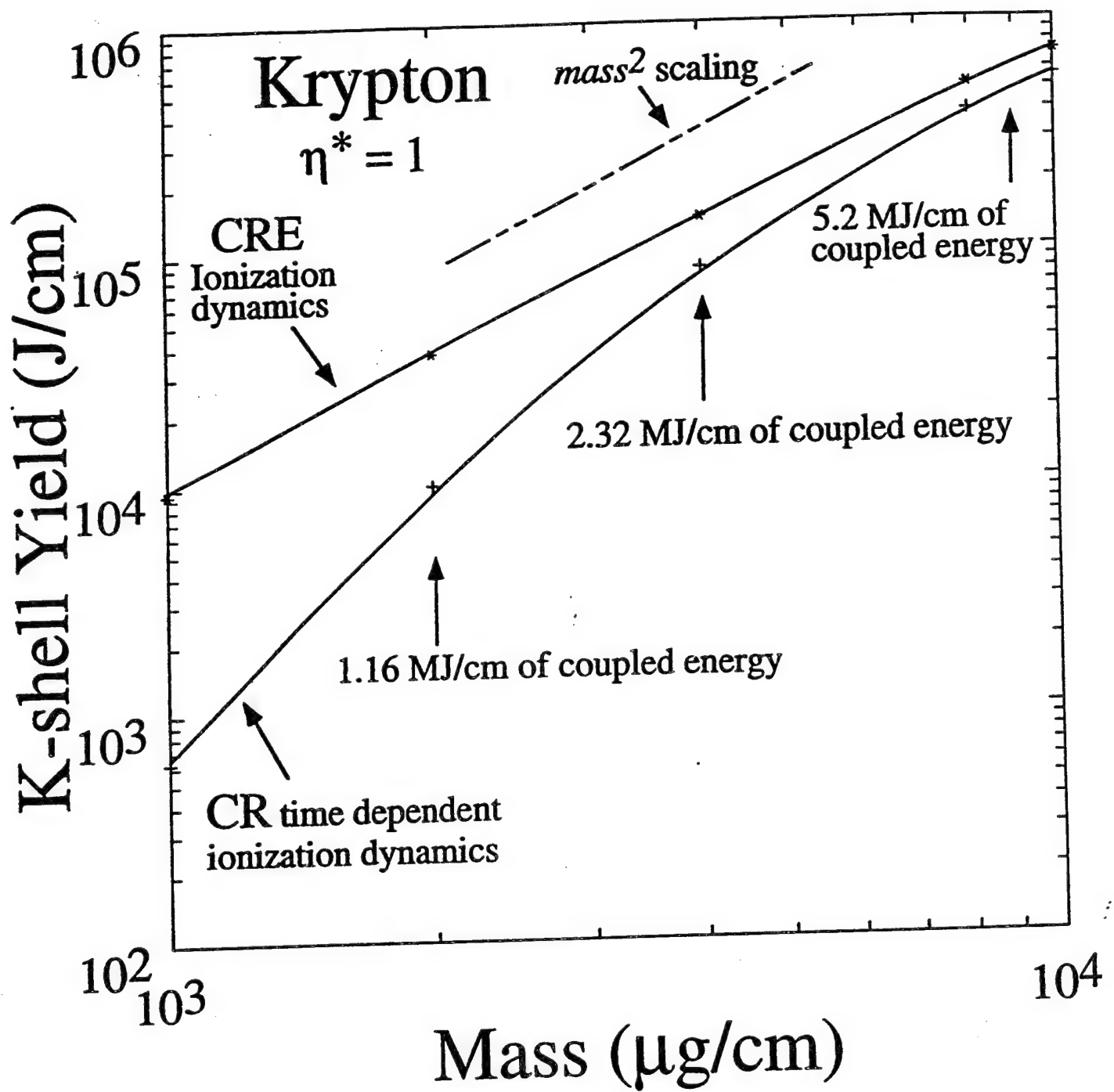


Figure 12. Krypton K-shell yields as a function of mass load for $\eta^* = 1$ z-pinch implosions as calculated using a collisional radiative equilibrium (CRE) ionization dynamics model and a time dependent collisional radiative (CR) model.

III. NONTHERMAL RADIATION FROM IMPLODING Z-PINCH PLASMAS

During the implosion and stagnation of a Z-pinch plasma a fraction of the current is carried by nonthermal electrons that produce energetic x-rays during collisions. Here we estimate the potential for producing nonthermal bremsstrahlung below 100 keV based on some extremely optimistic assumptions: 1) 100 % of the current is carried by nonthermal electrons, 2) all of the energy coupled to the pinch goes to generating this current, 3) The fast electron energy is completely absorbed in the plasma (thick target bremsstrahlung), and 4) there is no opacity.

The energy per incident electron that is emitted as bremsstrahlung, Q , is given by

$$Q = \int_0^E dE \frac{\frac{dE}{ds} |_{Rad}}{\frac{dE}{ds} |_{Rad} + \frac{dE}{ds} |_{Ion}}$$

where the kinetic energy of the incident electron is E (See Evans - "The Atomic Nucleus").

$$\frac{dE}{ds} |_{Rad} = N \int_0^{\infty} \chi(\omega) d\omega$$

is the relativistic radiative loss rate per unit path length ds , N is the ion density, and $\chi(\omega)$ is the radiative cross section (see Jackson - "Classical Electrodynamics", 1962 ed.).

$$\frac{dE}{ds} |_{Ion}$$

is the relativistic ionization loss rate per unit path length ds (see Dalgarno - "Atomic and Molecular Processes").

The radiative yield in a frequency range $\omega_1 - \omega_2$, which is due to a single incident electron with energy E , is calculated from

$$Y(\omega_1, \omega_2) = Q \frac{\int_{\omega_1}^{\omega_2} \chi(\omega) d\omega}{\int_0^E \chi(\omega) d\omega}$$

The percentage of the incident electron energy that appears as bremsstrahlung in the frequency range $\omega_1 - \omega_2$ is then

$$\frac{Y(\omega_1, \omega_2)}{E} = \frac{Q \int_{\omega_1}^{\omega_2} \chi(\omega) d\omega}{E \int_0^E \chi(\omega) d\omega}$$

Assuming that all of the machine energy that is coupled into the pinch goes into generating nonthermal electrons at a given incident energy E , then the total radiative yield in the frequency range $(\omega_1 - \omega_2)$ normalized to the machine energy is also given by

$$\frac{\text{Total Radiation}(\omega_1, \omega_2)}{\text{Machine Energy}} = \frac{Q}{E} \frac{\int_{\omega_1}^{\omega_2} \chi(\omega) d\omega}{\int_0^E \chi(\omega) d\omega}$$

This is the best that can be done because it also assumes: 1) 100 percent of the current is carried by nonthermals, 2) any arbitrarily large voltage V or reflexing that is needed to produce the electrons with energy E can occur across the pinch, i.e., it allows for voltage or power amplification, and 3) no radiative opacity. The results of this work as applied to a general pulse power machine and a tungsten target is shown in Fig. 1 and results specific to Double EAGLE and Saturn are shown in Figs. 2 and 3, respectively.

Nonthermal Electron Generated K-alpha Emission

We applied the same analysis as used for thick target bremsstrahlung to K-alpha emission from a tungsten plasma,

$$Q|_{K-\alpha} = \int_0^E dE \frac{\frac{dE}{ds}|_{K-\alpha}}{\frac{dE}{ds}|_{Brems} + \frac{dE}{ds}|_{K-\alpha} + \frac{dE}{ds}|_{Ion}}$$

where,

$$\frac{dE}{ds}|_{K-\alpha} = N\sigma(E, Z) \times \text{ionization potential}$$

σ is the cross section for knocking out an inner shell electron (Coulomb-Born-exchange calculation), which is dependent upon the atomic number Z of the absorber and the incident energy E of the electron. N is the ion number density. The K fluorescence yield is taken as unity for tungsten and the ionization potential is 69.5 keV. The results for nonthermal electron generated $K - \alpha$ emission from a general pulse power machine are shown in Fig. 4.

We conclude that our (overly optimistic) estimate shows that there is a potential for 2 % conversion of machine energy into nonthermal electron generated bremsstrahlung below 100 keV from tungsten (conversion efficiency is proportional to Z). In reality this estimate is probably generous by over an order of magnitude. This conclusion is supported by (Tiger code) three dimensional Monte-Carlo electron, photon transport calculations (thick target) that show conversion efficiencies that are two orders of magnitude below our simple optimistic estimates. Based on this analysis it does not appear that nonthermals are an interesting source for producing radiation in the 20 - 100 keV range.

Results

Under the assumptions of optically thin opacity and 100 % conversion of machine energy into nonthermal electrons.

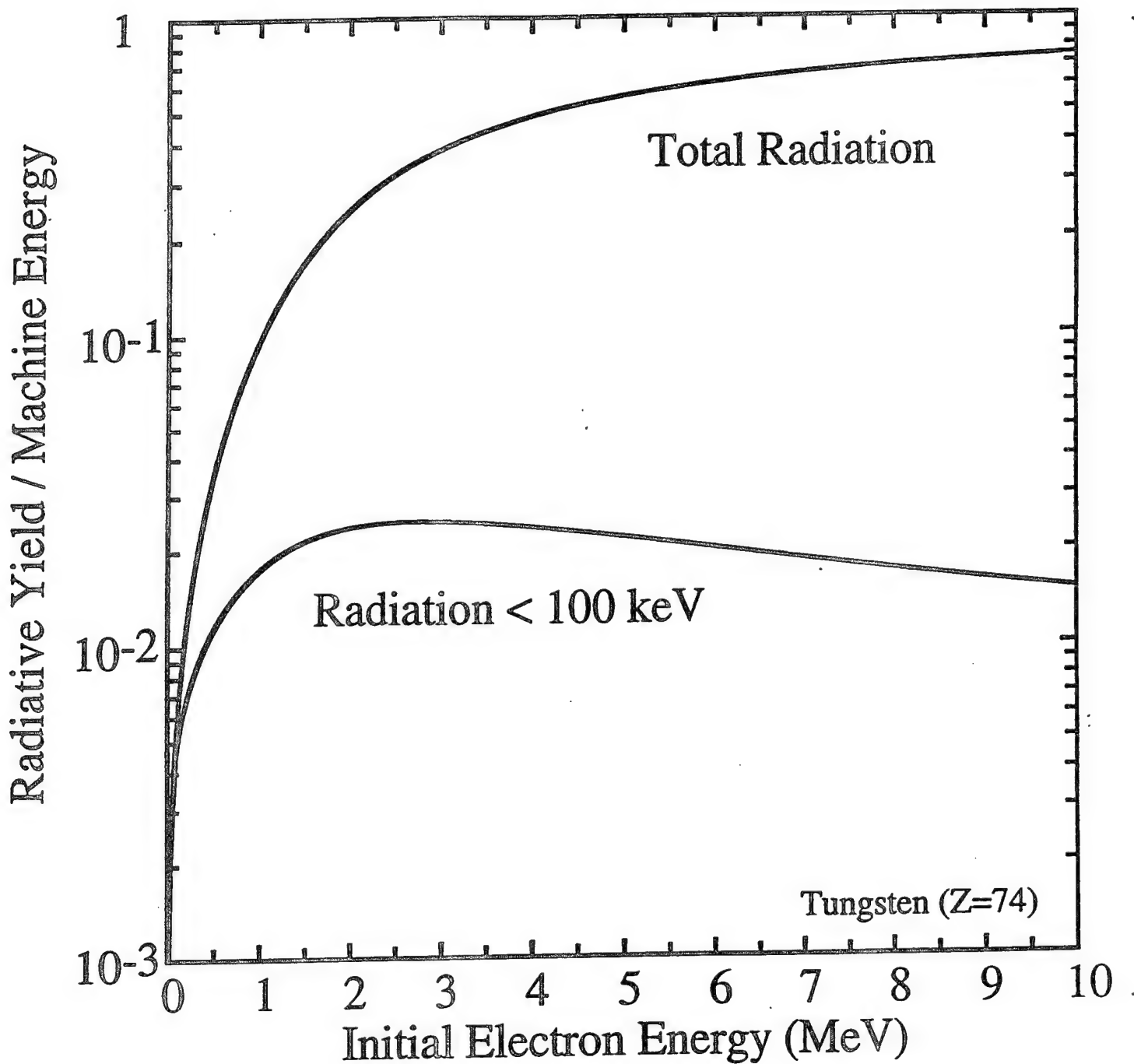


Fig. 1

Results

Under the assumptions of optically thin opacity and 100 % conversion of machine energy into nonthermal electrons.

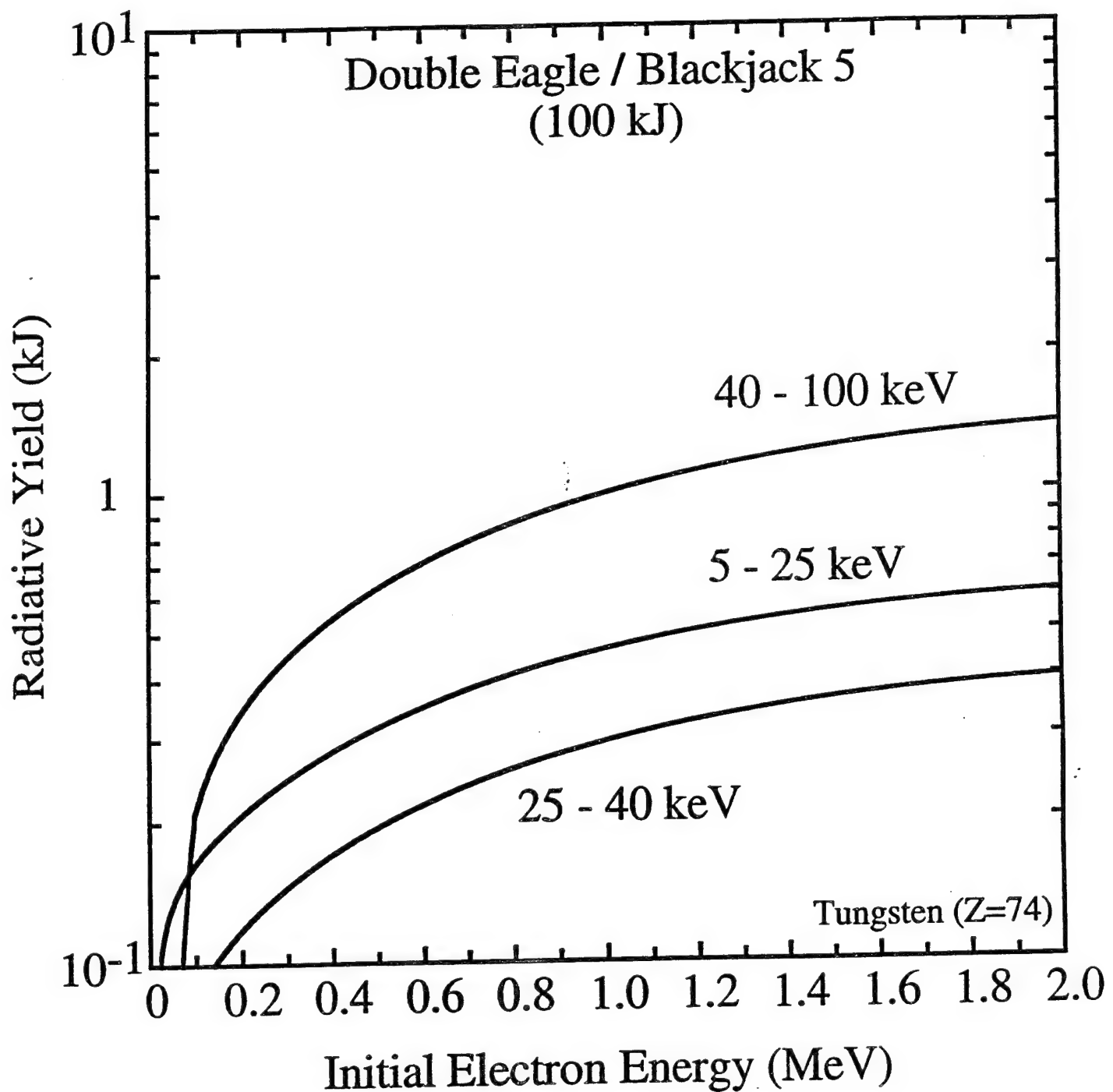


Fig. 2

Results

Under the assumptions of optically thin opacity and 100 % conversion of machine energy into nonthermal electrons.

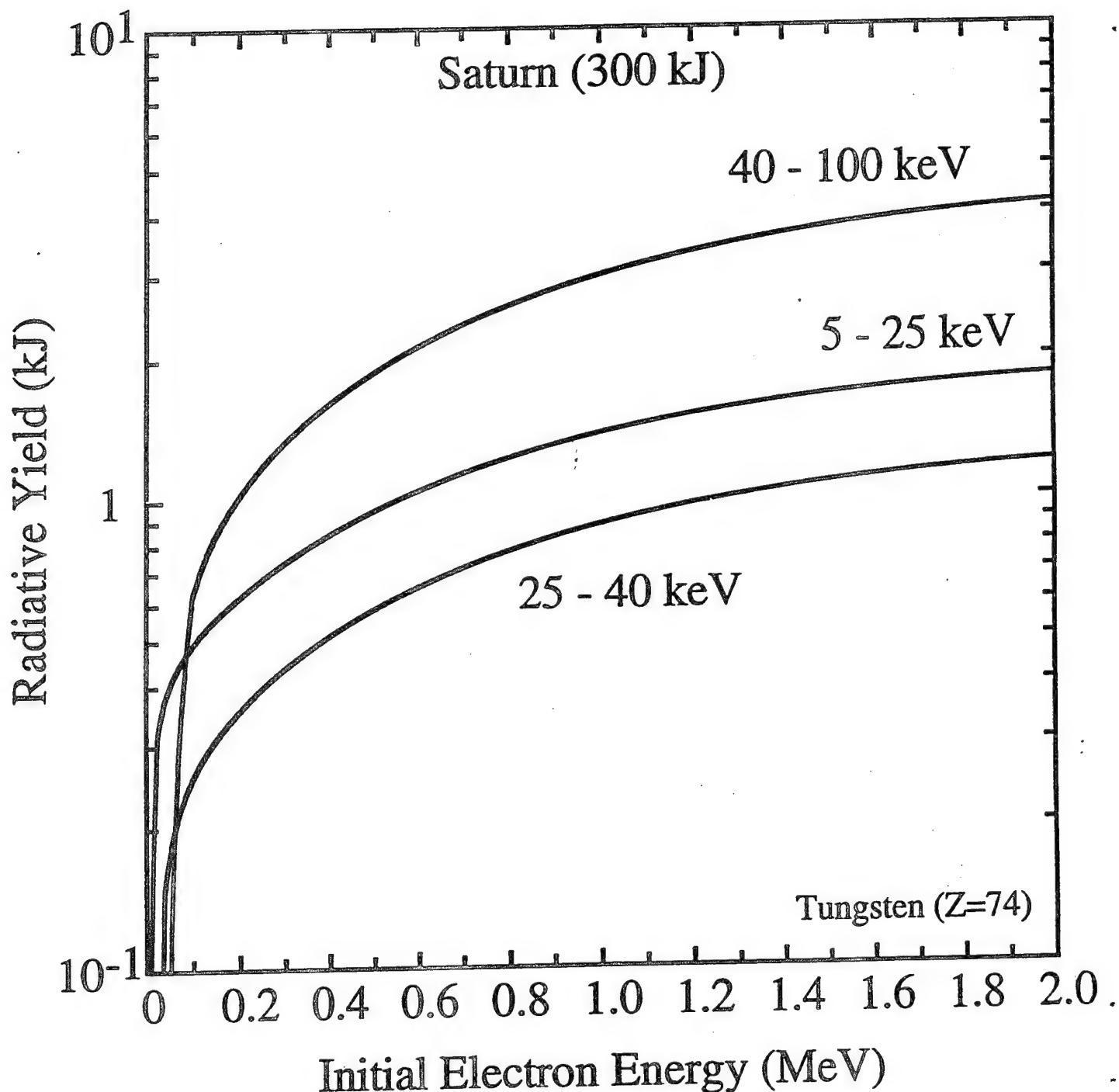


Fig. 3

K-alpha Results

Under the assumptions of optically thin opacity and 100 % conversion of machine energy to nonthermal electrons.

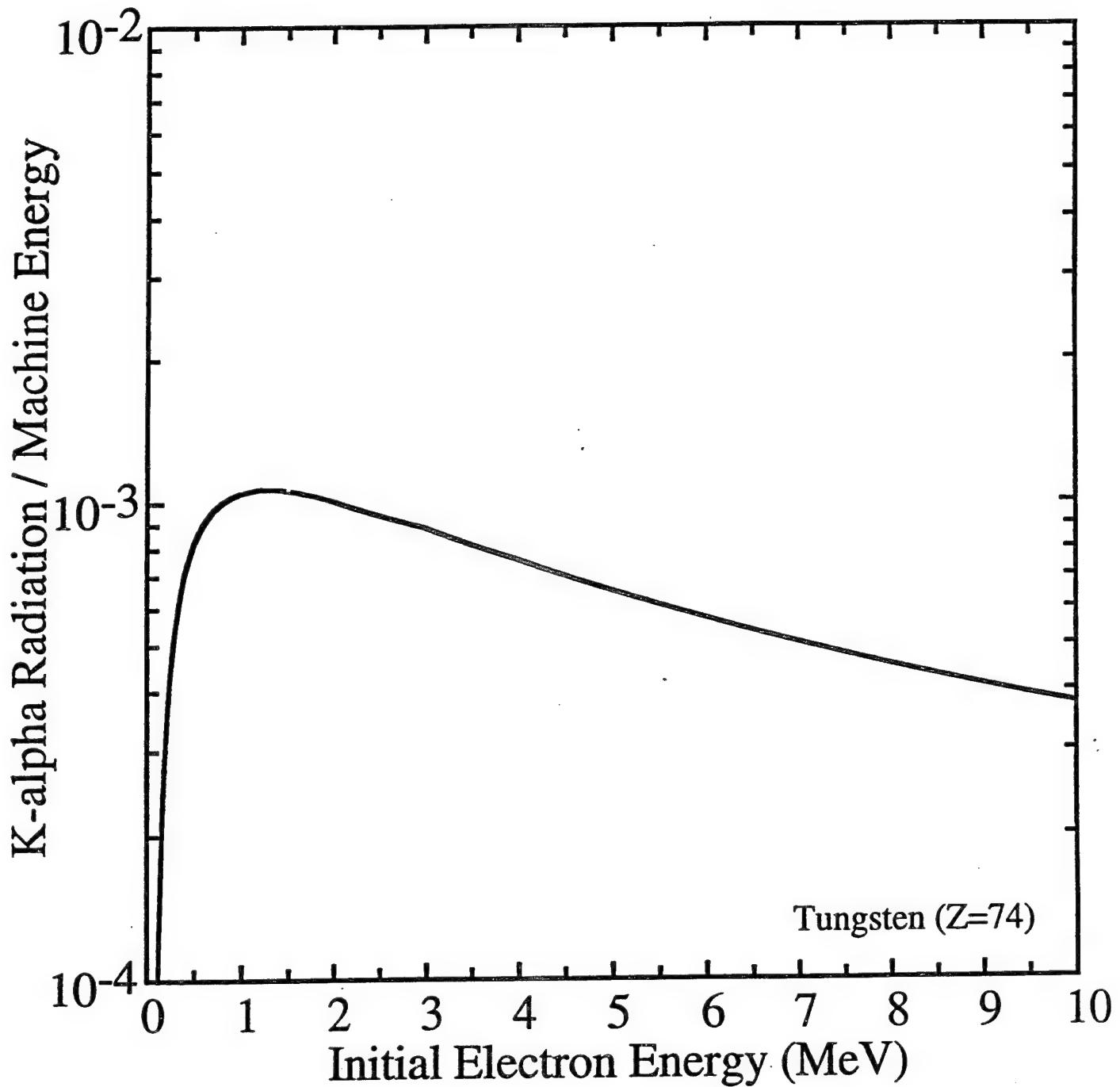


Fig. 4

IV. PUFF-ON-WIRE Z-PINCH LOADS

Earlier work by Clark, Davis and Cochran (Phys. Fluids 29, 1971, (1986)) had shown that stagnating an outer neon gas puff onto a high density neon core plasma did not enhance the K-shell emission from Z-pinch implosions. However, their work only examined K-shell emission behavior in the so called "efficient" scaling regime for which the K-shell emission increases linearly with the *mass* of the load. Whereas, in the "inefficient" scaling regime the K-shell yield increases as the square of the ion density (N_i^2) or *mass*², see Section II. Therefore it was hypothesized that the K-shell emission from relatively low mass plasmas could potentially be enhanced by putting a wire on axis because the wire should increase the axial ion density.

This idea was tested theoretically by comparing the dynamics of a 1-D model implosion of an argon gas puff to that of an argon gas puff stagnating onto a titanium wired located on axis. The model used is similar to the one described in Section II. The puff load consisted of a 2 cm length, 3 cm radius, 80 $\mu\text{g}/\text{cm}$ load of argon. The nozzle width was modeled as 0.5 cm. The same puff gas configuration was used for the puff on wire calculation and a 20 $\mu\text{g}/\text{cm}$ titanium wire was modeled on axis. The initial radius of the wire is 0.02 cm. The calculations were driven by a reduced Double EAGLE open circuit voltage profile and lumped circuit model (see Fig. 1) such that the peak current and energy delivered to the load were similar to that delivered by ACE 4 as it operated in the summer of 1994.

The results of this investigation should only be viewed as qualitative because experimentally the interaction of a gas puff with a wire plasma involves complicated physics which takes place in the core region of the plasma where the gas puff and wire meet during stagnation. It is not clear that the ad hoc increases in plasma transport coefficients that gave us reasonable phenomenological agreement with the stagnation state of numerous PI puff gas and wire array loads is also applicable to a puff on wire interaction. There are several other obvious limitations inherent in these calculations, they include: 1) the cold start physics responsible for the heating and expansion of the titanium wire is not known - the wire is modeled as a plasma initially at 2 eV that is not allowed to expand until the temperature exceeds 10 eV and 2) because of limitations on the probability of escape model used in these calculations to transport radiation there is no radiative heating of the cold titanium wire by the warmer argon plasma.

The results of the comparison between the puff and puff on wire (POW) load are presented below in Table 1.

	Puff	Puff on Wire
Energy coupled to load (kJ/cm)	15	20
Total radiative yield (kJ/cm)	7	13
Peak radiative power (TW/cm)	0.3	0.5
Radiation > 3 keV (kJ/cm)	0.5	0.9
Peak > 3 keV power (TW/cm)	0.04	0.08
Peak core $\langle N_i \rangle$ (cm^{-3})	2×10^{18}	4×10^{18}

Peak core $\langle T_e \rangle$ (keV)	1.8	1.6
Peak core $\langle T_i \rangle$ (keV)	40	20

Table 1.

where $\langle \rangle$ represents mass and time averaged quantities over the plasma that is emitting in the K-shell $\sim 10\%$ of the plasma (located in the core). These results clearly show that the POW configuration for the chosen conditions couples more energy into the load, radiates almost twice as much in the total yield and > 3 keV regime, and is twice as dense in the core than a pure gas puff.

An experimental/theoretical investigation into the puff on wire configuration was also initiated with PI. The experiments were performed using an argon gas puff and titanium wires. The experimental pinches were 4 cm in length and the nozzles were 1.25 cm in radius. The Double EAGLE circuit model consisted of 0.3 ohms in series with 20 nh inductance in series with the load. The open circuit voltage profile is described by $V_{oc} = 2.35MV(1 + (t/320)^2)\sin(\pi t/160)$, where t is in ns.

Table 2. shows a summary of results from these calculations. There are results for puff only calculations of 100, 150, 200 and 250 $\mu g/cm$ as well as results for these same gas puffs impinging upon 0.8 mil and 1.0 mil titanium wires. Note, we originally thought the pinches were 3 cm in length so most of the calculations were done at this length. We have not yet gone back and repeated the calculations at 4 cm. However, we did perform a calculation for a 4 cm long, 150 $\mu g/cm$ argon puff onto a 0.8 mil titanium wire load for which it appears to first order that the radiative energy that is lost per-unit-length is made up by having a longer pinch. Also the implosion time was 4 ns longer for the 4 cm length load because of its larger inductance.

Fig. 2 shows a comparison between experimental and calculated > 3 keV yields for puff-only and puff onto a 0.8 mil titanium wire. The implosion times are all fiduciated with the linear rise of the current and 4 ns has been added to the calculated implosion times in order to correspond more closely with the experimental times. From this figure we see that there is reasonable agreement between calculations and experiments for the puff-only configuration. However, more experimental data is needed at both longer (more massive) and shorter (less massive) implosions times. The experimental and theoretical yields are also in reasonable accord when the 0.8 mil wire is on axis. The ACE 4 calculation that was discussed above and the lower implosion time results (Fig. 1) show that at small mass loads the POW configuration out performs the puff-only configuration. Unfortunately, there were no puff-only experiments performed at low implosion times to verify these calculated trends. This is an important trend that should be investigated experimentally because the POW may be a technique for obtaining maximal K-shell yields from elements that can only be imploded in the inefficient scaling regime because of machine energy limitations, i.e., it may improve maximal titanium yields on Double EAGLE and Saturn, krypton yields on a Jupiter class machine, or argon yields on ACE 4.

Fig. 3 shows a comparison between experimental and calculated > 3 keV yields for puff-only and puff onto a 1.0 mil titanium wire. Because of the large differences between calculated and experimental yields at the larger implosion times, one has to question the validity of way the interaction of the inner puff gas and titanium wire is being modeled. One reason the calculated

yields drop off at the larger implosion times is that the 1 mil titanium wire cools the core of the argon plasmas to the extent that the cores do not reach temperatures needed to emit in the K-shell. The fact that the experiments do not exhibit as large a fall off in yield as the calculations at the larger implosion times is possibly an indication that we are overestimating the thermal conduction into the titanium wire or that the experimental core densities are not as large as predicted. A closer examination of the experimental data is needed in order to better asses the model.

In addition to optimizing K-shell emission for low mass loads, improving simulation fidelity was another reason for investigating the POW configuration. A goal of the experiments was to improve the yield above 4 keV. The data are still being analyzed but one encouraging preliminary result is that the best puff-only experiments produced 100 J of radiation between 4.5 and 5.0 keV, whereas the 91 ns implosion time puff onto a 0.8 mil titanium wire load produced in excess of 1 kJ of radiation in this range. The yield above 3 keV may have also increased above that of the puff-only configuration for this load - needs further experimental investigation. Of the calculations performed the one that best represents this experimental load is a 3 cm length, $100 \mu\text{g/cm}$ argon puff onto a 0.8 mil titanium wire calculation. The calculated yield in the 4.5 - 5.0 keV range is 2.6 kJ from this load and it is 225 J from the puff-only configuration. This result also indicates that the core ion densities may be overpredicted since the calculated puff-only yields in the range 4.5-5.0 keV are larger than measured.

PI Argon Puff onto Ti Wire Shot Matrix

Machine -- Double EAGLE

Charging voltage 60 kV

1.25 cm radius nozzle

3 cm length pinch

Argon only

	100 mg/cm	150 mg/cm	200 mg/cm	250 mg/cm
> 3 keV Yield (kJ/cm)	3.0	5.0	6.0	6.0
> 4 keV Yield (kJ/cm)	0.4	0.7	0.9	0.9
Implosion time (ns)	102	110	118	125
Coupled energy (kJ/cm)	24	29	34	36
η^*	2.5	2.0	1.9	1.6
Peak kinetic e. (kJ/cm)	8.4	10	11	11.5
η	0.9	0.7	0.6	0.5

1 mil Ti wire

	3.3	4.0	2.5	0.4
> 3 keV Yield (kJ/cm)	3.3	4.0	2.5	0.4
> 4 keV Yield (kJ/cm)	1.6	1.6	0.8	0.02
Implosion time (ns)	102	110	118	125
Coupled energy (kJ/cm)	24	29	34	36
η^*	2.5	2.0	1.9	1.6
Peak kinetic e. (kJ/cm)	8.4	10	11	11.5
η	0.9	0.7	0.6	0.5

0.8 mil Ti wire

	3.5	4.9	4.8	3.0
> 3 keV Yield (kJ/cm)	3.5	4.9	4.8	3.0
> 4 keV Yield (kJ/cm)	1.5	1.8	1.7	1.0
Implosion time (ns)	102	110	118	125
Coupled energy (kJ/cm)	24	29	34	36
η^*	2.5	2.0	1.9	1.6
Peak kinetic e. (kJ/cm)	8.4	10	11	11.5
η	0.9	0.7	0.6	0.5

Note, quoted implosion times are fiduciated at the zero of the open circuit voltage profile.
 Subtract 15 ns from these values to fiduciate with the linear rise of the current profile.

Table 2

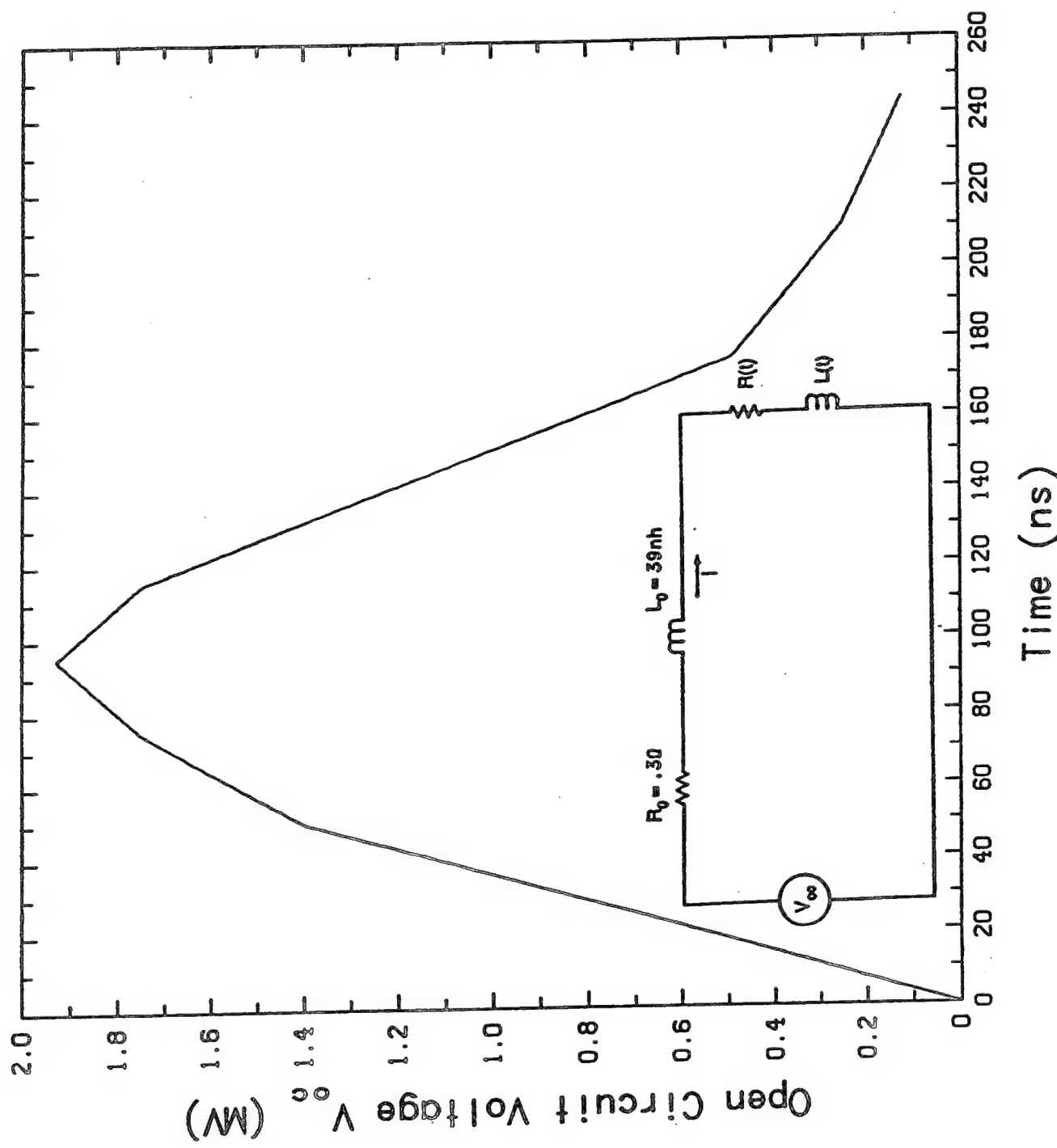


Fig. 1 Double Eagle circuit parameters and open circuit voltage profile.

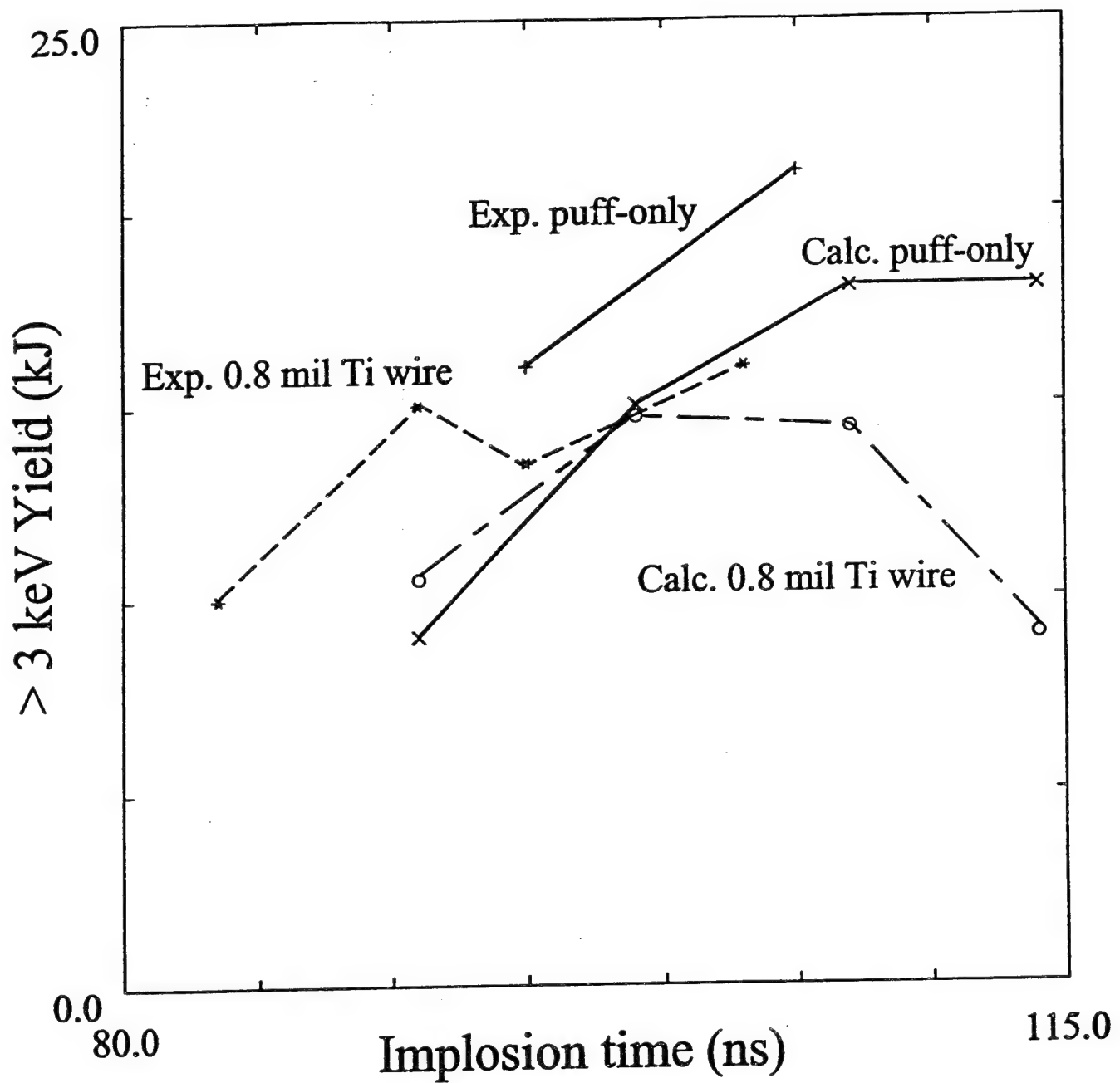


Fig. 2 Experimental and calculated K-shell emission above 3 keV for gas puff and 0.8 mil Ti wire on axis configurations.

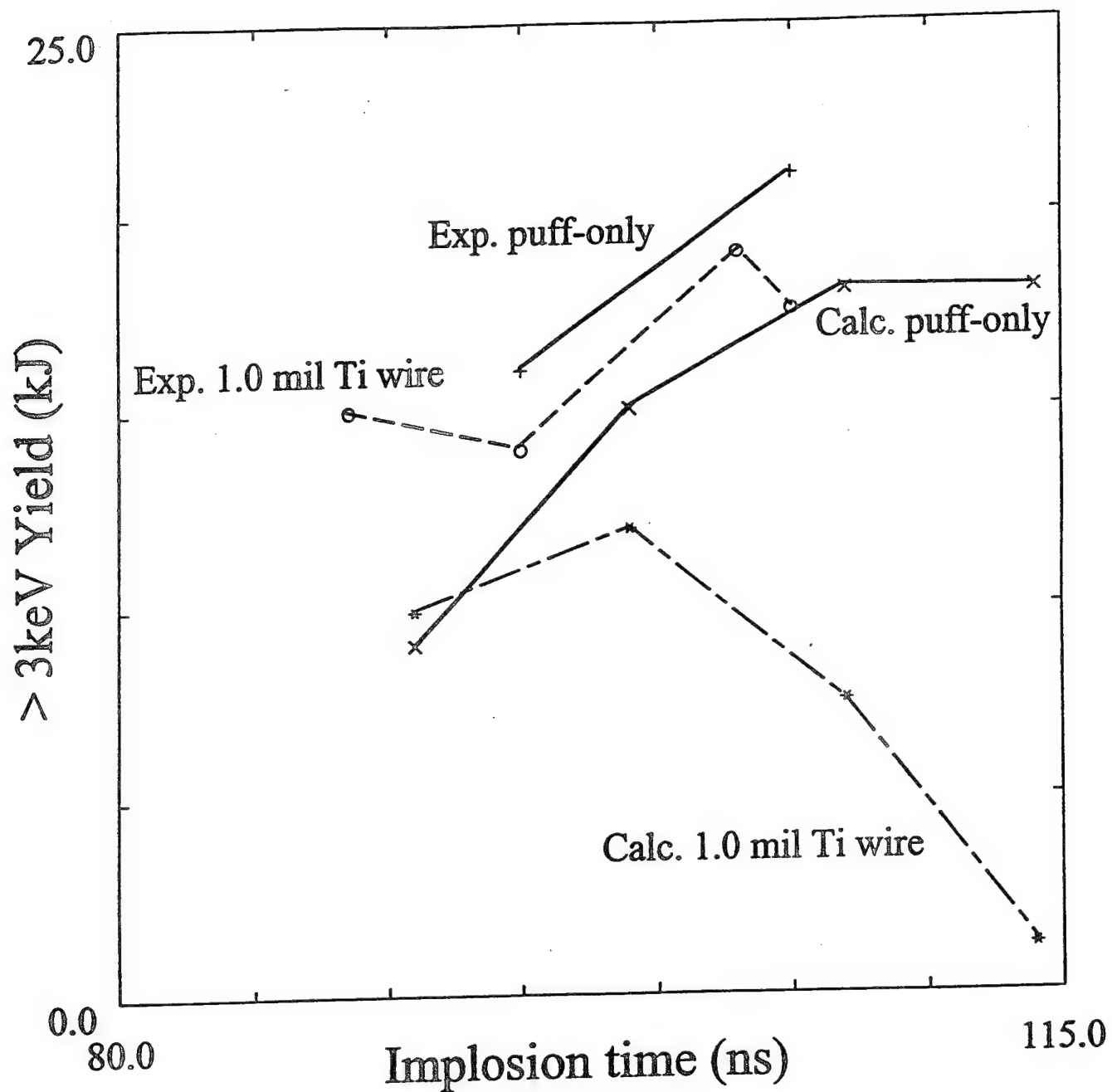


Fig. 3 Experimental and calculated K-shell emission above 3 keV for gas puff and 1.0 mil Ti wire on axis configurations.

V. IMPLOSION STABILITY

A. Introduction

Our investigations into the stability of PRS loads have shown that the outer radius is limited to about 3 cm if the load is a thin shell. Larger radius loads are Rayleigh-Taylor (R-T) unstable and are prone to breakup during the implosion. This produces a poor radiator at stagnation. We have found, however, that the stability of alternate loads including uniform fills, multiple shells, and tailored density loads can alleviate this constraint on radius.

Z-pinch implosions can be characterized by three major stages: pinch formation and initial compression, the run-in or kinetic energy phase, and a stagnation or radiation phase. In the first stage, gas breakdown takes place and an imploding shell is formed as the material on the outside edge of the load is compressed. Initially, the acceleration is slow and the internal energy produced by the compression is much larger than the kinetic energy of the plasma. In the case of a uniform fill, this phase and the next phase, the run-in, may overlap but there is still a period where these criteria will be met. Due to the low acceleration, hydrodynamic stability is not an issue during this phase. However, any initial unstable activity and/or irregularity in the initial electrical breakdown of the material may seed later instabilities. The duration of this phase varies depending on the driving current and mass distribution of the load. During the run-in phase, the plasma shell picks up kinetic energy as it accelerates towards the axis. If the initial mass distribution of the load is limited in radial extent, as is the case for foils, multiple wire, and high Mach number gas puffs, the mass in the shell remains fixed during the run-in and the compressed shell is accelerated uniformly. It is during this phase, that the Rayleigh-Taylor instability is most active. This is complicated in the case of a uniform fill load because mass is continuously being accreted onto the shell which changes the acceleration as well as the thickness of the shell¹. The final phase, or stagnation, occurs when the accelerated mass reaches the central axis. At this point, radial kinetic energy is converted to internal energy of which a portion is subsequently radiated away as X-rays. Large distortions caused by the R-T instability will decrease the X-ray yield since some fraction of the radial kinetic energy will be transferred to axial kinetic energy, and increased internal energy as well as enhanced magnetic field penetration will limit or fully disrupt the compression of the pinch. In this report, we confine ourselves to the second phase, or, run-in phase.

The Rayleigh-Taylor instability in the context of a Z-pinch is essentially the same as that of classical hydrodynamics except that the support of the heavy fluid is by the magnetic

field which also provides the acceleration, g , through the $J \times B$ term in the momentum equation. To illustrate the effects of this instability on an imploding Z-pinch load the following simple argument is given. In the case of classical R-T growth, the growth rate is \sqrt{kg} where $k = \sqrt{2\pi/\lambda}$ is the inverse wavelength and g is the effective gravity or acceleration of the imploding shell. This implies that the relationship between the distance traveled by the shell during the implosion and the amplification of an initial perturbation is $d = (\ln A)^2 \lambda / 4\pi$ where A is the ratio of the final to initial amplitudes. If an amplification factor as large as 1,000 can be tolerated and a wavelength of 0.5 cm is chosen, it follows that the distance traveled by the shell, d , is less than 2 cm. Although this is an idealized argument, it demonstrates how deleterious this instability is to the integrity of large radius implosions.

B. The Model

The numerical model which we use to simulate imploding Z-pinch loads is a two-dimensional (2-D) magnetohydrodynamic (MHD) model based on separate ion and electron temperatures. This computer code, PRISM (which stands for Plasma Radiating Imploding Source Model), has previously been used to simulate X-pinch² and Z-pinch gas puff experiments³. It includes thermal conduction, resistive heating, and magnetic diffusion. The finite difference equations are advanced in a two step process. First, the fluid variables are moved forward using a Lagrangian advance. This is followed by a remap phase during which the grid is moved to an orthogonal configuration. The remap phase is necessary in order to accommodate the movement of mass across the mesh. This would otherwise result in large distortions if the calculations were done in a purely Lagrangian mode.

The equations describing the model include the equations of hydrodynamics, Maxwell's equations, and atomic rate equations representing the population of the atomic levels as well as the charge states.

$$\frac{dp}{dt} = -\rho \nabla \cdot \mathbf{u} \quad [1]$$

$$\frac{d\mathbf{u}}{dt} = -\nabla(P_e + P_i + Q_a) + \mathbf{J} \times \mathbf{B} / c \quad [2]$$

$$\frac{d\epsilon_e}{dt} + P_e dV/dt = -V \nabla \cdot \mathbf{q}_e + P_{rad} + \eta J^2 + CV(T_i - T_e) \quad [3]$$

$$d\epsilon_i / dt + (P_i + Q_a) dV / dt = -V \nabla \cdot \mathbf{q}_i + CV(T_e - T_i) \quad [4]$$

To these equations are added Maxwell's equations, viz.,

$$\nabla \times \mathbf{B} = 4\pi \mathbf{J} / c \quad [5]$$

$$\nabla \times \mathbf{E} = -\partial \mathbf{B} / c \partial t \quad [6]$$

along with Ohm's law,

$$\mathbf{E} = \eta \mathbf{J} - \mathbf{u} \times \mathbf{B} / c \quad [7]$$

In Eqs.(1) through (7), $P_{e,i}$ are the material pressures for electrons and ions, $\epsilon_{e,i}$ are the specific energies, ρ is the density, V is the inverse of the density, $\mathbf{q}_{e,i}$ are the heat fluxes, C is the electron-ion energy exchange term. P_{rad} is the radiative power, and ηJ^2 is the ohmic heating. In Eqs. (2) and (4), Q_a is an artificial viscosity used for numerical stability in regions of strong compression. The remaining symbols have their conventional meaning.

The atomic physics model contains all the ground states and an extensive manifold of energetically and diagnostically important excited states distributed throughout the various ionization stages. In model used here, the radiation transport is only calculated in the local zone. Equation-Of-State tables are constructed from this model and used in the dynamic calculations. Table lookups for P_{rad} , T_e , and $\langle Z \rangle$ based on internal energy and density are employed. The tables were constructed using a detailed Collisional Radiative Equilibrium (CRE) ionization physics model⁴. The simulation uses a voltage waveform to drive a circuit model characteristic of the generator and load to calculate a self-consistent current.

During the implosion phase the radiation is not as critical as it is during the final collapse phase. Radiation is always emitted during all three phases of the implosion but it does not become energetically dominant until the plasma is reasonably ionized and dense. However, during the final run-in phase, the L-shell radiation from moderate- and high-Z materials becomes energetically important and can account for a substantial fraction of the total x-ray yield. The circuit model is equally important. Our model uses the self-consistent plasma resistivity and more importantly, the plasma inductance, to determine the magnitude of the driving current as a function of time. The initial inductance of the plasma is set by the radial placement of the return current rods. For these simulations, we initialized each calculation with a load inductance of 2.5 nH. The lumped inductance and resistance of the

circuit was taken to be 7.5 nH and 0.24 ohms, respectively. The magnitude of the voltage pulse was set so that a short-circuit load (i.e., heavy mass load with no motional impedance) would have a peak current of 60 MA. Although these calculations were made for 60 MA currents, the results can be scaled for other currents since the kinetic energy scales as I^2 . A current of 5 MA, for instance, would result in the same implosion velocity for a mass which is smaller by a factor of 7×10^{-3} . For the same implosion mass, the velocity would scale linearly with the current. Due to the arguments outlined above, the most important factors which need to be considered, in terms of stability, are the runin distance and the structure of the load.

C. Results and Discussion

Figure 1 shows computed growth rates, for a wavelength of 0.66 cm, as a function of load design (i.e., the initial load is smoothly varied from a shell to a uniform fill where the inside fill density and shell density are equal) for 5 cm initial radius, 60 MA implosions. Again, these results can be scaled to regimes of interest. The initial gas shell load had a thickness of 0.8 cm and there was no initial density variation along the z-axis. After the start of each simulation, a small density perturbation was used to initialize the instability. The growth rates were calculated from the change in the total axial (i.e., along the z-axis) kinetic energy as a function of time (which is zero for a non-perturbed, purely radial implosion). The independent variable is the ratio of the inside density to shell density (i.e., one defines a uniform fill and zero defines a shell). The growth rates shown in Fig. 1 were calculated during the final phase of linear growth before breakup, as is the case with a shell, or prior to saturation, as is the case with a uniform fill. Therefore, the growth rates shown in Fig. 1 represent a low growth rate estimate. Using this criterion, it is seen that as the fill density parameter is increased the measured growth rate falls. The acceleration of a thin shell towards the axis varies slowly, and is dependent on the shell radius $R(t)$ and current $I(t)$. In the case of a uniform fill, the acceleration is even faster than that for the thin shell, since the magnetic pressure is initially applied to the small mass in the region localized in the outer part of the flow, near the plasma/field interface. However, the growth rate decreases nearly continuously during the implosion due to the additional mass which is accreted onto the shell created by the snowplow. Also shown in Fig. 1 is the total mass ratio as a function of density ratio. Because of the large radius (i.e., 5 cm initial radius), the mass ratio is unity when the density ratio is only about 25 percent. The shaded region between $1.6 \times 10^8 \text{ sec}^{-1}$ and $2.2 \times 10^8 \text{ sec}^{-1}$ represents the range of classical growth rates as determined from the measured acceleration of the load during the rundown phase. The range in the computed

growth rate is due to the fact that the current and, consequently, the acceleration change continuously during the implosion. When the density ratio reaches 40 percent, the growth rate falls below the classical growth rate values determined from the acceleration. This is roughly the same point at which the total masses of the initial shell and inside fill are equal. Based on a growth rate of $2 \times 10^8 \text{ sec}^{-1}$, the time to amplify an initial perturbation by a factor of 1,000 is about 35 nsec. In these simulations, this is about one-half of the run-in time and implies that there is plenty of time for breakup of the load to occur. Growth rates which were measured at other wavelengths compared similarly with classical growth rates.

In order to make a fair comparison between these two kinds of load designs, we have to introduce a measure for instability growth which takes into account not only the fastest growth rate, but also the non-uniformity of perturbation. This is illustrated in Figure 2, where the fractional mass which is unstable during the implosion is plotted as a function of the fill percentage. Here, we have defined the fractional mass ratio as the mass with greater than the mean axial kinetic energy, divided by the total mass of the implosion. The points represent time averaged values measured during the linear growth phase. This fraction is greater than 40 percent for an imploding thin shell. For a uniform fill load, however, it is reduced to below 25 percent. Although the uniform fill loads experience an initially higher acceleration, the instability is effective in disrupting a small percentage of the total mass. The implication is that the R-T instability is more damaging to shell loads.

Implosions from 7 cm, 5 cm, 3 cm, and 2 cm were considered. Figure 3 shows the results of the 7 cm, 2-D simulation for an initial gas shell. As with the simulations shown in Fig. 1, the initial shell thickness was 0.8 cm. The wavelength of this simulation, and in the subsequent simulations discussed below, was 0.66 cm. Density contours are shown at 0, 66, 82, and 100 nsec. A small perturbation which initializes the instability is imposed early in the simulation. The instability then develops until, at 100 nsec, the shell has been disrupted to the point that the density at the center of the shell has been reduced to the background vacuum density. At this point, the simulation is terminated due to the inability of the MHD fluid code to handle vacuum over the entire radial span of the grid. The back edge of the compressed shell has only traveled approximately 1.5 cm before this disruption. This is in rough agreement with the simple estimate made earlier based on classical R-T growth. Because the shell was disrupted before significant compressional heating at on-axis stagnation could occur, there was no measurable K-shell yield.

The results from the 2 cm radius, 2-D simulation are shown in Fig. 4. In the second plot, at 76 nsec, the instability has pushed material away from the center. However, the load mass reaches the axis just before breaking apart at 84 nsec. At 86 nsec, a spot has formed at the center. Subsequently, the more massive plasma at $z = 0 \text{ cm}$ and at $z = 0.66 \text{ cm}$ reaches

the axis. The last density snapshot at 96 nsec shows the formation of dense spikes which result when the plasma "bounces" off the central axis.

In the 5 cm radius simulation, the result was similar to that of the 7 cm simulation where the breakup of the pinch prevents a final implosion on axis. In the 3 cm radius simulation, the breakup occurred prior to implosion but without creating the dense spot that occurs in the 2 cm simulation. The stability boundary, would therefore appear to be between 2 cm and 3 cm for thin shell implosions. Again, this is in accordance with the simple run-in stability estimate made previously.

In order to compare with the shell simulation of Figure 3, we concentrate on a 7 cm uniform fill implosion. The density contours shown in Fig. 5 were taken at 74, 110, 126, and 136 nsec. As in the shell implosion an initial small perturbation is imposed early in the simulation. The R-T instability is seen to grow after some initial short wavelength oscillations. However, the shell which is formed from the swept up material (i.e., the snowplow) remains intact despite the unstable activity since new material is continuously being added. At the last time shown in Fig. 5, 136 nsec, a large fraction of the material has been compressed on axis. A plot of the radial and axial kinetic energies as a function of time, for this simulation, are shown in Fig. 6. The growth of the instability appears to consist of two phases. In the first phase, between 50 nsec and 90 nsec, linear growth is evident. This is followed by a long period of saturated axial kinetic energy. That is, the level of axial kinetic energy remains constant but does not grow. The penalty, in terms of total kinetic energy which can be achieved by the load, is that the radial kinetic energy is also depressed below what it would be if this were a one-dimensional simulation. The calculated K-shell yield of this implosion was about one-half that of the scaling estimate yield of a 0-D implosion from the same distance. This is, however, significantly higher than the yield produced in a 2 cm thin shell implosion.

A third choice for a load design is to distribute the density non-uniformly. Examples include multiple shells, puffs impinging on shells, and density tailored or structured loads. Kinetic energy plots for a 1 cm puff-on-shell simulation are shown in Fig. 7. Linear growth is apparent up to about 60 nsec when the shell created by the imploding puff impacts the inner shell. At this time, the axial kinetic energy begins decreasing before increasing again at 75 nsec. Over this time period, the radial kinetic energy remains nearly constant. This is not a condition of free-fall, however, since the inside shell begins to carry some of the kinetic energy and the bulk velocity of the material in the outer puff decreases during the collision. The density contours are shown in Fig. 8 starting in time close to the moment of impact at 62 nsec. The amplitude of the perturbed shock wave, which is propagating inward, is seen to decrease during the time from $t=68$ nsec to $t=74$ nsec. The analytic theory of Velikovich *et*

al.⁵ predicts that for this case the time interval required for the shock wave perturbation to change sign (after that the perturbation amplitude exhibits decaying oscillations, remaining a small fraction of its initial value) is 15 nsec. This is very close to the oscillation time of 14 nsec measured in the 2-D simulation. This oscillation time is dependent on the Atwood number, sound speeds both upstream and downstream of the impact shock, and the velocity of the shock.

Similar results have been obtained with shell-on-shell implosions. Qualitatively, the same conditions exist at the point of impact for both shell-on-shell and puff-on-shell implosions. Differences between these two load designs are due to the acceleration and stability of the plasma outside the interior shell prior to the time of collision. Up to this time, an outside puff will behave in the same fashion as that of a uniform fill implosion. However, as with the uniform fill implosions, the penalty for the enhanced stability of the overall configuration is reduced radial kinetic energy of which a direct consequence is lower yield.

D. Density Tailored Loads

Direct drive implosions on PRS simulators with long risetimes present problems for stabilizing the PRS load against hydrodynamic instabilities. In order to couple sufficient kinetic energy into a load which is not too massive, the initial radius of the implosion must be larger than what is common in today's PRS experiments. Since the amplification of the perturbation is independent of the implosion time, but is instead dependent on the distance over which the runin occurs, a mechanism for stability must be found.

If the load is tailored properly, the acceleration of the snowplow shell will be reduced during the initial runin phase. The conventional Rayleigh-Taylor (R-T) instability growth rate will then be greatly reduced or even stabilized. The kinetic energy itself, on the other hand, can increase during this phase because mass is being accreted onto the shell while the velocity remains nearly constant. That is, $KE = 1/2mv^2$ increases because the mass, m, increases while the velocity, v, is nearly uniform. This requires that the density gradient is increasing from the outside to the inside surface. The inside radius for this type of load is set so that once the plasma has formed a thin shell the accelerated runin distance will be within the stability distance of roughly 2-3 cm for wavelengths in the 1/2 cm range. Note that the accelerated runin stable runin distance may be greater than the 2 -3 cm limit since that limit is based on a zero initial velocity. This is a topic which will be investigated in the future.

Even though the R-T instability is reduced or eliminated, there is a second hydrodynamic instability which may manifest itself during the implosion. This is the so-called Richtmyer-Meshkov (R-M) instability which was discovered theoretically by Richtmyer at Los Alamos in the early 1950s, and later observed in Meshkov's shock tube experiments (Russia, 1960s). This instability develops when a plane shock wave interacts with a corrugated interface separating two different materials. Since Richtmyer's discovery, it was widely believed that the R-M instability is in effect a particular case of the R-T instability, with constant acceleration replaced by the instantaneous, impulsive acceleration. The impulse at the interface is created by the shock wave passing through it. The approximate formulae based on this concept were in good agreement with most simulation results. The present research of Velikovich, however, has shown that this is not the case. An exact analytic linear theory of the R-M instability was developed and validated by favorable comparison of its results with earlier linear and nonlinear simulation results. This theory has demonstrated that the R-M instability can develop in symmetrical configurations (head-on collisions of identical plane gas layers, or of shock waves of identical strength, etc.), with zero acceleration of the unperturbed contact interface. There is no simple qualitative explanation of the R-M instability, alternative to Richtmyer's concept of impulsive acceleration, but it appears to be caused by the surface vorticity deposited at the contact interface by the shock wave. That is, the instability is produced as the shock wave interacts with differing phases of the surface wave. This topic is presently being investigated by several researchers. Fortunately, the R-M instability growth is algebraic and not exponential. This is a much slower rate of growth than the exponential growth of the R-T instability and can be tolerated during the implosion.

A simple density distribution which is analytically known to satisfy the criteria to reduce the Rayleigh-Taylor instability is one which varies as $1/r^3$. For simplicity, in this simulation we have assumed a fixed % MA current. The results of a simulation using this profile is shown in Fig. 9 where the kinetic energy is plotted as a function of time. Two regions of growth in the axial kinetic energy can be seen. The first is a slow growth phase which occurs during the mass snowplow. The second is the R-T growth phase which occurs after all of the mass has been accumulated into a shell. Density contours, taken at 100 nsec and at 250 nsec (stagnation), which show that the amplitude of the instability, grows on the outside of the load but leave the inner portion unaffected are shown in Figure 10. Finally, in Fig. 11 the quantity $\langle KE_z \rangle g^{1/2}$ is plotted as a function of time. This is an indicative measure of whether the growth is algebraic or exponential since the growth goes as $g^{-1/4}$ and the axial kinetic energy varies approximately as the square of the perturbation. The kinetic energy, square root of the acceleration product should then be a measure of whether the

growth is algebraic or exponential. In the R-M slow growth phase this quantity should oscillate around a fixed value. This behavior is seen in Fig. 11 prior to 150 nsec. Thereafter, the steep rise of this quantity reflects the exponential growth during the acceleration phase.

E. Conclusion

At large diameters, implosions initiated by thin gas puff shells are extremely unstable. The distance over which they travel before being disrupted is severely limited by the large R-T growth rate. Based on the measured growth rates of the shell implosions investigated here, they are limited to approximately 2-3 cm run-in distance. This effect is reduced for uniform fill loads where the imploding shell contains only a fraction of the total mass.

In terms of converting kinetic energy, thin shells are the most efficient load designs. These loads, therefore, place an upper limit on radiative performance for a given machine design and current level. However, as we have shown, these loads are most susceptible to instability and breakup. Less efficient kinetic energy converters are uniform fill and structured loads such as puff on shell, shell on shell, and tailored density profiles. However, these designs are more stable and can be placed out at larger initial radii. The overall result, at least for the conditions studied here, is that these types of loads may do as well or better than thin shell loads when 2-D stability is taken into account. Uniform fill and structured load designs also have the advantage of easing the stiffness of the machine requirements by going to large radius and long implosion times.

References

1. S. M. Gol'berg and A. L. Velikovich, *Phys. Fluids B* **5**, 1164 (1993).
2. F. L. Cochran and J. Davis, *Phys. Fluids B* **2**, 1238 (1990).
3. C. Deeney, P. D. Lepell, F. L. Cochran, M. C. Coulter, K. G. Whitney, and J. Davis, *Phys. Fluids B* **5**, 992 (1993).
4. J. Davis, J. L. Giuliani Jr., and M. Mulbrandon, to be published in *Phys. Plasmas*.
5. A. L. Velikovich, L. Phillips, and J. Dahlburg, "Analytic Theory of the Richtmyer-Meshkov Instability in Compressible Fluids", submitted to *Phys. Rev. E* (1995).

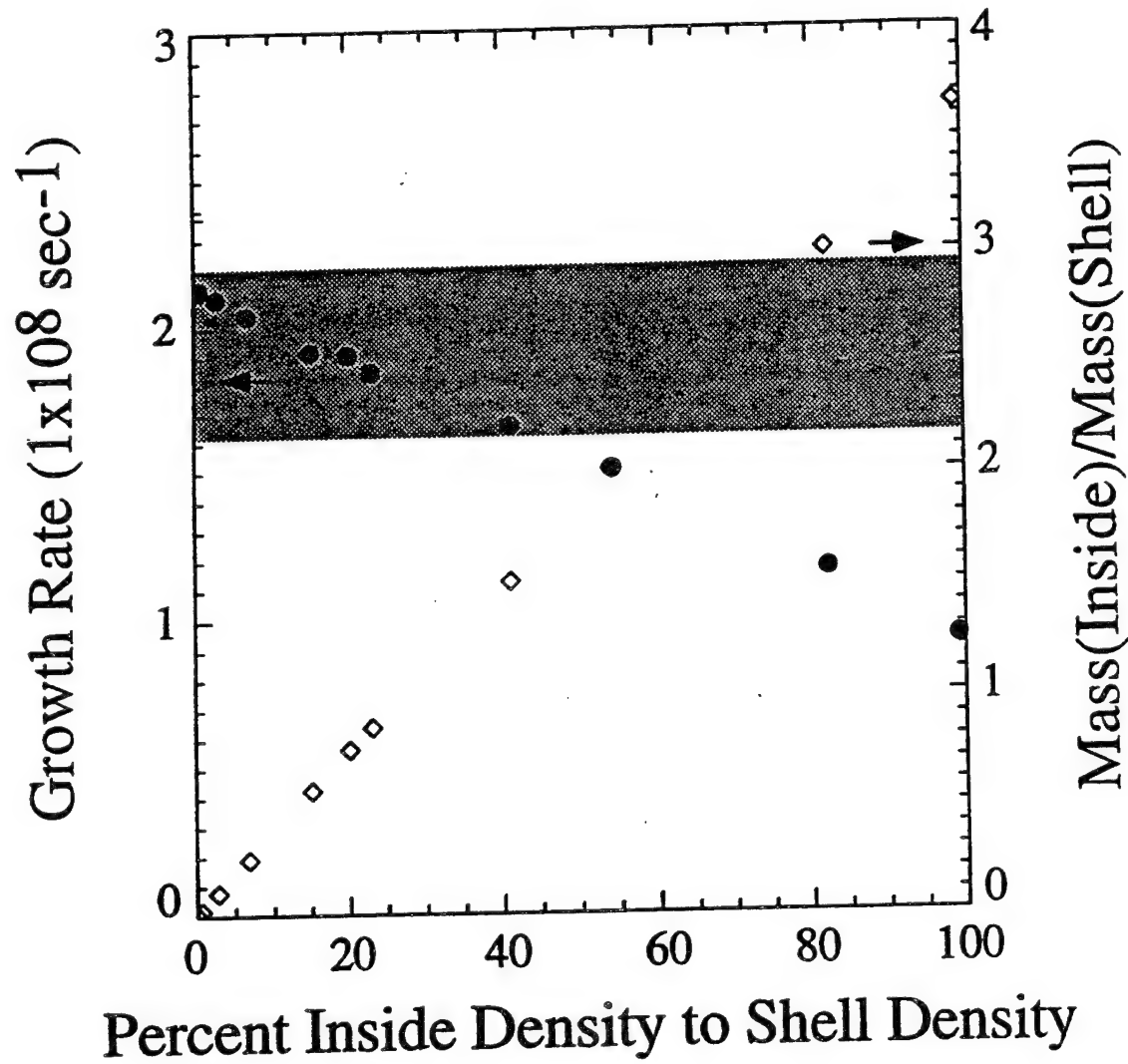


Figure 1: Growth rate for the Rayleigh-Taylor instability as a function of the ratio of inside density to shell density for a wavelength of 0.66 cm, assuming an initial shell radius of 5 cm and shell thickness of 0.8 cm. The shaded region represents the range of classical growth rates calculated from the acceleration measured during the run-in phase.

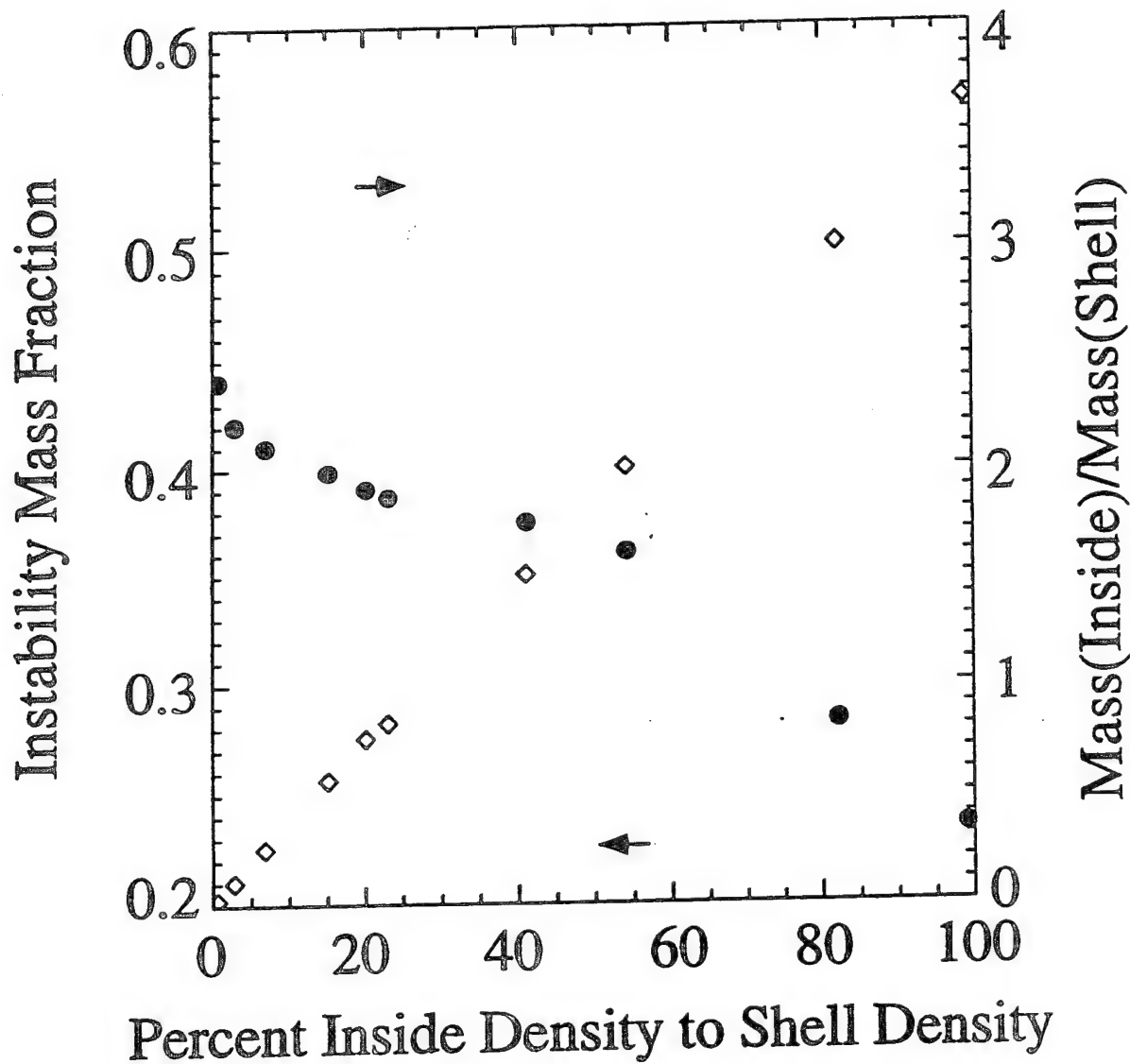


Figure 2: Instability mass fraction as a function of the ratio of inside density to shell density for a wavelength of 0.66 cm, assuming an initial shell radius of 5 cm and shell thickness of 0.8 cm. The mass fraction is taken to be the percentage of material with axial kinetic energy greater than the mean axial kinetic energy.

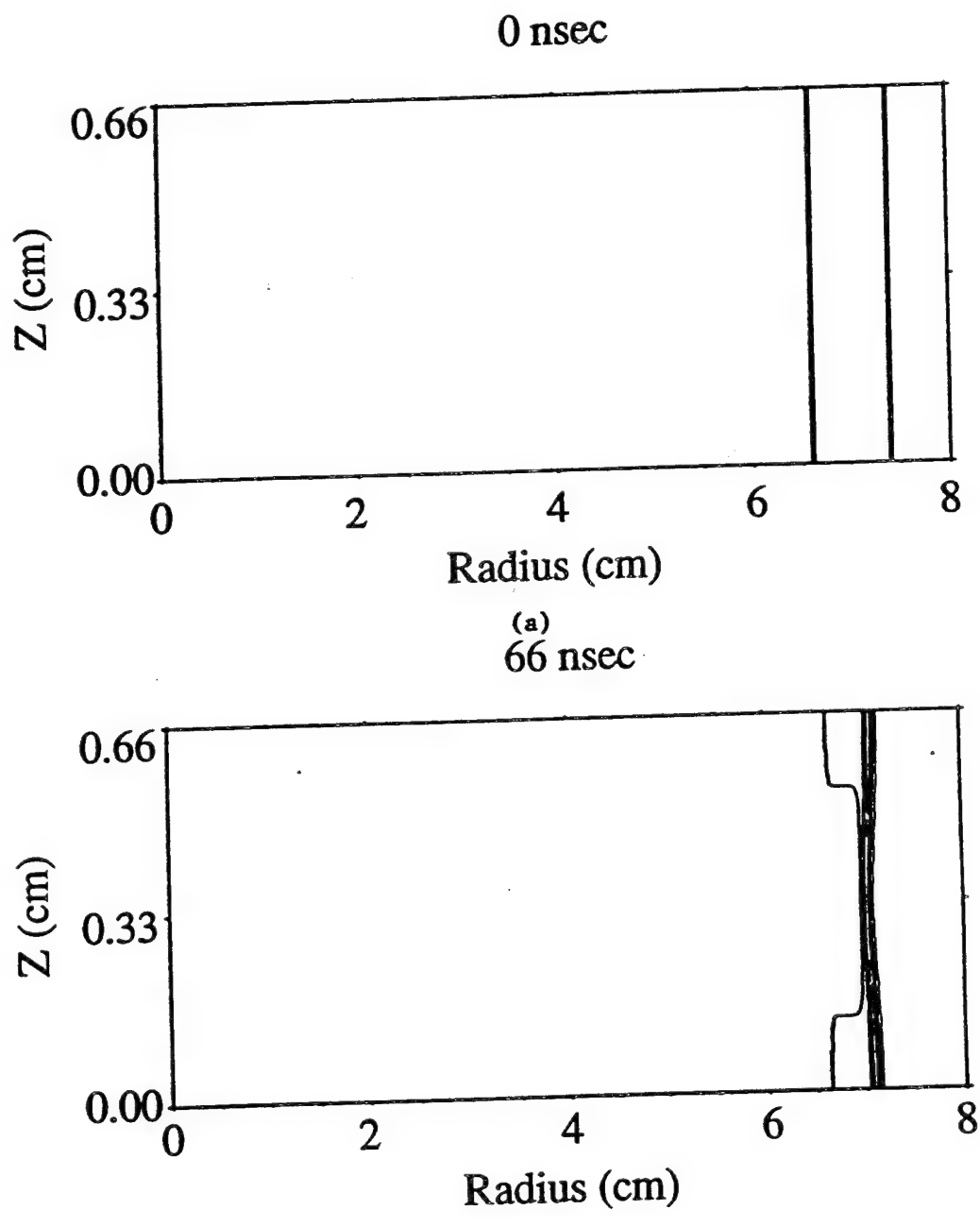


Figure 3: Density contours for the 7 cm thin shell implosion: (a) 0 nsec, (b) 66 nsec, (c) 82 nsec, and (d) 100 nsec. The density contours are spaced linearly and normalized to the peak value at each time.

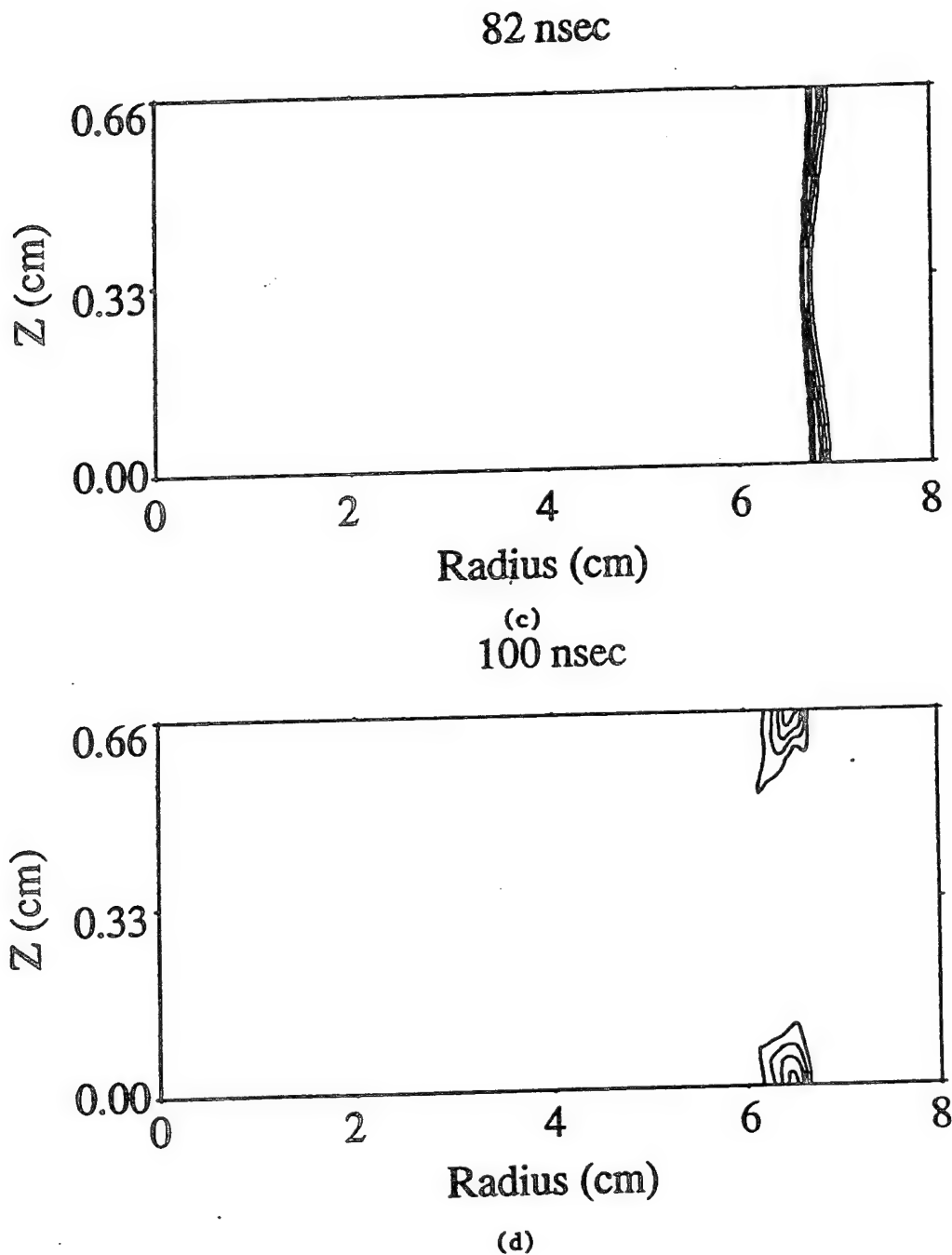


Figure 3: (Continues) Density contours for the 7 cm thin shell implosion: (a) 0 nsec, (b) 66 nsec, (c) 82 nsec, and (d) 100 nsec. The density contours are spaced linearly and normalized to the peak value at each time.

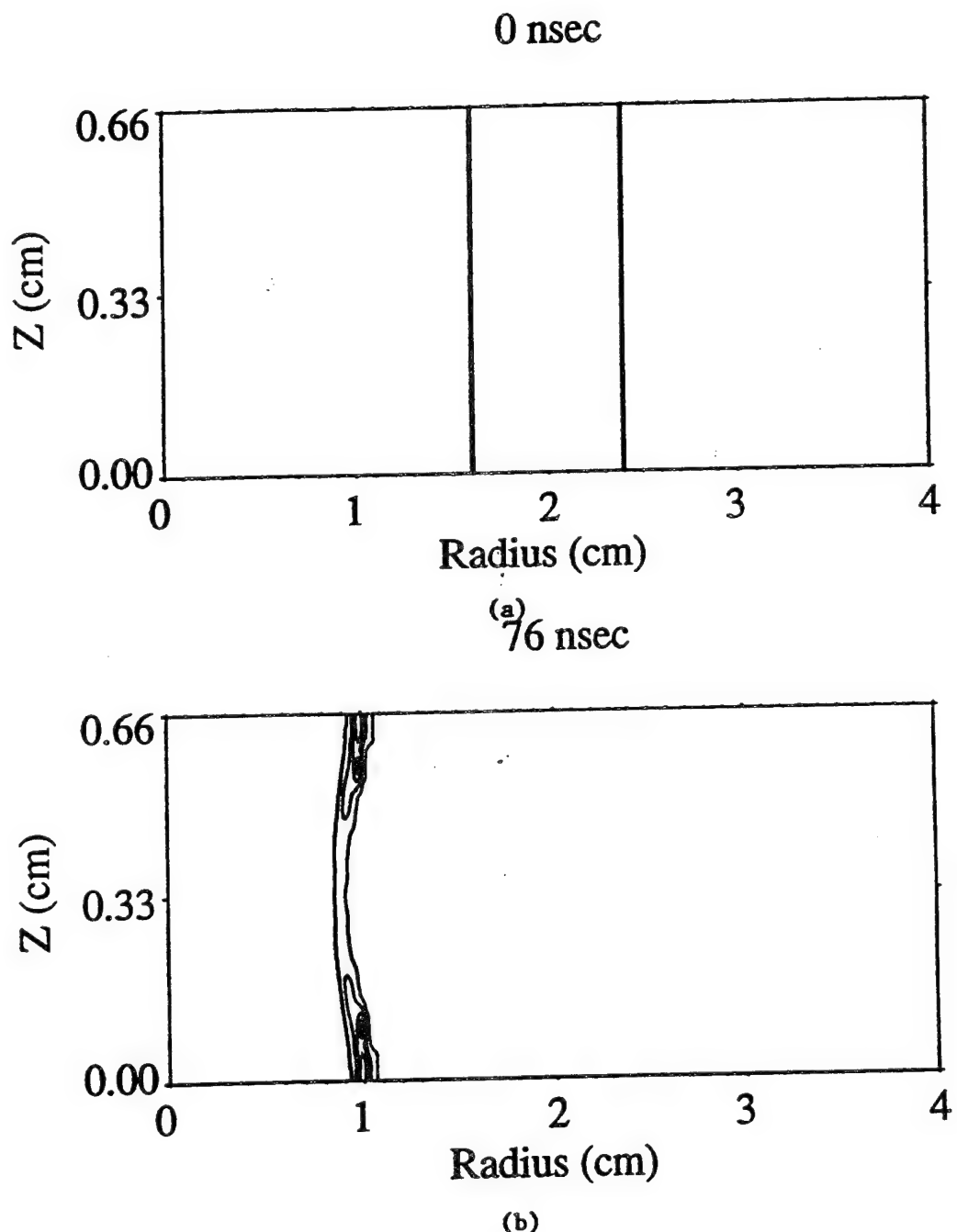
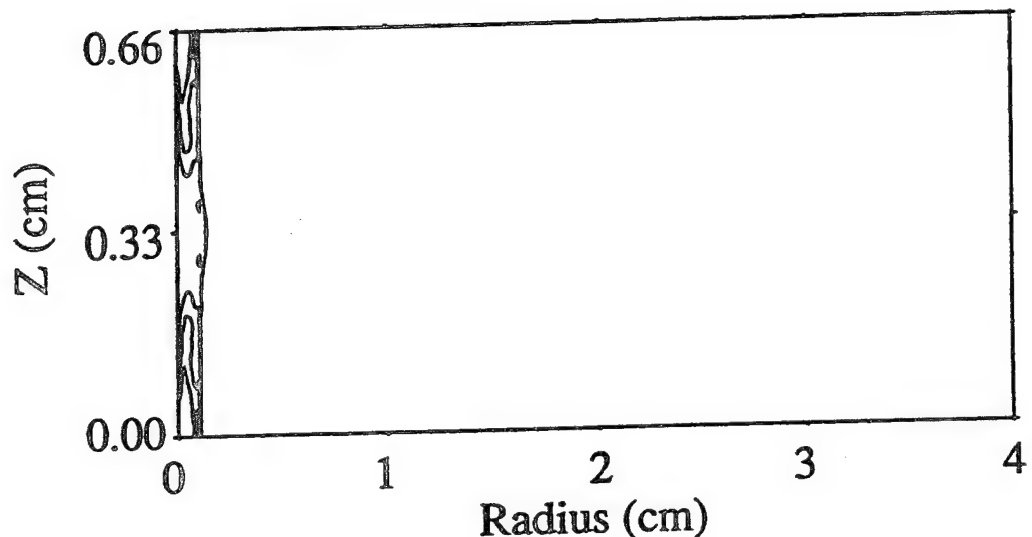
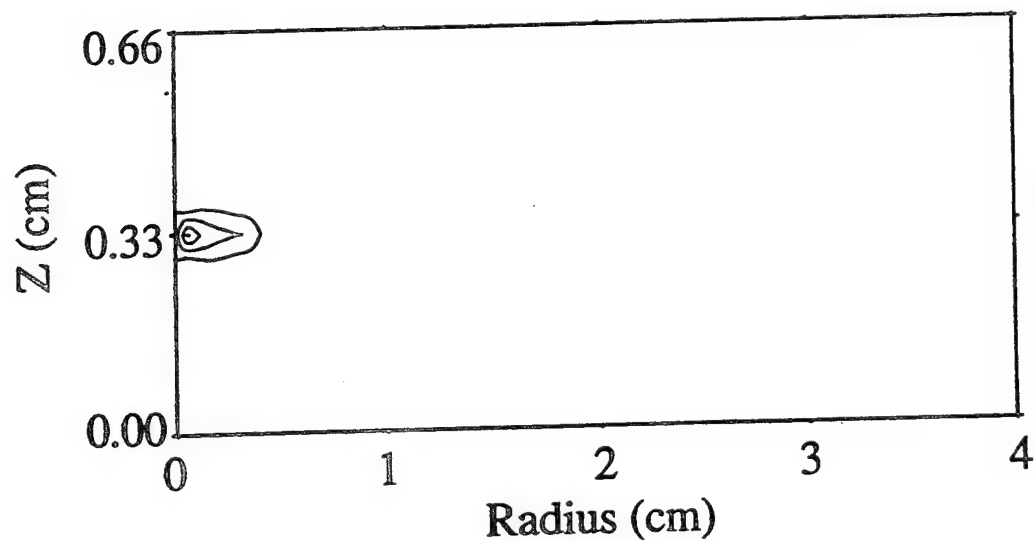


Figure 4: Density contours for the 2 cm thin shell implosion: (a) 0 nsec, (b) 76 nsec, (c) 84 nsec, (d) 86 nsec, and (e) 96 nsec.

84 nsec



(c) 86 nsec



(d)

Figure 4: (Continues) Density contours for the 2 cm thin shell implosion: (a) 0 nsec, (b) 76 nsec, (c) 84 nsec, (d) 86 nsec and (e) 96 nsec.

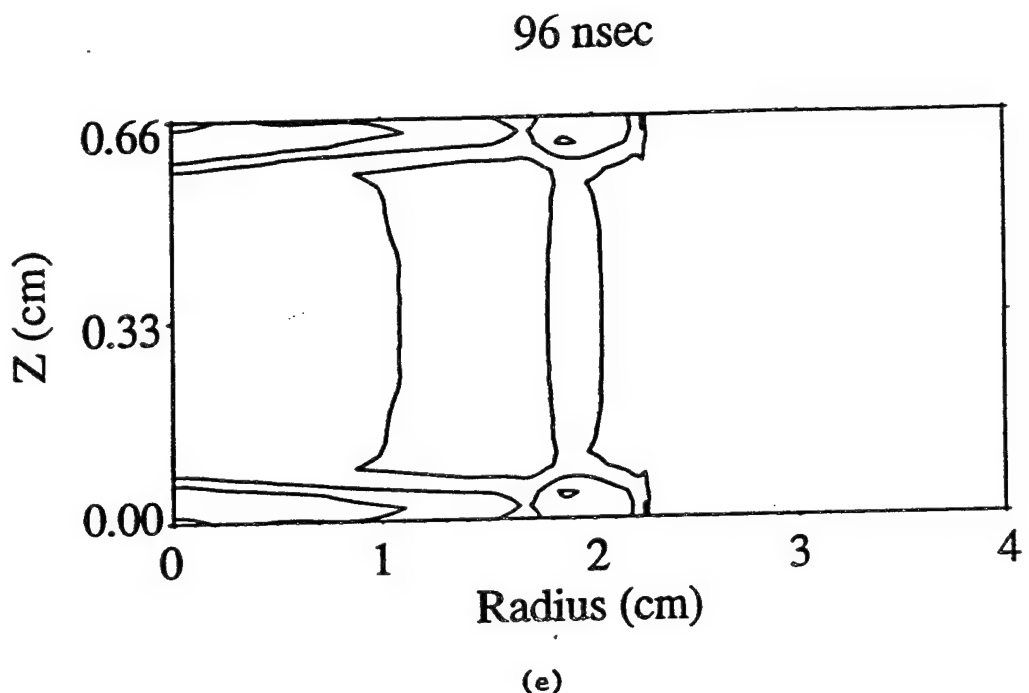


Figure 4: (Continues) Density contours for the 2 cm thin shell implosion: (a) 0 nsec, (b) 76 nsec, (c) 84 nsec, (d) 86 nsec and (e) 96 nsec.

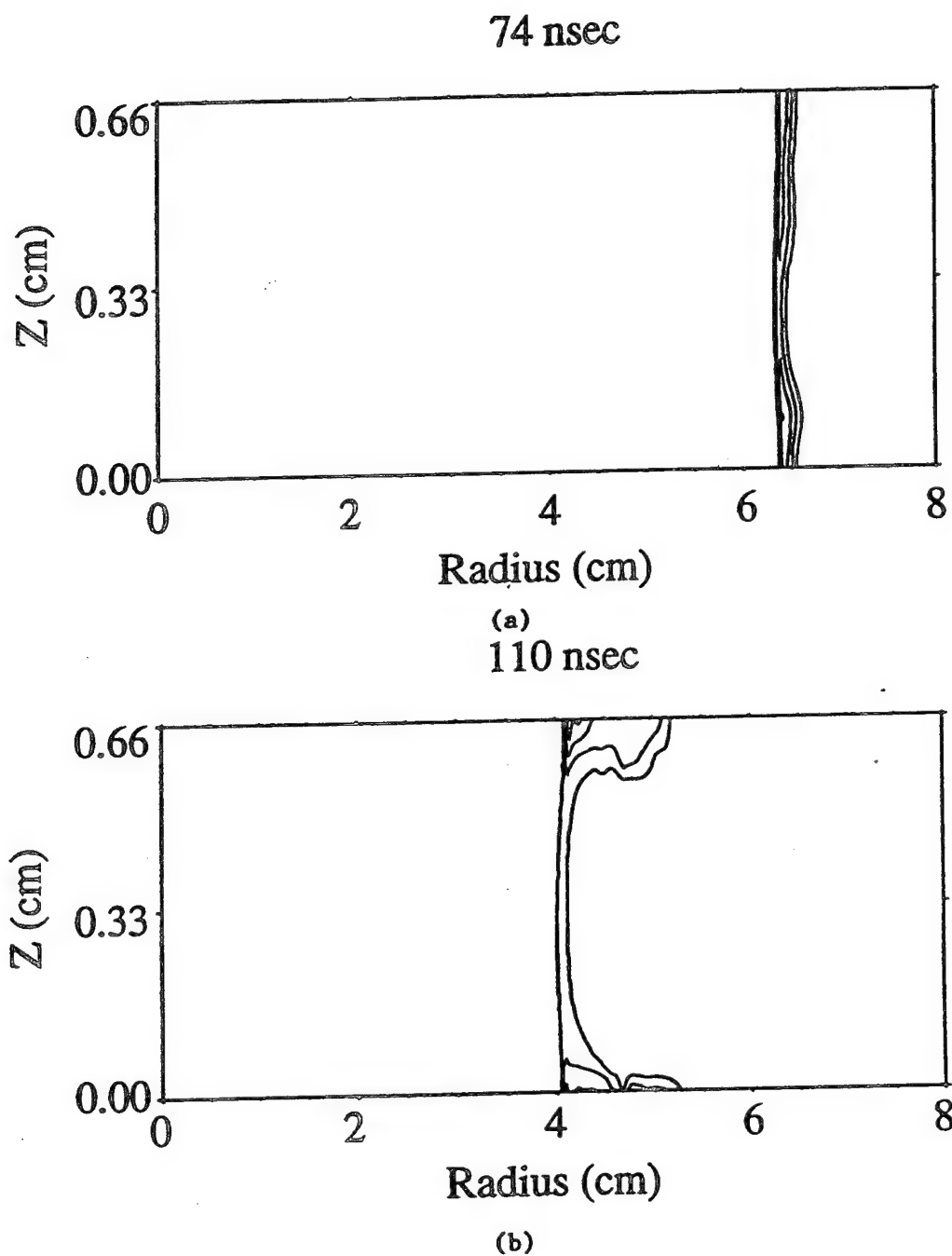


Figure 5: Density contours for the 7 cm uniform fill implosion: (a) 74 nsec, (b) 110 nsec, (c) 126 nsec, and (d) 136 nsec.

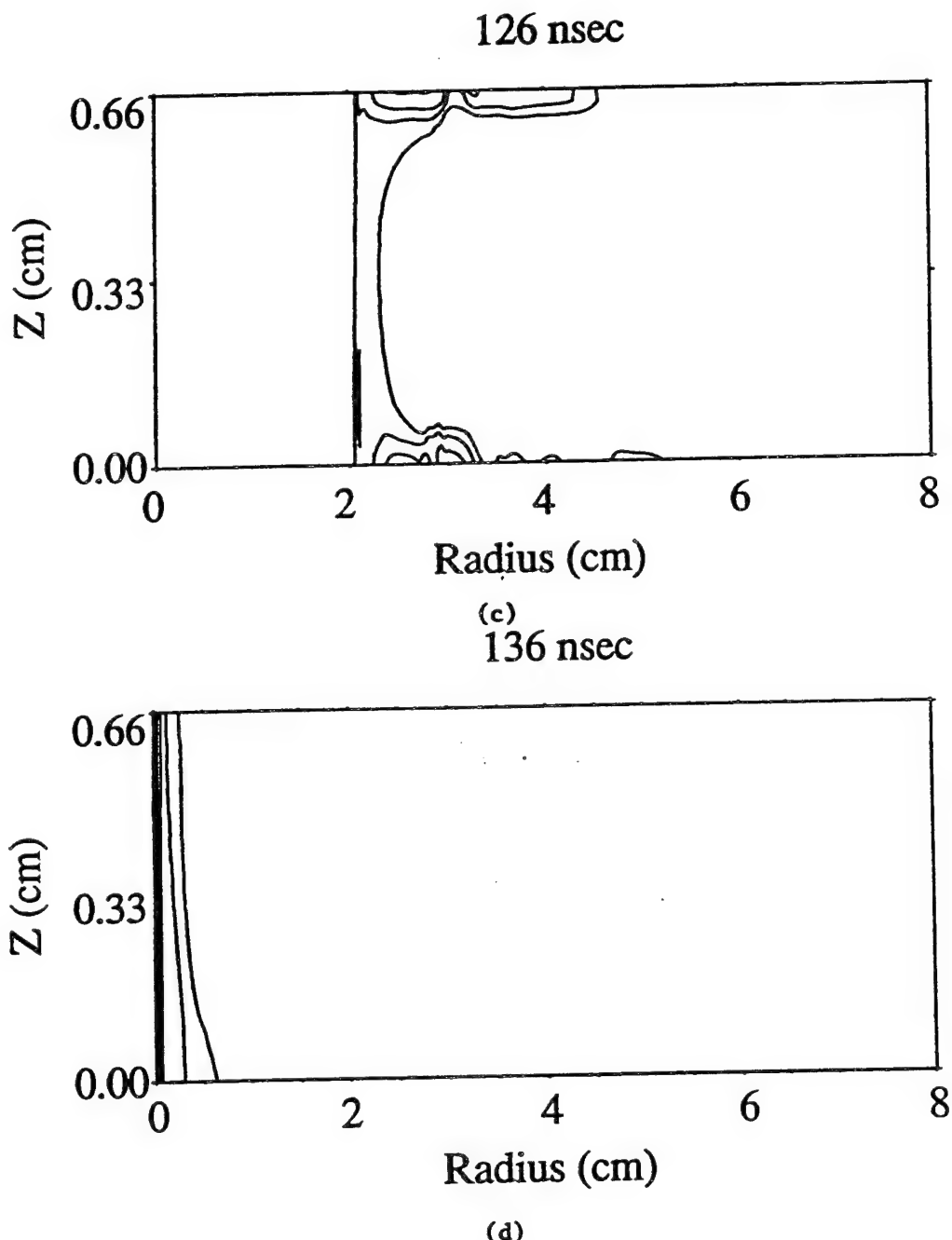


Figure 5: (Continues) Density contours for the 7 cm uniform fill implosion: (a) 74 nsec, (b) 110 nsec, (c) 126 nsec, and (d) 136 nsec.

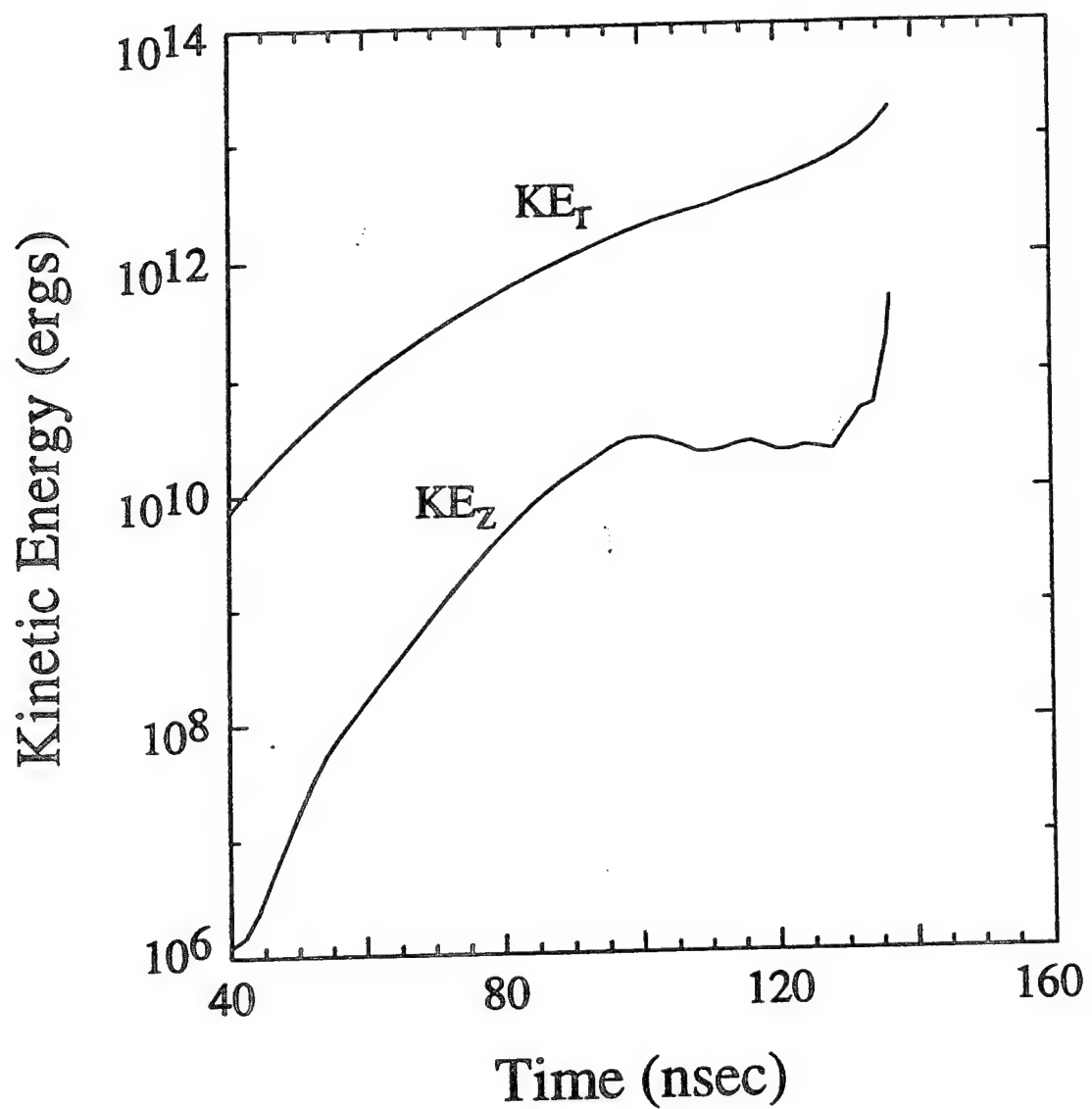


Figure 6: Radial and axial kinetic energy plots for the 7 cm uniform fill implosion.

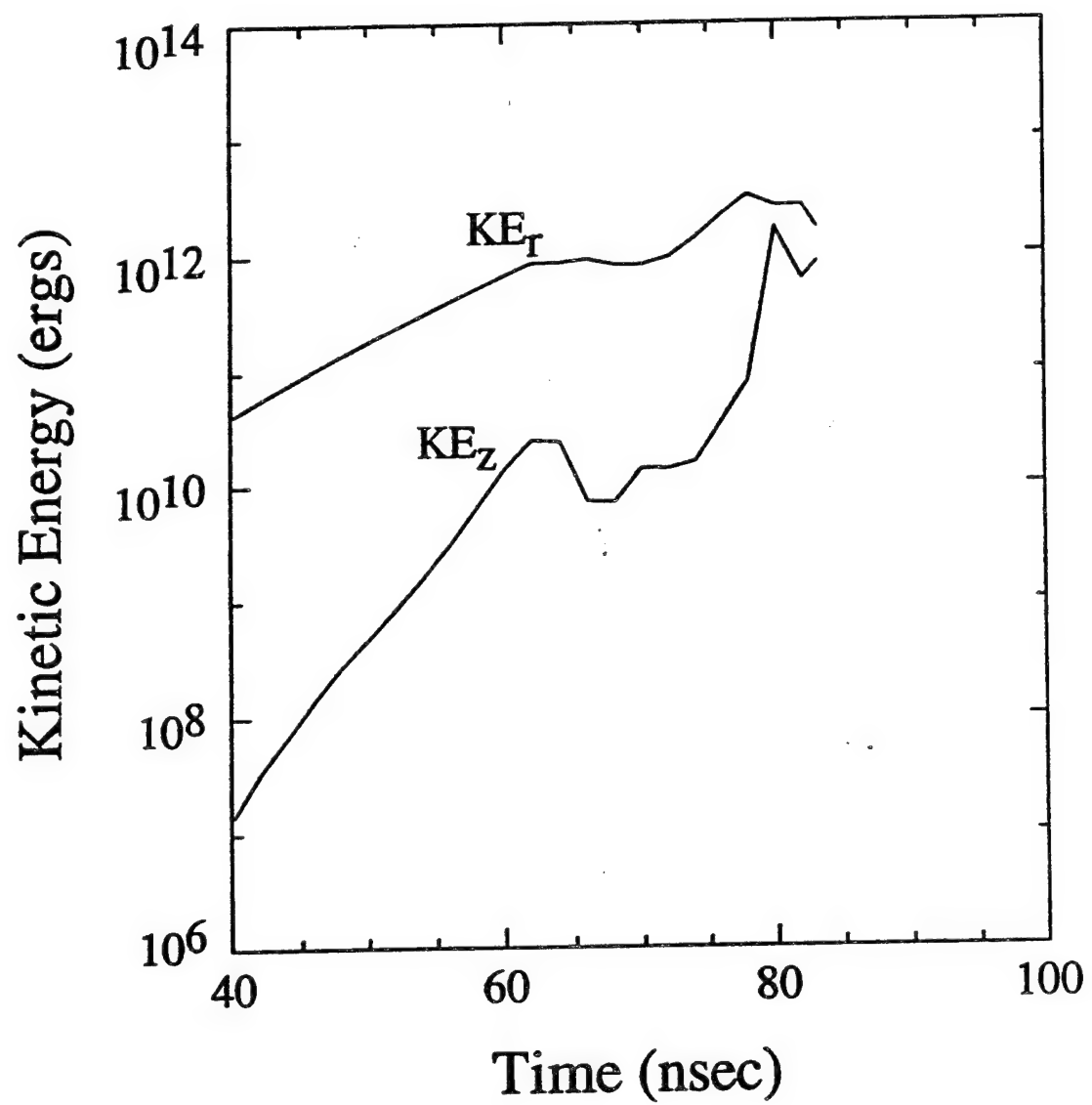
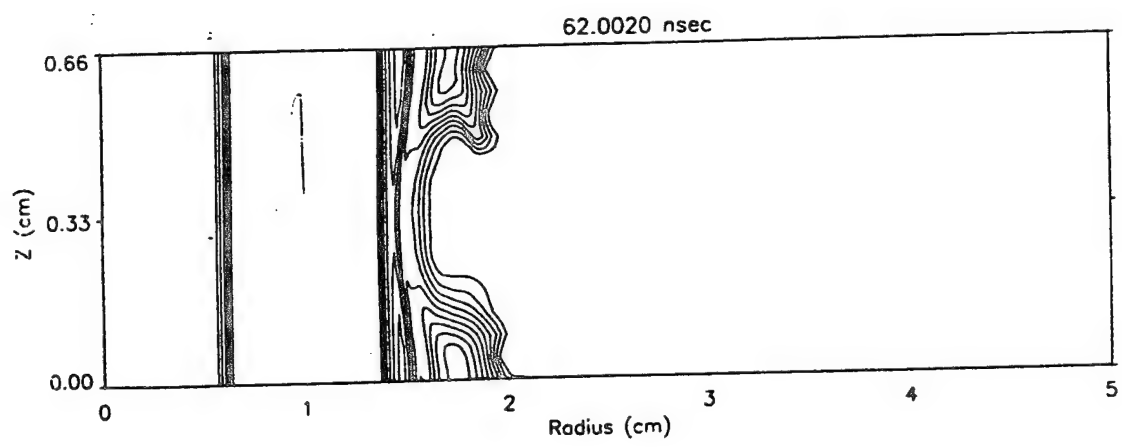
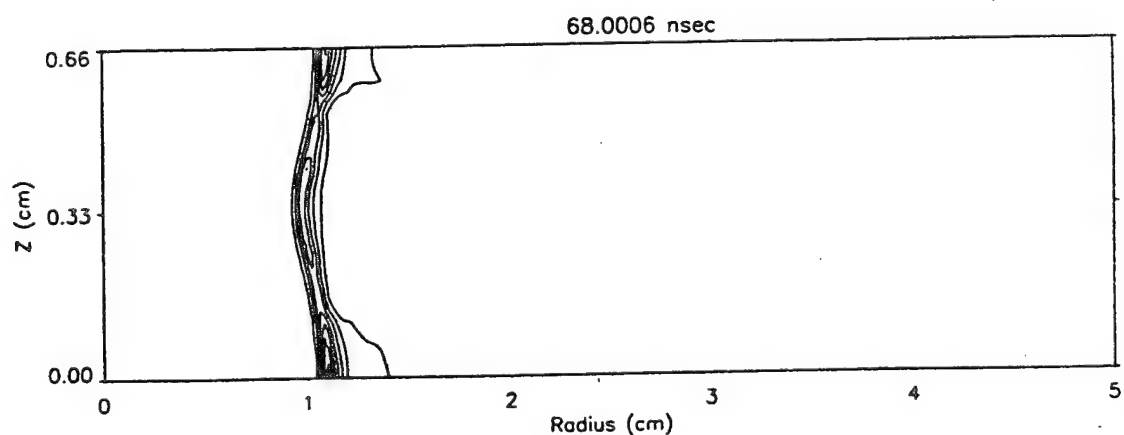


Figure 7: Radial and axial kinetic energy plots for the 1 cm puff-on-shell implosion.

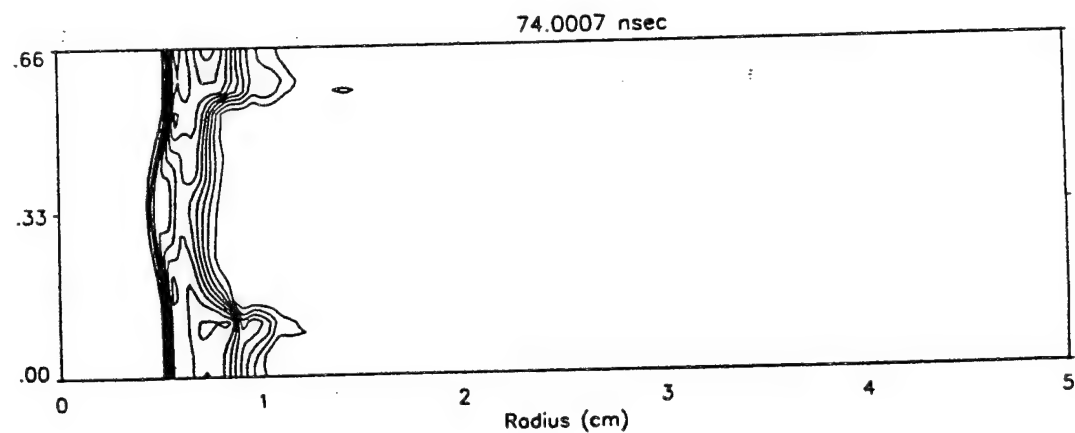


(a)

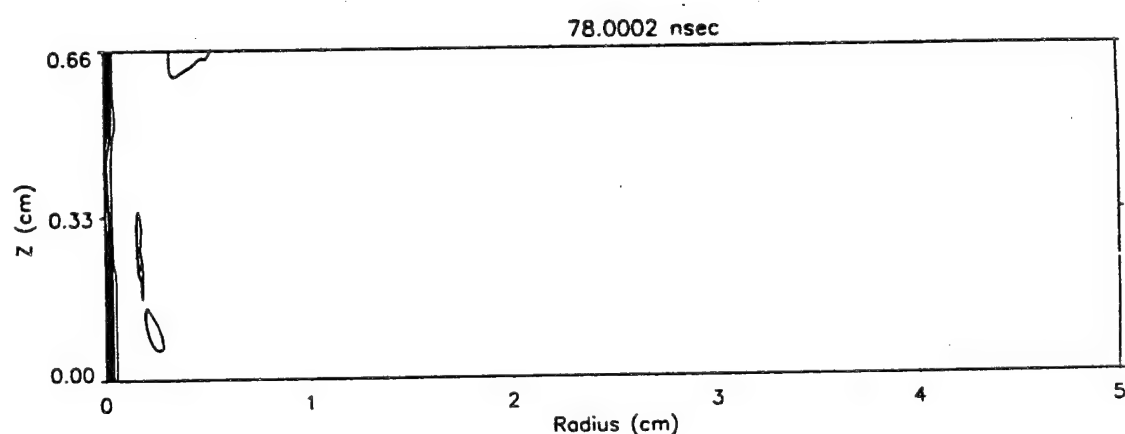


(b)

Figure 8: Density contours for the 1 cm puff-on-shell implosion: (a) 62 nsec, (b) 68 nsec, (c) 74 nsec, and (d) 78 nsec.



(c)



(d)

Figure 8: (Continues) Density contours for the 1 cm puff-on-shell implosion: (a) 62 nsec, (b) 68 nsec, (c) 74 nsec, and (d) 78 nsec.

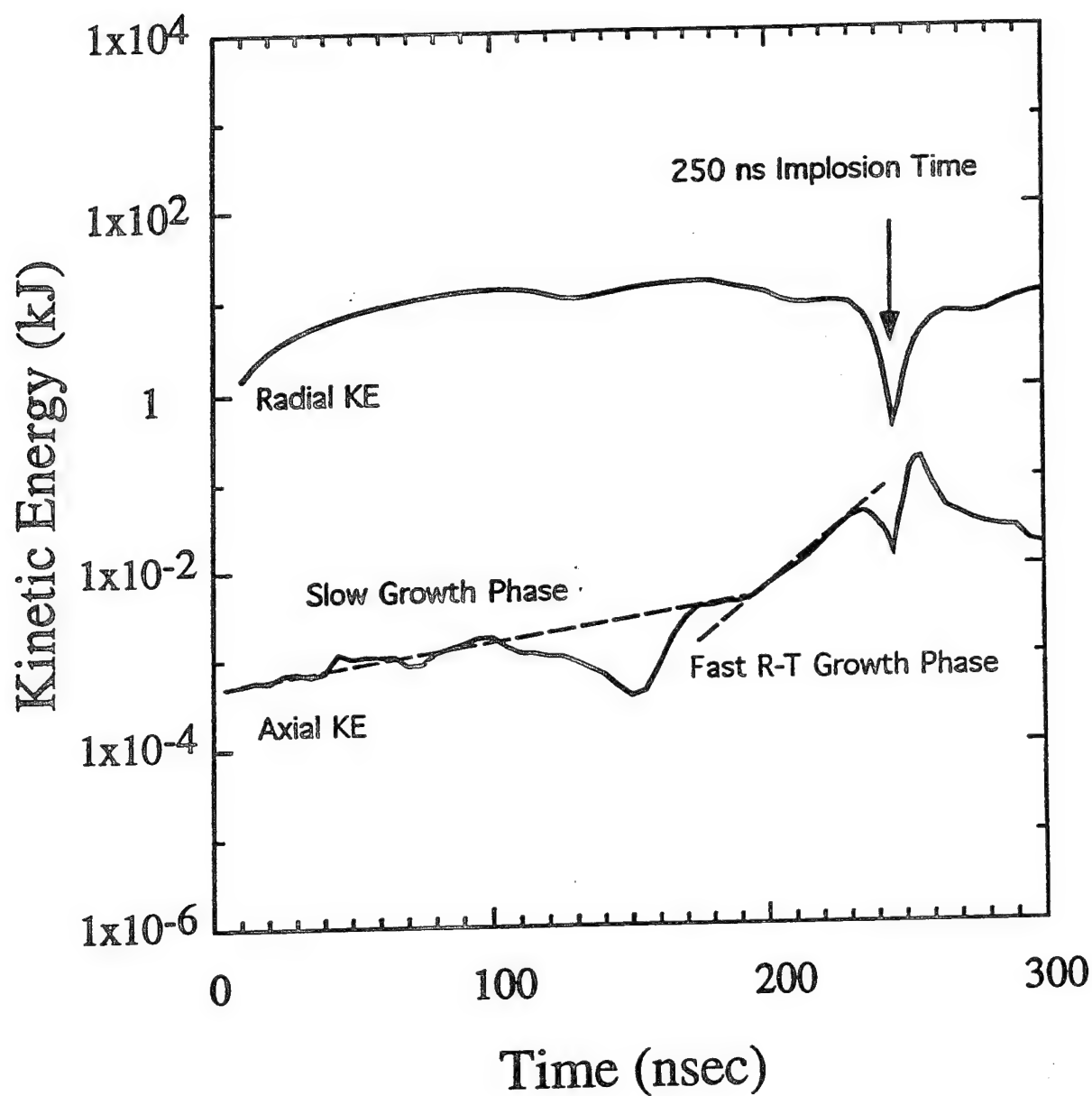


Figure 9: Kinetic energy as a function of time for the $1/r^3$ density profile.

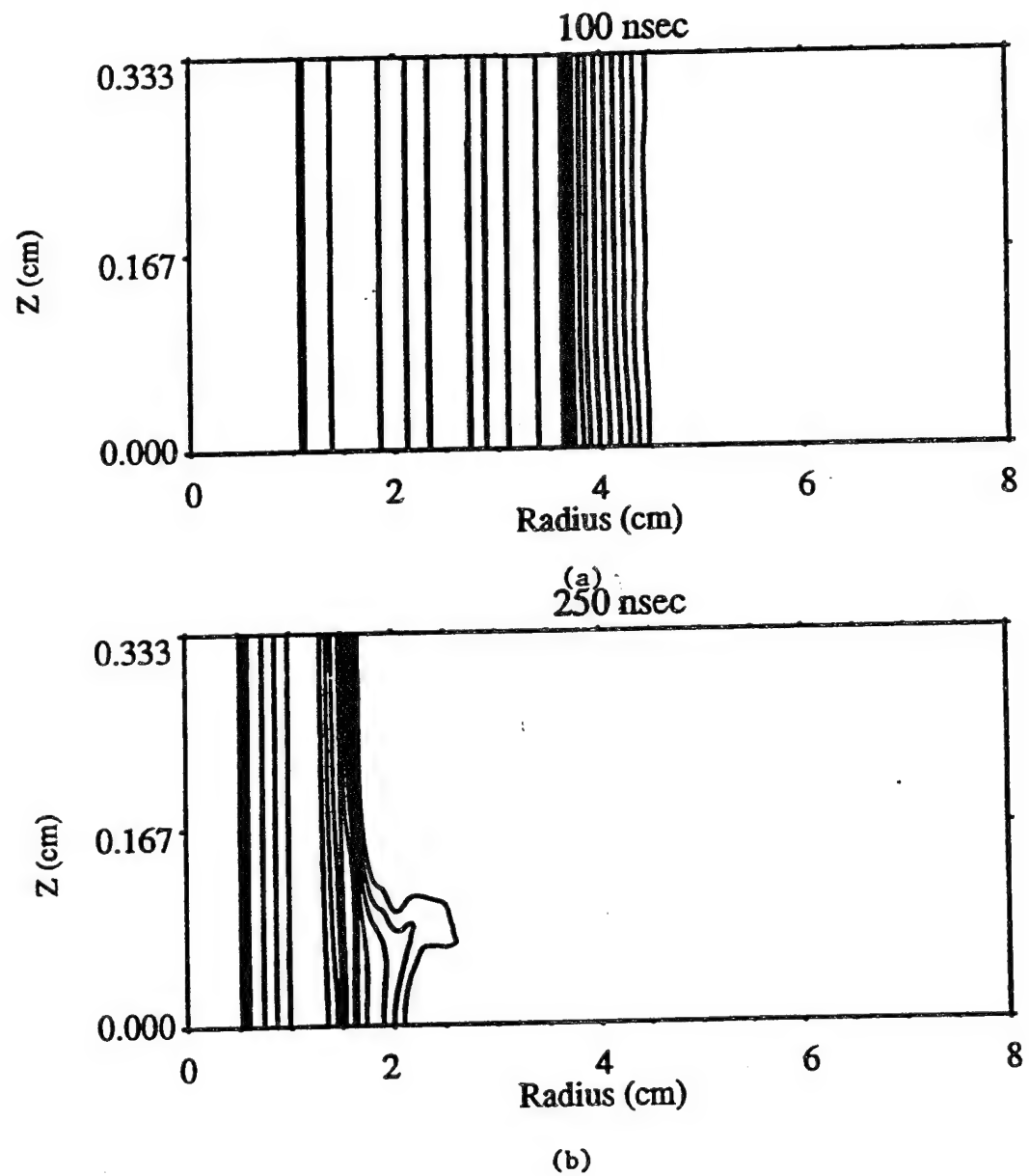


Figure 10: Density contours for the $1/r^3$ initial density profiles: (a) 100 nsec and (b) 250 nsec.

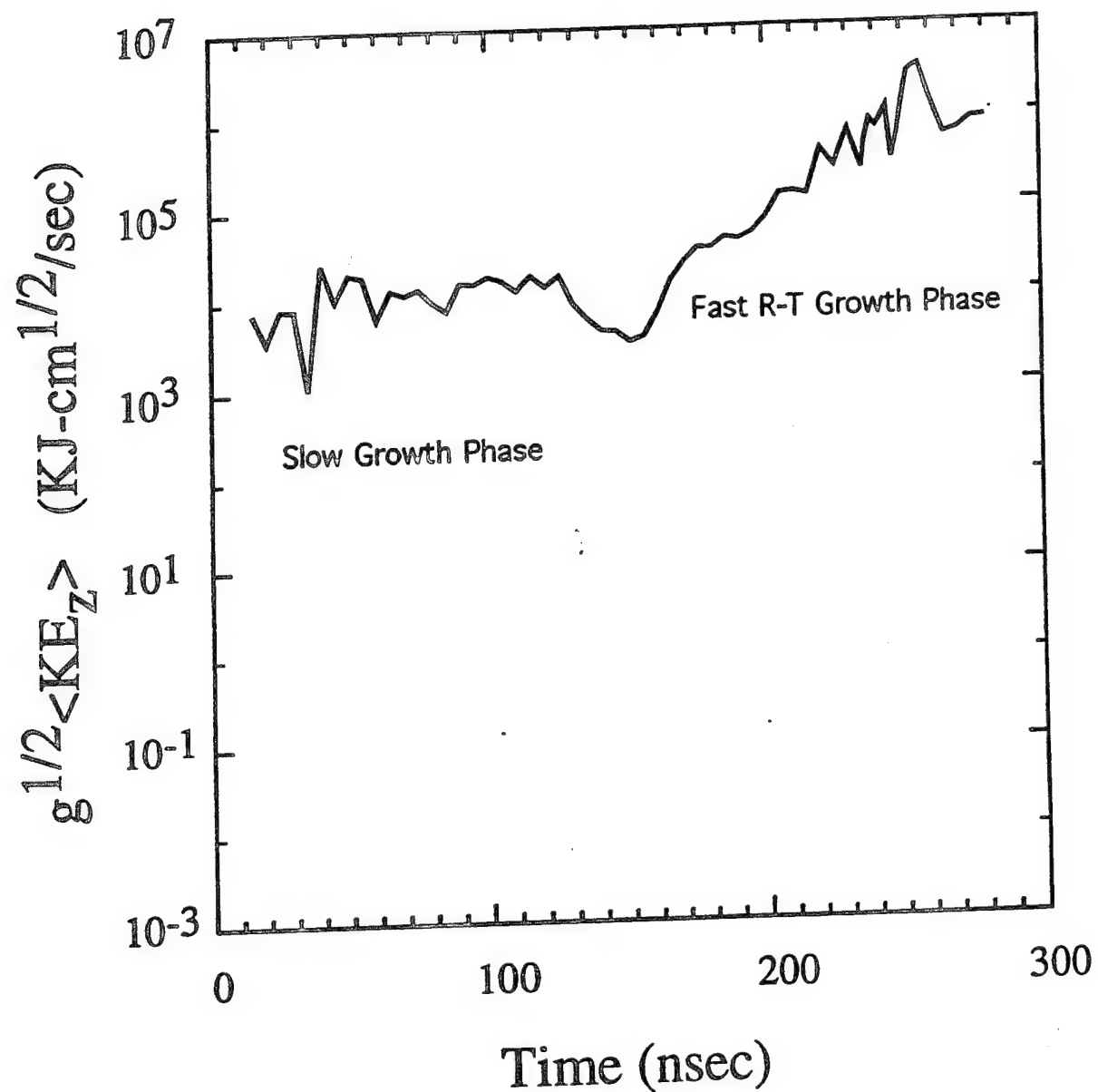


Figure 11: The quantity $\langle KE_z \rangle g^{1/2}$ as a function of time for the $1/r^3$ initial density profile simulation.

VI. IMPLOSIONS, EQUILIBRIA AND STABILITY OF ROTATING RADIATING Z-PINCH PLASMAS

A. Introduction

The idea of using rotation to suppress the Rayleigh-Taylor (RT) instability of an imploding plasma goes back about 20 years ago to the LINUS project developed at the Naval Research Laboratory.¹ Recently, it was discussed again by Rostoker and his collaborators², who proposed to use spin control of the RT instability in high-density Z-pinches. The technical feasibility of producing a spinning plasma column which, like a conventional gas-puff jet, could be used as a Z-pinch load driven by a pulsed power machine, has been demonstrated in the experiment³. Rotation was shown in this experiment to produce homogeneous plasmas, smoothing out the azimuthal non-uniformities like those typically produced in gas-puff Z-pinches during initial gas breakdown and observed in ref. 4.

This concept of controlling the RT instability is aimed at stabilizing the final, stagnation phase of implosion, by eliminating the acceleration that may cause instability. Indeed, the inward motion of the shell coasting to the axis in the absence of any external forces - that is, with its acceleration identically zero, -could be stopped and reversed simply due to conservation of angular momentum, see example in Section III. (The value of \ddot{R} characteristic of radial deceleration could be quite large, although the radial component of the acceleration, $\ddot{R} - R\dot{\theta}^2$ vanishes.) Being most important for controlled fusion applications, this aspect of stability does not appear to be a major issue when applications like plasma radiation sources are considered. In this context, the development of the RT instability during the run-in phase is one mostly damaging the quality of implosions (e.g., see ref. 5). The dominant mode of this instability is known to be the sausage, $m=0$ mode, which in the absence of an external axial magnetic field is the only one that can develop without bending the magnetic field lines. The filamentation RT modes with nonzero m are also developing in imploding plasmas, but their growth rates are

smaller than those of the sausage mode - for short wavelengths, by factor of $\sqrt{\sqrt{2} - 1} = 0.643$, see^{6,7}. Hence, although decreasing the amplitudes of the initial azimuthal perturbations, either through rotation or by other means (like increasing the number of return current rods) would certainly improve the quality of implosion, it is unlikely to become a major stabilizing factor.

Could rotation help control the RT instability during the run-in phase? This is one of the problems addressed in the present paper. The earlier results⁸ indicate that a rotating plasma column is more unstable than a resting one, and therefore are not optimistic. Nevertheless, since the presence of angular momentum is shown to have exactly the same dynamic effect on 1-D motion of ideal Z-pinch plasma as the presence of frozen-in axial magnetic flux, it is natural to inquire if it has also a similar stabilizing effect, and why not, if it does not.

Whether or not the Z-pinch plasma is deliberately spun before implosion, its deviation of symmetry is likely to produce some angular momentum in the start-up phase. Being conserved, and increasingly important for higher compression, non-zero angular momentum can strongly affect possible final stages of the implosion. In particular, spinning can change the flow pattern drastically if in the absence of rotation a radiative collapse is predicted to occur.

This paper is structured as follows. In Section II, the Bennett and Pease-Braginskii's steady-state equilibria (and slowly varying "time-dependent equilibria") of rotating, radiating cylindrically-symmetric plasma are studied. In Section III, dynamics of rotating, radiating ideal plasmas is studied analytically. In Section IV, stability of a rotating Z-pinch column is studied using a very simple model. In Section V, we conclude with a discussion.

B. Bennett and Pease-Braginskii equilibria

Let us start with the equation describing radial pressure balance in a cylindrically-symmetric, uniformly rotating Z-pinch:

$$(1+Z) \frac{d}{dr}(nT) + \frac{B_\theta}{4\pi r} \frac{d}{dr}(rB_\theta) = \rho\Omega^2 r \quad , \quad (1)$$

where Z is the average ion charge, Ω is the angular velocity. Multiplying (1) by $2\pi r^2$ and integrating over r from 0 to R , we obtain the Bennett relation:

$$(1+Z)N\bar{T} + \frac{1}{2}J\Omega^2 = \frac{I^2}{2c^2}, \quad (2)$$

where N is the ion line density, \bar{T} is the average temperature, J is the moment of inertia per unit length of the column. This could also be presented as

$$(1+Z)N\bar{T} = \frac{1}{2c^2}(I^2 - I_\Omega^2), \quad (3)$$

where I_W is a characteristic of rotation with dimensionality of current:

$$I_W (\text{kA}) = 31 (\mu, \text{mg/cm})^{1/2} (\bar{V}, \text{km/sec}), \quad (4)$$

\bar{V} being some average velocity of rotation, $\mu = m_i N$ - the line mass of the column. As long as the current $I \gg I_\Omega$, Eq. (4) represents the conventional Bennett equilibrium. For instance, with $\mu = 100 \text{ mg/cm}$ and $\bar{V} = 100 \text{ km/sec}$, we find: $I_W = 1 \text{ MA}$. Thus the effect of rotation could be noticeable if the characteristic velocity \bar{V} were of the same order as the implosion velocity, which for the multi-MA pulsed-power machines is about $3 \times 10^7 \text{ cm/sec}$.

Now consider the simplest equilibrium profiles, corresponding to flat profiles of temperature and current density: $T(r) = \bar{T} = \text{const}$, and $j(r) = I / \pi R^2 = \text{const}$. Then equation (1) is easily solved for $n(r)$. Introducing a dimensionless parameter

$$\lambda = \frac{m_i R^2 \Omega^2}{2(1+Z)\bar{T}} \quad (5)$$

characteristic of the rotation (the limits $\lambda \ll 1$ and $\lambda \gg 1$ correspond to low and high importance of rotation, respectively), and the dimensionless coordinate

$$\eta = \frac{r}{R}, \quad (6)$$

one can present the solution as

$$n(\eta) = \frac{N}{\pi R^2} \frac{\lambda}{\lambda - 1 + \exp(-\lambda)} \{1 - \exp[-\lambda(1 - \eta^2)]\}. \quad (7)$$

The equilibrium density profiles are shown in Fig. 1 for several values of the parameter λ . In the limit $\lambda \rightarrow 0$ the conventional parabolic profile $n = (2N / \pi R^2)(1 - \eta^2)$ is reproduced. The opposite extreme $\lambda \rightarrow \infty$ corresponds to uniform density $n = (N / \pi R^2)\Theta(1 - \eta)$, where $\Theta(z)$ is the Heaviside's step function.

Consider now an infinitely slow variation of equilibrium conditions. The current I , the pinch radius R , temperature T , angular velocity Ω and the parameter λ may vary, whereas the ion line density N remains invariant. Another invariant is the conserved angular momentum:

$$M = J\Omega = \text{const}. \quad (8)$$

With the aid of (7), we can express the moment of inertia J via the parameter λ , and substitute into (8), to obtain

$$I^2 R^2 \cdot \frac{[2 - 2\lambda + \lambda^2 - 2\exp(-\lambda)]^2}{\lambda^2 [\lambda - 1 + \exp(-\lambda)]} = \frac{2c^2 M^2}{m_i N} = \text{const}. \quad (9)$$

Now consider the power balance. Following Pease⁹ and Braginskii¹⁰, let us assume that Ohmic heating due to classical Spitzer resistivity is balanced by the bremsstrahlung radiative losses from the optically thin plasma column (this might refer to a Z-pinch in a hydrogen or deuterium). The power density of Ohmic heating is given by $Q_j = T^{-3/2} j_z^2 / \sigma_0$, where the Spitzer expression for plasma conductivity $\sigma = \sigma_0 T^{3/2}$ has been used, σ_0 being a known constant for a given plasma composition. In our case of uniform temperature and current density, so that the total ohmic power per unit length of the plasma column is

$$P_j = 2\pi \int_0^R Q_j r dr = \frac{T^{-3/2} I^2}{\pi R^2 \sigma_0}. \quad (10)$$

The power density of bremsstrahlung losses is given by $Q_r = Q_0 n^2 T^{1/2}$, where Q_0 is also a known constant. Integrating this expression with the aid of Eq. (7), we find the total power of bremsstrahlung losses:

$$P_r = 2\pi \int_0^R Q_r dr = \frac{Q_0 T^{1/2} N^2}{2\pi R^2} \frac{\lambda [2\lambda - 3 + 4\exp(-\lambda) - \exp(-2\lambda)]}{[\lambda - 1 + \exp(-\lambda)]^2}. \quad (11)$$

Since the Ohmic heating is supposed to be balanced by radiative cooling,

$$P_r = P_j, \quad (12)$$

after some algebra we can transform (12) into

$$I = I_{PB} \sqrt{\frac{2\lambda^3}{3[2\lambda - 3 + 4\exp(-\lambda) - \exp(-2\lambda)]}}. \quad (13)$$

Here, I_{PB} is the conventional value of the Pease-Braginskii's current in the absence of rotation (about 1.4 MA for deuterium plasma), and the left-hand side of Eq. (13) tends to this value in the limit $\lambda \rightarrow 0$. However, Eq. (13) shows that with rotation taken into account, the power balance (12) is possible not only for $I = I_{PB}$, but for any current greater than I_{PB} , provided that the value of λ is sufficiently high. The dependence (13) is illustrated by Fig. 2.

Suppose we maintain an almost Pease-Braginskii equilibrium, with I very close to I_{PB} , and small but non zero $\lambda = \lambda_0$, and then start increasing the current very slowly, so that there is enough time to establish the power balance (12) for any current value of I . With I and λ related by (13), we can express R via λ from (9). This relation

$$\frac{R}{R_0} = \sqrt{\frac{F(\lambda_0)}{F(\lambda)}}, \quad (14)$$

where

$$F(\lambda) = \frac{[2 - 2\lambda + \lambda^2 - 2\exp(-\lambda)]^2}{[\lambda - 1 + \exp(-\lambda)][2\lambda - 3 + 4\exp(-\lambda) - \exp(-2\lambda)]}, \quad (15)$$

together with (13) expresses in a parametric form the relation between I and R for a slowly varying, "time-dependent equilibrium".

Figure 3 presents the ratio R / R_0 versus the normalized current I / I_{PB} for two values of the parameter $\lambda_0 = 0.1$ and 0.01 . In both cases, there is no radiative collapse: the radius of the Z-

pinch and the angular frequency of its rotation adjust in such a way that the power balance is realized with finite R for any value of I .

Of course, higher compression is needed to reach the balance for low values of λ_0 . For instance, with $\lambda_0=0.01$ increasing the current from $I = I_{PB}$ to $I = 3I_{PB}$ should be accompanied by an almost 50-fold radial compression, that is, by a 2.5×10^3 -fold density jump. But this is still smaller than a 10^6 -fold or higher density increase predicted by the models of radiative collapse,¹¹⁻¹⁴ involving a thousandfold or higher radial compression.

Does the value $\lambda_0=0.01$ correspond to an unrealistically fast rotation? The ratio of kinetic energy of rotation E_k to the thermal energy of the Z-pinch column E_T in the initial state with $\lambda_0 \ll 1$ equals

$$\frac{E_k}{E_T} = \frac{\gamma - 1}{3} \lambda_0, \quad (16)$$

which means only 2×10^3 even for $\gamma = 5/3$ (and for radiating Z-pinches, lower values of γ are appropriate). A small deviation from ideal cylindrical symmetry of mass and current distribution in the Z-pinch load would be quite sufficient to produce initially slow ($\lambda_0=0.01$) rotation, which would nevertheless be sufficient to stop the radiative collapse long before the ultra-high densities¹¹⁻¹⁴ are produced. We will show that the same conclusion would be valid if dynamics of compression is taken into account more accurately.

C. Self-similar implosion dynamics

To estimate the degree of compression which could be achieved when an optically thin radiating Z-pinch column rotates around its axis, we use exact self-similar solutions of ideal MHD equations with radiative losses:

$$\frac{\partial n}{\partial t} + (\mathbf{u} \nabla) n + n \nabla \cdot \mathbf{u} = 0, \quad (17)$$

$$\frac{\partial T}{\partial t} + (\mathbf{u} \nabla) T + (\gamma - 1) T \nabla \cdot \mathbf{u} = -\frac{(\gamma - 1) Q_r}{(1 + Z)n}, \quad (18)$$

$$\frac{\partial \mathbf{B}}{\partial t} - \nabla \times (\mathbf{u} \times \mathbf{B}) = 0, \quad (19)$$

$$\frac{\partial \mathbf{u}}{\partial t} + (\mathbf{u} \nabla) \mathbf{u} = -\frac{1+Z}{m_i n} \nabla(nT) + \frac{1}{4\pi m_i n} (\nabla \times \mathbf{B}) \times \mathbf{B}, \quad (20)$$

All notation here is standard. The power density of radiative losses Q_r could be expressed either by the above formula $Q_r = Q_0 n^2 T^{1/2}$ for bremsstrahlung radiative losses, or by $Q_r = Q_1 n^2 T^{-1}$, if line radiation is supposed to be a major energy sink. We did not include the Ohmic heating and magnetic diffusion terms in the right-hand sides of Eqs. (18) and (19), respectively, because with these terms we would not be able to separate the variables. Physically, this means that we consider currents greater than the Pease-Braginskii's value I_{PB} , so that radiative energy losses are supposed to be greater than the Ohmic heating.

Exact self-similar solutions for a 1-D motion with uniform (homogeneous) deformation are obtained in a standard way, and below we present only the results. (Details and references could be found in¹⁵⁻¹⁷). All the variables are presented as separable function of the self-similar coordinate h given by (6) [where $R = R(t)$ is the time-dependent radius of the plasma column, $R_0 \equiv R(t = 0)$] and of dimensionless degree of compression $\alpha(t) = R(t) / R_0$:

$$u_r = R_0 \frac{d\alpha}{dt} \eta, \quad u_\theta = R_0 Q_0 \alpha^{-1} \eta, \quad n = n_0 N(\eta) \alpha^{-2}, \\ T = T_0 \Theta(\eta) \theta(t) \alpha^{-2(\gamma-1)}, \quad B_\theta = B_{\theta 0} H_\theta(\eta) \alpha^{-1}, \quad B_z = B_{z0} H_z(\eta) \alpha^{-2}, \quad (21)$$

where Q_0 , n_0 , T_0 , $B_{\theta 0}$, B_{z0} are normalization constants, $N(\eta)$, $\Theta(\eta)$, $H_\theta(\eta)$, and $H_z(\eta)$ are self-similar profiles of density, temperature, azimuthal, and axial magnetic field, respectively, $\theta(t)$ is a dimensionless function describing loss of entropy due to radiation.

With time measured in units of $t_0 = (4\pi m_i n_0)^{1/2} R_0 / B_{\theta 0}$, equation of motion for $\alpha(t)$ could be presented in the form

$$\alpha' = -\frac{1}{\alpha} + \frac{\beta\theta^2}{\alpha^{2\gamma-1}} + \frac{b}{\alpha^3}, \quad (22)$$

where the constants are

$$\beta = \frac{4\pi(1+Z)n_0T_0}{B_{\theta 0}^2} \quad \text{and} \quad b = \Omega_0^2 t_0^2 + \frac{B_{z0}^2}{B_{\theta 0}^2}. \quad (23)$$

The parameter β has the conventional meaning of ratio of thermal pressure (or energy density) to the magnetic one. The parameter β includes contributions from the centrifugal term and from the axial magnetic field. Since the two positive terms are added, the effects of rotation and of axial magnetic field on the radial compression are quite similar, their relative importance being determined by the ratio of the two terms in the expression (23) for b . To explain the similarity, we note that conservation of angular momentum implies $\Omega R^2 = \text{const}$, so that the centrifugal acceleration $\Omega^2 R \propto R^{-3}$. Conservation of axial magnetic flux implies $B_z R^2 = \text{const}$, so that external force per unit length of the plasma column needed to contain it is $2\pi R \times (B_z^2 / 8\pi) \propto R^{-3}$. Equation of motion (22) clearly shows that the presence of angular momentum and/or axial magnetic field is dynamically equivalent to addition of some ideal gas with $g=2$ to the Z-pinch column.

The self-similar profiles $N(\eta)$, $\Theta(\eta)$, $H_\theta(\eta)$, and $H_z(\eta)$, as well as the equation for $\theta(t)$, depend on the mechanism of radiative energy losses. For bremsstrahlung losses

$$N(\eta) = \left(\frac{1-\eta^2}{3}\right)^{1/2}, \quad \Theta(\eta) = \frac{1-\eta^2}{3}, \quad H_z(\eta) = 2^{1/2} \left(\frac{1-\eta^2}{3}\right)^{3/4},$$

$$H_\theta(\eta) = \frac{(2/5)^{1/2}}{3^{3/4}\eta} \left[(1-\eta^2)^{1/2} (3\eta^4 - \eta^2 - 2) + 2\right]^{1/2}, \quad (24a)$$

and

$$\dot{\theta} = -\varepsilon \theta^{1/2} \alpha^{\gamma-3}, \quad (25a)$$

where dimensionless parameter $\varepsilon = (\gamma-1)(4\pi m_i)^{1/2} n_0^{3/2} \Omega_0 R_0 / (1+Z) B_{\theta 0} T_0^{1/2}$ has the meaning of a ratio of the time needed to radiate away all the thermal energy of the plasma

column to the characteristic time t_0 (this is essentially the same as given in¹⁷). For line radiative losses

$$N(\eta) = \left(\frac{1-\eta^2}{6} \right)^2, \quad \Theta(\eta) = \frac{1-\eta^2}{6}, \quad H_z(\eta) = \frac{3^{1/2}}{18} (1-\eta^2)^{3/2},$$

$$H_\theta(\eta) = \frac{\eta}{36} (18 - 24\eta^2 + 9\eta^4)^{1/2}, \quad (24b)$$

and

$$\dot{\theta} = -\varepsilon \theta^{-1} \alpha^{2(2\gamma-3)}, \quad (25b)$$

with $\varepsilon = (\gamma - 1)(4\pi m_i)^{1/2} n_0^{3/2} Q_1 R_0 / (1 + Z) B_{\theta 0} T_0^2$. As seen from Eqs. (25a, b), the self-similar profiles are independent from the parameters b , b , and ε , which determine the time history of the Z-pinch motion. In Fig. 4a, b, the dimensionless profiles of $N(\eta)$, $\Theta(\eta)$, $H_\theta(\eta)$, $H_z(\eta)$, and axial current density $J_z(\eta) = (1/\eta)(d/d\eta)[\eta H_\theta(\eta)] = \eta N(\eta) / H_\theta(\eta)$ are plotted for bremsstrahlung and line radiative losses, respectively. The profiles are basically quite similar, with current density more sharply peaked near the axis in the case of line radiation.

To study the dynamics of the Z-pinch column, Eq. (22) and either Eq. (25a) or (25b) should be integrated with the initial conditions $\alpha(0) = 1$, $\dot{\alpha}(0) = 0$, $\theta(0) = 1$. For each case the solution is fully determined by the values of parameters b , b , and ε . To start with the implosion phase, the sum $\beta + b$ must be less than unity. The results are very similar for both cases, and we present in Figs. 5-6 only those calculated for line radiative losses, $\gamma = 1.3$, $\varepsilon = 0.03$.

Figure 5 is plotted for the case of no rotation and/or axial magnetic field ($b=0$, $\beta=0.5$). Then the solution describes a radiative collapse: Z-pinch radius R and the characteristic value p/p^γ , proportional to the exponential of its entropy vanish after a number of bounces in the same way as described in¹⁷. With nonzero angular momentum and/or axial magnetic field (Fig. 6, plotted for $b=0.1$ and $\beta=0.4$), we see that no radiative collapse does take place. After a while, all the thermal energy gets radiated away, just as in the case of Fig. 5. Then, in contrast with Fig. 5, the pressure of azimuthal magnetic field is balanced by the centrifugal force and/or by the

pressure of azimuthal magnetic field. With no instability that could limit the number of bounces taken into account, the final state of the Z-pinch column is represented by undamped oscillations. Just as in Section II, no radiative collapse is predicted, unless the both the angular momentum and the magnetic flux of axial magnetic field are exactly zero. As it is obviously hard to produce real Z-pinches with exactly zero angular momentum, we conclude once again that the radiative collapse predicted by 0-D, 1-D, and even 2-D (r-z) modeling for cylindrical Z-pinches with $I > I_{PB}$ might be a consequence of unrealistically high symmetry imposed on these simulations. Since a rotating plasma column is itself unstable (see⁸ and Section IV), formation of complicated 3-D patterns appears to be a more likely result of its evolution than an essentially one-dimensional, cylindrically-symmetric radiative collapse.

D. Sausage instability of a uniformly rotating Z-pinch

Axial magnetic field is well known to suppress the dominant sausage ($m=0$) mode of the RT instability in dynamic Z-pinches (e.g., see¹⁸⁻²⁰). Equation (22) demonstrates that dynamic effect of rotation is the same as of the axial magnetic field. Does rotation have similar stabilizing effect on the sausage modes? To answer this, we study a simple, analytically tractable stability problem for a rotating Z-pinch.

Consider solid rotation of a column of cold plasma carrying axial current, both current density and plasma density being uniform in the unperturbed steady state. Then the unperturbed azimuthal magnetic field has linear profile, and, as seen from Eq. (1),

$$B_\theta^{(0)} = (2\pi\rho^{(0)})^{1/2}\Omega r, \quad (26)$$

where the superscript (0) marks the unperturbed variables, $\rho^{(0)} = \text{const}$ is the unperturbed density, Ω is the constant unperturbed angular velocity of rotation. Being steady, the Z-pinch is nevertheless accelerated inward, to the axis, by the azimuthal magnetic field, and hence should

exhibit kind of Rayleigh-Taylor instability. Let us find out whether there is any kind of stabilization due to rotation, since the local gravity $g(r) = \Omega^2 r$ is provided by the centrifugal acceleration.

For our illustrative purposes, we use the ideal MHD model, and will not discuss its validity here, although it appears to be applicable to the case of solid rotation (see²¹). It is convenient to use the non-inertial, uniformly rotating frame of reference. Then in the unperturbed state the plasma particles are resting, and their motion is due solely to perturbation. The time variable is thus separated, and we can seek solutions proportional to $\exp(Gt + ikz)$, where G is the growth rate, k is the perturbation wavenumber (the exponential factor will be omitted below). The velocity u then is itself a first-order perturbation, which could be conventionally expressed via the displacement ξ of a plasma particle: $u = \partial \xi / \partial t = G \xi$. Equations (17) and (19), which remain valid in the rotating frame, are integrated in a conventional way to give

$$\frac{\rho^{(1)}}{\rho^{(0)}} = -\nabla \cdot \xi, \quad (27)$$

$$\mathbf{B}^{(1)} = \nabla \times (\xi \times \mathbf{B}^{(0)}), \quad (28)$$

where the superscript (1) marks the first-order perturbation. In the equation of motion (20) we neglect the pressure term, and second-order term in velocity, but have to include the terms representing the Coriolis force and the centrifugal force, to obtain

$$\begin{aligned} \Gamma^2 \rho^{(0)} \xi = & \frac{1}{4\pi} [(\nabla \times \mathbf{B}^{(1)}) \times \mathbf{B}^{(0)} + (\nabla \times \mathbf{B}^{(0)}) \times \mathbf{B}^{(1)}] + 2\Gamma \rho^{(0)} \xi \times \Omega + \\ & + \rho^{(1)} \Omega \times (\mathbf{r} \times \Omega). \end{aligned} \quad (29)$$

We find from (27) that for $m=0$ perturbations and $B_z = 0$ in the unperturbed state, the only nonzero component of perturbed magnetic field is $B_\theta^{(1)}$. Using (26), (27), and expressing ξ_z from (28), we can find that

$$\frac{B_\theta^{(1)}}{B_\theta^{(0)}} = \frac{\rho^{(1)}}{\rho^{(0)}} = -\frac{v^2}{k^2 r^2 + v^2} \left(\frac{d\xi_r}{dr} + \frac{\xi_r}{r} \right). \quad (30)$$

where the dimensionless eigenvalue n is defined as $\nu = 2^{1/2} \Gamma / \Omega$. Substituting (30) into the r -component of Eq. (29), we obtain a modified Bessel equation

$$r^2 \frac{d^2 Y}{dr^2} + r \frac{dY}{dr} - \left(\frac{\nu^2 + 8}{\nu^2} k^2 r^2 + \nu^2 + 8 \right) Y = 0 \quad (31)$$

for a variable Y defined as $Y = -(k^2 r^2 / \nu^2) B_\theta^{(1)} / B_\theta^{(0)}$ and related to x_r by

$$k^2 \xi_r = \frac{\nu^2}{\nu^2 + 8} \frac{dY}{dr}. \quad (32)$$

Solution of Eq. (31), which is not singular at $r=0$, is given by

$$Y(r) = I_{(\nu^2 + 8)^{1/2}} \left[\frac{(\nu^2 + 8)^{1/2}}{\nu} kr \right]. \quad (33)$$

The boundary condition on the perturbed free surface of the pinch states continuity of magnetic pressure there, which in our case is the same as continuity of B_θ (since the unperturbed velocity of rotation is parallel to the magnetic field, no electric field emerges in our rotating frame of reference):

$$\delta B_\theta^{(ext)} = \delta B_\theta^{(int)}. \quad (34)$$

Being both curl-free and divergence free, the perturbed magnetic field in vacuum could be presented as $\nabla \Phi$, where Φ is some scalar function. Due to azimuthal symmetry, $\nabla \Phi$ has no azimuthal component, and therefore the external perturbation of B_θ is due to displacement of the boundary:

$$\delta B_\theta^{(ext)} = \left(\frac{dB_\theta^{(0)}}{dr} \right)_{r=R} \xi_r(R) = -B_\theta^{(0)}(R) \frac{\xi_r(R)}{R} \quad (35)$$

whereas for the internal perturbation we find:

$$\delta B_\theta^{(int)} = B_\theta^{(1)}(R) + \left(\frac{dB_\theta^{(0)}}{dr} \right)_{r=R} \xi_r(R) = B_\theta^{(0)} \left[\left(\frac{B_\theta^{(1)}}{B_\theta^{(0)}} \right)_{r=R} + \frac{\xi_r(R)}{R} \right]. \quad (36)$$

Substituting (35) and (36) into (34), and using Eqs. (30), (32), (33), we find the dispersion relation, which is a transcendental equation for Γ :

$$\frac{\kappa I_{\mu+1}(\kappa)}{I_\mu(\kappa)} = \frac{1}{2} \mu(\mu - 2), \quad (37)$$

where

$$\Gamma = \frac{\Omega}{\sqrt{2}}(\mu^2 - 8)^{1/2} \quad \text{and} \quad kR = \frac{\kappa}{\mu}(\mu^2 - 8)^{1/2}, \quad (38)$$

and, once we are interested in real-valued solutions, the real parameter m should vary between $2\sqrt{2}$ and infinity.

In the long-wavelength limit $kR \rightarrow 0$ [which means $\kappa \rightarrow 2\sqrt{2}$, see (38)], the right-hand side of Eq. (37) tends to a finite value $4 - 2\sqrt{2}$, so that the real root $\kappa = \kappa_0 = 3.1781$ is found as a numerical solution of a transcendental equation

$$\frac{\kappa I_{2\sqrt{2}+1}(\kappa)}{I_{2\sqrt{2}}(\kappa)} = 4 - 2\sqrt{2}. \quad (39)$$

The growth rate for long wavelengths is thus proportional to the wavenumber

$$\Gamma \approx \frac{2}{\kappa_0} \Omega kR = 0.629 \Omega kR. \quad (40)$$

In the opposite, short-wavelength limit $kR \rightarrow \infty$, the leading term in the right-hand side of Eq. (37) is $\mu^2 / 2$, implying that κ should be of the same order (if the arguments of the modified Bessel functions are much larger than their orders, then the ratio of Bessel functions tends to unity). Then the relation $\kappa \approx \mu^2 / 2$ is equivalent to

$$\Gamma \approx \Omega (kR)^{1/2} = (gk)^{1/2}, \quad (41)$$

where $g = \Omega^2 R$ is the local gravity acceleration at the surface of the plasma column. We see that the classical expression for RT instability growth rate is reproduced here in the short-wavelength limit.

To calculate the dispersion curve $\Gamma(k)$ shown in Fig. 7 (curve 1), Eq. (37) was solved numerically. For comparison, the RT dependence $\Gamma(k)$ given by the right-hand side of Eq. (41), is plotted there as curve 2. No stabilizing effect is seen for short wavelength. As for long

wavelength, the linear dependence like (40) is quite typical for accelerated Z-pinches with distributed current, see¹⁸. This also cannot be regarded as stabilization.

Now we can explain why rotation, which in 1-D flow produces the same dynamic effect as the axial magnetic field, does not help to stabilize. Indeed, as seen from Eq. (22), introduction of both of these terms is equivalent to addition of some fluid with $\gamma = 2$, effectively shifting the plasma's γ toward this value. But variation of γ within finite limits is known to produce little effect on sausage instability,²¹ with the dominant RT mode in the short-wavelength limit independent from γ , and hence, not affected at all, as confirmed once again by Eq. (41). The stabilizing effect of the axial magnetic field is basically two-dimensional. This stabilization is due to the energy required to bend the force lines of axial magnetic field, which is represented in the dispersion relations by the terms proportional to $(kB_z)^2$. There is nothing to match it in the case of rotation.

E. Discussion

We have shown that plasma rotation is not likely to help stabilize the most dangerous sausage modes of the RT instability of imploding Z-pinches in the run-in phase. Although it might be helpful in stabilizing filamentation modes ($m \geq 2$), (see Ref 21) as well as in decreasing the initial amplitudes of the corresponding perturbations, since these are not dominant instability modes, it is not likely to improve overall implosion stability. Consequently, the idea of making a rotating Z-pinch load shows little promise for applications like plasma radiation sources, unless a major stabilizing effect of sheared rotation (not studied here) on the sausage instability modes is discovered.

In real imploding Z-pinches, however, some angular momentum is always present, even if no efforts are made to produce it deliberately. We have demonstrated above that even small initial angular momentum is sufficient to stop radiative collapse for a current above the Pease-Braginskii value long before the ultra-high densities are achieved (for instance, starting rotational

kinetic energy of about 10^3 of the thermal energy is enough to limit radial compression of a quasi-steady plasma column carrying current $I = 3I_{PB}$ at the level below 50). This is why the radiative collapse of a cylindrical plasma column predicted for $I > I_{PB}$ might be a consequence of unrealistically high symmetry imposed on analytic studies and numerical simulations, including even 2-D ones.

Both trapped flux of axial magnetic field and nonzero angular momentum are capable of stopping radiative collapse. Although their dynamic effects in ideal MHD model are shown to be similar, the mechanisms of their dissipative losses are quite different. The axial magnetic field can simply diffuse through plasma into vacuum, and it could easily be dissipated if the plasma radius is sufficiently small. In contrast with this, angular momentum could only be lost in axial direction, either through ejection of mass carrying momentum, or through viscosity. The former mechanism is evidently more effective. Hence, the actual high compression of radiating plasmas in Z-pinches, which leads to formation of bright spots, being necessarily accompanied by loss of angular momentum, should produce not cylinder-like regions of dense plasma (U-shaped necks), but rather point-like ones (V-shaped necks). This seems to be in agreement both with the available theoretical data, and with earlier theoretical results²³ based on different assumptions.

References

1. Boris and R. A. Shanny, Proc. 2nd Topical Conference on Pulsed High Beta Plasma. Garching, Germany, July 3-6, 1972.
2. N. Rostoker, G. G. Peterson, and H. Tahsiri, *Spin Control of the Rayleigh-Taylor Instability in a High Density Pinch*, Technical Report No. 93-35, University of California, Irvine, November 1993.
3. A. Ben-Amar Baranga, A. Fisher, and D. Tzach, Rev. Sci. Instrum. **56**, 1472 (1985).
4. G. G. Peterson, F. J. Wessel, N. Rostoker, and A. Fisher, in *Dense Z-Pinches*, edited by M. Haines and A. Knight, AIP, New York, 1994, p. 396.
5. R. B. Baksh et al., *GIT-4 Plasma Radiation Source. Test Report*, High Current Electronics Institute, Tomsk, Russia, August 1994.
6. E. G. Harris, Phys. Fluids **5**, 1057 (1962).
7. A. I. Kleev and A. L. Velikovich, Plasma Phys. Contr. Fusion **32**, 763 (1990).
8. E. Gerjuoy and M. N. Rosenbluth, Phys. Fluids **4**, 527 (1961).
9. R. S. Pease, Proc. Phys. Soc. London **B70**, 11 (1957).
10. S. I. Braginskii, Zh. Eksp. Teor. Fiz. **33**, 645 (1957).
11. J. W. Shearer, Phys. Fluids **19**, 1426 (1976).
12. B. E. Meierovich, Phys. Rep. **92**, 85 (1982); **104**, 259 (1984).
13. A. E. Robson, Phys. Fluids B **1**, 1834 (1989).
14. M. G. Haines, Plasma Phys. Controlled Fusion **31**, 759 (1989).
15. F. S. Felber, Phys. Fluids **25**, 643 (1982).
16. M. A. Liberman and A. L. Velikovich, Nucl. Fusion **26**, 709 (1986).
17. B. E. Meierovich, Sov. J. Plasma Phys. **11**, 831 (1985).
18. A. B. Bud'ko, M. A. Liberman, and A. L. Velikovich, Phys. Fluids B **2**, 1159 (1990).

19. F. S. Felber, M. M. Malley, F. J. Wessel, M. K. Matzen, M. A. Palmer, R. B. Spielmann
M. A. Liberman, and A. L. Velikovich , Phys. Fluids **31**, 2053 (1988).
20. S. A. Sorokin and S. A. Chaikovsky, in *Dense Z-Pinches*, edited by M. Haines and A. Knight, AIP, New York, 1994, p. 83.
21. X. Shan and D. Montgomery, Phys. Rev. Letts., **73**, 1624 (1994).
22. I. B. Bernstein and D. Book, Phys. Fluids **26**, 453 (1983).
23. D. Mosher and D. Colombant, Phys. Rev. Lett. **68**, 2600 (1992).

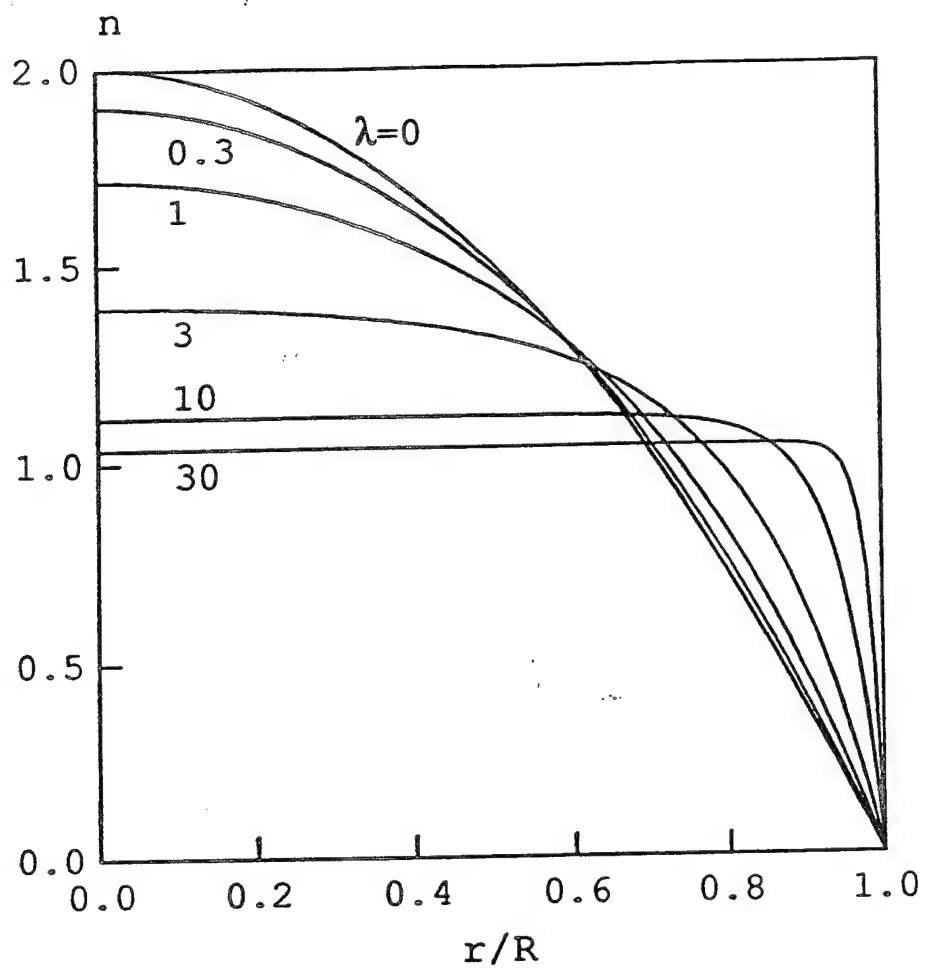


Fig. 1. Profiles (7) of density n expressed in units of $N/\pi R^2$, versus r/R for given values of λ .

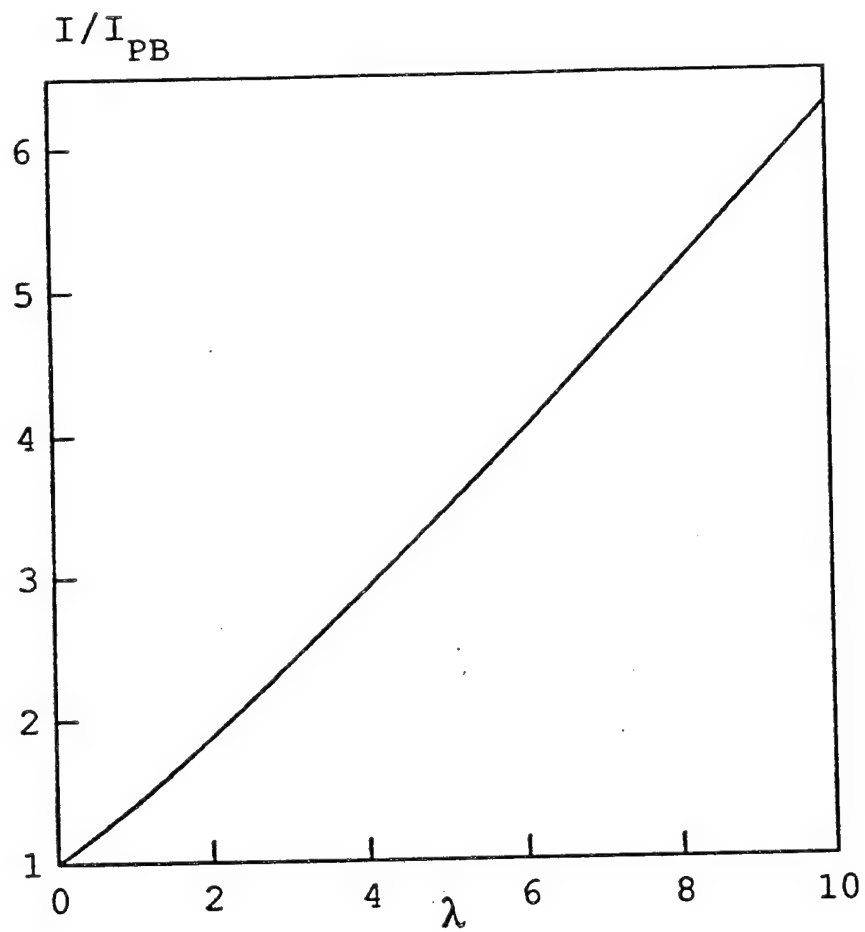


Fig. 2. Current I maintaining a power balance in a steady rotating plasma column (expressed in units of Pease-Braginskii's current I_{PB}) versus the parameter λ .

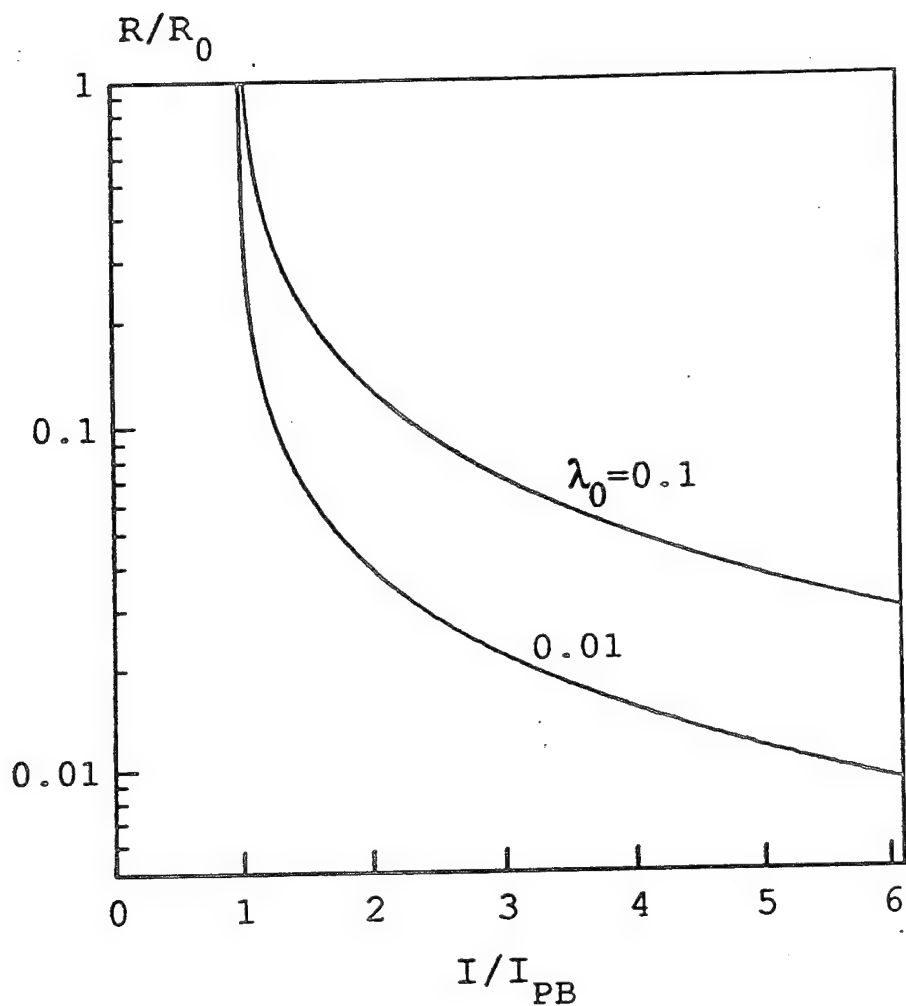


Fig. 3. Degree of quasi-steady radial compression R/R_0 versus I/I_{PB} , for two initial values of the parameter $\lambda = \lambda_0$

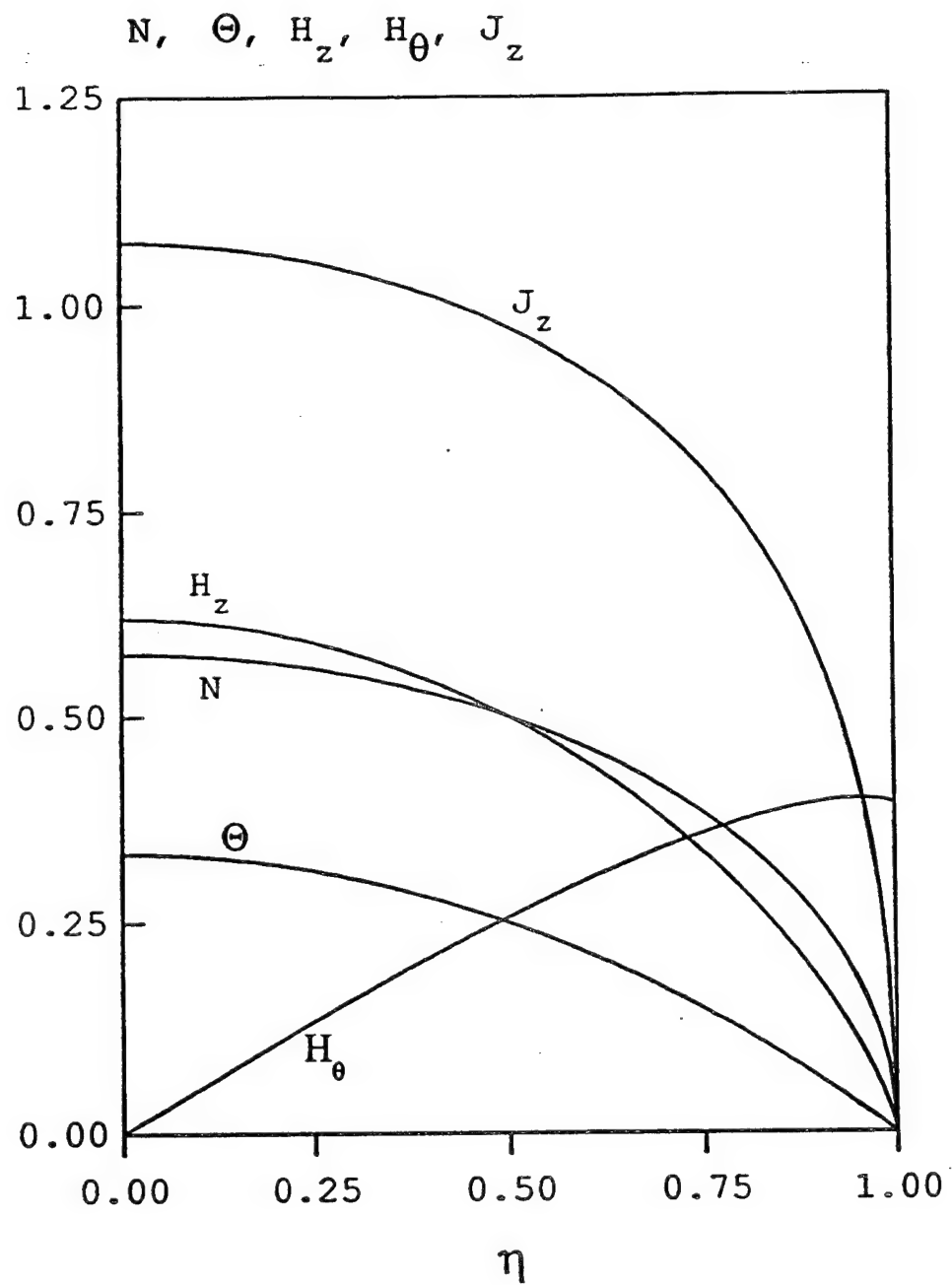


Fig. 4. (a) Self-similar profiles of density, temperature, magnetic field and current density for a Z-pinch with bremsstrahlung radiative energy losses. (b) Same for line radiative losses.

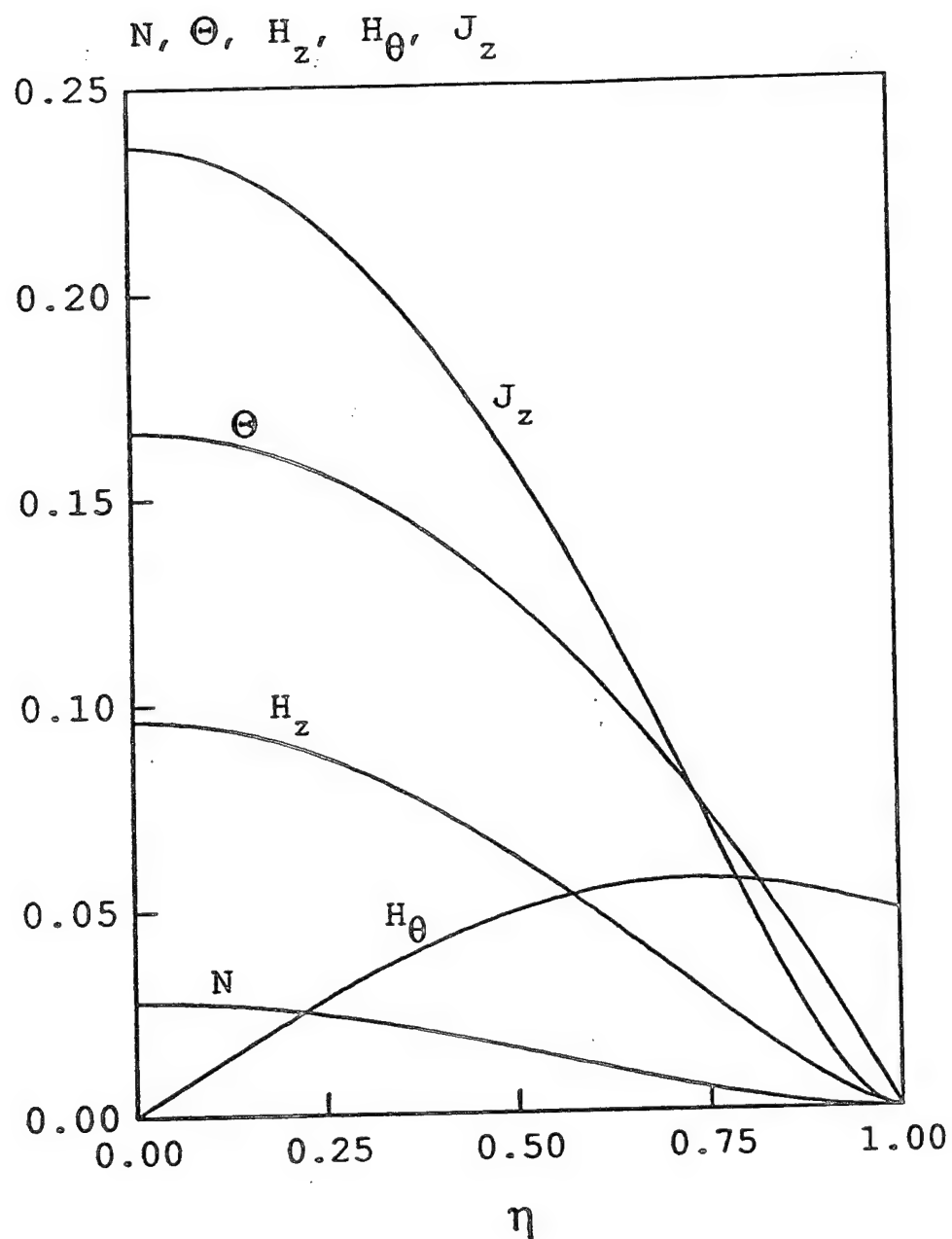


Fig. 4. (Continues) (a) Self-similar profiles of density, temperature, magnetic field and current density for a Z-pinch with bremsstrahlung radiative energy losses. (b) Same for line radiative losses.

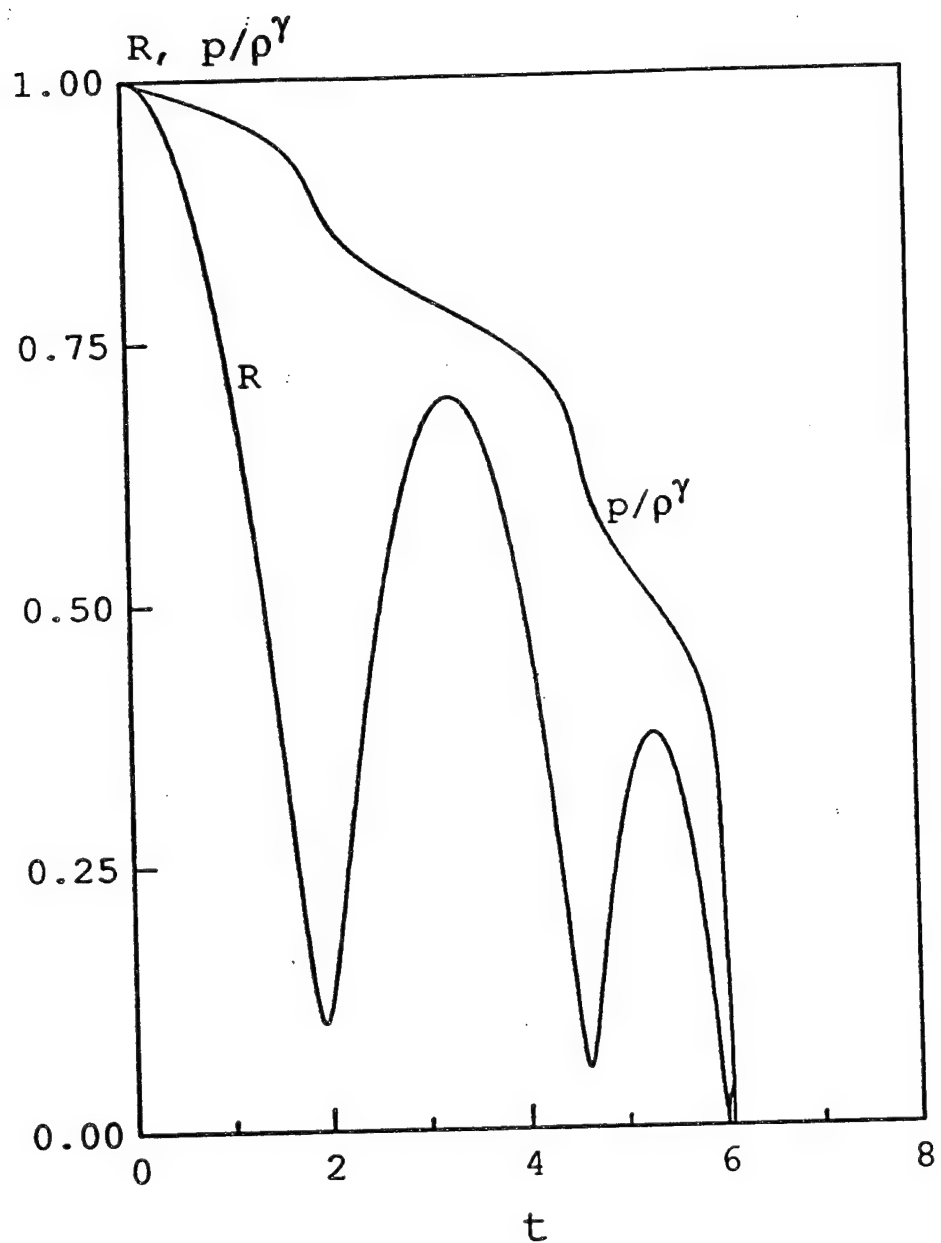


Fig. 5. Time history of Z-pinch radius R and the ratio p/ρ^γ (both normalized to their values at $t=0$, time expressed in units of t_0) without rotation and/or axial magnetic field.

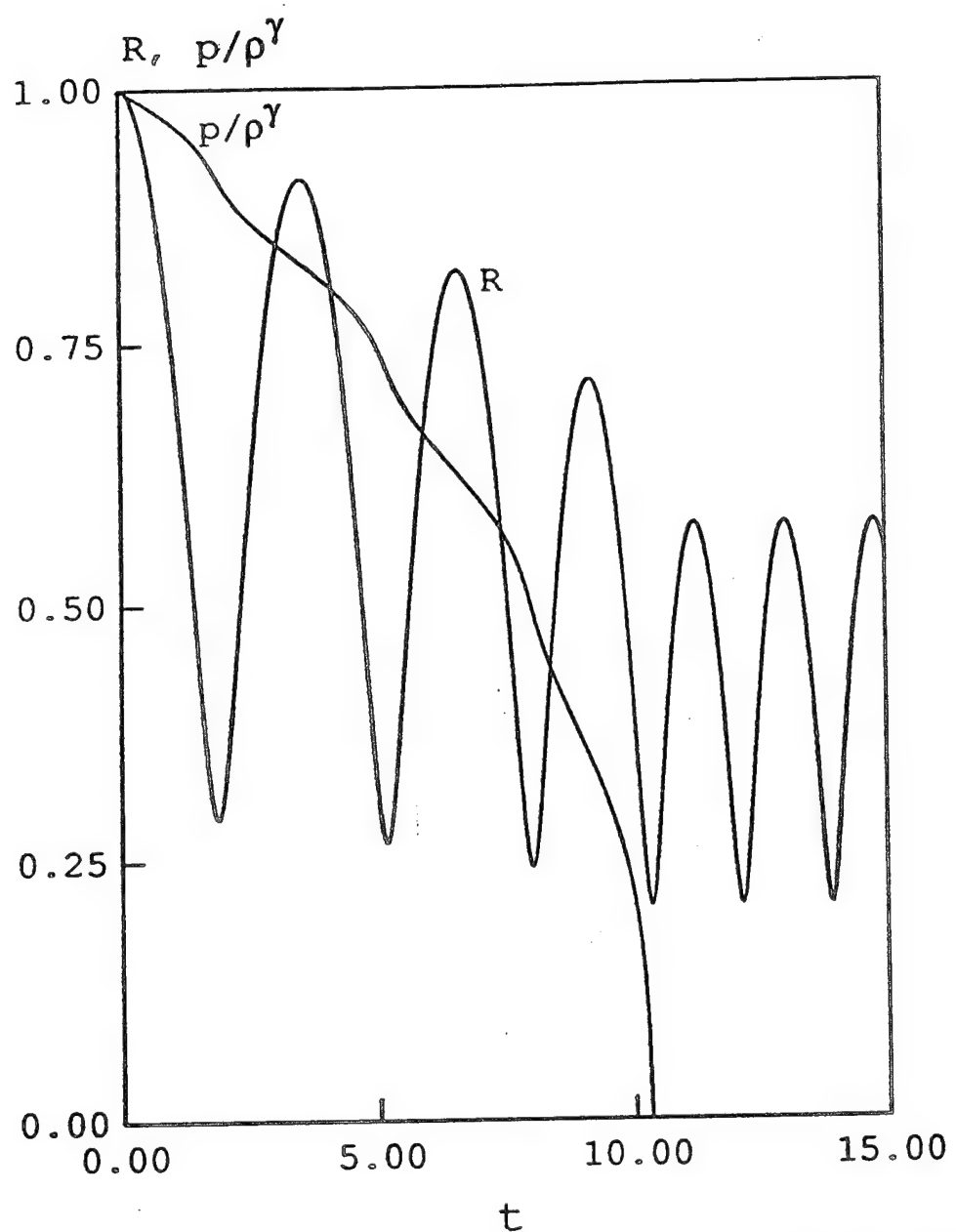


Fig. 6. Same as in Fig. 5 in the presence of rotation and/or axial magnetic field.

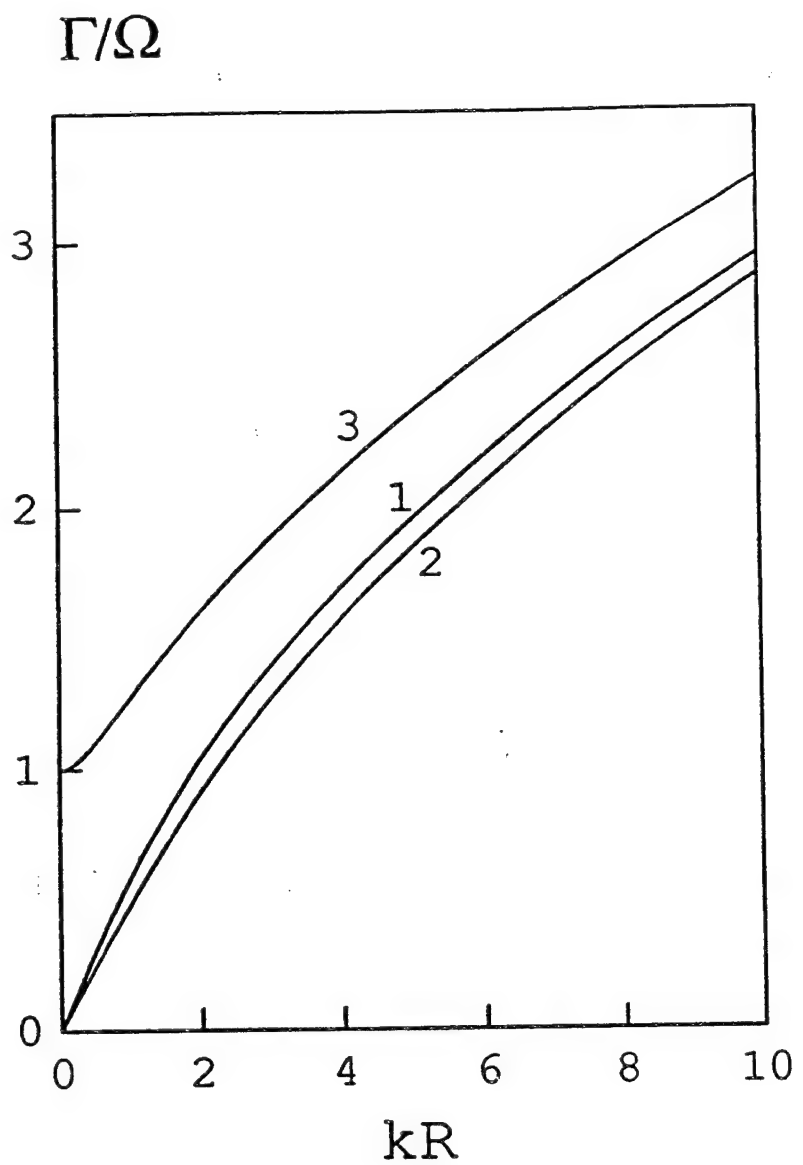


Fig. 7. Growth rate Γ expressed in units of angular velocity Ω versus kR : 1, numerical solution of Eq. (39); 2 - classical RT growth rate (41).

VII. DIAGNOSING MID-ATOMIC NUMBER Z-PINCH PLASMAS USING F- AND NE-LIKE RESONANCE AND SATELLITE LINE RATIOS IN THE L-SHELL

A. Introduction

X-ray emission spectra from the K-shell provide valuable information with which to assess plasma conditions and X-ray emission performance in Z-pinch plasmas. These soft X-ray lines are routinely used to diagnose K-ions¹⁻⁴ for both laboratory and astrophysical plasmas. Since ratios involving H and He lines are so useful in obtaining diagnostics in low-Z pinches, ratios of lines for F and Ne-like systems should provide useful X-ray diagnostics for higher atomic number(Z) Z-pinch plasmas. Since the L-shell ions are many electron systems, their X-ray spectra are rich in structure due to a large number of resonance and satellite lines, many of which overlap with one another. Identification of these lines for diagnostic calculations pose challenges that can be addressed and hence diagnostics research involving L-shell ions, while not as extensive as that involving K-shell ions, offers potentially more rewards. Efforts have already been underway for the L-shell diagnostics of Ne-like⁵⁻⁸ ions due to its closed shell configuration for the ground state.

The intensity ratios of Ne- and F-like emission lines are sensitive to electron temperature, density, and rates of ionization and different line ratios need to be used to infer these different plasma parameters. The intensity ratios of two allowed lines of the same ion generally cannot be used to infer the plasma temperature. In addition, the density of a plasma can only be inferred from the ratios of two lines in different ions when they have different density sensitivities. This is more true in the L-shell than in the K-shell. The different excitation mechanisms and multiplet structures of the lines imply different dependences on the plasma parameters.^{9,10} The line ratios of resonance to dielectronic satellite lines is another very good temperature diagnostic tool since the resonance lines are populated mainly by direct collisional excitation whereas dielectronic recombination (DR) is the dominant process that excites the satellite lines. The intensity ratios of two resonance lines or satellite lines from neighboring ions is a good source for inferring the state of ionization stages of the plasma. Thus the ratio of two collisionally excited lines or line clusters from neighboring ion stages can generate a temperature-dependent expression for the relative ion fractions. The intensity ratios of the resonance lines of two neighboring ions is also density sensitive. We will investigate the various line ratios as diagnostic tools in both time-independent, collisional-radiative equilibrium (CRE) and transient plasmas.

In Z-pinch plasmas the principal excited levels are populated by electron impact excitation from the ground state, and depopulated by radiative decay. When these processes are much faster than any characteristic changes in the plasma, steady state equations can adequately describe

the plasmas. For mid-Z plasmas that can be made to radiate in the K-shell however, ionization and recombination relaxation times in the L-shell may be longer than the plasma hydrodynamic times and time-dependent or transient equations must be used for ionization calculations. But, in order to infer plasma characteristics using time dependent calculations and then compare them to experimental observations one will require time resolved spectra that are some times not available. Satellites of multiply charged ion resonance lines in time integrated spectra might however be used as reliable ionization gauges provided these line ratios can be calculated using detailed and accurate time dependent calculations. If future experimental endeavors are geared towards generating spectrally informative, spatially and time resolved data, then it will need to be analyzed in accordance with accurate theoretical predictions.

This present diagnostic work involves the strong resonance and satellite lines of transitions from the $n=3$ levels of F- and Ne-like selenium. The $n=3$ F-like and Ne-like states of selenium are non-statistically distributed in the density region of diagnostic interest, $10^{19} \leq n_i \leq 10^{22}$, and this provides the basis for plasma diagnostics using line emissions from these states. Figures 1(a) and (b) show the L-shell spectrum of selenium and krypton under low spectral resolution so that the satellite structures are not resolved. Since the Ne-like ground state has a closed basic shell structure and the ground state configuration $2s^2 2p^6$ has only one level 1S_0 , the short-wavelength spectrum is simple having only seven allowed resonance transitions and these lines along with their satellites can be reliably identified and detected provided experimental observations are carried out with high spectral resolutions. A high resolution X-ray spectrum for a mid-Z Ne-like ion is shown in Fig. 1(c).

For F-like ions, on the other hand, the spectrum is quite complicated. There are 34 allowed transitions of the $2p^5-2p^4 3d$ type alone between the $2p-3d$ and $2s-3p$ Ne-like lines. For reliable diagnostic work using individual lines, it is important that these resonance lines be isolated and properly identified as individual lines. The satellites of these F-like $2p-3d$ and $2p-3s$ resonance lines have a very large number of lines whose individual detection with absolute certainty will be difficult even with extreme high experimental spectral resolution. Thus for the F-like resonance lines, we consider the sum of overlapping lines originating from the same configuration as one single line cluster. For example, all the lines for the $2p-3s$ resonance transitions are summed up and is treated as a single transition and the same treatment is followed for $2p-3d$ and $2s-3p$ transitions. We do the same lumping when we consider the Ne-like satellites to these F-like resonance lines. These $2p-3d$ and $2p-3s$ line clusters for F-like and Ne-like selenium are non-overlapping and distinct and therefore the intensity ratios involving these lines as references are reliable for plasma diagnostics. We analyze the individual fine-structure lines of the Ne-like spectra in order to obtain an accurate sum. When we calculate the intensity ratios of F-like to Ne-like resonance lines, we do the same

lumping for the Ne-like lines by summing those individual ones.

B. Atomic Model

We have developed a prototype atomic model specifically for the fluorine and neon ionization stages that is necessary for analyzing highly resolved X-ray line emission from these ionization stages. This model can be used in the analysis of wire implosions if selenium is coated on as a diagnostic element or it can be used in the analysis of gas puff implosion if krypton is used as an impurity element. The energy level diagram of our model is shown in Fig. 2. The Ne-like model consisted of 31 states including the ground level, 26 $n=3$ fine-structure levels of the $2p^53s$, $2p^53p$, and $2p^53d$ configurations, 3 lumped inner-shell excited configurations of $2s2p^63s$, $2s2p^63p$, and $2s2p^63d$ and a lumped $n=4$ level.¹¹ We have updated our F-like ionization stage by including the fine-structure levels for the $n=3$ singly excited states. Thus the F-like stage contains a lumped ground state, the $\Delta n=0$ excited state, 57 fine-structure levels of the $2p^43s$, $2p^43p$, and $2p^43d$ configurations, 3 lumped inner-shell excited configurations of $2s2p^53s$, $2s2p^43p$, and $2s2p^43d$ and two lumped $n=4$ states. For the Na-like $n=3$ excited states, all fine structure levels of the $2p^63l$ as well as doubly excited $2p^53l3l'$ and $2s2p^63l3l'$ states are included. We have also considered all fine-structure levels of the double excited $2p^43l3l'$ and $2s2p^53l3l'$ levels of the Ne-like states for the calculation of satellite lines formation. The fluorine-like and neon-like models are embedded in a detailed configuration accounting (DCA) atomic model of selenium from which the ionization balance is calculated.¹² The $n=3$ singly excited states for both F- and Ne-like ions are fully coupled to the ground states and among themselves.

The following line formation mechanisms are considered in our calculations. For the resonance lines the most dominant contributions come from direct electron-impact excitation from the ground state. We have included direct collisional excitations, deexcitations and radiative decay from or to the ground states, among the $n=3$ excited states and cascades from the $n=4$ states of Se^{25+} and Se^{24+} . In this calculation we have also included resonance excitation to the $n=3$ excited states of Ne-like selenium. Collisional ionization from the $n=3$ states of both F- and Ne-like ionization stages are included in this work. The excited states are substantially populated by DR and we have included a detailed state specific contribution of DR for recombination from the ground and $\Delta n=0$ states of Se^{26+} and Se^{25+} to the $n=3$ singly excited states of Se^{25+} and Se^{24+} respectively. The contributions from the DR satellites due to high Rydberg levels that are unresolved from the resonance lines have important consequences¹³ and they must be taken into account in order to compare the line ratios with experiments. Previous diagnostic models were unable to predict accurately because they lacked these necessary theoretical considerations in their calculations and experimental refinements.¹⁴⁻¹⁷

Satellite lines are formed on the long wavelength sides of the resonance lines if the spectator electron is in the $n=3$ states of the doubly excited states that are formed due to the DR process. As mentioned before, for the $n \geq 4$ states, the satellite lines formed are often blended with the resonance lines. For the formation of the Ne- and Na-like satellite lines we have included the results of detailed calculations of DR from the ground states of Se^{25+} and Se^{24+} states to the $3l3l'$ doubly excited states of each ion. These satellite lines can also be formed due to an alternative mechanism of direct inner-shell excitation (ISE) of an electron of the ground or the $\Delta n=0$ state of the ion. We have included the contribution of ISE for the formation of Na-like satellite lines. The sodium-like and neon-like ground states are independent source terms and thus the populations of the upper levels for the satellite lines due to DR from the ground state and ISE from the Na-like states are added as separate contributions.

The atomic data for this calculation was either calculated or obtained from very detailed and sophisticated atomic codes. The atomic structure data such as the energies, oscillator strengths and the radiative rates for all the 64 F-like levels were calculated from the atomic code developed at Penn State University by H. L. Zhang and D. H. Sampson. Electron-impact collision strengths for excitation from the ground to all the excited states and the collisional coupling among all the excited F-like levels are calculated by using the relativistic distorted wave code (DFW) of Sampson *et al.*¹⁸ and the electron impact ionization cross sections for ionization from the ground as well as as excited F-like states were also calculated from the ionization DFW codes. DR rates for recombination from O- to F-like states were calculated by us¹⁹ using Cowan's code.²⁰ For Ne-like selenium collision strengths for excitation from the ground state were obtained from Zhang *et al.*²¹ and the collisional couplings among the $n=3$ levels were obtained from Hagelstein and Jung.²² The collisional ionization cross sections from the $n=3$ Ne-like levels were obtained from Golden *et al.*²³ and Moores *et al.*²⁴ The DR data for recombination from F- to Ne-like levels were calculated by us.¹¹ The excitation and ionization rate coefficients were obtained by numerically integrating the collision strengths or cross sections over a Maxwellian distribution.

The power emitted per unit volume for the F-like or Ne-like resonance lines are given by:

$$P_R = \sum_j N_{j(F/Ne)}^* (A_r(j \rightarrow i) E_{ji} + N_e \alpha_d)$$

and the power emitted per unit volume in a Ne-like or Na-like satellite line is:

$$P_S = N_e [N_{F/Ne} C_d + N_{Ne/Na} C_e] \frac{A_r}{A_o + A_r} E_{ji}$$

where α_d is the additional contribution due to unresolved satellite lines emission and the power emitted for the Ne-like satellite lines do not include the contributions due to ISE in this present

calculation. N_i and N_i^* are densities of the ground and excited states of the ions and N_e is the electron density, C_E and C_{DR} are the excitation and DR rate coefficients, $A(j \rightarrow i)$ is the radiative decay rate from level j to level i and E_{ji} is the energy for this transition. The population densities of the excited states that are analyzed for both CRE and time dependent calculations and the time histories of electron and ion temperatures are imported into our analysis from the coupled rate equation calculations.

C. Results

In this present diagnostic calculations we considered the $2p-3s$, $2p-3d$, and $2s-3p$ resonance clusters and their satellites for both F-like and Ne-like selenium. The fine-structure lines investigated for Ne-like selenium are identified in Table 1. To test the ionization calculation, a prototypical case of rapid heating and cooling was investigated. The time histories of the electron and ion temperatures are shown in Fig. 3. The rapid time variation of the electron temperatures will affect the ionization stages of selenium and alter the strengths of recombination vs excitation and ionization. In fact, when the plasmas burn through the L-shell to the K-shell quite rapidly, this will have significant effects on the line ratios. Figure 4 shows the time variation of the three F-to Ne-like resonance line ratios for the electron density of $5.95 \times 10^{20} \text{ cm}^{-3}$. The temperature sensitivity of the F to Ne resonance line ratios for two different densities are shown in Figs. 5 and 6. As can be seen from these two graphs, the intensity ratio of the $2p-3s$ resonance line is insensitive to temperature variations for electron temperatures $T_e > 400 \text{ eV}$ and thus is not a good tool for temperature diagnostic. The density dependences of the F to Ne resonance line ratios can be seen in Figs. 7 and 8. The density sensitivities of ratios of resonance lines for both F-like and Ne-like selenium is shown in Fig. 9. In the experimental observations of X-ray resonance lines from Ne-like bromine,⁷ the line ratios were found to be density sensitive. At low densities the majority of the excited populations are in the $2p^5 3s$ and $2p^5 3p$ states and most of the intensity in the $2p-3s$ resonance lines come from cascade to the $3s$ states from the higher excited states. As the density increases, some of the higher excited metastable states depopulate by collisional deexcitation to lower lying excited states. This causes the $2p-3s/2s-3p$ resonance line ratio to be density dependent. This density dependency due to depopulation of metastable excited states for the line ratios of $2p-3d/2s-3p$ and $2p-3s/2s-3p$ for both F-like and Ne-like selenium can be seen from Fig. 9.

The line ratios of satellite to the resonance lines for both F-like cluster lines and Ne-like fine structure lines provide extremely good temperature diagnostics. Figures. 10 and 11 show these line ratios for F-like and Ne-like selenium for an electron density of 10^{19} cm^{-3} . As can be seen from Fig. 11, the contribution to the intensity of the satellite lines due to ISE is significant for some

strong lines compared to some others. The effect of ISE on the formation of the satellite lines and hence on the line ratios become more important with the increase of plasma heating. This can be seen from Fig. 12 where we show these line ratios for a transient calculation. The ratio of the satellite lines whose upper levels are formed including both DR and ISE, to the resonance lines for Ne-like selenium depend strongly on the ratio of Ne-like to Na-like ion populations. Thus as the plasma burns through the ionization stages, the depletion of Na-like selenium ions compared to that of the Ne-like ions will have important consequences on the line ratios and hence on the diagnostics of plasma parameters. The ratio of the sum of the satellites ($n>3$) and that of the sum of the same satellite to resonance lines can be used to obtain a fractional population abundance ratio of two ionization stages in selenium. The maximum plasma electron temperature can be determined from the dielectric component of a satellite to the excitation component of a resonance line for both F-like and Ne-like selenium in time dependent calculations. The time variation of the ratios of satellite to resonance lines for Ne-like selenium is much more significant than those for F-like selenium. For the F-like calculations we consider the clusters of lines as a single line and we also do not include any contributions of ISE of the Ne-like states to the intensity calculations for the satellite lines and the for some cases the contributions of ISE increase the line ratios by orders of magnitude.

D. Summary

We have considered a Maxwellian electron distribution for this present calculations. However, it is possible that intense heating will generate non-Maxwellian distributions which are predicted to have non-negligible effects on the line ratios and hence on the diagnostics of these strongly heated plasmas.^{1,25,26} To complete these calculations, we will include the effects of non-Maxwellian distributions in the future.

It is apparent that in future high-current driven Z-pinch experiments involving medium to high Z plasmas, rapid "burn through" the L-shell is required. Thus an accurate and detailed analysis of the line emission in the L-shell spectra of these plasmas will be extremely relevant for a correct understanding of the dynamics of medium to high Z material pinches that are composed of different charged states. These diagnostic studies for densities achieved well above 10^{19} , where excited states are collisionally coupled, it is essential to have an atomic model, such as ours, that includes all the dominant atomic processes to all the important excited levels and a detailed level accounting cannot be simplified by an averaging process such as used in the average atom model, which will inhibit all the important and relevant atomic dynamics. This point is emphasized by Fig. 13 which illustrates graphically how structurally different the $n=3$ states of F- and Ne-like ions are. This present study will also help us to predict how long the plasma remains in the L-shell and how

fast will the plasma ionize and burn through the K-shell states. We can conclude that the analysis presented here can predict the energy absorbed per unit mass of the plasma and the amount of mass participation in the L-shell plasma. Such mass inferences provide a good indication of the quality of implosion and of the X-ray production in Z-pinch experiments.²

References

1. J. P. Matte, J. C. Keifer, S. Ethier, M. Chaker, and O. Peyrusse, Phys. Rev. Lett. **72**, 1208 (1994).
2. M. C. Coulter, K. G. Whitney, and J. W. Thornhill, J. Quan. Spectro. Radiat. Transf. **44**, 443 (1990).
3. V. A. Boiko, S. A. Pikuz, and A. Ya. Faenov, J. Phys. B **12**, 1889 (1979).
4. A. Zigler et. al., Phys. Rev. A **45**, 1569 (1992).
5. W. H. Goldstein, R. S. Walling, J. Bailey, M. H. Chen, R. Fortner, M. Klapisch, T. Phillips, and R. E. Stewart, Phys. Rev. Lett. **58**, 2300 (1987).
6. S. Ya. Khakhalin, B. A. Bryunetkin, I. YU. Skobelev, A. Ya. Faenov, J. Nilsen, A. L. Osterheld, and S. A. Pikuz, JETP **78**, 633 (1994).
7. J. Bailey, R. E. Stewart, J. D. Kilkenny, R. S. Walling, T. Phillips, R. J. Fprtnner, and R. W. Lee, J. Phys. B **19**, 2639 (1986).
8. D. A. Liedahl, S. M. Khan, A. L. Osterheld, W. H. Goldstein, in *High Resolution X-Ray Spectroscopy of Cosmic Plasmas*, edited by P. Georenstein and M. Zombeck (Cambridge: Cambridge Univ. Press 1990) IAU Colloq. **115**, p. 49.
9. A. H. Gabriel, Mon. Not. R. Aston. Soc. **160**, 99 (1972).
10. A. H. Gabriel and T. M. Paget, J. Phys. B **5**, 673 (1972).
11. A. Dasgupta and K. G. Whitney, Phys. Rev. A **42**, 2640 (1990).
12. K. G. Whitney and M. C. Coulter, IEEE Trans. on Plasma Sci. **16**, 552 (1988).
13. J. C. Raymond and B. W. Smith, Astrophys. J. **306**, 762 (1986).
14. E. V. Aglitski, V. A. Bioko, O. N. Krokhin et al., Kvant. Elektron. **1**, 2067 (1974).
15. V. A. Boiko, A. Ya. Faenov, and S. A. Pikuz, J. Quant. Spectr. Radiat. Transf. **19**, 11 (1978)
16. P. G. Burkhalter and D. J. Nagel, Phys. Rev. A **11**, 782 (1985).
17. J. F. Seely, T. W. Phillips, R. S Walling et al., Phys. Rev. A **34**, 2942 (1986).
18. D. H. Sampson, H. L. Zhang, and C. J. Fontes, At. Data Nucl. Data Tables **48**, 25 (1991).

19. A. Dasgupta and K. G. Whitney, At. Data Nucl. Data Tables **58**, 77 (1994).
20. Atomic structure code of R. D. Cowan following his book *The Theory of Atomic Structure and Spectra* (University of California Press, Berkeley, CA, 1981).
21. H. L. Zhang, D. H. Sampson, R. H. Clark, and J. B. Mann, At. Data Nucl. Data Tables **37**, 17 (1987).
22. P. Hagelstein and R. K. Jung, At. Data Nucl. Data Tables **37**, 121 (1987).
23. L. B. Golden, D. H. Sampson, and K. Omidvar, J. Phys. B **11**, 3235 (1978).
24. D. L. Moores, L. B. Golden, and D. H. Sampson, J. Phys. B **13**, 385 (1980).
25. R. Bartiromo, F. Bombarda, and R. Giannella, Phys. Rev. A **32**, 531 (1985).
26. A. H. Gabriel and K. J. H. Phillips, Mon. Not. R. Astr. Soc. **189**, 319 (1979).

TABLE 1. IDENTIFICATION OF NE-LIKE LINES AND RATIOS

	Transitions	Energy(eV)
R_1	$[2p_{3/2}3d_{5/2}]_1 \rightarrow ^1S_0$	1574.9
R_2	$[2p_{3/2}3d_{3/2}]_1 \rightarrow ^1S_0$	1613.5
S_1	$[2p_{3/2}3d_{5/2}3d_{5/2}]_{7/2} \rightarrow [3d_{5/2}]$	1557.94
S_2	$[2p_{3/2}3d_{3/2}3d_{5/2}]_{5/2} \rightarrow [3d_{5/2}]$	1562.17
S_3	$[2p_{1/2}3d_{5/2}3d_{5/2}]_{5/2} \rightarrow [3d_{5/2}]$	1598.96
S_4	$[2p_{1/2}3d_{3/2}3d_{5/2}]_{7/2} \rightarrow [3d_{5/2}]$	1600.20
S_5	$[2p_{1/2}3d_{3/2}3d_{3/2}]_{3/2} \rightarrow [3d_{3/2}]$	1602.39

S_1 and S_2 are satellites to R_1

S_3, S_4 and S_5 are satellites to R_2

We will use the designations A and B for ratios of power emitted by S_1 and S_2 to R_1 respectively and C, D and E for the same ratios for lines S_3, S_4 and S_5 to R_2 respectively.

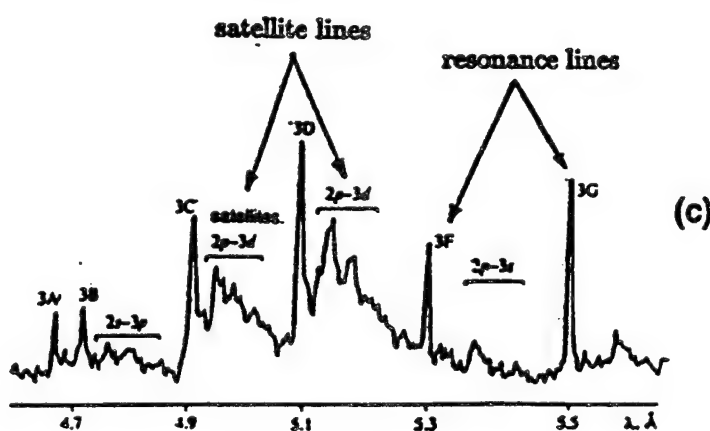
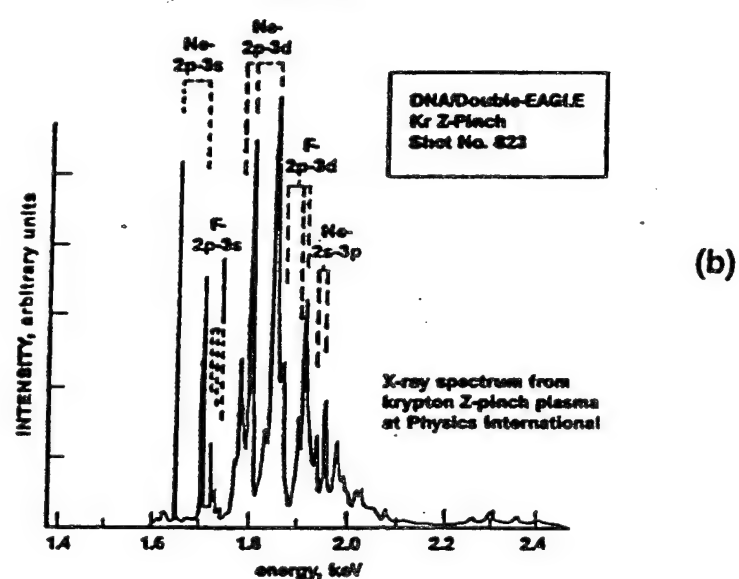
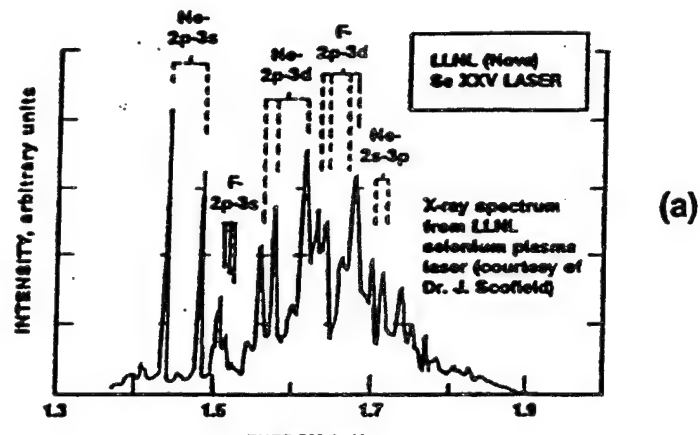


Fig. 1

PRESENT MODEL

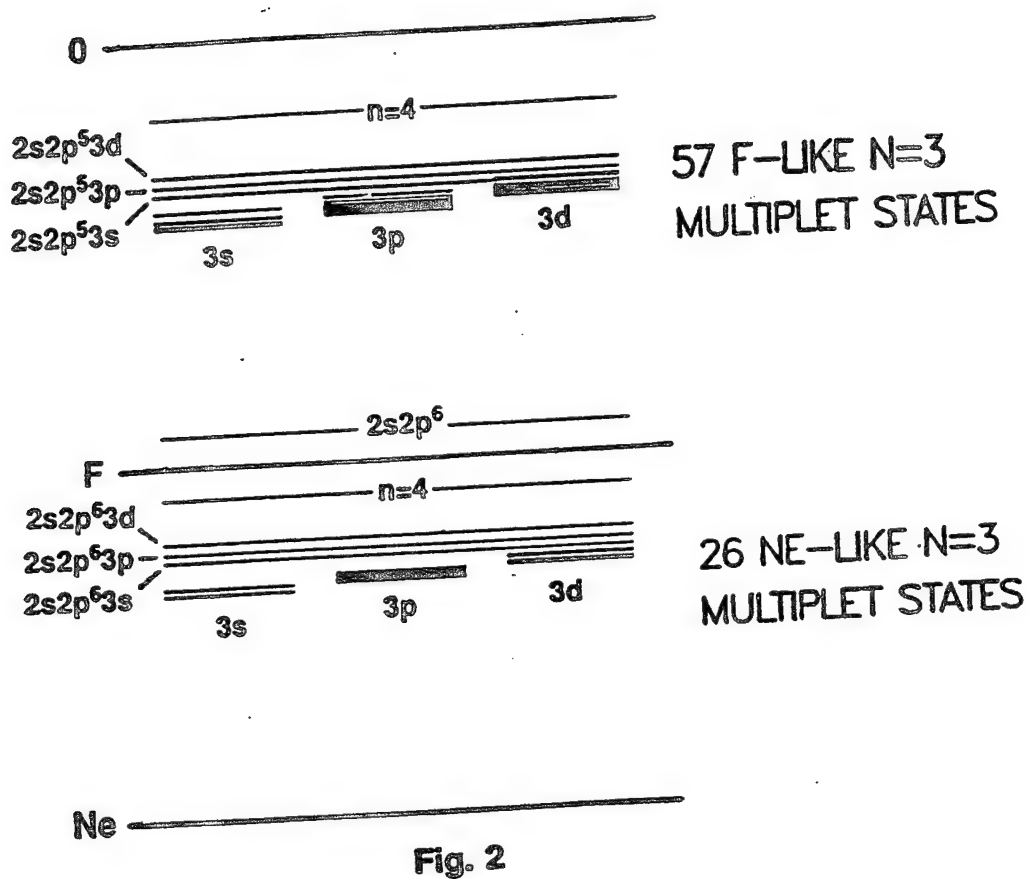


Fig. 2

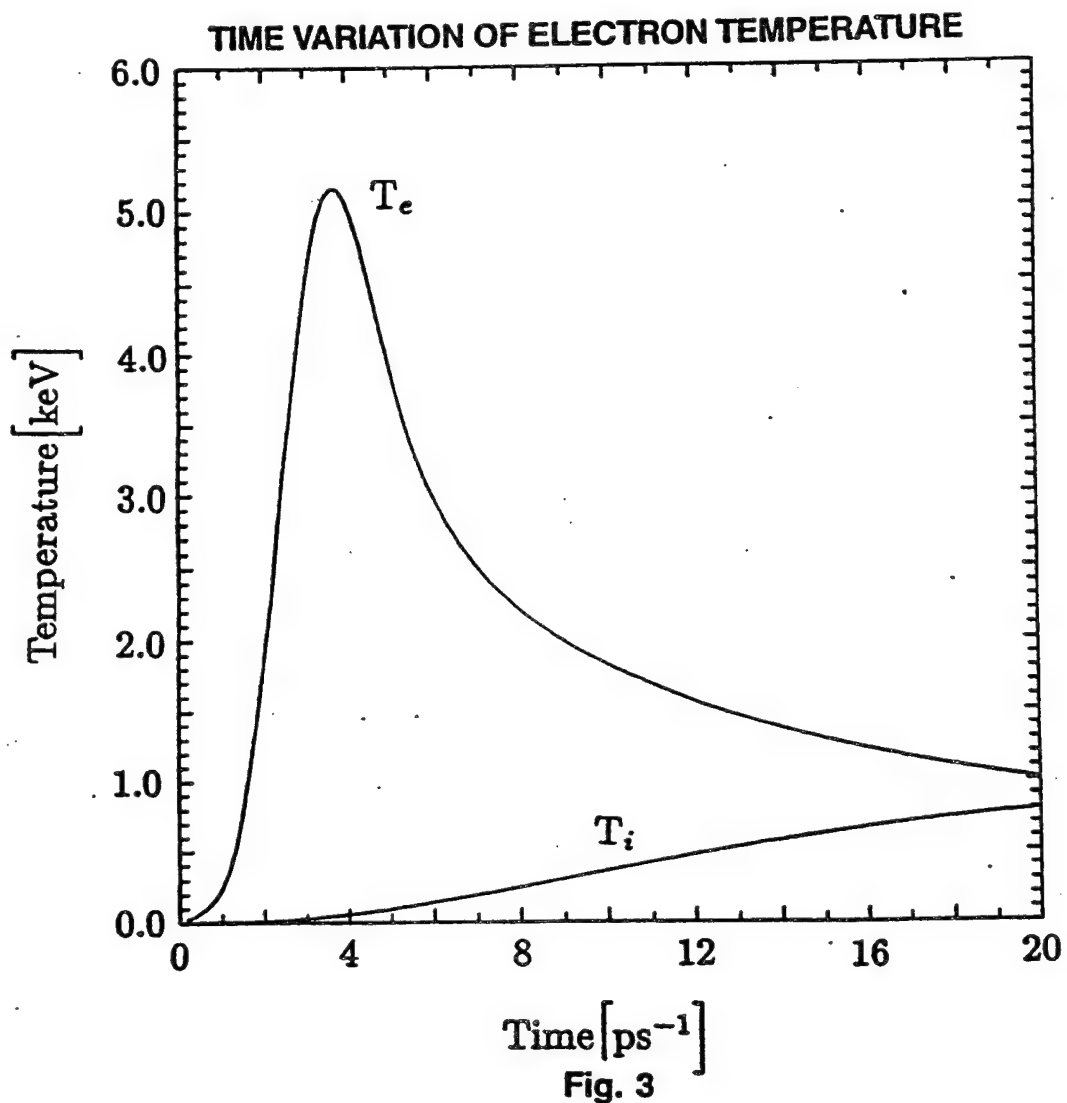


Fig. 3

F TO NE RESONANCE LINE RATIO

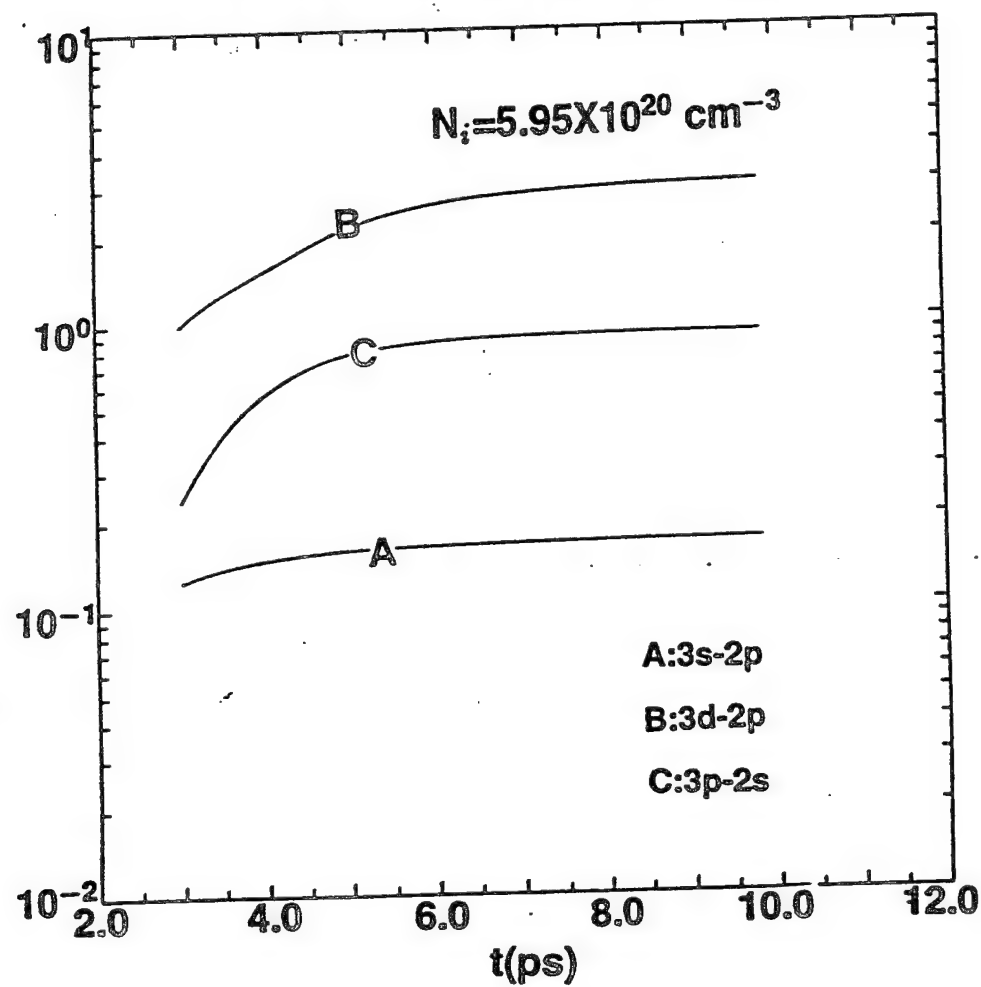


Fig. 4

F TO NE RESONANCE LINE RATIOS

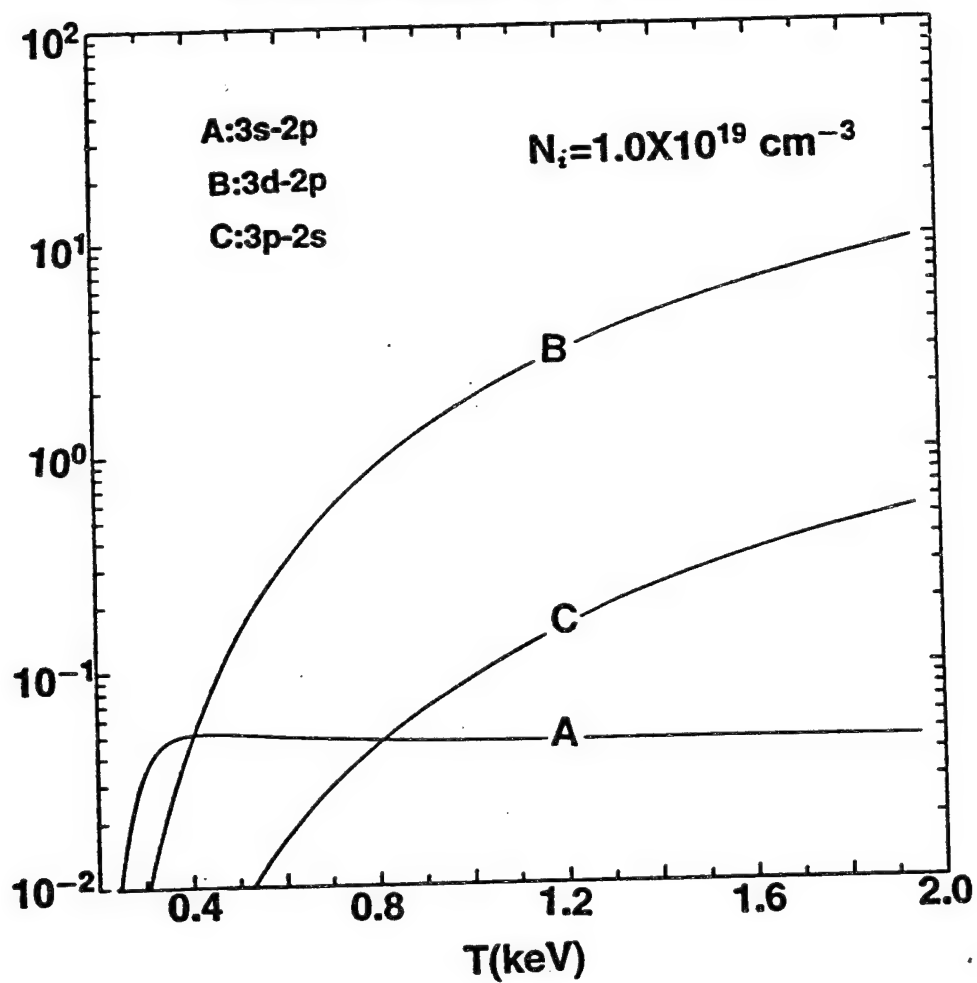


Fig. 5

F TO NE RESONANCE LINE RATIOS

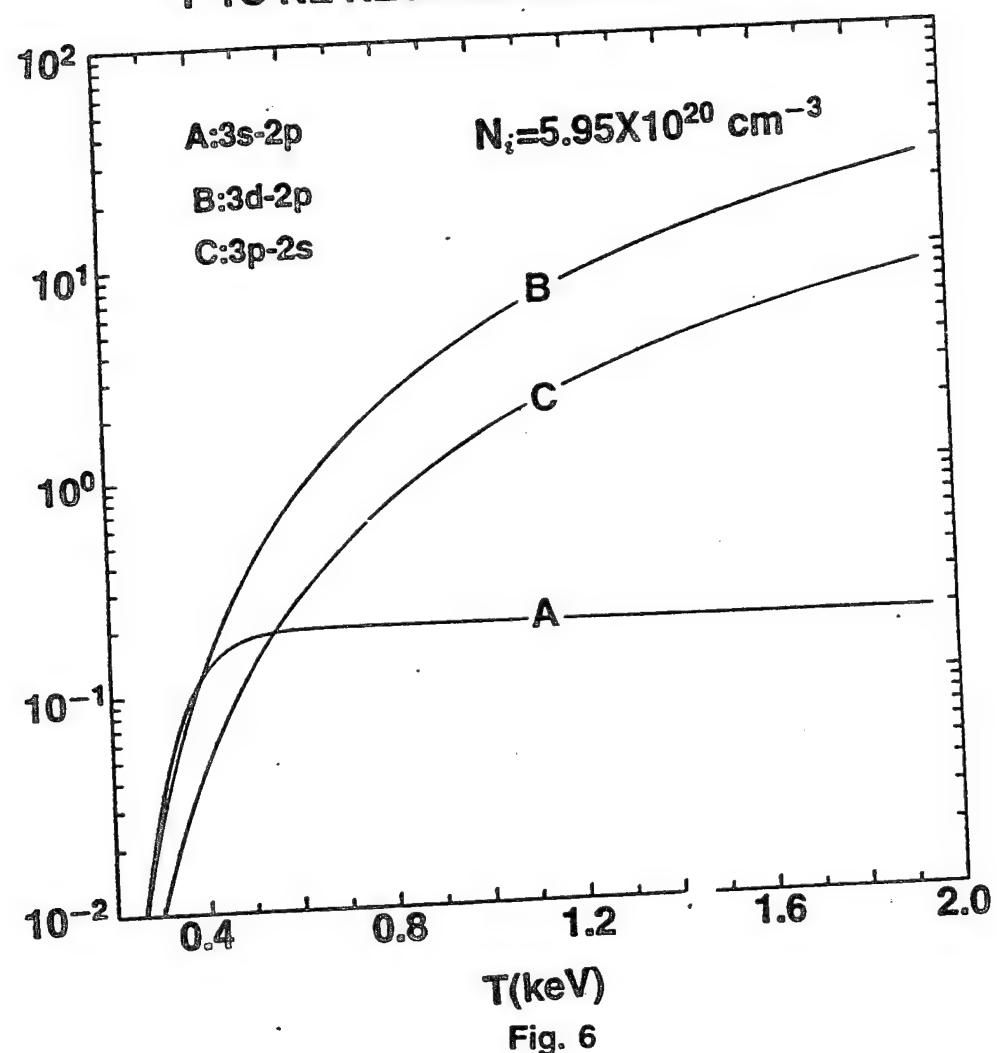


Fig. 6

F TO NE RESONANCE LINE RATIOS

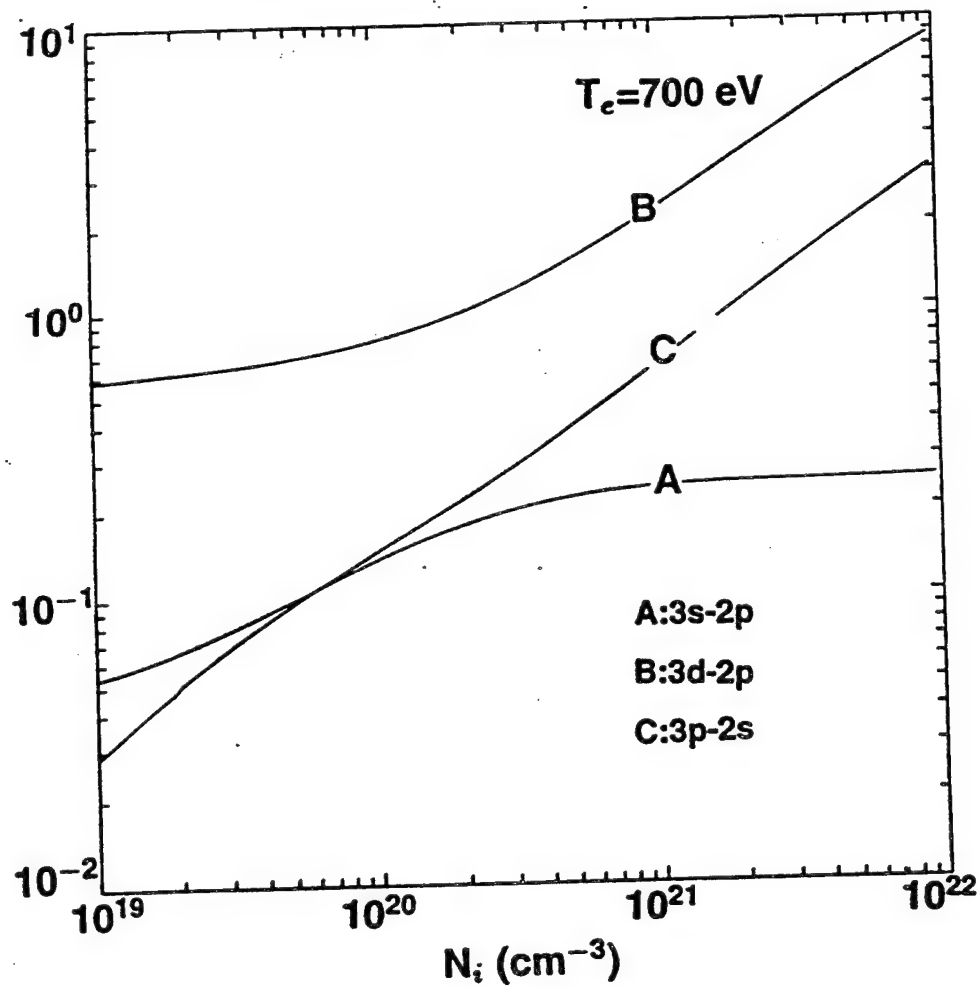


Fig. 7

F TO NE RESONANCE LINE RATIOS

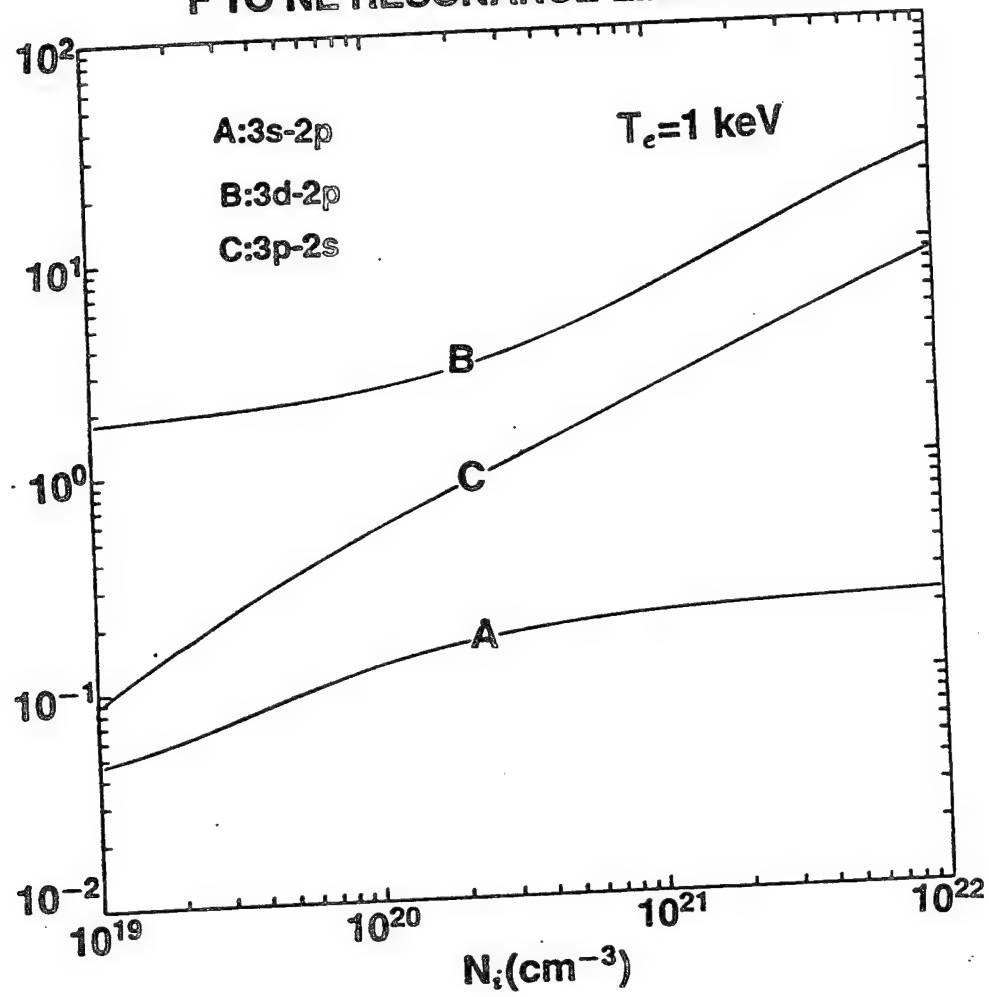


Fig. 8

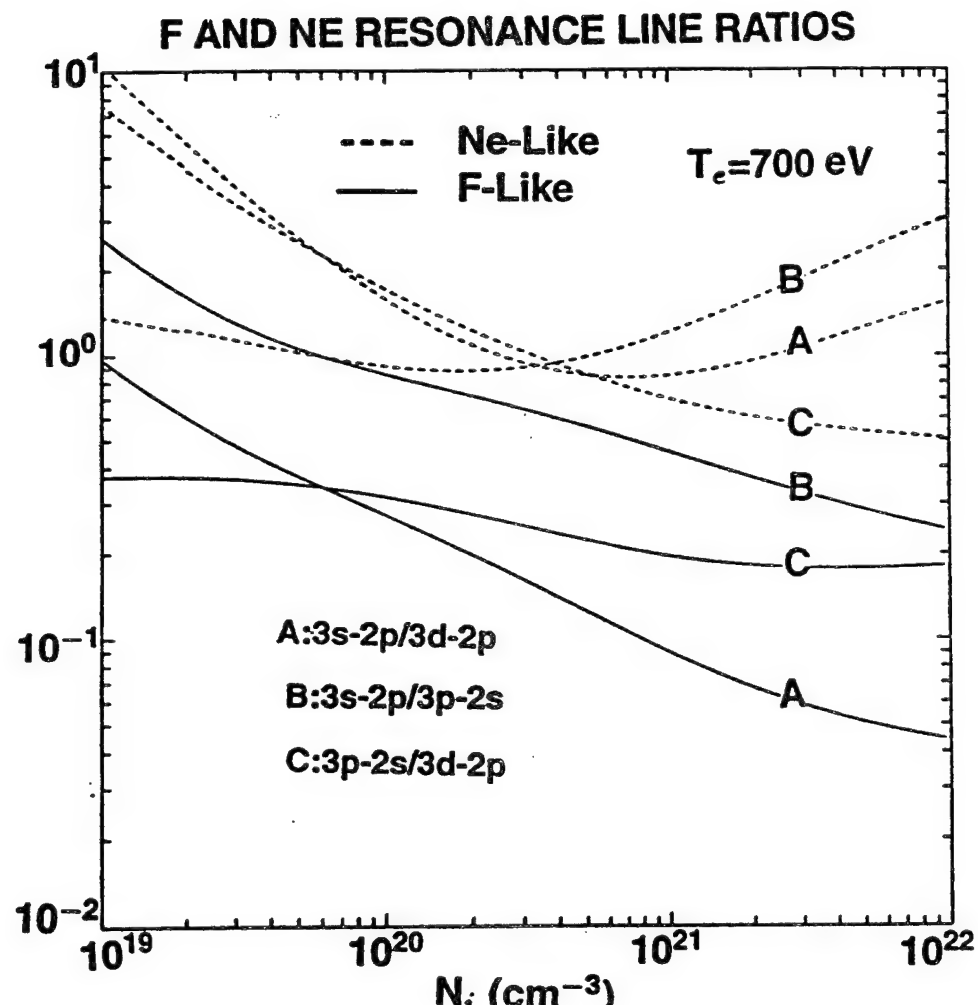


Fig. 9

F SATELLITES TO RESONANCE LINE RATIOS

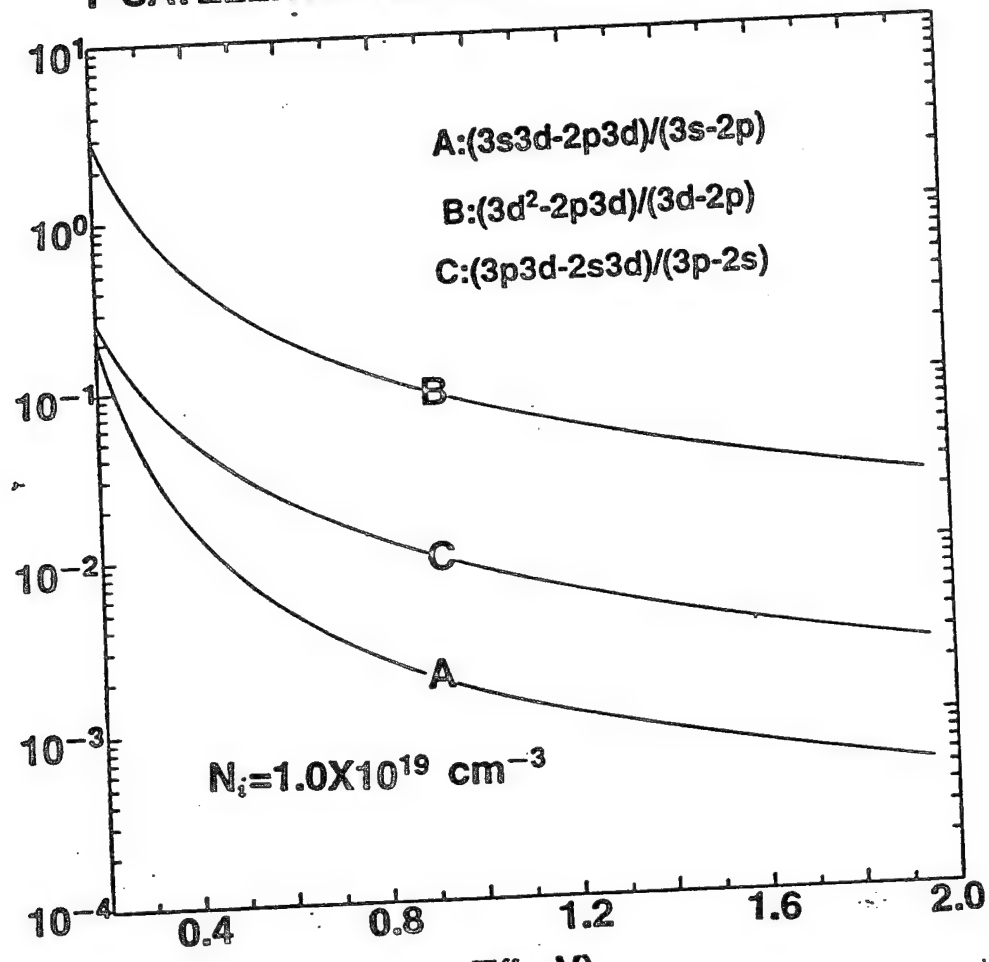


Fig. 10

NE SATELLITES TO RESONANCE LINE RATIOS

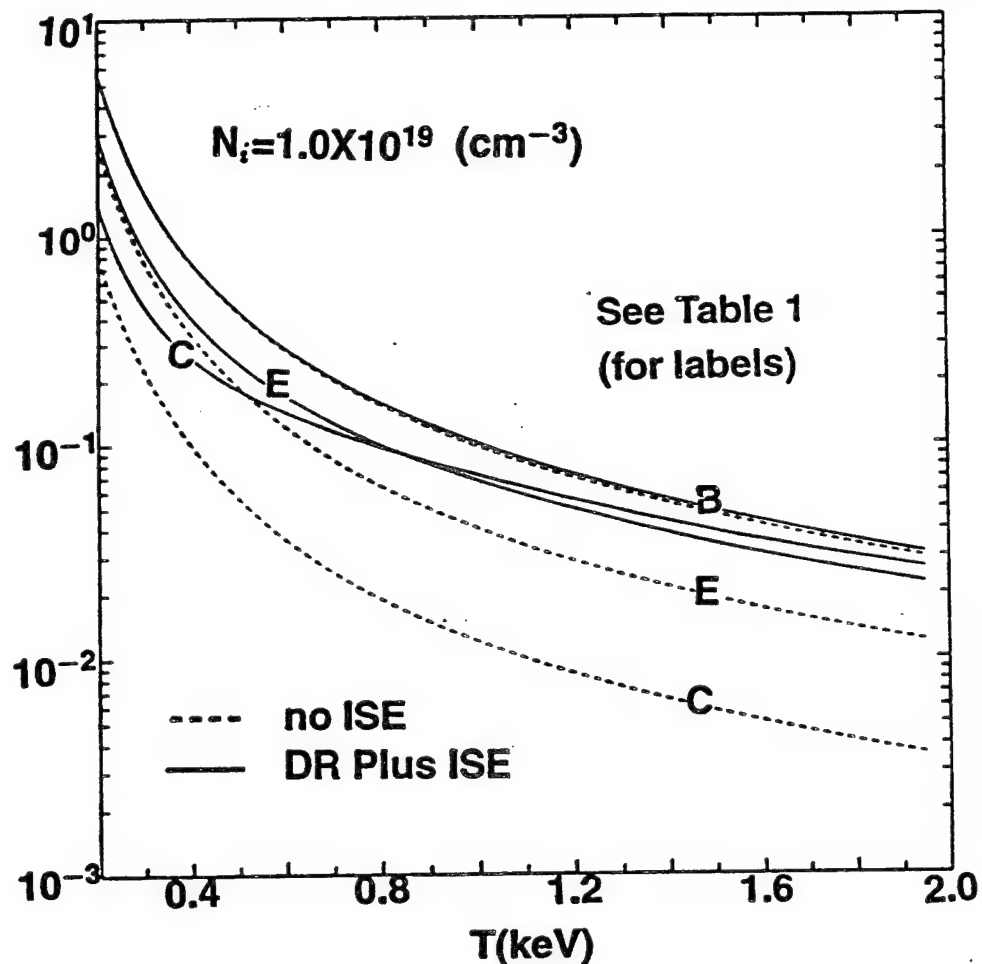


Fig. 11.

NE SATELLITES TO RESONANCE LINE RATIOS

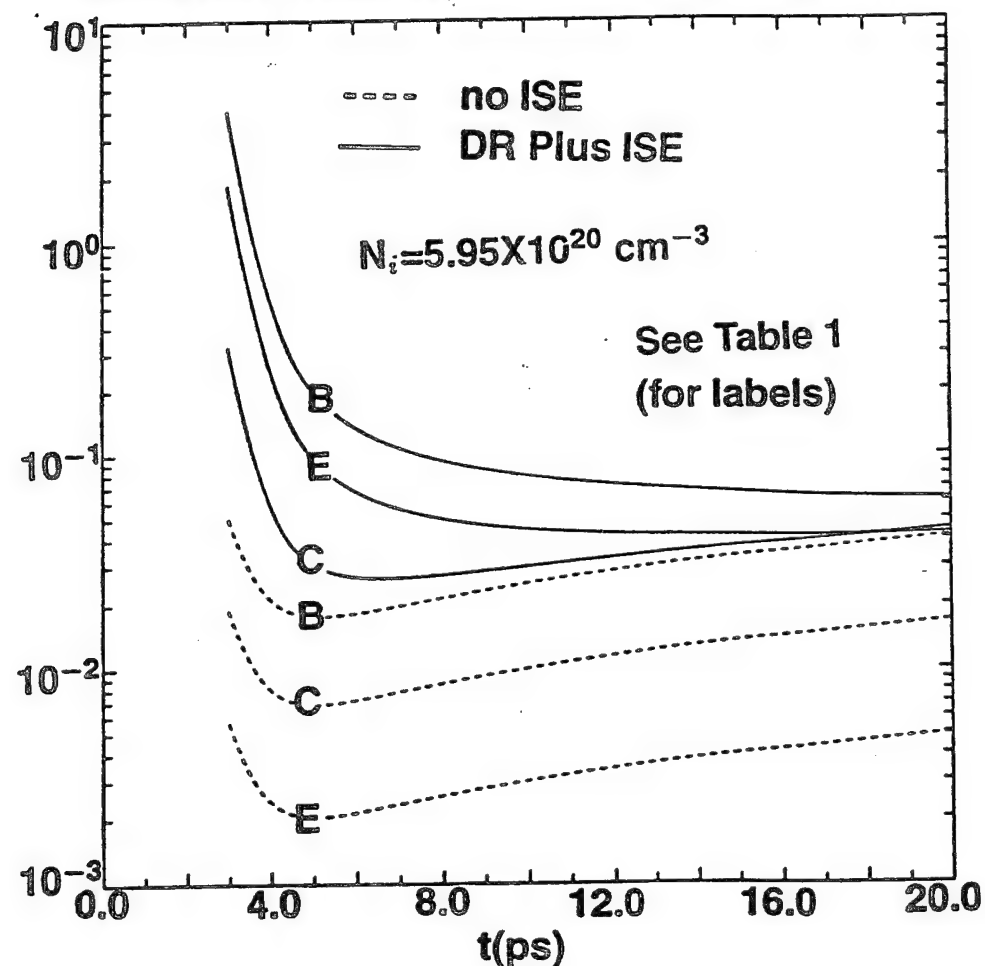


Fig. 12

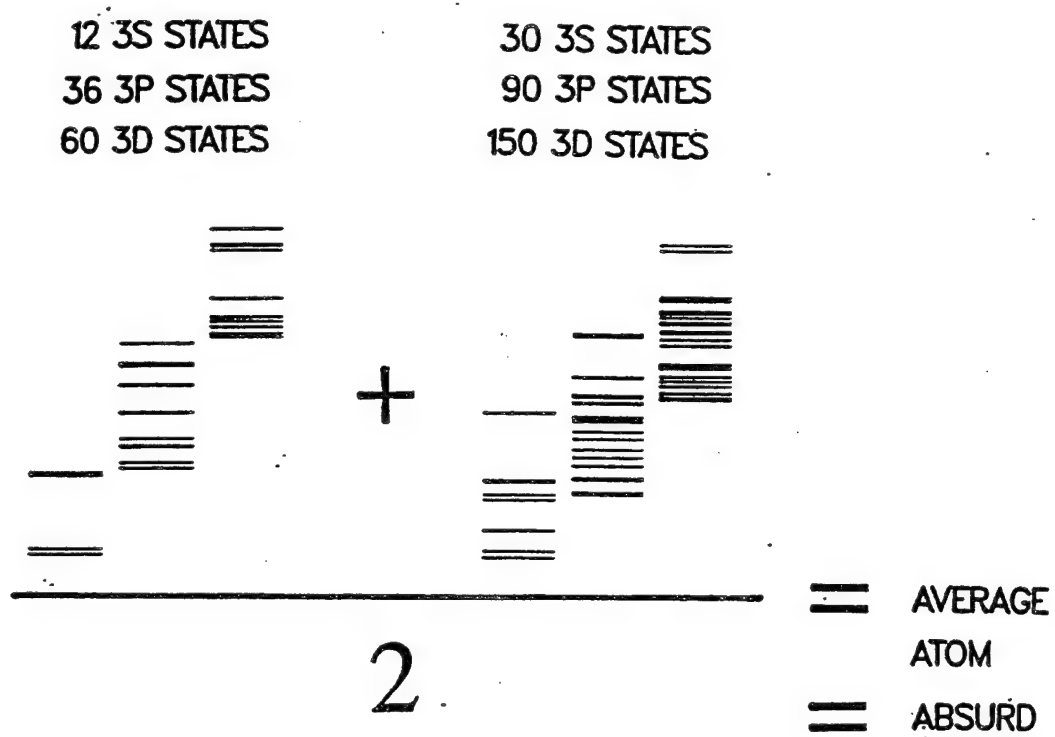


Fig. 13

VIII. CALCULATING MEASURABLE X-RAY QUANTITIES FROM SIMULATED PRS IMPLOSIONS

In recent years, significant progress has been made towards developing the tools necessary to determine the plasma conditions generated in imploding z-pinches. Progress has also been made in improving MHD simulations of PRS implosions, which improve the effectiveness of the experiments by providing an inexpensive way to explore the consequences of varying experimental parameters. For the most productive interaction, identical experimental and simulation quantities must be compared. To do this, the available experimental measurements must be analyzed to infer plasma conditions, and the detailed theoretical calculations must be meaningfully interpreted using the same methods and procedures that were used to analyze the experiments. This section describes a procedure for processing MHD calculation results to produce filtered pinhole photographs and spatially resolved spectral data, as well as time-resolved power outputs in analogy to experimentally observed quantities. These quantities can then be readily and meaningfully compared with experimental measurements.

Analysis of Experimental Data

Experimental measurements of PRS implosions yield a wealth of data, including voltage and current traces, pinhole photographs, yield measurements from calorimeters and diodes (which may be filtered to restrict the frequency band), and quantitative spectra (energy emission in spectral lines). In analyzing this data, the challenge is to infer from these instrumental readings the values of the physical quantities which are most likely to have produced the observed yield, spectrum and pulselwidth of the implosion.

The NRL Radiation Hydrodynamics Branch has developed an analysis procedure¹ that uses calculations of average x-ray power and plasma diameter, together with x-ray spectroscopic measurements, to infer the average ion density and electron temperature in the implosion. This procedure has been successfully used to optimize aluminum wire-array implosions.² It builds on a comprehensive theoretical atomic model, but also requires a careful and systematic treatment of the experimental data³ in order to determine useful values for bulk parameters like average power and diameter. The procedure derives time and space averaged results for the radiating region, and has been used to diagnose time-averaged measurements.⁴ It is important to note that it can be used with time-resolved measurements as well, as long as the experimental timescale is long enough to establish collisional-radiative equilibrium (CRE); this condition is typically well satisfied on the nanosecond scales typical of present-day experiments and of high-quality time-resolved measurements.

Analysis of Simulation Data

MHD simulations involve detailed calculation of plasma parameters at each point in space and time. The plasma parameters include electron and ion density and temperature, ionization state, and radiated energy at all important energies (line and continuum). This large amount of information must then be reduced to that which is observed in the experiment in order to make meaningful comparisons with experiment. The reduction process will necessarily depend on the nature of the observation; for example, the plasma diameter will be different for K-shell photons than for L-shell photons. For this reduction, we are primarily interested in obtaining the quantities used in the experimental data analysis, namely the radiated x-ray power and spectrum (at least including the Lyman and Helium series), and the plasma diameter.

The main objective here is to conduct the same analysis with simulation data as was done with the experimental data, and compare the two as a function of time. Accordingly, we used a set of aluminum wire-array implosions on Saturn with a fairly high x-ray yield and a very symmetric implosion profile, and modeled these with a 1-D MHD simulation. The MHD code⁵ has been used extensively in the past, and includes a comprehensive atomic radiation model. It regards the cylindrically symmetric plasma as being divided into 30 zones, which are annular shells. The MHD run used the same circuit parameters as the experimental shot, and obtained a very similar pulse profile and x-ray power (cf. Fig. (1) and Fig. (2)). (The most notable difference is the absence of a "bounce" after stagnation, due in part to the arbitrary zeroing of current after stagnation). Other data measured or inferred from experiment are the calculated pinch radius $r(t)$, and the aluminum K-shell spectra. The experimental values for the time-varying electron temperature and ion density, as determined by the NRL procedure discussed above, are shown in Fig. (3). The range of MHD-determined temperature and density can be seen in Fig. (4), which show these as a function of time in each zone.

It is evident from these figures that the complete set of simulation temperatures and densities can vary widely from the experimental values. The diagnostic significance of this variation depends largely on the radiative importance of the region; zones with very low mass or which are obscured from the detector by intervening optically thick plasma might have a significantly different temperature or density from the rest of the plasma, without affecting the radiation measurements. These variations might nevertheless significantly change the implosion dynamics, and a future application of the present work will be to find ways to detect such otherwise hidden plasma variations.

Theoretical Generation of Pinhole Photographs

A pinhole photograph is a direct representation of the radiative profile of the source. The

pinhole image at a point is the sum of the radiative emission and absorption in the plasma along the ray that connects the image point and the source. This is depicted in Fig. (5), which also gives some of the geometrical relations characterizing the problem (discussed below). The darkness of a point in the pinhole image should be proportional to the energy that reaches that point. For a time-resolved (or a streak) image, this can be taken as proportional to the instantaneous radiative power at the time of the image, but for a time-integrated image, the power must be integrated to obtain the energy.

The intensity along each ray in Fig. (5) is given by the equation of transfer:

$$\frac{dI_\nu}{d\tau_\nu} = I_\nu - S_\nu \quad (1)$$

where I_ν is the specific intensity at frequency ν (units, e.g., W cm^{-2}), and S_ν is the source function, τ_ν is the optical depth along the ray:

$$\tau_\nu(s) = \int_{s_0}^s \kappa_\nu(s) ds \quad (2)$$

and κ_ν is the absorption coefficient (units, e.g., cm^{-1}). The sign in Eq. (1) is chosen such that the optical depth increases from the observer towards the radiation source. We wish to solve this equation for the specific intensity at the observer. The formal solution of the equation of transfer at the near point τ_0 is

$$I_\nu(\tau_0) = e^{\tau_0} \int_{\tau_0}^{\tau} S(\tau') e^{-\tau'} d\tau' + I(\tau) e^{\tau - \tau_0} \quad (3)$$

The boundary condition is that the specific intensity in the direction of the observer vanishes at the far edge of the plasma. If the outermost zone's optical depth along the ray is $\Delta\tau$, the specific intensity I_{out} at the inner edge of this zone is then

$$I_{out} = S_{out} [1 - e^{-\Delta\tau}] \quad (4)$$

The intensity at each successive inner zone along the ray is readily found by extending this procedure, using I_{out} in Eq. (3) to get the specific intensity at the next inner zone, and so on; the specific intensity at the plasma edge facing the observer gives the radiative energy producing the pinhole image.

The source function S_ν and absorption coefficient κ_ν are determined by the plasma conditions in the implosion, and these functions are in fact used for energy balance in the MHD model. The MHD radiation transport, however, is concerned primarily with energy balance (radiation to full 4π steradians); in this case, the probability-of-escape method⁶ is effective, and is extremely efficient. For pinhole photographs, on the other hand, the main concern is ray tracing and energy transport to the recorder, and the procedure outlined above must be used, with multifrequency transport of each spectral line along each ray.

The frequency-dependent intensity on the edge of the plasma can be used to construct synthetic pinhole images of the evolving implosion in any wavelength band. These can be used to determine the plasma diameter and spectral properties at the observer.

For experimental observations, filters are commonly used to restrict the spectrum of the radiation generating the pinhole photograph. The filter attenuates the incident radiation along each ray in proportion to the filter thickness s_0 and the absorption function κ_ν^f characteristic of the filter material, so that the specific intensity actually producing the image is

$$I_\nu^{(image)} = I_\nu e^{-[\kappa_\nu^f s_0]} \quad (5)$$

Filters can be used singly or in combination to highlight features of interest. Use of experimental filter absorption functions is important in processing theoretical results because the filters can significantly alter the incident spectrum, affecting the observed size and motion of the imploding plasma as well as possibly changing spectral features such as which lines are most prominent. In the present calculations, however, the filter function has been set to unity, in order to focus on opacity effects in the imploding plasma.

An example synthetic pinhole image is shown in Fig. (6) for the Saturn aluminum wire array implosions chosen for comparison. The effective pinch diameter is plotted as a function of time in Fig. (7), where it can be seen that it is at greatest compression about a factor of 2 larger than the experimentally-observed pinch diameter, also shown. For this presentation, a simplified version of the pinhole photograph procedure was used, which assumed that the radiative emission from each zone was isotropic, and that the net emission at any radial position is given by the total power absorbed or emitted in that zone. This simplified model does not include the geometrical factors that are found in the detailed ray-tracing procedure described above, but the predicted diameter is nonetheless close to that inferred from experiment (and to the mass-averaged diameter). These simplified results are intended as an computationally inexpensive illustration of the method; later calculations will use the more accurate procedure.

Table I. Preliminary results from analysis of simulation data

Time	α ratio	Radius	Power	T_e	n_i
-1.2 ns	0.85	2 mm	3.2 TW	350 eV	$2.2 \times 10^{20} \text{ cm}^{-3}$
0.3 ns	1.40	2 mm	3.8 TW	550 eV	$1.8 \times 10^{20} \text{ cm}^{-3}$
2.4 ns	1.37	3 mm	2.8 TW	550 eV	$9 \times 10^{19} \text{ cm}^{-3}$
4.8 ns	0.71	4 mm	1.4 TW	400 eV	$7 \times 10^{19} \text{ cm}^{-3}$

If the simulation results are analyzed using the same procedure¹ as the experimental measurements, with the pinch diameter given as above, x-ray power obtained directly from the

simulation, and spectral line energies (Ly α and He α) given by the net pinch radiative output, values can be found for the effective electron temperature and ion density at times near the peak of the radiation. These results are shown in Table I, and are generally comparable to those inferred from experiment (shown in Fig. (3)).

Conclusions

We have briefly described a procedure for expressing theoretical data in the same vocabulary as experimental observation. Future work will capitalize on the theoretical capability to construct "what-if" scenarios. Goals:

1. Use filter and device response functions in the calculation.
2. Identify what radial parts of the plasma dominate in producing each spectral line. Frequency variation in opacity could allow filtered spectral diagnosis of the radial (temperature, density) profile in the implosion.
3. Refine the ray-tracing algorithm to allow quantitative comparisons of line strengths, and include 2D images (see Y.K. Chong, Ph.D. dissertation, U. Michigan, *in press*).

References

1. M.C. Coulter, K.G. Whitney and J.W. Thornhill, *J. Quant. Spectrosc. Rad. Transfer* **44**, 443 (1990); M.C. Coulter, K.G. Whitney and N.G. Loter, "Analysis of Maxwell Laboratory Wire Experiments," *NRL Memorandum Report 6383* (1988).
2. Radiation Hydrodynamics Branch, "Advanced Radiation Theory Support Annual Report 1994," *NRL Memorandum Report 7656* (1995), pg. 24ff.
3. P.E. Pulsifer, J.P. Apruzese, K.G. Whitney, R.B. Spielman, T.J. Nash, J.S. McGurn and L.E. Ruggles, "Systematic Analysis of Saturn Wire Array Implosion Observations," *NRL Memorandum Report 7659* (1995).
4. K.G. Whitney, J.W. Thornhill, J.L. Giuliani, Jr., J. Davis, L.A. Miles, E.E. Nolting, V.L. Kenyon, W.A. Speicer, J.A. Draper, C.R. Parsons, P. Dang, R.B. Spielman, T.J. Nash, J.S. McGurn, L.E. Ruggles, C. Deeney, R.R. Prasad, L. Warren, *Phys. Rev. E* **50**, 2166 (1994).
5. J.W. Thornhill et al., *J. Quant. Spectrosc. Rad. Transfer* **44**, 251 (1990); K.G. Whitney et al., *J. Appl. Phys.* **67**, 1725 (1990).
6. J.P. Apruzese, *J. Quant. Spectrosc. Radiat. Transfer* **25**, 419 (1981); R.W. Clark, J. Davis, J.P. Apruzese, J.L. Giuliani, Jr., *J. Quant. Spectrosc. Radiat. Transfer* **53**, 307 (1995).

S2095: Power from PCD215AW (TW)

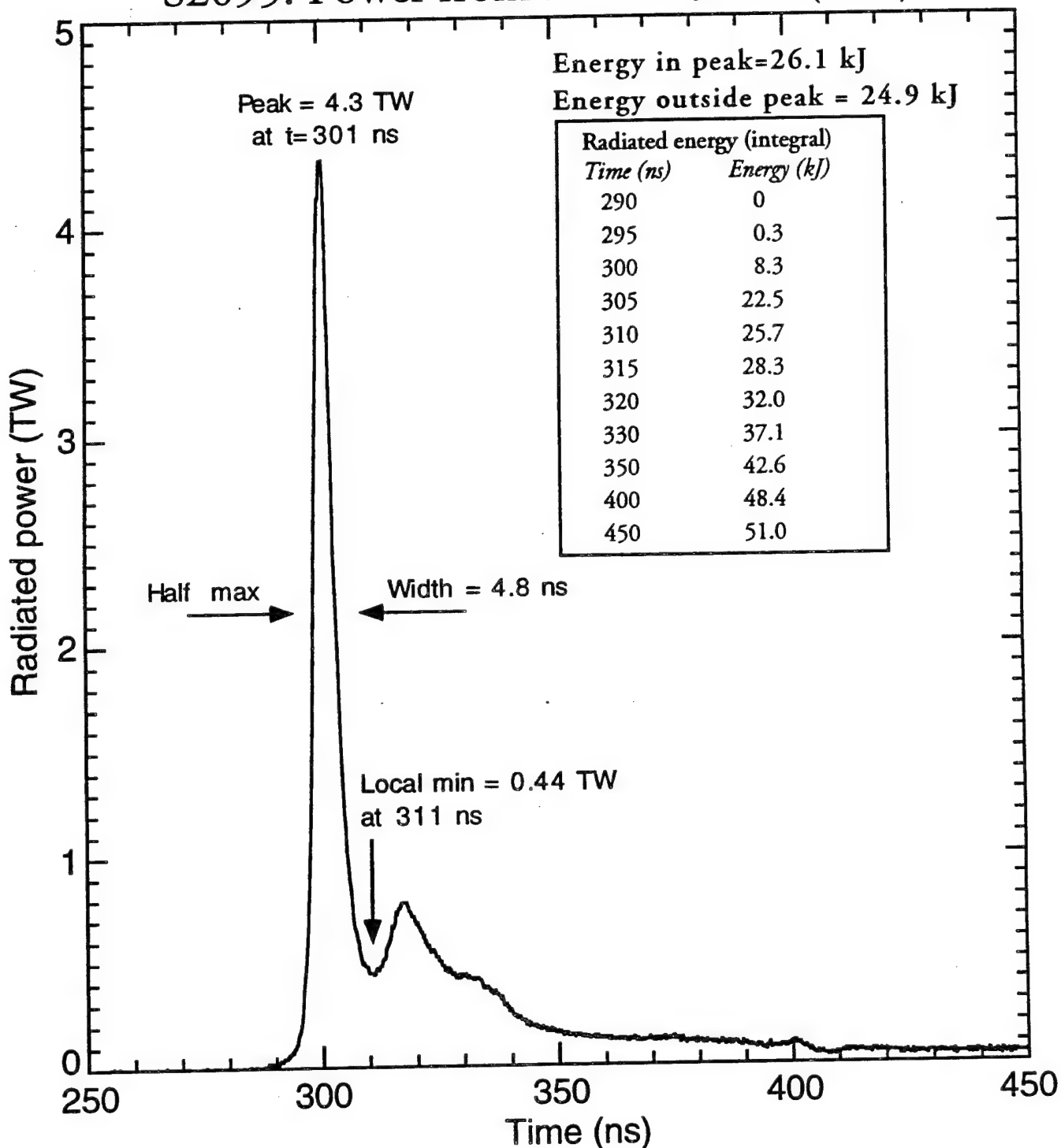


Figure 1. Experimentally observed x-ray power from a single implosion on Saturn (shot 2095), as measured by a PCD. The experiment used an array 90 aluminum wires with total mass $300 \mu\text{g}/\text{cm}^2$. Total reported x-ray yield was 53 kJ.

Theoretical power output

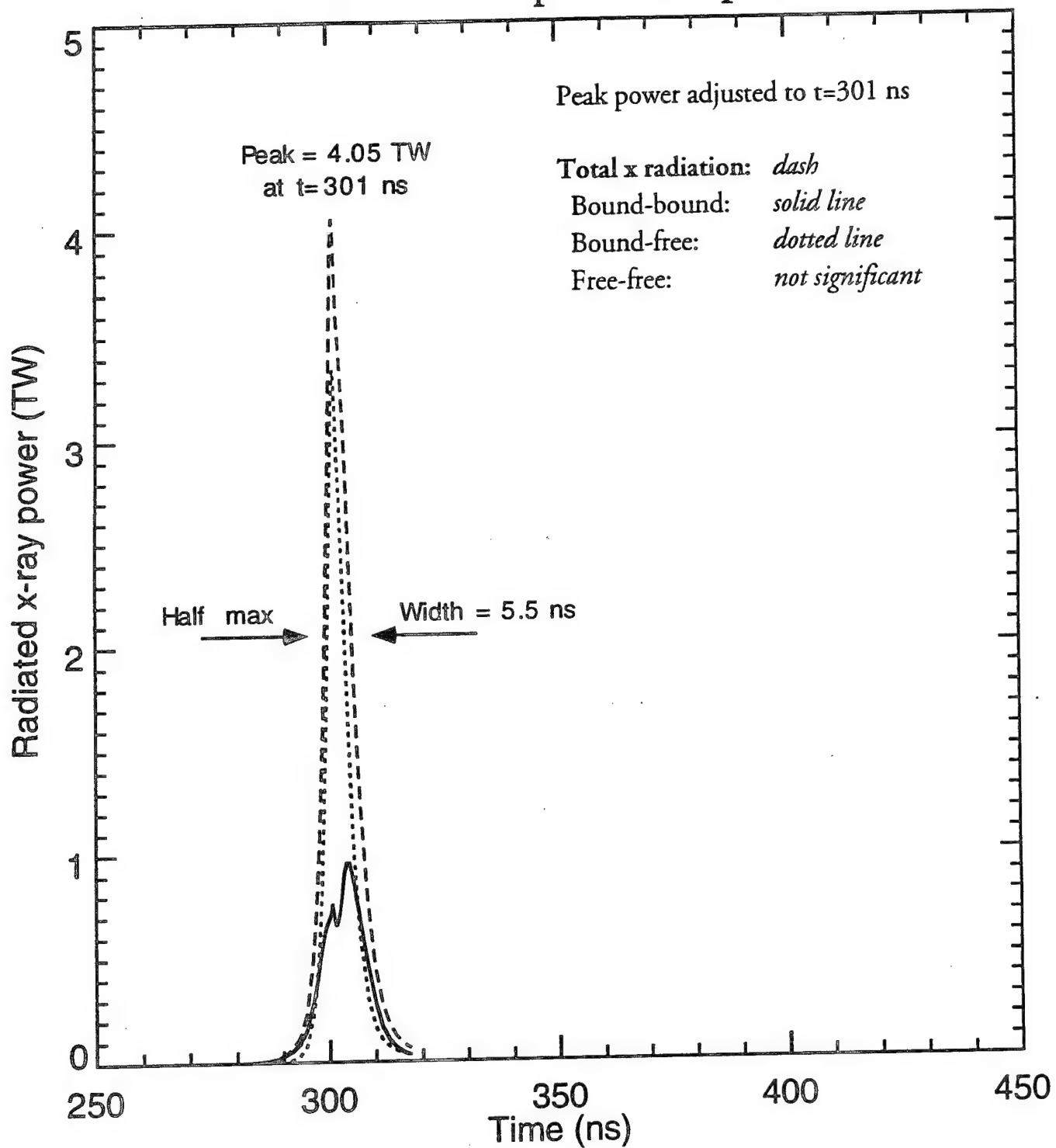


Figure 2. Theoretically (MHD) predicted x-ray power for a wire-array implosion with the same circuit and load parameters as were used in the implosion of Fig. (1)

Inferred Experimental Implosion Parameters

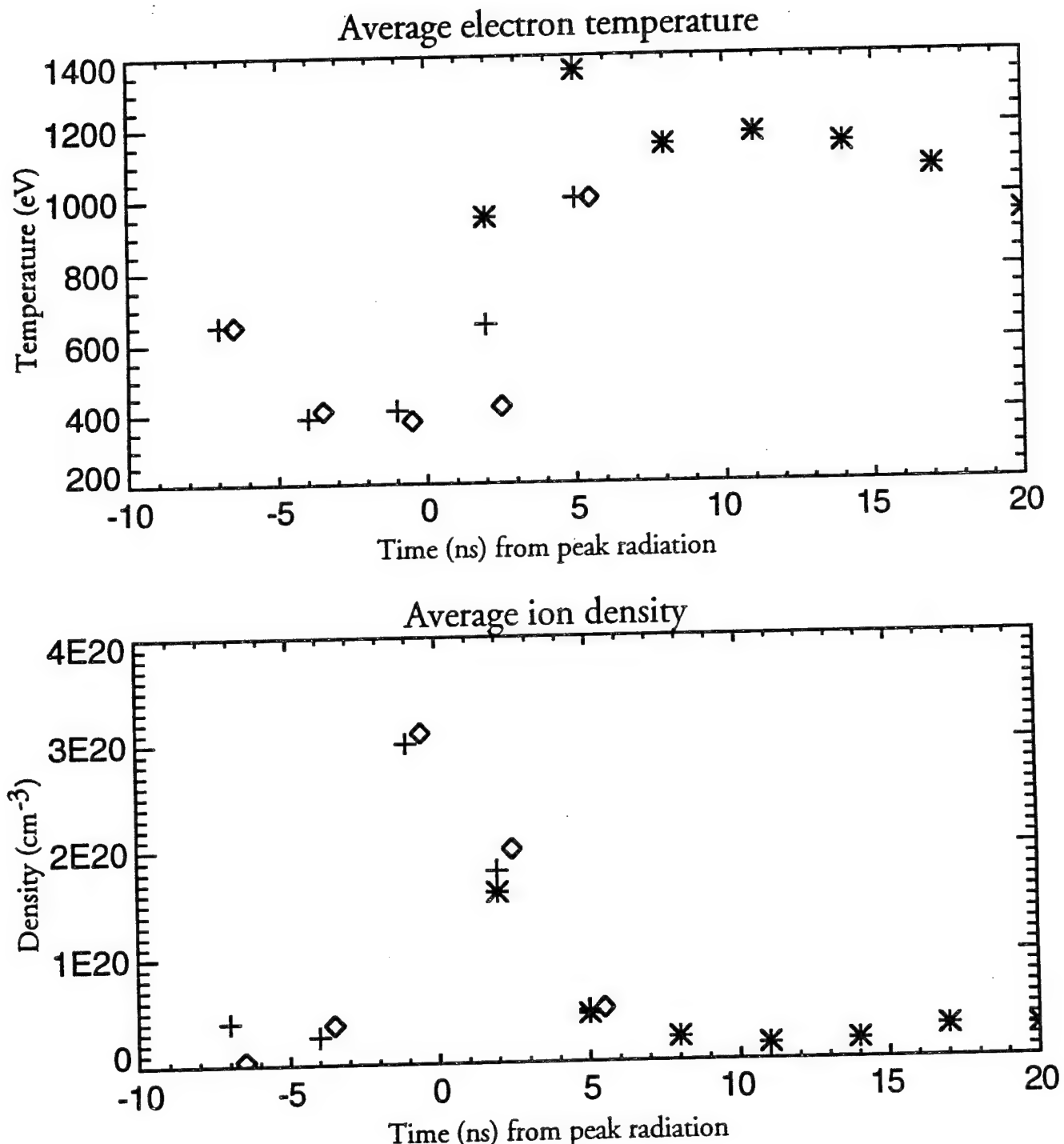


Figure 3. Experimentally-determined electron temperature and ion density for Saturn aluminum wire array implosions (90 wires), obtained according to the procedure in Ref.3. The points represent data for three different shots (2085, 2094 and 2095), all of which used identical parameters and generated very similar radiation pulses.

The symbols indicate: \diamond = shot 2085, $+$ = shot 2094, $*$ = shot 2095.

MHD Simulation Implosion Parameters

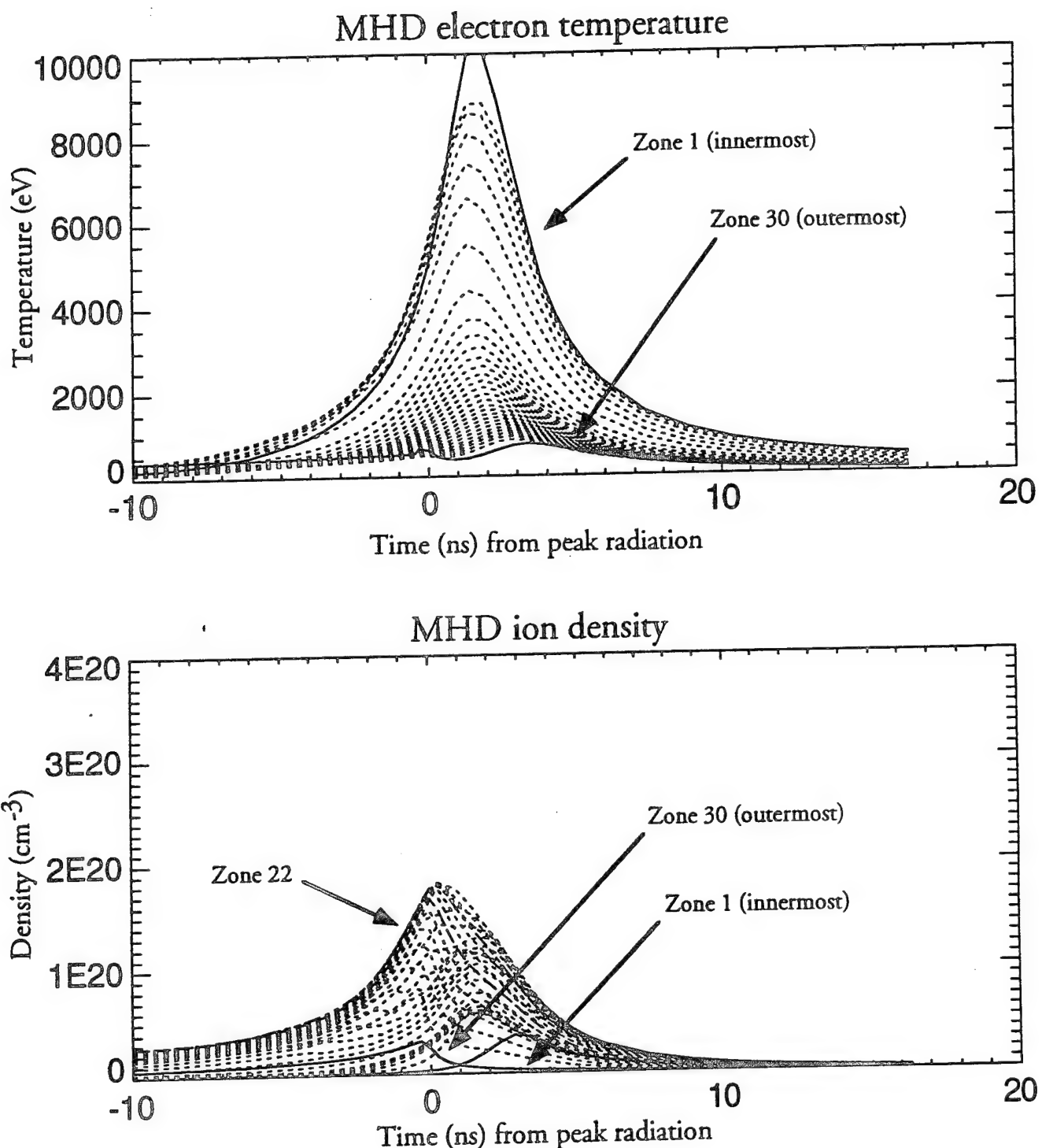


Figure 4. MHD simulation electron temperature and ion density in each radial zone of the plasma, as a function of time. Shot parameters were identical to those used in the experiments of Fig. 3.

Basic Ray tracing geometry

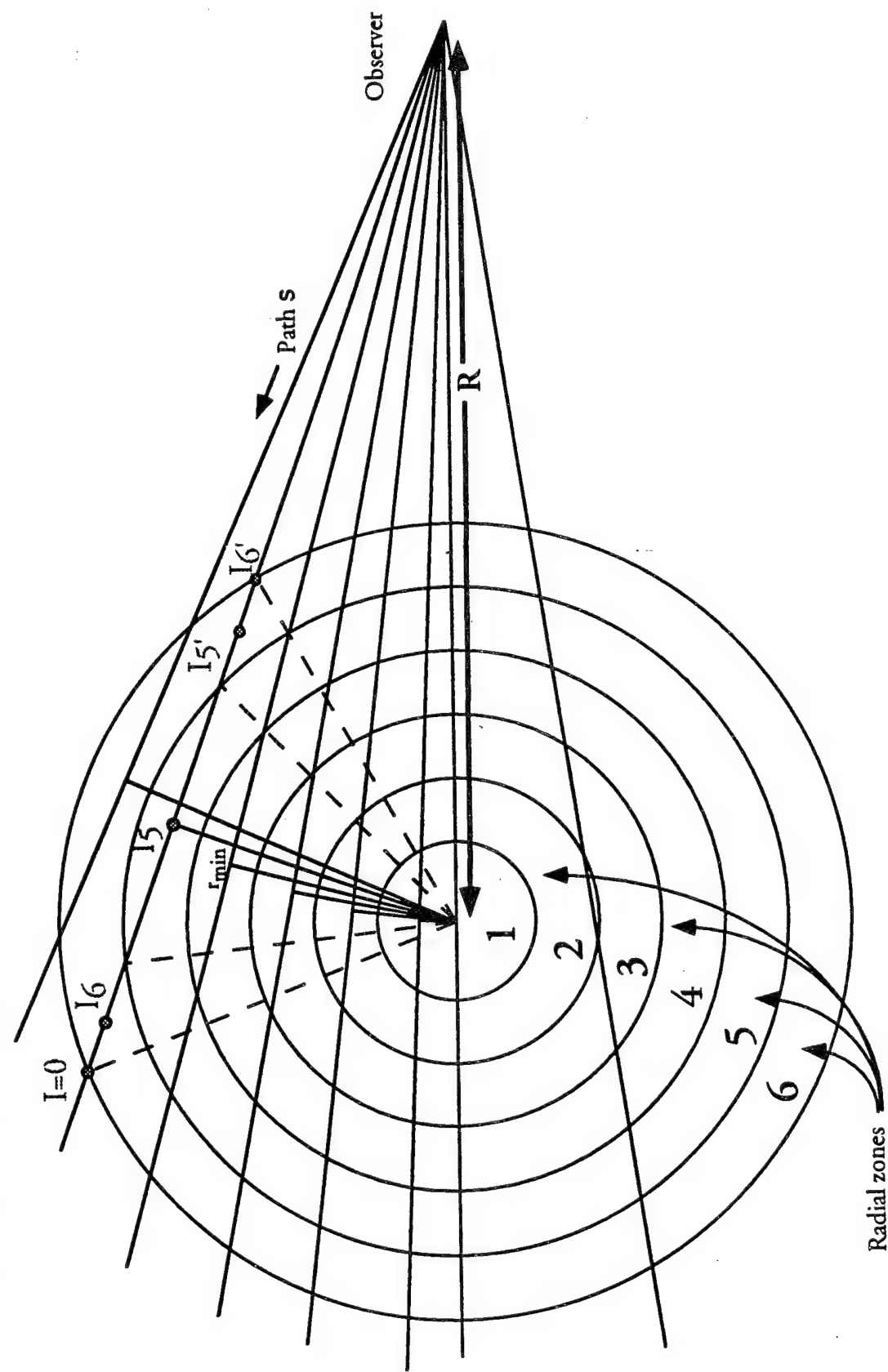


Figure 5. Basic geometry of pinhole photograph generation. The implosion is considered to be essentially cylindrical, with axial and azimuthal symmetry, and the diagram is in the plane perpendicular to the axial direction in a cylindrical coordinate system. The plasma is divided into multiple zones (6 pictured), which are cylindrical shells of outer radius r_i . The observer is located a distance R from the pinch center. Pinhole images result from radiation which follows the ray paths pictured; a ray is defined by its distance of closest approach r_{\min} to the center.

Model-generated Pinhole photographs

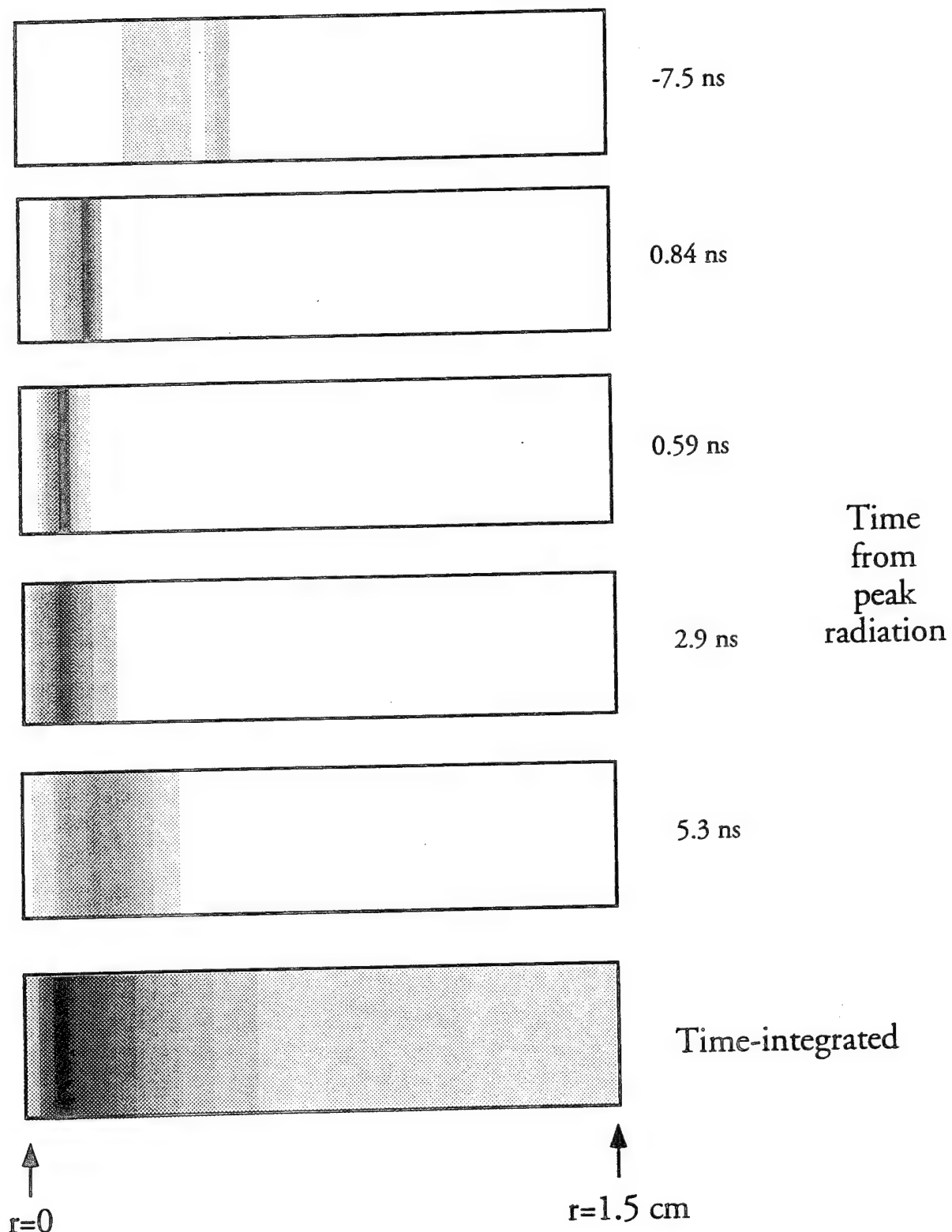


Figure 6. Synthetic pinhole photographs generated from MHD simulation data, at different times in the implosion (for total radiation output at each time see Fig. 1).

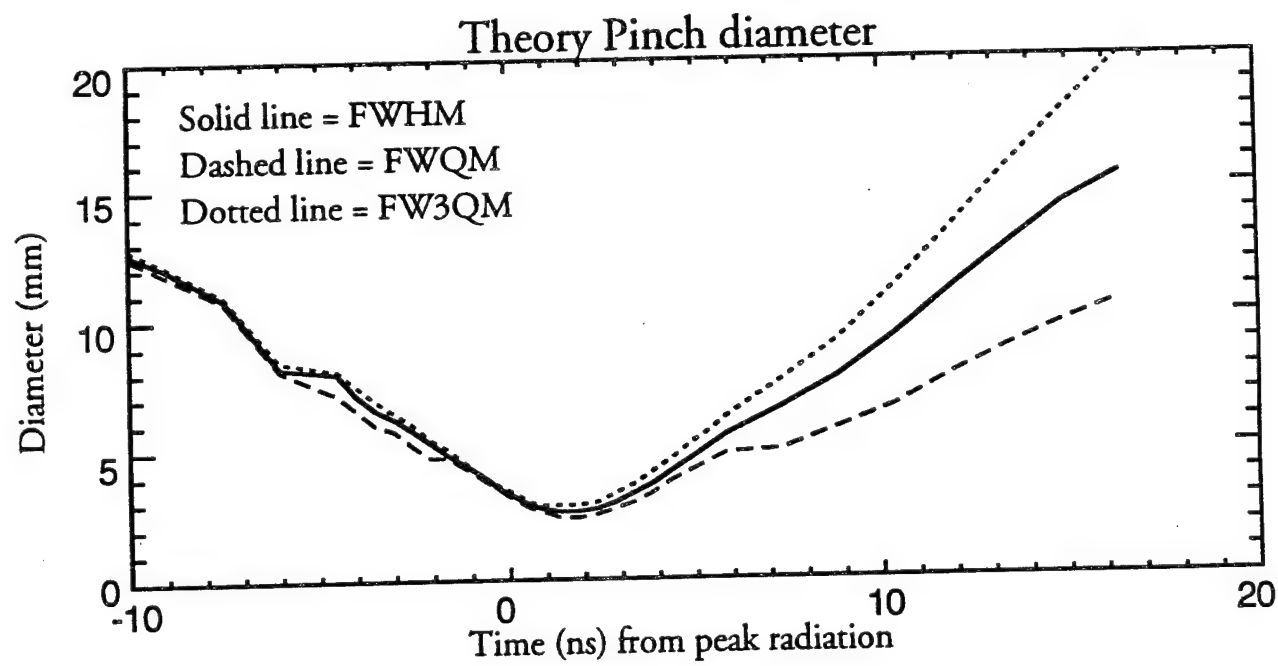
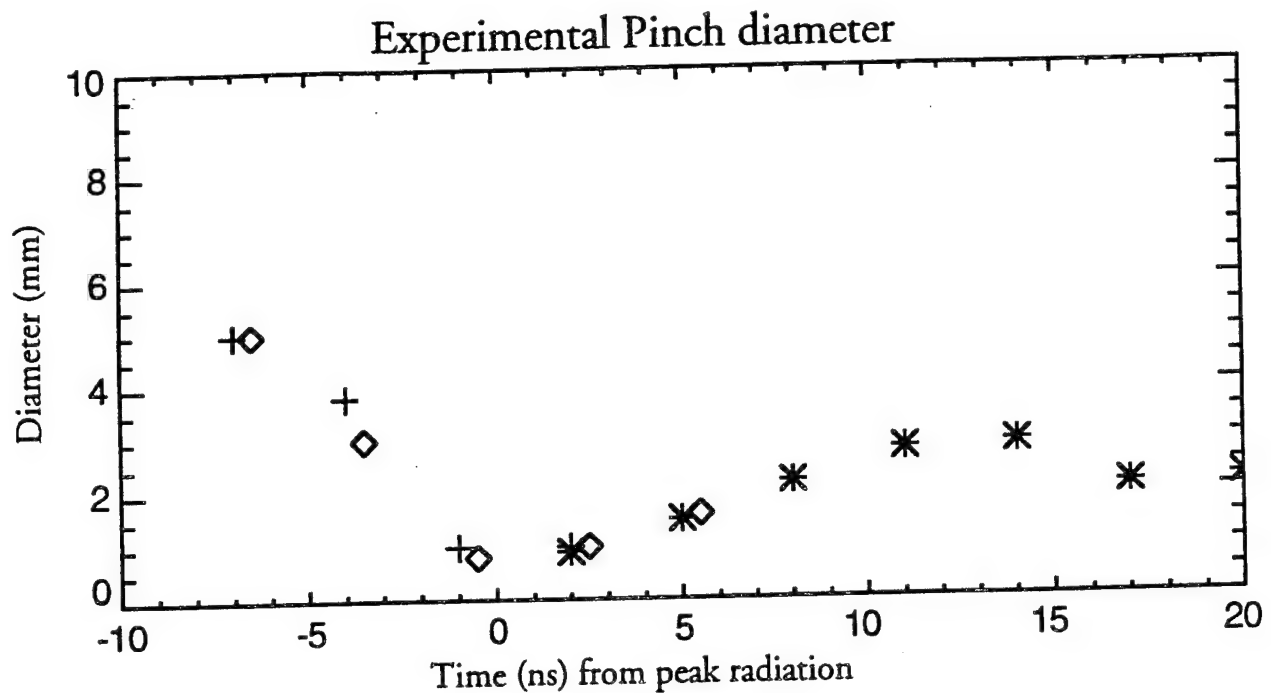


Figure 7. Pinch diameter, as measured experimentally (top) and as determined from MHD-predicted radiative output (bottom). Experimental diameter was determined by fitting a Gaussian to the axially averaged profile; symbols correspond to the 3 shots modeled, as in Fig. 3

IX. YIELD AND FIDELITY ENHANCEMENT BY OPTIMIZING THE RADIATION PHYSICS OF MIXTURES

In last year's final report, a series of experiments carried out at Physics International's Double EAGLE facility using Mg-coated Al wires was described. Initial analysis of the data available indicated that the K shell radiation was enhanced by the use of this near-Z element mixture. Since that time, more data has become available and the analysis was finalized. None of the preliminary conclusions have changed. The K shell yield increased from 28-50% for an 80:20 Al:Mg mixture compared to pure Al loads. Furthermore, the Mg was found to be hotter than the Al, 600 eV, as opposed to Al's 300 eV. Time resolved data supports the following picture: the Mg coat boils off the Al wire and is drawn into the axis where it is compressed and heated. The Al core straggles behind, and eventually arrives near axis where it becomes half as hot as the Mg that preceded it.

We believe that these results reflect both opacity and temperature effects. The theory of opacity enhancement of mixed loads was presented a decade ago in Ref. 1. When some of the Al wire is, in effect, shaved off and replaced with Mg, the two dominant He- and H-like 1-2 lines of K shell Al are somewhat less optically thick, 20% less in the most interesting case of the 80:20 Al:Mg mixture. Furthermore, the strong analogous lines of Mg are subject to much less opacity attenuation than those of Al, since Mg represents only one-fifth of the load. The result is an increase of the K shell power even if the temperature of the elemental constituents is the same. The extra heating of the Mg enhanced the effect. This data, representing an important advance in our understanding of Z pinches, has now been published in the Physical Review (Ref. 2).

This very encouraging experimental result with two specific elements represents the confirmation of an effect predicted a decade ago in Ref. 1. However, there is no *a priori* reason to believe that Al and Mg are necessarily the optimal pair of elements or that more than two elements might not do an even better job of yield enhancement. Note that there is another DNA goal which this effect serves well: fidelity enhancement. The use of mixtures provides x-rays in different regions of the spectrum rather than concentrating them in one narrow region of K shell line emission. *The fact that there are so many easily adjustable parameters: the number of elements used, their atomic numbers, and their proportions in the load gives reason for optimism that very*

useful combinations will be found and become a staple of DNA's simulation capability.

To get closer to a determination of what would be optimal, a series of calculations was done using all of the elements of atomic numbers between 11 and 14: Na, Mg, Al, and Si, respectively. Temperatures of 100 to 1000 eV were examined, covering most of the range in which these elements are stripped to the K shell. Fig. 1 shows the fraction of each element which exists in the H-like or He-like stages as a function of temperature for typical pinch conditions. This calculation displays quantitatively the need for increasing temperature with increasing atomic number. The K shell ionization fraction for each element is a major determinant of its ability to radiate copious K shell emission.

Two other factors are also important in determining the emitted K shell power for a given element. First is the collisional excitation rate for the levels which radiate the lines. This rate generally increases with temperature. The other important physical process is self-absorption of the line radiation due to the generally high opacity of the strong lines. The result of these latter two factors is that the radiated power tends to increase even when ionization reduces the fraction of the radiating ion. As ionization proceeds, the optical depth of the strong lines is reduced since there are fewer absorbers in the line of sight. The increased collisional creation of photons further augments the emission. The result for these four elements is displayed in Fig. 2, which presents the K shell radiated power as a function of temperature up to a keV. In each case, a rapid initial rise with temperature is followed by a gentler increase at higher temperatures. Note that, for temperatures in excess of 400 eV, the higher the atomic number, the greater the radiated power. A key effect contributing to this result is the atomic number (Z) scaling of the optical depth of a given transition. Such scaling depends upon the line Doppler width and some fundamental atomic parameters, and shows that the optical depth of a specific line at a given density varies as Z^{-3} , i.e., a sharp reduction in opacity with increasing atomic number. Therefore, if Si can be stripped to the K shell, it is a better radiator than, for instance, Mg. For the pinch conditions found in the Al:Mg experiments performed at PI, we find that had the Mg coat been Si, the K shell yield would have doubled rather than increasing by up to 50%. A lower atomic number element such as Na would be useful if the load can be designed to place it in the cooler outer region of the pinch. It is clear that both yield and fidelity can be improved by further exploration of these effects in well-considered experiments.

One of the more exciting aspects of the mixture concept is that higher atomic number elements generating harder photons are even more susceptible to positive results than the elements already successfully demonstrated.

REFERENCES

1. J. P. Apruzese and J. Davis, *J. Appl. Phys.* **57**, 4349 (1985).
2. C. Deeney *et al.*, *Phys. Rev. E* **51**, 4823 (1995).

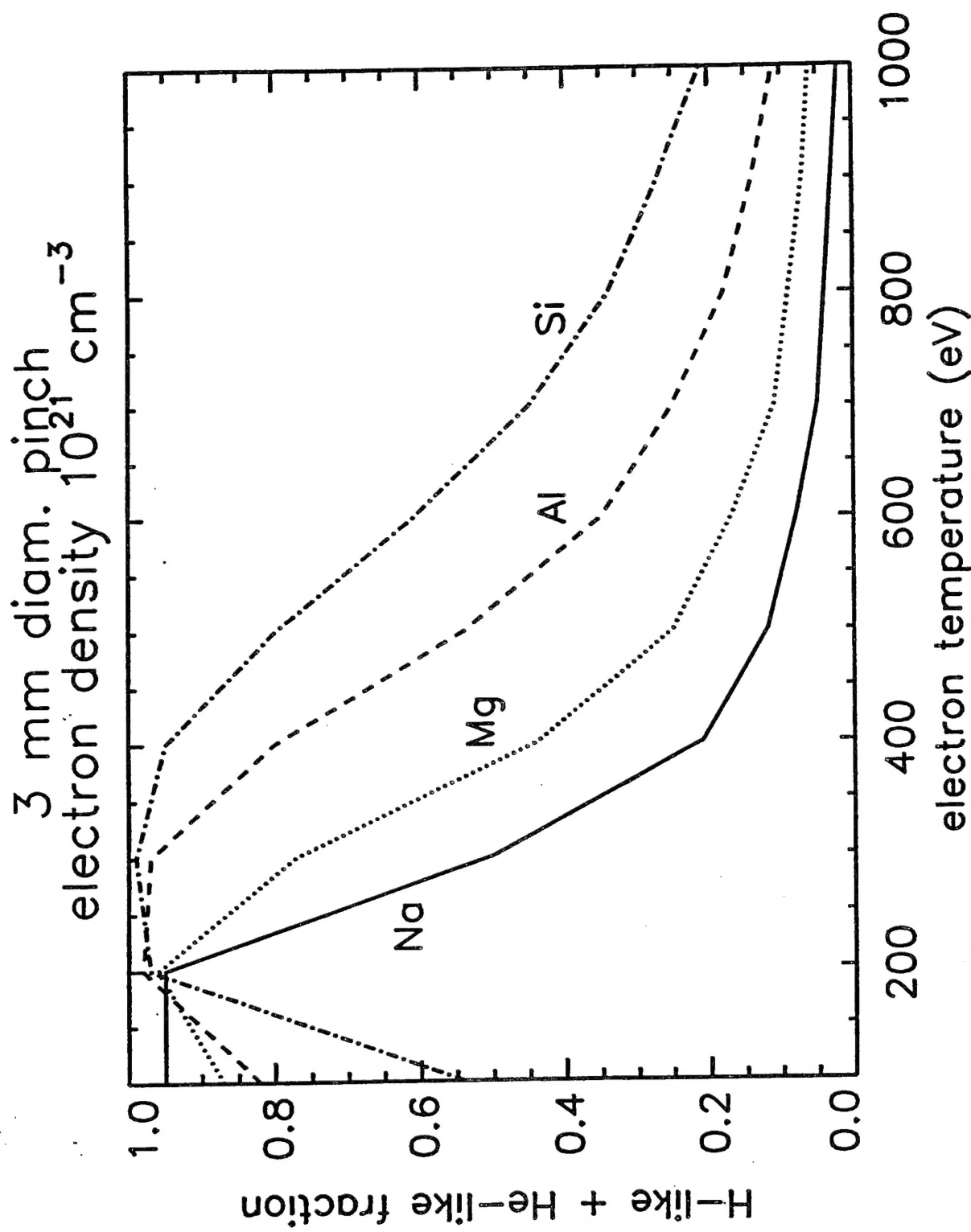


FIG. 1. Sums of the H- and He-like fractions are plotted as a function of electron temperature for the indicated plasma conditions for Na, Mg, Al, and Si.

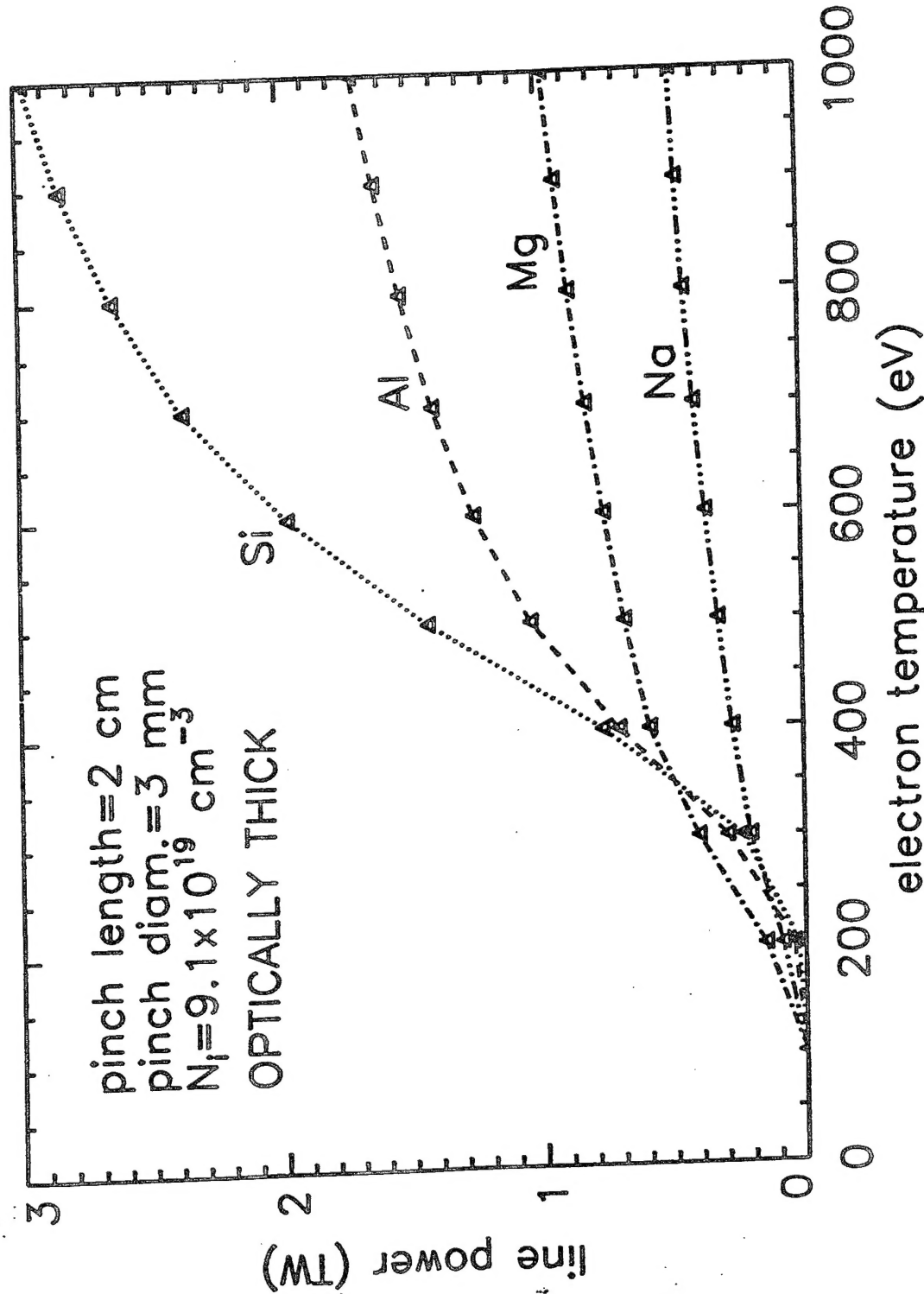


FIG. 2. K shell line power is shown vs. electron temperature for Na, Mg, Al, and Si, for the indicated pinch conditions.